Universitat Autònoma de Barcelona

Supersymmetry and topology in coupled optical waveguides

Gerard Queralt o Isach

ADVERTIMENT. L'accés als continguts d'aquesta tesi queda condicionat a l'acceptació de les condicions d'ús establertes per la següent llicència Creative Commons: http://cat.creativecommons.org/?page_id=184

ADVERTENCIA. El acceso a los contenidos de esta tesis queda condicionado a la aceptación de las condiciones de uso establecidas por la siguiente licencia Creative Commons: http://es.creativecommons.org/blog/licencias/

WARNING. The access to the contents of this doctoral thesis it is limited to the acceptance of the use conditions set by the following Creative Commons license: https://creativecommons.org/licenses/?lang=en

Supersymmetry and topology in coupled optical waveguides

Gerard Queraltó Isach

Submitted in fulfillment of
the requirements for the degree of
Doctor of Physics

Thesis supervisor:
Dr. Jordi Mompart Penina
Dr. Verònica Ahufinger Breto

Departament de Física
Universitat Autònoma de Barcelona

Bellaterra, September 2020

A la meva família,
amb un record especial
per a la meva tieta

Agraïments

Aquestes línies signifiquen el final d'una etapa de més de deu anys en el món de la física que va començar amb el grau a la UB, va continuar amb el màster a la UPC i culmina amb aquest doctorat a la UAB. Ha estat una gran experiència viure aquesta etapa en la que he crescut tant a nivell personal com intel·lectual i en la que m'han acompanyat moltes persones a qui vull dedicar les següents línies d'agraïment.

Primer de tot vull donar les gràcies al Jordi i a la Verònica per haver-me donat l'oportunitat de realitzar el doctorat amb ells. Quan em vaig plantejar fer el doctorat, tenia clar que els directors de tesis eren una peça fonamental i que aquests no només havien de ser bons en el seu vessant acadèmic sinó també en el personal. I la veritat és que heu complert totes les expectatives, acompanyant-me tant a nivell científic com personal. D'una banda, sempre estàveu disponibles quan tenia dubtes al començament, però d'altra banda, també m'heu sabut deixar l'espai necessari perquè emprengués noves col·laboracions i projectes en l'etapa final. En particular, vull agrair al Jordi el seu optimisme en tots els projectes que ens proposàvem, sempre veient noves oportunitats, i a la Verònica la seva feina incansable de polir fins l'últim detall els nostres treballs, sempre millorant-ne la seva qualitat. Crec que formeu un equip magnífic i que us complementeu perfectament. Ha estat un plaer treballar amb vosaltres.

També vull agrair a la resta de professors amb qui he compartit grup aquests anys. En particular, al Francesc, a l'Àngel, al Gaspar i al Juan Carlos per tot el que m'heu ensenyat del Laboratori d'Òptica, a la Sònia per fer-ho tot tant fàcil quan donàvem junts els problemes d'Ones i Òptica, a l'Alessio per la infinitat de cafès i idees compartides, al Todor per les seves històries i anècdotes, al Juan i a la Marifí per ajudar quan ha fet falta, i al Ramón, per compartir sempre un somriure quan te'l creuaves pel passadís. També vull agrair a l'Anna del grup d'Informació Quàntica que em dirigís la tesi del màster i m'encaminés a seguir aquest camí.

Amb qui més hores he compartit durant aquests quatre anys però ha estat amb el Gerard i el Josep, i més recentment també amb l'Eulàlia, companys de despatx i d'etapa. Durant aquests anys hem compartit des de discussions sobre física a dubtes existencials sobre què estàvem fent allà i cap on encaminar les nostres vides. Sempre hi ha hagut bon ambient i això ha fet el dia a dia més agradable. També agrair al Juanlu que sempre hagi aportant la seva alegria i les seves anècdotes quan ha estat pel grup i a la Irene, l'Albert i el Haolin els moments compartits, sobretot amb les activitat de divulgació. També agrair al Joan que ens introduís tant bé al grup els primers mesos, al Dani pel bon ambient els mesos que va estar aquí i a l'Àlex per estar sempre disponible per ajudar en qualsevol cosa tot i no haver coincidit directament al grup. Ha estat un plaer compartir aquests anys amb vosaltres.

I would like to express my gratitude to Prof. Szameit for hosting me in his research group in Rostock Universität to perform my short stays and for contributing to the research presented in this thesis. It was a pleasure for me to be there and I felt really comfortable during those months. Moreover, I would also want to thank Matthias, Mark and Luckas for making easy to work with them and also Steffen, Rike, Nora, Marco, Eric, Sebastian, Tobias and Max for welcoming me and sharing moments together. In particular, I want to thank Rike for always being available for any plan.

I would also like to express my gratitude to Prof. von Freymann for inviting me to visit his research group in Kaiserslautern Universität and for supporting the idea of experimentally implementing our proposal based on light carrying OAM. I would also want to thank Christina for all the work that she has done for this project and for working on it even when the results were not accompanying. I also want to thank Julian for his collaboration in this work.

Fora de l'àmbit acadèmic també vull donar les gràcies a tota aquella gent que heu estat presents en el meu dia a dia durant aquests anys. En especial, a tots els amics del Pla, que tot i les meves absències ja sigui per les estades fora, pels congressos o pels castells, sempre hi són quan torno. Tot i que molts m'ho hagueu preguntat i encara no sapigueu ben bé què estic investigant, que sapigueu que si acabo aquesta etapa també és gràcies a vosaltres. En particular, vull agrair a l'Anna el seu suport quan he viscut moments complicats, gràcies per ser-hi sempre. També vull agrair a tots els amics de castells, i en especial, als Puretes, totes les estones compartides fent castells, festes, àpats i viatges. Tota aquesta activitat social ha estat complementària i necessària per arribar fins aquí.

També vull agrair les persones que han compartit d'una manera més propera aquests anys amb mi. A l'Elena, per compartir amb mi els primers anys quan tot just m'endinsava al món de la física. A la Xènia, per viure plegats els anys del màster i el començament del doctorat. Em fa especial il·lusió acabar aquesta etapa al mateix moment en què tu arribes al teu cim particular i ja ets graduada en Medicina! Un plaer haver compartit part del camí plegats. I finalment a la Clara, per haver compartit amb mi aquesta etapa final del doctorat. En especial, vull agrair-te el teu suport constant i els teus ànims durant aquests últims mesos que han estat especialment complicats. Gràcies per donar-me la mà i estirar-me en aquest tram final. És una sort tenir-te al costat.

Finalment, voldria agrair a la meva família que sempre hagueu estat al meu costat. Si avui estic escrivint aquestes línies és per què vosaltres m'heu proporcionat l'entorn i el suport necessaris per aconseguir-ho. Sempre m'heu animat a seguir endavant amb els meus projectes, encara que això impliqués que em perdés pel món i que passessim temps sense veure'ns. En especial, vull agrair al meu pare el seu suport sempre que he necessitat qualsevol cosa i el seu exemple en aquest món acadèmic, en el que ha arribat a ser doctor en Filosofia fa tot just tres anys. Jo no vaig entendre res de la teva tesi i tu no entendràs res de la meva, però els dos sabem la feina que requereix aconseguir-ho i el valor que té. A la meva mare, per haver-me cuidat en el dia a dia durant molts anys, proporcionant-me un entorn perfecte on poder créixer. Tot i que aquesta tesi a tu et quedi encara més lluny, sempre m'has animat i m'has donat suport per aconseguir aquest repte. També agrair a la meva germana que sempre estigui allà per a qualsevol cosa encara que passin dies sense que sapiguem res l'un de l'altre. Els dos sabem que hi som per a les coses importants. No puc acabar però sense dedicar unes línies a la meva tieta. Has marxat injustament i abans d'hora, et quedava molt per viure. Sé que haguessis estat molt orgullosa de mi i haguessis portat un pica-pica boníssim el dia de la defensa de la tesi. No saps com et trobem a faltar. Una abraçada ben forta allà on siguis.

Gerard Queraltó Isach
Bellaterra, juliol de 2020.

List of publications by Gerard Queraltó

The research contained in this thesis is supported by the following publications:

Chapter 4: Mode-division (de)multiplexing using adiabatic passage and supersymmetric waveguides

1. G. Queraltó, V. Ahufinger and J. Mompart, *Mode-division (de)multiplexing using adiabatic passage and supersymmetric waveguides*, Optics Express **25**, 27396 (2017).

Chapter 5: Integrated photonic devices based on adiabatic transitions between supersymmetric structures

2. G. Queraltó, V. Ahufinger and J. Mompart, *Integrated photonic devices based on adiabatic transitions between supersymmetric structures*, Optics Express **26**, 33797 (2018).

Chapter 6: Topological state engineering via supersymmetric transformations

3. G. Queraltó, M. Kremer, L. Maczewsky, M. Heinrich, J. Mompart, V. Ahufinger and A. Szameit, *Topological state engineering via supersymmetric transformations*, Communications Physics **3**, 49 (2020).

Chapter 7: Artificial gauge field switching using orbital angular momentum modes in optical waveguides

4. C. Jörg, G. Queraltó, M. Kremer, G. Pelegrí, J. Schulz, A. Szameit, G. von Freymann, J. Mompart, V. Ahufinger, *Artificial gauge field switching using orbital angular momentum modes in optical waveguides*, to be published in Light Science & Applications (2020).

Other publications by Gerard Queraltó not included in this thesis:

5. A. Gallemí, G. Queraltó, M. Guilleumas, R. Mayol, and A. Sanpera, *Quantum spin models with mesoscopic Bose-Einstein condensates*, Physical Review A **94**, 063626 (2016).

Contents

1 Introduction **1**

2 Physical platform: optical waveguides **7**
2.1 Optical waveguides . . . 8
2.2 Electromagnetic theory of light . . . 9
2.2.1 Light propagation in homogeneous media . . . 9
2.2.2 Light propagation in optical waveguides . . . 10
2.3 Coupled-mode theory . . . 15
2.3.1 Directional coupler . . . 15
2.3.2 Arrays of waveguides . . . 19
2.4 Quantum-optical analogies . . . 20
2.4.1 Mathematical analogies . . . 20
2.4.2 Applications in this thesis . . . 23

3 Supersymmetry in optics **25**
3.1 Introduction . . . 26
3.2 Supersymmetric quantum mechanics . . . 27
3.3 Supersymmetry in optics . . . 29
3.3.1 Single waveguide . . . 30
3.3.2 Array of waveguides . . . 33
3.4 Discrete supersymmetry . . . 34
3.4.1 Cholesky factorization . . . 35
3.4.2 QR factorization . . . 36
3.5 Two-dimensional supersymmetry . . . 37
3.6 Conclusions . . . 40

4 Mode-division (de)multiplexing using adiabatic passage and supersymmetric waveguides 41
4.1 Introduction . . . 42
4.2 Physical system . . . 43
4.3 Theoretical background . . . 44
4.3.1 Spatial adiabatic passage technique . . . 46
4.3.2 Supersymmetric waveguides . . . 47
4.4 Results and discussion . . . 48
4.5 Conclusions . . . 57

5 Integrated photonic devices based on adiabatic transitions between supersymmetric structures 59
5.1 Introduction . . . 60
5.2 Theoretical model . . . 61
5.3 Physical system . . . 63
5.3.1 Single-waveguide structure . . . 64
5.3.2 Two-waveguide structure . . . 66
5.4 Numerical results . . . 69
5.4.1 Tapered waveguide . . . 69
5.4.2 Single-waveguide mode filter . . . 71
5.4.3 Beam splitter . . . 72
5.4.4 Mach-Zehnder interferometer . . . 74
5.5 Conclusions . . . 76

6 Topological state engineering via supersymmetric transformations 77
6.1 Introduction . . . 78
6.2 Theory . . . 79
6.2.1 The Su-Schrieffer-Heeger (SSH) model . . . 79
6.2.2 Discrete SUSY transformations . . . 84
6.3 Supersymmetric topological photonic structures . . . 86
6.3.1 Experimental set-up . . . 90
6.3.2 Design of the superpartner structures . . . 93
6.3.3 Robustness of the topological states . . . 96
6.4 Experimental verification . . . 98
6.5 Conclusions . . . 105

7 Artificial gauge field switching using orbital angular momentum modes in optical waveguides 107
7.1 Introduction . . . 108
7.2 Physical system . . . 109

7.2.1 Unit cell structure and coupling amplitudes 110
7.2.2 Band-structure 115
7.2.3 Light dynamics 119
7.2.4 Robustness of the Aharonov-Bohm caging effect 122
7.3 Experimental verification 124
7.3.1 Sample fabrication 124
7.3.2 Experimental observation of Aharonov-Bohm caging 126
7.4 Conclusions 132

8 Conclusions and outlook **133**

1 Introduction

The notion of light dates back to the ancient Egypt and Mesopotamia, where mirrors and lenses were used, for instance, to illuminate the inside of pyramids [1]. Nevertheless, the systematic study of light generation, propagation and interaction with objects i.e., optics, remained elusive until ancient Greek philosophers investigated them in order to understand vision. Specifically, around 300 B.C., Euclid explained in *Optics* that light propagates following straight lines and enunciated the reflection law [2]. Four centuries latter, Hero of Alexandria discovered that light propagates following the shortest path possible and Ptolemy investigated light refraction from air to water [3]. Their postulates would last until the 11^{th} century, when the Arabic polymath al-Haytham compiled a rigorous research in *Book of Optics* [4]. His methodology arrived in western countries two centuries later by the hand of Grosseteste, who contributed to introduce a mathematical description of light, and Witello, who wrote the standard book in optics of the epoch [5]. The scientific advances in the field flourished again in the 17^{th} century [4], when Kepler laid the foundations of classical optics [6] and the discussion over light nature became the center of attention in the field. In this context, scientists such as Huygens proposed a wave theory of light [7] while others like Newton supported a corpuscular theory of light [8]. Newton's corpuscular theory prevailed until the 19^{th} century, when Young and Fresnel performed interference experiments with light [9] and Maxwell presented an electromagnetic theory of light [10], vindicating light wave nature. Nevertheless, this turned around again by the beginning of the 20^{th} century, when Planck explained the black-body radiation [11] and Einstein described the photoelectric effect [12] considering that light is quantized in photons. The discussion over light nature ended in 1928 when Bohr introduced the concept of complementarity, stating that light can behave both as a wave or as a particle depending on the experimental arrangement, which was later connected to the wave-particle duality of quantum mechanics (QM) [13].

In the early 20$^{\text{th}}$ century, QM emerged as a theory to explain the black-body radiation [11], the photoelectric effect [12], the spectral lines of atomic gases [14] and the internal structure of atoms [15]. Twenty years later, the standard formulation of QM unified Born's matrix formalism [16], the Schrödinger's and de Broglie's wave formalism [17, 18] and the Heisenberg's uncertainty principle [19]. In the field of optics, the appearance of QM had a direct impact with the birth of quantum optics [20, 21], which studies photons and their interactions with matter, and, later on, with the invention of the laser [22]. Due to its exceptional properties of high spatial and temporal coherence, lasers have boosted science and technology until nowadays, with uncountable applications in sectors ranging from industry to medicine [23]. In particular, its discovery played a fundamental role in the development of integrated optics, which revolutionized modern optics with the idea proposed by Miller in 1969 [24] of creating planar optical circuits guiding light in a similar way than electrons are guided in electronic circuits [25]. The key elements to achieve it were optical waveguides with low losses, whose discovery by Kao was awarded in 2009 with the Nobel Prize [26], connecting the passive and active elements required for optical operations in integrated circuits [27]. Their development occurred in a relatively short period of time, with the fabrication of the first optical waveguides around the 70's and its integration in telecommunication systems by the 80's [28]. Moreover, the capabilities of integrated optical circuits were enhanced in the 2000's with their extension to two-dimensional arrangements accomplished using optical induction in photorefractive crystals [29, 30] and femtosecond laser direct writing methods [31, 32]. Note that, unlike electronics where silicon is the predominant material, optical circuits have been written in a vast variety of materials including lithium niobate, silica on silicon, silicon, indium phosphide, gallium arsenide, polymers and glasses, depending on specific functionality that want to be strengthened [33, 34].

The combination of waveguides with other technologies such as electronics, lasers and detectors merged in the field know as integrated photonics, which has the final aim of miniaturizing photonic systems by including all the basic components for light generation, manipulation and detection in a single-optical chip [28]. The progress in this field is boosting the technology of the 21$^{\text{th}}$ century [35] in a similar manner than electronics did in the 20$^{\text{th}}$ century [36]. For instance, it is having a huge impact in the development of information technology and data communications [37–39], in sensing devices [40, 41] or in quantum technologies [42–45]. In the latter, integrated photonic circuits have become a prominent platform for cryptography e.g., quantum key distributions [46–48] and quantum random number generation [49, 50], for quantum signal processing [51–53] e.g., boson sampling [54–56] and quantum walks [57–59], and for quantum computation [60–62], competing with other platforms such as ultracold atoms, trapped ions, or superconducting circuits [63].

Furthermore, integrated photonic structures have also been consolidated as an ideal playground for quantum simulation [64] i.e., for emulating quantum phenomena appearing in other branches of physics such as condensed-matter physics, high-energy physics or atomic physics [65, 66], by exploiting quantum-optical analogies [67]. In particular, the main advantages of photonic systems over other platforms like ultracold atoms [68], trapped ions [69] or superconducting circuits [70], are their flexibility, scalability and the possibility to directly observe the evolution of the wavefunction density using simple imaging techniques [71–73]. These exceptional features have allowed to investigate a huge variety of coherent quantum phenomena using classical light in systems of coupled optical waveguides (see [74–76] for extended reviews) like: (i) coherent quantum transport in solid-state physics [77] such as Bloch oscillations [78, 79], Zener tunneling [80, 81], dynamic localization [82, 83] or Anderson localization [84, 85]; (ii) coherent effects of atoms or molecules driven by laser fields like Rabi oscillations [86, 87], adiabatic passage processes for population transfer [88, 89] or electromagnetically-induced transparency [90, 91]; and (iii) general quantum phenomena as Aharonov-Bohm and Berry phases [92, 93], coherent control of quantum tunneling [94, 95], quantum mechanical decay [96, 97], decoherence [98, 99] or entanglement [100, 101]. Note that the flexibility offered by femtosecond laser written waveguides to create one- and two-dimensional discrete systems with arbitrary distributions has bolstered photonic simulators [76, 102].

Besides, quantum optical-analogies have also been exploited to design photonic structures with non-trivial properties and enhanced performances, opening a new paradigm for photonic circuits design [103]. For example, by mimicking a two-site Bose-Hubbard Hamiltonian to engineer polarization splitters with superior performances [104], by applying quantum engineering protocols [89, 105] to design robust integrated photonic devices [106–108] or by taking profit of non-trivial topological properties to transmit optical signals without back-scattering using topological edge states [109–113]. In addition, integrated photonics has also contributed to fundamental science for itself due to its unique intrinsic properties [114] that have allowed, for instance, to investigate non-trivial phenomena such as vortex solitons [77], to explore synthetic dimensions [115, 116] or to enquire quantum inspired symmetries such as Supersymmetry (SUSY) [117] and Parity-Time (PT) symmetry [118, 119]. On the one hand, the concept of SUSY, discovered in the 70's and originally proposed to unify the mathematical treatment of bosons and fermions [120–122], was extended to classical [123] and quantum [124] optics in the middle of the 90's by taking profit of the analogies with SUSY in QM [125–127]. Similarly, the concept of PT symmetry was proposed in QM by the end of the 90's [128] and extended to optical waveguides [129], where it can be easily implemented due to the possibility of incorporating gain and loses in photonic structures [130, 131].

In this line, this thesis is devoted to design integrated photonic devices with new functionalities and enhanced performances with respect to the standard ones as well as to design novel photonic simulators by taking profit of non-trivial properties stemming from quantum physics. More precisely, we investigate the possibility of applying adiabatic passage processes [89], SUSY [132] and non-trivial topological geometries [75] to: (i) design efficient and robust mode-division (de)multiplexing devices in Chapter 4; (ii) engineer tapered waveguides, mode filters, beam splitters and Mach-Zehnder interferometers in Chapter 5; (iii) investigate the interplay between SUSY and Topology in Chapter 6, and (iv) generate artificial gauge fields in Chapter 7.

Since optical waveguides constitute the physical platform in which the research of this thesis is sustained, Chapter 2 is devoted to provide the theoretical background regarding light propagation in these structures. To this end, we present the different types of waveguide geometries and we derive the Helmholtz equation and the coupled-mode equations describing light propagation in arrays of evanescently-coupled optical waveguides. Moreover, we also introduce the analogies between the Helmholtz and the Schrödinger equations, the second cornerstone in which this thesis sustains.

In a similar vein, Chapter 3 is focused on introducing another fundamental pillar of this thesis, optical SUSY. The chapter starts by briefly reviewing the state-of-the-art of SUSY in optics, explaining how SUSY transformations applied to systems of coupled optical waveguides [117, 133–136] and optical fibers [137, 138] have allowed to design novel mode filtering and multiplexing devices [139–144], to engineer structures with the same scattering characteristics [145–150], to investigate extremely disordered potentials [151–154] and to fabricate enhanced laser arrays [155–159]. To continue, the basic mathematical concepts regarding SUSY in QM are introduced, laying the groundwork for its mapping onto optics, and the different types of SUSY transformations that can be used to synthesize supersymmetric photonic structures are also presented. In particular, we first present SUSY transformations applied to one-dimensional refractive index profiles and we explain how they allow to manipulate the modal content, illustrating it in a single waveguide and, later on, in an array of coupled waveguides. Note that this type of transformations is used in Chapters 4 and 5. Moreover, we also explain the concept of discrete SUSY (DSUSY) transformations that can be used in one- and two- dimensional arrays of waveguides described by the coupled-mode formalism. This kind of transformation is used in Chapter 6.

In Chapter 4, we present a promising method for mode division (de)multiplexing rooted on SUSY waveguides, which are engineered along the propagation distance following a Spatial Adiabatic Passage (SAP) protocol. Adiabatic passage processes [160], based on adiabatically following an eigenmode [161], have been used the last decades to efficiently transfer population between internal atomic levels, ultracold atoms between

potential traps or light intensity between optical waveguides [105]. In particular, to efficiently and robustly transfer light intensity between the outermost waveguides in a system of three evanescently-coupled waveguides, we apply the SAP technique [162, 163]. This technique is the spatial analog of the Stimulated Raman Adiabatic Passage technique [88] based on applying two temporally delayed laser pulses to transfer the atomic population between the two ground states in a Λ-type three-level atomic system [89]. Besides, to engineer the modal content of the different waveguides such that some of the modes cannot be coupled while the others do, we apply a SUSY transformation to the central waveguide. Therefore, by taking advantage of the strongest features of both techniques, we show how a superposition of two Transverse Electric modes can be demultiplexed with high efficiency and robustness, aiding to solve the increasing demand of high-capacity optical transmissions [164].

Similarly, in Chapter 5, we develop a novel technique to design integrated photonic devices based on adiabatically connecting SUSY refractive index profiles along the propagation direction rather than coupling them in the transverse one. Thus, adding a new degree of freedom to manipulate the modal content of optical waveguides. Specifically, since the system has a discrete number of eigenvalues and eigenmodes, the refractive index profile can be engineered such that an eigenmode of the system adiabatically evolves between two superpartner structures without being coupled to the other eigenmodes. To illustrate the technique's potential, we design (i) a tapered waveguide and a mode filter by connecting the refractive index profile of a single-waveguide structure with its superpartner, and (ii) a beam splitter and an interferometer by joining the refractive index profile of a two-waveguide structure with its superpartner. The efficiency and robustness of the designed devices is assured by performing the connection in an adiabatic fashion, hence, contributing to enhance the capabilities of integrated photonic circuits for classical and quantum information processing [51, 53].

In Chapter 6, we explore the effect that SUSY transformations induce in systems with non-trivial topological properties, which are intrinsically connected with the system's internal symmetries [165, 166]. Originated with the discovery of the quantum Hall effect in condensed-matter physics [167, 168], topological phases have been extended to other systems such as atomic, molecular or optical systems [169, 170]. Precisely, in photonics, topological phases have opened a path to discover new states of light such as topological insulators [171–173] or topological edge states [174–177], which have led to reflection-free sharply bent waveguides, robust delay lines, spin-polarized switches or non-reciprocal devices [109–112]. In this framework, we consider the simplest system with non-trivial topological properties, the Su-Schrieffer-Heeger model [178], and demonstrate how the topological protection of a targeted state can be suspended and reestablished by applying SUSY transformations. Particularly, we employ waveguide arrays fabricated using femtosecond laser writing techniques [76] to show how the topological protection of the

edge states propagating in the SSH-like waveguide lattice can be modified. With these results, we shed light to the interplay between SUSY and Topology and we present a novel technique for topological state engineering.

Moreover, to access these non-trivial topological phases, a key step is the introduction of Artificial Gauge Fields (AGF), controlling the dynamics of uncharged particles that otherwise elude the influence of standard electromagnetic fields. Therefore, developing new techniques to induce AGF is essential to boost quantum simulation in photonic structures. To this end, in Chapter 7 we investigate the possibility of inducing AGF by injecting light beams carrying Orbital Angular Momentum (OAM), characterized by a helical phase front, rather than manipulating the geometry of the system or imposing external fields. Note that light beams carrying OAM have been extensively used in classical and quantum optical communications [179–186]. To be specific, we use direct laser written optical waveguides [187] to verify the appearance of an AGF in the form of a synthetic magnetic flux, which is responsible of the resulting Aharonov-Bohm (AB) caging effect that traps the light in a single cage composed by a few waveguides. The proposed technique paves the way towards accessing different topological regimes in one single structure, an important step forward for quantum simulation in photonic structures.

Finally, in Chapter 8, to conclude the thesis we summarize the main results and discuss future perspectives and possible extensions of the presented works.

2

Physical platform: optical waveguides

Optical waveguides constitute the physical platform in which the theoretical and experimental works of this thesis are developed. In particular, coupled optical waveguides are systems of major current interest in our investigations for: (i) the application of quantum techniques to the design of photonic devices with advanced characteristics; and (ii) the simulation of the physics of relevant quantum systems such as, for instance, electrons in crystals. In this vein, this first chapter is aimed to explain what optical waveguides are and how light propagation is mathematically described in such structures, setting the basis for the rest of the thesis.

This chapter is organized as follows. In Section 2.1, we present the basic waveguide geometries for one-dimensional light confinement, used in Chapters 4 and 5, and two-dimensional light confinement, used in Chapters 6 and 7. This is followed by Section 2.2, where we derive the equations governing light propagation in optical waveguides. To this aim, we start with Maxwell's equations describing electromagnetic waves propagating in homogeneous dielectric media and we extend this derivation to optical waveguides. To continue, in Section 2.3, we introduce the concept of evanescent coupling between waveguides and we discuss under which conditions light dynamics can be described using the coupled-mode theory. Finally, in Section 2.4, we present the quantum-optical analogies that are applied to systems of coupled optical waveguides in this thesis.

2.1 Optical waveguides

A dielectric optical waveguide, consisting of a core embedded in a cladding of lower refractive index, can guide light confined in its core due to total internal reflection occurring at the interfaces between the core and the cladding [27, 28, 188, 189]. Depending on the dimensionality of the light confinement, an optical waveguide can be classified as

(i) a one-dimensional or planar waveguide as represented in Fig. 2.1(a),

(ii) a two-dimensional or channel waveguide as displayed in Fig. 2.1(b).

One-dimensional and two-dimensional optical waveguides are characterized by a spatial dependence of the refractive index $n(x)$ and $n(x, y)$, respectively, which can be a step-index profile in which the index of refraction is constant in each region but presenting an abrupt change between the refractive index of the core, n_{core}, and the refractive index of the cladding, n_{clad}, see Fig. 2.1(c), or graded-index profiles in which the refractive index distribution changes smoothly between the core and the cladding, as it is displayed in Fig. 2.1(d).

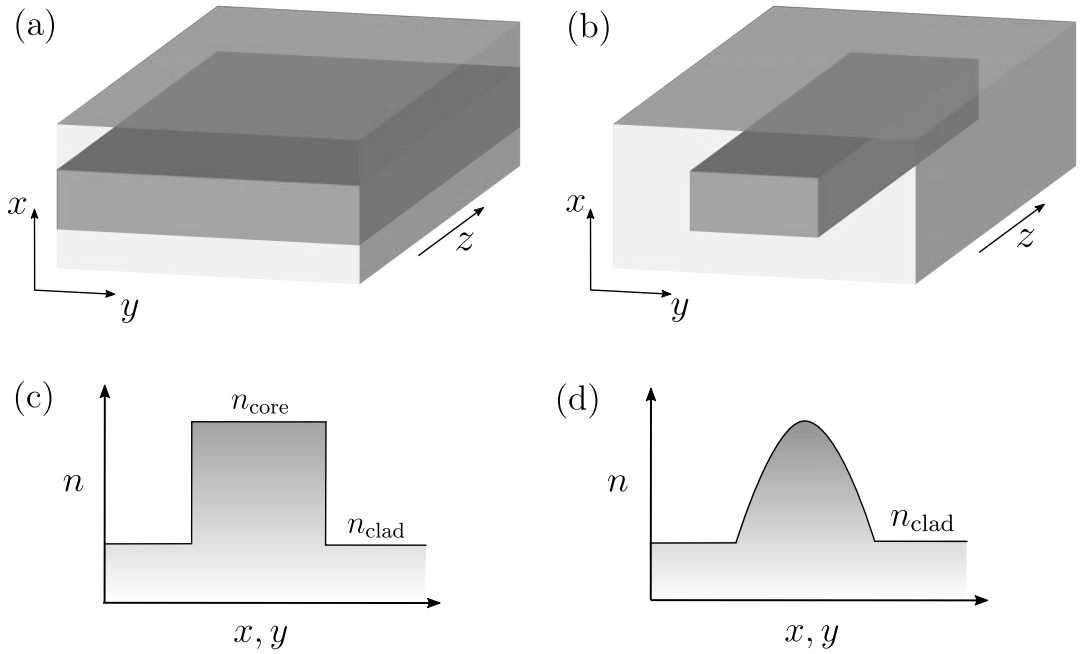

Figure 2.1: (a) One-dimensional or planar optical waveguide and (b) two-dimensional or channel optical waveguide. The core (dark region) is surrounded by a cladding of lower refractive index. Spatial dependence of the refractive index corresponding to (c) a step-index profile and (d) a graded-index profile.

2.2 Electromagnetic theory of light

2.2.1 Light propagation in homogeneous media

Light is an electromagnetic wave composed of coupled electric $\boldsymbol{\mathscr{E}}(\mathbf{r},t)$ and magnetic $\boldsymbol{\mathscr{H}}(\mathbf{r},t)$ fields whose dynamics are governed by Maxwell's equations. Assuming a linear, homogeneous, and isotropic dielectric medium, Maxwell's equations read

$$\nabla \cdot \boldsymbol{\mathscr{E}}(\mathbf{r},t) = 0, \tag{2.1}$$
$$\nabla \cdot \boldsymbol{\mathscr{H}}(\mathbf{r},t) = 0, \tag{2.2}$$
$$\nabla \times \boldsymbol{\mathscr{E}}(\mathbf{r},t) = -\mu \frac{\partial \boldsymbol{\mathscr{H}}(\mathbf{r},t)}{\partial t}, \tag{2.3}$$
$$\nabla \times \boldsymbol{\mathscr{H}}(\mathbf{r},t) = \epsilon \frac{\partial \boldsymbol{\mathscr{E}}(\mathbf{r},t)}{\partial t}, \tag{2.4}$$

where $\mathbf{r} = (x, y, z)$ is the position, t is the time, μ is the absolute medium permeability and ϵ its permittivity, which are related with their respective values in vacuum as $\mu = \mu_0$ (non-magnetic medium) and $\epsilon = \epsilon_0 n^2$, where n is the refractive index of the medium. By applying the curl operator to (2.3) and (2.4), using the vector identity $\nabla \times (\nabla \times \mathbf{A}) = \nabla(\nabla \cdot \mathbf{A}) - \nabla^2 \mathbf{A}$, and imposing (2.1) and (2.2), one can derive the wave equations

$$\nabla^2 \boldsymbol{\mathscr{E}}(\mathbf{r},t) = \mu\epsilon \frac{\partial^2 \boldsymbol{\mathscr{E}}(\mathbf{r},t)}{\partial t^2}, \tag{2.5}$$
$$\nabla^2 \boldsymbol{\mathscr{H}}(\mathbf{r},t) = \mu\epsilon \frac{\partial^2 \boldsymbol{\mathscr{H}}(\mathbf{r},t)}{\partial t^2}, \tag{2.6}$$

where $v = 1/\sqrt{\epsilon\mu}$ is the wave velocity. Moreover, considering monochromatic waves

$$\boldsymbol{\mathscr{E}}(\mathbf{r},t) = \mathrm{Re}\left[\mathbf{E}(\mathbf{r})e^{i\omega t}\right], \tag{2.7}$$
$$\boldsymbol{\mathscr{H}}(\mathbf{r},t) = \mathrm{Re}\left[\mathbf{H}(\mathbf{r})e^{i\omega t}\right], \tag{2.8}$$

where ω is the angular frequency and $\mathbf{E}(\mathbf{r})$ and $\mathbf{H}(\mathbf{r})$ denote complex amplitudes, Maxwell's equations (2.1)-(2.4) can be rewritten in frequency domain as

$$\nabla \cdot \mathbf{E}(\mathbf{r}) = 0, \tag{2.9}$$
$$\nabla \cdot \mathbf{H}(\mathbf{r}) = 0, \tag{2.10}$$
$$\nabla \times \mathbf{E}(\mathbf{r}) = -i\mu\omega \mathbf{H}(\mathbf{r}), \tag{2.11}$$
$$\nabla \times \mathbf{H}(\mathbf{r}) = i\epsilon\omega \mathbf{E}(\mathbf{r}). \tag{2.12}$$

Applying the curl operator in both sides of Eqs. (2.11) and (2.12) and combining them, one derive the Helmholtz equations

$$\left[\nabla^2 + k^2\right] \mathbf{E}(\mathbf{r}) = 0, \tag{2.13}$$
$$\left[\nabla^2 + k^2\right] \mathbf{H}(\mathbf{r}) = 0, \tag{2.14}$$

where $k^2 \equiv \mu\epsilon\omega^2 = k_0^2 n^2$, being $k_0 = 2\pi/\lambda_0$ the vacuum wavenumber and λ_0 the vacuum wavelength. By solving the Helmholtz equations (2.13) and (2.14), one obtains solutions in the form of plane waves

$$\mathbf{E}(\mathbf{r}) = \mathbf{e}\exp(-i\mathbf{k}\cdot\mathbf{r}) \tag{2.15}$$

$$\mathbf{H}(\mathbf{r}) = \mathbf{h}\exp(-i\mathbf{k}\cdot\mathbf{r}), \tag{2.16}$$

where $\mathbf{e}$ and $\mathbf{h}$ are complex envelopes and $\mathbf{k} = (k_x, k_y, k_z)$ is the wavevector. Furthermore, by introducing (2.15) and (2.16) into (2.11) and (2.12), one obtains

$$\mathbf{k}\times\mathbf{h} = -\omega\epsilon\mathbf{e} \quad \text{and} \quad \mathbf{k}\times\mathbf{e} = \omega\mu\mathbf{h} \tag{2.17}$$

Therefore, since $\mathbf{E}$ and $\mathbf{H}$ oscillate in a normal plane with respect to the propagation direction $\mathbf{k}$, these waves are known as Transverse Electromagnetic (TEM) waves.

2.2.2 Light propagation in optical waveguides

The equations derived above stand for linear, homogeneous and isotropic media, however, for optical waveguides characterized by a refractive index distribution $n(\mathbf{r}) \equiv \sqrt{\epsilon_0\epsilon(\mathbf{r})}$ some modifications have to be performed. Assuming a linear, inhomogeneous and isotropic dielectric medium, the Maxwell's equations (2.3) and (2.4) become

$$\nabla\times\boldsymbol{\mathscr{E}}(\mathbf{r},t) = -\mu\frac{\partial\boldsymbol{\mathscr{H}}(\mathbf{r},t)}{\partial t}, \tag{2.18}$$

$$\nabla\times\boldsymbol{\mathscr{H}}(\mathbf{r},t) = \epsilon(\mathbf{r})\frac{\partial\boldsymbol{\mathscr{E}}(\mathbf{r},t)}{\partial t}, \tag{2.19}$$

and considering monochromatic waves given by Eqs. (2.7) and (2.8), Maxwell's equations (2.18) and (2.19) read

$$\nabla\times\mathbf{E}(\mathbf{r}) = -i\mu\omega\mathbf{H}(\mathbf{r}), \tag{2.20}$$

$$\nabla\times\mathbf{H}(\mathbf{r}) = i\omega\epsilon(\mathbf{r})\mathbf{E}(\mathbf{r}). \tag{2.21}$$

Applying the curl operator in both sides of Eqs. (2.20) and (2.21) and considering that $\nabla\cdot\epsilon\mathbf{E} = \epsilon\nabla\cdot\mathbf{E} + \mathbf{E}\cdot\nabla\epsilon$, one obtains $\nabla\cdot\mathbf{E} = -\epsilon^{-1}\nabla\epsilon\cdot\mathbf{E}$, which leads to the vectorial Helmholtz equations for inhomogeneous media [188]

$$\left[\nabla^2 + k_0^2\epsilon(\mathbf{r})\right]\mathbf{E}(\mathbf{r}) = -\nabla\left[\frac{\nabla\epsilon(\mathbf{r})}{\epsilon(\mathbf{r})}\cdot\mathbf{E}(\mathbf{r})\right], \tag{2.22}$$

$$\left[\nabla^2 + k_0^2\epsilon(\mathbf{r})\right]\mathbf{H}(\mathbf{r}) = -\frac{\nabla\epsilon(\mathbf{r})}{\epsilon(\mathbf{r})}\times\nabla\times\mathbf{H}(\mathbf{r}). \tag{2.23}$$

Therefore, if $\nabla\epsilon(\mathbf{r}) \neq 0$ e.g., in graded-index waveguides, the different components of the electric $\mathbf{E}(\mathbf{r})$ and magnetic $\mathbf{H}(\mathbf{r})$ fields are coupled and one cannot derive an independent

scalar wave equation for each component of the fields. Nevertheless, if $n(\mathbf{r})$ is locally homogeneous i.e., $n(\mathbf{r})$ varies in space in a much slower rate than $\mathbf{E}(\mathbf{r})$ and $\mathbf{H}(\mathbf{r})$, the right hand side terms of Eqs. (2.22) and (2.23) can be neglected, obtaining

$$\left[\nabla^2 + k_0^2 n^2(\mathbf{r})\right] \mathbf{E}(\mathbf{r}) \approx 0, \tag{2.24}$$

$$\left[\nabla^2 + k_0^2 n^2(\mathbf{r})\right] \mathbf{H}(\mathbf{r}) \approx 0. \tag{2.25}$$

Considering that the refractive index profile is constant along the propagation direction (z direction) and only depends on the x and y directions i.e., $n = n(x, y)$, the solutions of the inhomogeneous Helmholtz equations (2.22) and (2.23) can be written as

$$\mathbf{E}(x, y, z) = [\mathbf{e}_\perp(x, y) + e_z(x, y)\hat{z}] \exp(-i\beta z), \tag{2.26}$$

$$\mathbf{H}(x, y, z) = [\mathbf{h}_\perp(x, y) + h_z(x, y)\hat{z}] \exp(-i\beta z), \tag{2.27}$$

where $\perp$ and z denote the transverse and longitudinal components, respectively, $\beta \equiv k_z$ is the propagation constant and $\hat{z}$ is the unitary vector along the z direction. In addition, by introducing (2.26) and (2.27) into (2.20) and (2.21), one obtains [188]

$$\mathbf{e}_\perp(x, y) = \frac{i\left[\beta \nabla_\perp e_z(x, y) - \omega\mu\hat{z} \times \nabla_\perp h_z(x, y)\right]}{\beta^2 - k^2(x, y)}, \tag{2.28}$$

$$\mathbf{h}_\perp(x, y) = \frac{i\left[\beta \nabla_\perp h_z(x, y) + \omega\epsilon(x, y)\hat{z} \times \nabla_\perp e_z(x, y)\right]}{\beta^2 - k^2(x, y)}. \tag{2.29}$$

Thus, in general, to determine the transverse components of the fields one needs to find the longitudinal ones. This means, solving the Helmholtz equations (2.22) and (2.23) with the appropriate boundary conditions to find $e_z(x, y)$ and $h_z(x, y)$ in each region, which typically requires the use of numerical techniques such as finite-difference methods [190]. An exception are weakly-guiding waveguides characterized by $\Delta n(x, y) = n(x, y) - n_{\text{clad}} \ll n_{\text{clad}}$, in which $|\nabla_\perp e_z| \ll |\beta \mathbf{e}_\perp|$ and $|\nabla_\perp h_z| \ll |\beta \mathbf{h}_\perp|$. Thus, one can neglect the longitudinal components over the transversal ones and approximate the wave as a TEM plane wave [188]. Another exception in which one of the longitudinal components is zero are one-dimensional waveguides defined by $n(x)$, where the electric (2.26) and magnetic (2.27) fields are no longer y-dependent, becoming

$$\mathbf{E}(x, z) = [e_x(x)\hat{x} + e_y(x)\hat{y} + e_z(x)\hat{z}] \exp(-i\beta z), \tag{2.30}$$

$$\mathbf{H}(x, z) = [h_x(x)\hat{x} + h_y(x)\hat{y} + h_z(x)\hat{z}] \exp(-i\beta z). \tag{2.31}$$

where $\hat{x}$, $\hat{y}$ and $\hat{z}$ are the unitary vectors along the x, y and z directions, respectively.

Light propagation in one-dimensional optical waveguides

In the particular case of one-dimensional optical waveguides, both longitudinal components $e_z(x)$ and $h_z(x)$ are decoupled and one obtains two independent modes propagating along the z direction: (i) the Transverse Electric (TE) mode ($e_z(x) = 0$) and (ii)

the Transverse Magnetic (TM) mode ($h_z(x) = 0$), with transversal components $e_y(x)$ and $h_y(x)$, respectively. In the following, we are considering TE modes but a similar derivation can be performed for TM modes [28]. By introducing (2.30) and (2.31) into (2.20) and (2.21), one obtains that the only non-zero components for TE modes are $e_y(x), h_x(x)$ and $h_z(x)$, which are related as

$$h_x(x) = -\frac{\beta}{\omega\mu} e_y(x), \tag{2.32}$$

$$h_z(x) = \frac{i}{\omega\mu}\frac{\partial e_y(x)}{\partial x}, \tag{2.33}$$

$$i\beta h_x(x) + \frac{\partial h_z(x)}{\partial x} = -i\omega\epsilon_0 n(x)^2 e_y(x). \tag{2.34}$$

Therefore, by introducing (2.32) and (2.33) into (2.34), one can derive the scalar Helmholtz equation for the e_y component

$$\frac{d^2 e_y(x)}{dx^2} + [k_0^2 n(x)^2 - \beta^2] e_y(x) = 0, \tag{2.35}$$

which is also typically written in terms of $E_y(x, z) = e_y(x)\exp(-i\beta z)$ as

$$\frac{\partial^2 E_y(x,z)}{\partial x^2} + \frac{\partial^2 E_y(x,z)}{\partial z^2} + k_0^2 n(x)^2 E_y(x,z) = 0. \tag{2.36}$$

By solving Eq. (2.35) for the appropriate boundary conditions a discrete number of solutions i.e., guided modes, is obtained. Note that the rest of the non-zero components i.e., $h_x(x)$ and $h_z(x)$, can be found by substituting $e_y(x)$ into Eqs. (2.28) and (2.29). The E_y component of the electric field is typically expressed as a superposition of all the allowed modes, reading

$$E_y(x,z) = \sum_m a_m e_{y,m}(x)\exp(-i\beta_m z), \tag{2.37}$$

where a_m is the amplitude, $e_{y,m}(x)$ the transverse field distribution and β_m the propagation constant of mode m. Note that, while there is a finite number of guided modes whose propagation constants satisfy $k_0 n_{\text{clad}} < \beta_m < k_0 n_{\text{core}}$, there is an infinite number of radiation modes propagating at $\beta_{rad} < k_0 n_{\text{clad}}$ [28, 188, 189]. Moreover, guided modes are orthonormal between them, satisfying [188]

$$\int_{-\infty}^{\infty} e^*_{y,m}(x) e_{y,m'}(x) dx = \delta_{m,m'}, \tag{2.38}$$

where $\delta_{m,m'}$ is the Kronecker delta.

As an example, let us consider a step-index waveguide consisting of a core of width d and refractive index n_{core} embedded in a medium of lower refractive index n_{clad}. Precisely, we select the width and the refractive index contrast of the waveguide such that

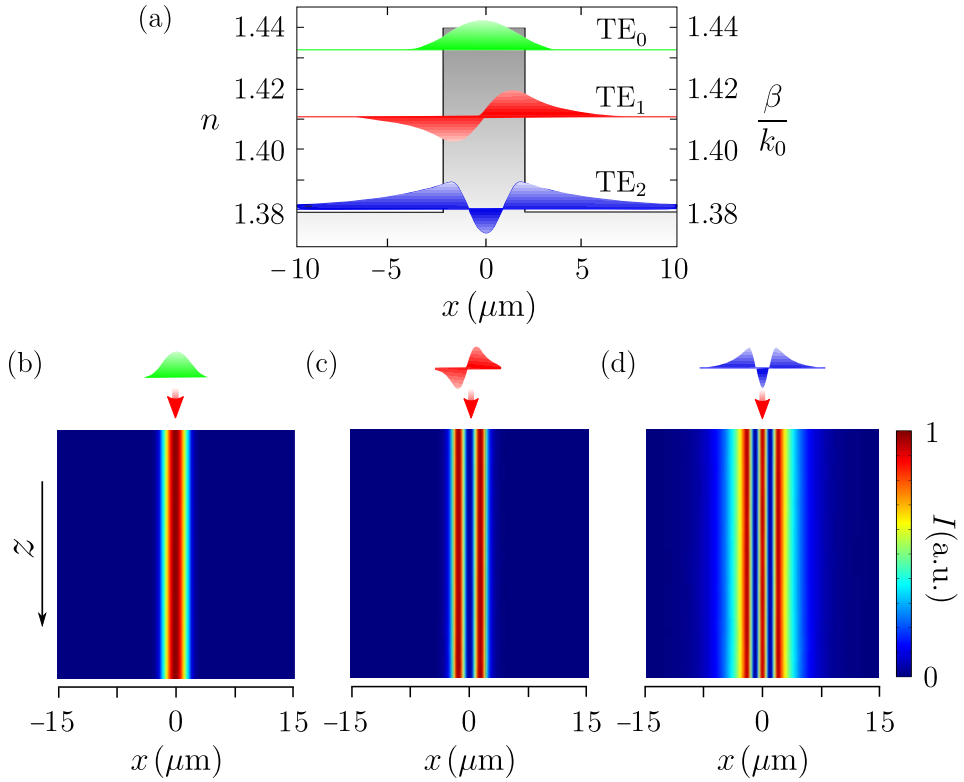

Figure 2.2: (a) Refractive index and transverse mode profiles in a step-index optical waveguide of core width $d = 4\,\mu$m, $n_{\text{core}} = 1.44$, $n_{\text{clad}} = 1.38$ and $\lambda_0 = 1.55\,\mu$m. Numerical simulations of light intensity propagation in the waveguide of (a) when the (b) TE_0, (c) TE_1 and (d) TE_2 modes are injected.

three TE_m modes can propagate, as it is represented in Fig. 2.2(a). Moreover, the transverse field distributions $e_{y,m}(x)$ are obtained by solving Eq. (2.35), which read [189]

$$e_{y,m}^{\text{core}}(x) \propto \begin{cases} \cos(k_{x,m}x), & m = 0, 2 \\ \sin(k_{x,m}x), & m = 1 \end{cases}, \quad |x| \leq d/2 \tag{2.39}$$

$$e_{y,m}^{\text{clad}}(x) \propto \begin{cases} \exp(-\gamma_{x,m}x), & x > d/2 \\ \exp(\gamma_{x,m}x), & x < -d/2 \end{cases}, \quad m = 0, 1, 2 \tag{2.40}$$

where $k_{x,m} = (k_0^2 n_{\text{core}}^2 - \beta_m^2)^{1/2}$ and $\gamma_{x,m} = (\beta_m^2 - k_0^2 n_{\text{clad}}^2)^{1/2}$ are the wavevector and the extinction coefficient along the x direction, respectively. Note that the fundamental TE_0, first excited TE_1 and second excited TE_2 modes are eigenmodes of the waveguide, hence, they propagate confined in the waveguide core without modifying its transverse spatial distribution, as represented in Fig. 2.2(b), (c) and (d), respectively.

Light propagation in two-dimensional optical waveguides

Unlike in planar waveguides, where light propagation can be described in terms of TE and TM modes, when dealing with two-dimensional waveguides one has to consider hybrid modes. A particular case of interest that is considered in Chapter 7 are step-index cylindrical waveguides of radius R characterized by a refractive index profile $n(r)$, as it is represented in Fig. 2.3(a). In cylindrical coordinates, the electric (2.26) and magnetic (2.27) fields can be expressed, respectively, as

$$\mathbf{E}(r,\phi,z) = [\mathbf{e}_\perp(r,\phi) + e_z(r,\phi)\hat{z}]\exp(-i\beta z), \tag{2.41}$$
$$\mathbf{H}(r,\phi,z) = [\mathbf{h}_\perp(r,\phi) + h_z(r,\phi)\hat{z}]\exp(-i\beta z), \tag{2.42}$$

where r and ϕ are the polar coordinates with respect to the center of the waveguide in the transverse plane and z the propagation direction. Moreover, these waveguides sustain $\mathrm{TE}_{0,m}$ and $\mathrm{TM}_{0,m}$ modes, which are rotationally symmetric, and $\mathrm{HE}_{\ell,m}$ and $\mathrm{EH}_{\ell,m}$ hybrid modes, where ℓ and m are the azimuthal and radial mode numbers, respectively. Note that, in the following, we consider weakly-guiding waveguides i.e., $\Delta n(x,y) \ll n_{\mathrm{clad}}$, in which the longitudinal components are nearly zero and the modes can be approximated as linearly polarized $\mathrm{LP}_{\ell,m}$ modes.

Considering that the electric field (2.41) is polarized along the x direction i.e., $\mathbf{E} = E_x(r,\phi,z)\hat{x}$, it satisfies the Helmholtz equation (2.24) in the core and in the cladding regions, which in cylindrical coordinates reads [189]

$$\left[\frac{\partial^2}{\partial r^2} + \frac{1}{r}\frac{\partial}{\partial r} + \frac{\partial^2}{\partial z^2} + n_j^2 k_0^2\right] E_x(r) = 0, \tag{2.43}$$

where n_j with $j = \mathrm{core}, \mathrm{clad}$ accounts for the refractive index of the core and the cladding, respectively. Moreover, considering a solution of the form

$$E_x(r,\phi,z) = e_r(r)\exp(-i\ell\phi)\exp(-i\beta z), \tag{2.44}$$

where $\phi \in (0, 2\pi)$, the Helmholtz equation (2.43) for each region of the waveguide becomes [189]

$$\left[\frac{d^2}{dr^2} + \frac{1}{r}\frac{d}{dr} + n_j^2 k_0^2 - \beta^2 - \frac{\ell^2}{r^2}\right] e_r(r) = 0. \tag{2.45}$$

By solving (2.45) for the appropriate boundary conditions, one obtains that the radial distribution of the mode is given by

$$e_{r,\ell}(r) \propto \begin{cases} J_\ell(k_{r,\ell} r) & \text{if } \mathrm{r} \leq \mathrm{R} \\ K_\ell(\gamma_{r,\ell} r) & \text{if } \mathrm{r} > \mathrm{R} \end{cases}, \tag{2.46}$$

where J_ℓ is the Bessel function of the first kind and order ℓ, K_ℓ is the modified Bessel function of the second kind and order ℓ, $k_{r,\ell}^2 = n_{core}^2 k_0^2 - \beta_\ell^2$ and $\gamma_{r,\ell}^2 = \beta_\ell^2 - n_{clad}^2 k_0^2$ are

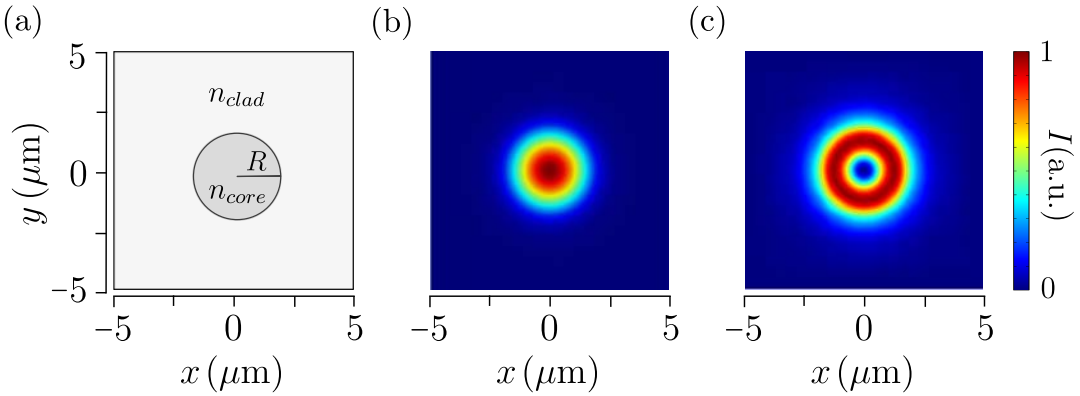

Figure 2.3: (a) Refractive index distribution for a cylindrical waveguide with radius $R = 1.9\,\mu$m, $n_{\text{core}} = 1.548$ and $n_{\text{clad}} = 1.540$. Intensity distributions corresponding to (b) the $\ell = 0$ mode and (c) the $\ell = 1$ mode. The wavelength used is $\lambda_0 = 0.7\,\mu$m.

the wavevector and the extinction coefficient along the radial direction, respectively. As an example, the field distributions corresponding to the $\mathrm{LP}_{0,0}$ and the $\mathrm{LP}_{1,1}$ modes are represented in Fig. 2.3(b) and (c), respectively. Note that an analogous derivation can be performed for the magnetic field polarized along the x direction or by exchanging the x and y polarization [188].

2.3 Coupled-mode theory

In the previous section, we have studied different modes propagating in isolated waveguides. However, in general, integrated optical circuits are composed of two or more waveguides. In this section, we discuss the power exchange between two optical waveguides when they are close enough due to the coupling between their modes. Although light propagation in systems of coupled waveguides can be computed using Maxwell's equations and imposing boundary conditions for the entire structure, its description in the weakly-coupling regime is considerable simplified within the coupled-mode theory [28, 188, 189]. To introduce the coupled-mode theory we consider a directional coupler composed of two parallel evanescently-coupled waveguides and then we generalize the formalism to arrays of evanescently-coupled waveguides.

2.3.1 Directional coupler

We consider two parallel step-index single-mode waveguides, see Fig. 2.4(a), with cores of refractive index n_L and n_R for the left and right waveguides, respectively, embedded in a cladding of lower refractive index n_{clad}, as it is illustrated in Fig. 2.4(b).

When the waveguides are isolated, the electric field (2.26) in each waveguide reads

$$E_L(x,z) = a_L e_L(x)\exp(-i\beta_L z), \tag{2.47}$$
$$E_R(x,z) = a_R e_R(x)\exp(-i\beta_R z), \tag{2.48}$$

where a_j is the mode amplitude, $e_j(x)$ the transverse spatial distribution and β_j the propagation constant of the mode in waveguide j. Instead, if the separation between waveguides is reduced such that the evanescent tails of the modes overlap, the waveguides become weakly-coupled and one can approximate the electric field of the entire structure as a superposition of both fields, reading

$$E(x,z) = a_L(z)e_L(x)\exp(-i\beta_L z) + a_R(z)e_R(x)\exp(-i\beta_R z), \tag{2.49}$$

where the amplitudes $a_L(z)$ and $a_R(z)$ change along the propagation direction while the transverse field distributions $e_L(x)$ and $e_R(x)$ and the propagation constants β_L and β_R are not altered.

Considering the presence of the right (left) waveguide as a perturbation for the field propagating in the left (right) waveguide, due to the excess of refractive index $n_R^2 - n_{\text{clad}}^2$ ($n_L^2 - n_{\text{clad}}^2$) that acts as a source of radiation, the Helmholtz equation (2.24) for each region can be expressed as [189]

$$\left[\nabla^2 + k_0^2 n_L^2\right] E_L(x,z) + k_0^2(n_R^2 - n_{\text{clad}}^2)E_R(x,z) = 0, \tag{2.50}$$
$$\left[\nabla^2 + k_0^2 n_L^2\right] E_R(x,z) + k_0^2(n_L^2 - n_{\text{clad}}^2)E_L(x,z) = 0. \tag{2.51}$$

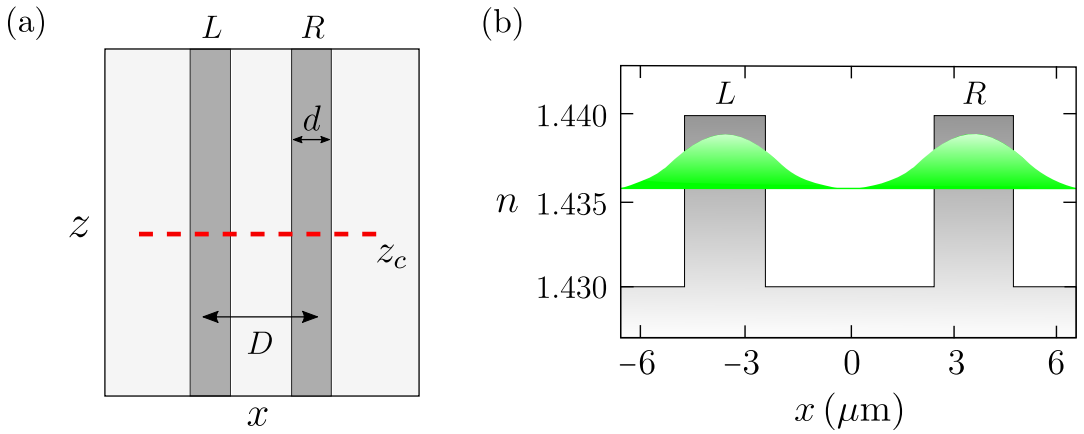

Figure 2.4: (a) Schematic representation of a directional coupler viewed from above. (b) Refractive index distribution at z_c and transverse mode profiles supported for each isolated waveguide. The parameter values used are $d = 2\,\mu$m, $D = 8\,\mu$m, $n_{\text{core}} = 1.44$, $n_{\text{clad}} = 1.43$ and $\lambda_0 = 1.55\,\mu$m.

Introducing (2.47) and (2.48) with $a_j(z)$ into equations (2.50) and (2.51) and neglecting da_j^2/dz^2 since the mode amplitudes vary slowly with respect to z, one obtains [189]

$$i2\beta_L \frac{da_L}{dz} e_L(y)\exp(-i\beta_L z) = k_0^2(n_R^2 - n_{\text{clad}}^2)a_R e_R(y)\exp(-i\beta_R z), \quad (2.52)$$

$$i2\beta_R \frac{da_R}{dz} e_R(y)\exp(-i\beta_R z) = k_0^2(n_L^2 - n_{\text{clad}}^2)a_L e_L(y)\exp(-i\beta_L z). \quad (2.53)$$

Multiplying both sides of (2.52) and (2.53) by $e_L(y)$ and $e_R(y)$, respectively, and integrating over x, one obtains the coupled-mode equations [189]

$$\frac{da_L(z)}{dz} = -ic_{RL}e^{i(\beta_L-\beta_R)z}a_R(z), \quad (2.54)$$

$$\frac{da_R(z)}{dz} = -ic_{LR}e^{i(\beta_R-\beta_L)z}a_L(z), \quad (2.55)$$

where

$$c_{RL} = \frac{1}{2\beta_L}k_0^2(n_R^2 - n_{\text{clad}}^2)\int_{D/2-d/2}^{D/2+d/2} e_L(x)e_R(x)dx, \quad (2.56)$$

$$c_{LR} = \frac{1}{2\beta_R}k_0^2(n_L^2 - n_{\text{clad}}^2)\int_{-D/2-d/2}^{-D/2+d/2} e_R(x)e_L(x)dx. \quad (2.57)$$

are the coupling coefficients quantifying the coupling of the mode propagating in the left and right waveguide to the right and left waveguide, respectively. Moreover, using $\tilde{a}_j(z) = a_j(z)\exp(-i\beta_j z)$, coupled-mode equations can be written as

$$i\frac{d}{dz}\begin{pmatrix}\tilde{a}_L\\ \tilde{a}_R\end{pmatrix} = \begin{pmatrix}\beta_L & c_{RL}\\ c_{LR} & \beta_R\end{pmatrix}\begin{pmatrix}\tilde{a}_L\\ \tilde{a}_R\end{pmatrix}. \quad (2.58)$$

Solving Eq. (2.58) with the appropriate boundary conditions and considering, for instance, that light is injected in the left waveguide i.e., $a_L(0) \neq 0$ and $a_R(0) = 0$, one obtains that the power $P_j \propto |a_j|^2$ in each waveguide j oscillates as [189]

$$P_L(z) = P_L(0)\left[\cos^2(\gamma z) + \left(\frac{\Delta\beta}{2\gamma}\right)^2 \sin^2(\gamma z)\right], \quad (2.59)$$

$$P_R(z) = P_R(0)\frac{|c_{LR}|^2}{\gamma^2}\sin^2(\gamma z), \quad (2.60)$$

where $\gamma^2 = (\Delta\beta/2)^2 + c^2$ and $c = \sqrt{c_{LR}c_{RL}}$. In particular, for modes sharing the same propagation constant $\Delta\beta = 0$, the power carried in each waveguide simplifies, becoming

$$P_L(z) = P_L(0)\cos^2(cz) \quad \text{and} \quad P_R(z) = P_R(0)\sin^2(cz). \quad (2.61)$$

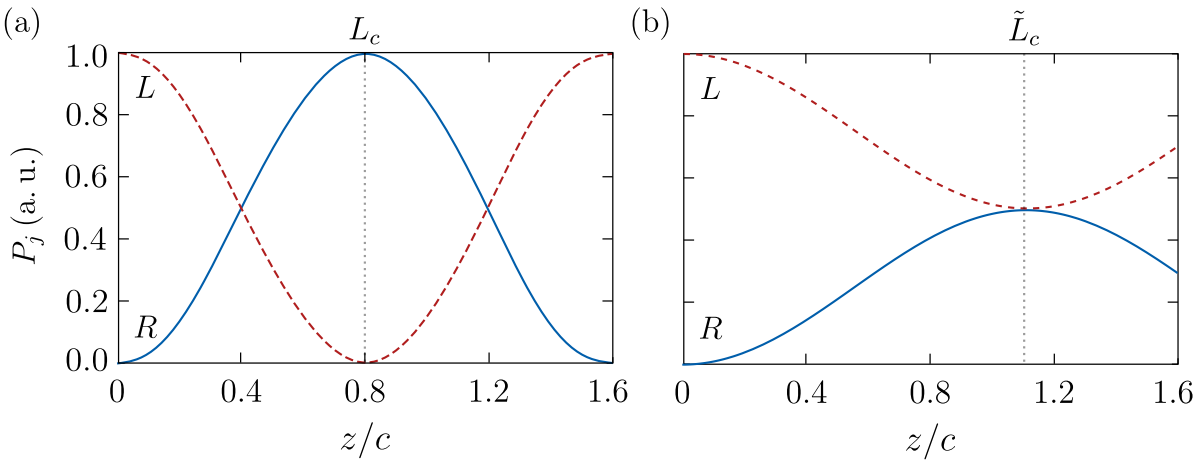

Figure 2.5: Spatial evolution of the power P_j in each waveguide $j = L, R$ when the mode is injected in the left waveguide of the two straight waveguide structure represented in Fig. 2.4(a) with (a) $\beta_L = \beta_R$ and (b) $\beta_L/\beta_R = 1/3$. The red dashed lines correspond to the power in the left waveguide while the blue solid lines correspond to the power in the right waveguide. The vertical dotted lines indicate the coupling length L_c and $\tilde{L}_c$ for each case.

Therefore, as it can be observed in Fig. 2.5(a), light injected in the left waveguide (red dashed line) is fully transmitted to the right waveguide (blue solid line) and vice-versa. Alternatively, as it is illustrated in Fig. 2.5(b), only part of the power injected in the left waveguide (red dashed line) is transferred to the right waveguide (blue dashed line) and vice-versa, when modes have different propagation constants. Moreover, the spatial period of the power oscillation i.e., the coupling length L_c, can be used to compute the coupling between waveguides without knowing the analytical expressions of the transverse field distributions or the exact refractive index profiles, which are required in Eqs. (2.56) and (2.57). Thus, along the thesis, we characterize the couplings by numerically simulating or experimentally implementing directional couplers and measuring the coupling length. For the case of equal propagation constants, represented in Fig. 2.5(a), the coupling strength can be calculated as

$$c = \frac{\pi}{2L_c}. \tag{2.62}$$

On the other hand, for the case of different propagation constants represented in Fig. 2.5(b), the coupling strength can be calculated using

$$c = \frac{\pi\sqrt{V}}{2\tilde{L}_c}, \tag{2.63}$$

where

$$V = \frac{\max(I_L) - \min(I_L)}{\max(I_L)}, \tag{2.64}$$

is the intensity contrast and I_L is the intensity in the left waveguide [139]. The obtained results in both cases can be fitted into an exponential decaying function given by

$$c(D) = K \exp(-\kappa D), \tag{2.65}$$

where K and κ are constants, allowing to characterize the coupling strength for any separation D between them.

2.3.2 Arrays of waveguides

The coupled-mode formalism introduced for a directional coupler can be generalized to arrays of evanescently-coupled waveguides [114]. For a one-dimensional array of N evanescently-coupled single-mode waveguides, as the one represented in Fig. 2.6, coupled-mode equations read

$$i\frac{d\tilde{a}_j(z)}{dz} = \sum_j \left[\beta_j \tilde{a}_j(z) + c_{j+1,j}(z)\tilde{a}_{j+1}(z) + c_{j-1,j}(z)\tilde{a}_{j-1}(z)\right], \tag{2.66}$$

which can be rewritten in matrix form as

$$i\frac{d}{dz}\begin{pmatrix} \tilde{a}_1 \\ \tilde{a}_2 \\ \tilde{a}_3 \\ \vdots \\ \tilde{a}_N \end{pmatrix} = \begin{pmatrix} \beta_1 & c_{2,1} & 0 & \dots & 0 \\ c_{1,2} & \beta_2 & c_{3,2} & \ddots & \vdots \\ 0 & c_{2,3} & \ddots & \ddots & 0 \\ \vdots & \ddots & \ddots & \ddots & c_{N,N-1} \\ 0 & \dots & 0 & c_{N-1,N} & \beta_N \end{pmatrix} \begin{pmatrix} \tilde{a}_1 \\ \tilde{a}_2 \\ \tilde{a}_3 \\ \vdots \\ \tilde{a}_N \end{pmatrix}. \tag{2.67}$$

where $c_{j\pm1,j}$ is the coupling strength between adjacent waveguides and β_j is the propagation constant of the mode in waveguide j. Note that, Eq. (2.67) is typically rewritten

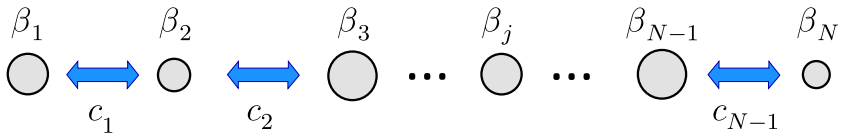

Figure 2.6: Schematic representation of a discrete array of N evanescently-coupled single-mode waveguides, whose coupling strengths $c_j \equiv c_{j,j\pm1}$ depend on the separation between waveguides. The different propagation constants β_j of the mode in waveguide j are illustrated by the size of the circle.

subtracting β_1 from the diagonal terms, reading

$$i\frac{d}{dz}\begin{pmatrix}\tilde{a}_1\\ \tilde{a}_2\\ \tilde{a}_3\\ \vdots\\ \tilde{a}_N\end{pmatrix}=\begin{pmatrix}0 & c_1 & 0 & \dots & 0\\ c_1 & \Delta\beta_2 & c_2 & \ddots & \vdots\\ 0 & c_2 & \ddots & \ddots & 0\\ \vdots & \ddots & \ddots & \ddots & c_{N-1}\\ 0 & \dots & 0 & c_{N-1} & \Delta\beta_N\end{pmatrix}\begin{pmatrix}\tilde{a}_1\\ \tilde{a}_2\\ \tilde{a}_3\\ \vdots\\ \tilde{a}_N\end{pmatrix}, \tag{2.68}$$

where $\Delta\beta_j = \beta_j - \beta_1$ is named the detuning between waveguide j and waveguide 1 and where we have considered real couplings coefficients i.e., $c_{i,j} = c_{j,i} \equiv c_j$. For multi-mode waveguides, one would have a set of coupled-mode equations (2.67) for each mode m.

2.4 Quantum-optical analogies

Optical waveguides constitute an ideal playground to visualize and experimentally demonstrate a huge variety of phenomena stemming from other fields of physics (see [74–76] for extended reviews). For instance, coherent quantum transport in solid-state physics e.g., Bloch oscillations [78, 79] and Zener tunneling [81], coherent effects of atoms driven by laser fields e.g., Rabi oscillations [86] and adiabatic passage processes [105], or even gravitational effects such as the equivalence principle [191]. In this section, we discuss the similarities between the Helmholtz and the Schrödinger equations in different regimes, introducing the quantum-optical analogies implemented along the thesis.

2.4.1 Mathematical analogies

Non-paraxial regime

The Helmholtz equation for TE modes propagating in planar waveguides (2.35) can be rewritten as an eigenvalue equation of the form

$$\left[-\frac{d^2}{dx^2} - k_0^2 n^2(x)\right] e_{y,m}(x) = -\beta_m^2 e_{y,m}(x), \tag{2.69}$$

which is analogous to the time-independent Schrödinger equation

$$\left[-\frac{d^2}{dx^2} + V(x)\right] \Psi_m(x) = E_m \Psi_m(x), \tag{2.70}$$

where $k_0^2 n^2(x)$ is playing the role of the potential $V(x)$ in quantum mechanics, $-\beta_m^2$ the role of the energy E_m, and $e_{y,m}$ the role of the wavefunction $\Psi_m(x)$ of state m. Note that, for the analogy, we have set $\hbar^2/2M \equiv 1$, being $\hbar = h/2\pi$ the reduced Planck

constant and M the mass of the particle. Moreover, Eqs. (2.69) and (2.70) also stand for one-dimensional lattice potentials and waveguide lattices with the only difference that $\Psi_m(x)$ and $e_{y,m}(x)$ are the supermodes of the entire structure.

The analogy between Eqs. (2.69) and (2.70) enables to investigate quantum inspired symmetries such as Supersymmetry (SUSY) [117] or Parity-Time (PT) symmetry [118] in optical waveguides. On the one hand, SUSY in quantum mechanics generates superpartner potentials $V^{(1)}(x)$ and $V^{(2)}(x)$ sharing their eigenvalues $E_m^{(2)} = E_{m+1}^{(1)}$, except for $E_0^{(1)}$ that is removed from the spectrum of $V^{(2)}(x)$ [132]. This technique can be mapped onto optical waveguides to engineer superpartner refractive index profiles $n^{(1)}(x)$ and $n^{(2)}(x)$, with global phase-matching conditions among their modes except for the fundamental mode of $n^{(1)}(x)$ [117]. On the other hand, PT-symmetry [118], which requires a potential satisfying $V(x) = V^*(-x)$ i.e., the real (imaginary) part of the potential should be an even (odd) function under space inversion $x \leftrightarrow -x$ [130, 131], can be easily achieved by engineering the refractive index profile as $n(x) = n_{\mathbb{R}}(x) + in_{\mathbb{I}}(x)$, where $n_{\mathbb{R}}(x)$ represents the refractive index distribution and $n_{\mathbb{I}}(x)$ the gain and loss profiles. Both symmetries are still valid in the paraxial regime.

Paraxial regime

Assuming light propagation in weakly-guiding waveguides i.e., $\Delta n(x,y,z) \ll n_{\text{clad}}$ and $\beta \approx k_0 n_{\text{clad}}$, characterized by refractive index profiles slowly varying along the propagation direction, each of the components of the electric fields can be expressed as

$$E(x,y,z) \approx e(x,y,z)\exp(-ik_0 n_{\text{clad}} z). \tag{2.71}$$

Therefore, by introducing (2.71) into the Helmholtz equation (2.24), and assuming the slowly varying envelope approximation

$$\left|\frac{\partial^2 e}{\partial z^2}\right| \ll \left|2k_0 n_{\text{clad}}\frac{\partial e}{\partial z}\right|, \tag{2.72}$$

one obtains the paraxial Helmholtz equation

$$i\lambda\!\!\!^{-}\frac{\partial}{\partial z}e(x,y,z) = \left[-\frac{\lambda\!\!\!^{-2}}{2n_{\text{clad}}}\nabla^2 - \Delta n(x,y,z)\right]e(x,y,z), \tag{2.73}$$

where $\lambda\!\!\!^{-} = \lambda/2\pi$ is the reduced wavelength and we have assumed that $[\Delta n(x,y,z)]^2/2n_{\text{clad}} \approx \Delta n(x,y,z)$. Equation (2.73) is analogous to the time-dependent Schrödinger equation

$$i\hbar\frac{\partial}{\partial t}\Psi(x,y,t) = \left[-\frac{\hbar^2}{2M}\nabla^2 + V(x,y,t)\right]\Psi(x,y,t). \tag{2.74}$$

Therefore, the time evolution of the wavefunction $\Psi(x, y, z)$ can be mapped onto the spatial evolution of the electric field envelope $e(x, y, z)$ along the z direction. Note that an analogous derivation can be done for the magnetic field [28]. The main advantage of optical waveguides is that they allow to directly observe the evolution in space of the wavefunction probability density. For example, the experimental observation of Bloch oscillations took almost 65 years since its theoretical prediction due to the short lifetime of the electron coherence [75]. Instead, analogous optical Bloch oscillations [78, 79] has been directly observed in optical waveguides using standard techniques such as simple fluorescence imaging [71, 73] or scanning tunneling microscopy techniques [72]. Moreover, the dynamics of a single quantum particle trapped in a lattice potential can be mapped into the dynamics of a mode propagating in a system of evanescently-coupled optical waveguides, with the evanescent coupling of the light between the waveguides resembling the role of quantum tunneling. This permits to apply quantum engineering protocols to control light dynamics along the propagation direction.

Discrete regime

Paraxial light evolution in arrays of weakly-coupled optical waveguides can be simplified using the coupled-mode formalism discussed in Section 2.3. In this regime, the transverse mode profiles can be assumed to be constant and only the mode amplitudes change along the propagation direction. In this regard, light dynamics in an array of N evanescently-coupled single-mode waveguides can be described using coupled-mode equations (2.66), which can be rewritten as

$$i\frac{d}{dz}\boldsymbol{\psi} = \mathcal{H}\boldsymbol{\psi}, \tag{2.75}$$

where $\boldsymbol{\psi} = (\tilde{a}_1, \ldots, \tilde{a}_N)^T$, with $\tilde{a}_j$ describing the complex modal field amplitude in waveguide j, and $\mathcal{H}$ is the Hamiltonian whose matrix elements are $\mathcal{H}_{i,j} = c_i(\delta_{j-1,i} + \delta_{j+1,i}) + \beta_j\delta_{i,j}$, where $\delta_{i,j}$ is the Kronecker delta. Equation (2.75) is analogous to

$$i\hbar\frac{d}{dt}\boldsymbol{\Psi} = \hat{\mathcal{H}}\boldsymbol{\Psi}, \tag{2.76}$$

where $\boldsymbol{\Psi} = (\Psi_1, \ldots, \Psi_N)^T$ is a discrete wavefunction and $\hat{\mathcal{H}}$ is a Hamiltonian in the tight-binding nearest-neighbor approximation [75]. As before, the time evolution in Eq. (2.76) can be mapped by the spatial evolution in Eq. (2.75). This analogy enables to visualize discrete phenomena emerging from other fields of physics such as ultracold atoms trapped in periodic potentials or electrons in the crystalline structure of solids using coupled optical waveguides [76]. Moreover, the success of optical waveguides to simulate discrete phenomena was boosted after the discovery of femtosecond laser writing techniques [31], which allow to inscribe two-dimensional waveguide arrays with arbitrary configurations [102, 192].

2.4.2 Applications in this thesis

In this thesis we use the quantum-optical analogies presented above to design novel photonic devices with improved performances with respect to the standard ones and to explore phenomena stemming from other fields of physics such as topological phases or the generation of artificial gauge fields.

Specifically, by exploiting the similarities between Eqs. (2.69) and (2.70) and between Eqs. (2.75) and (2.76), we are able to extend SUSY from quantum mechanics to optics, which allows to manipulate the modal content of optical waveguides as described in detail in Chapter 3. Besides, we combine these transformations with quantum engineering protocols, which improve the performance of photonic devices. To be precise, in Chapter 4 we propose an efficient and robust mode-division (de)multiplexing device based on the combination of spatial adiabatic passage techniques, first proposed to transfer population between spatially separated potential wells [105] and later mapped onto optical waveguides by using the analogies between Eqs. (2.75) and (2.76), and SUSY techniques [141]. This combination leads to a great improvement in terms of robustness and efficiency compared to conventional devices. Similarly, in Chapter 5 we introduce a new technique based on the application of SUSY transformations combined with an adiabatic modification along the propagation direction, allowing to engineer efficient and robust photonic devices such as tapered waveguides, single-waveguide mode filters, beam splitters, and interferometers. Furthermore, in Chapter 6, we propose to use DSUSY transformations to systematically address, alter and reconfigure the topological properties of a system. Therefore, by exploiting the analogies between Eqs. (2.75) and (2.76), we explore phenomena stemming from topological phases of matter using optical waveguides, providing a deeper understanding of topological physics [170]. In this line, we theoretically propose and experimentally verify using femtosecond-laser written waveguides how SUSY transformations can selectively suspend and re-establish topological protection of specific states, establishing SUSY-inspired techniques as a powerful tool for topological state engineering [193].

Finally, in Chapter 7, by exploiting the analogies between Eqs. (2.73) and (2.74) and between Eqs. (2.75) and (2.76), we experimentally verify using direct laser written waveguides the generation of artificial gauge fields induced by modes carrying Orbital Angular Momentum (OAM) [185, 194], first proposed with ultracold atoms [195, 196]. Specifically, we show how an effective magnetic flux naturally appears when light beams carrying OAM are injected into cylindrical waveguides arranged in a diamond-chain configuration, producing the Aharonov-Bohm (AB) caging effect [92]. These findings pave the way of switching on and off artificial gauge fields just by changing the topological charge of the input state, representing a step forward for optical quantum simulation.

3 Supersymmetry in optics

In the last few decades, the mathematical concept of supersymmetry has been extended from particle physics to other fields of physics such as condensed-matter, quantum mechanics or optics. In this regard, optical supersymmetry, based on applying supersymmetric transformations to engineer photonic devices, has been recently consolidated as an area of research on its own. In this chapter, the different mathematical tools used to design supersymmetric photonic structures are presented, establishing the basis to follow the rest of the thesis. Specifically, we focus on explaining how supersymmetric transformations can be used to synthesize superpartner phase-matched structures, except for some target modes that can be eliminated.

This chapter is organized as follows. In Section 3.1, we briefly discuss the origin of supersymmetry and its applications in optics. This is followed by the derivation of the basic mathematical tools of supersymmetric quantum mechanics in Section 3.2, and its mapping onto optics in Section 3.3. There, we discuss the simplest case corresponding to supersymmetric transformations of a single optical waveguides, which is used in Chapter 4, and their extension to waveguide arrays, which is implemented in Chapter 5. To continue, in Section 3.4, we introduce discrete supersymmetric transformations that can be applied to weakly-coupled waveguides, which are used in Chapter 6. Finally, in Section 3.5 we discuss the application of discrete SUSY transformations to two-dimensional waveguide arrays and in Section 3.6 we present the conclusions.

3.1 Introduction

Supersymmetry (SUSY), proposed in the 70's as an attempt to unify the mathematical treatment of bosons and fermions [120–122, 197, 198], states that every fermion has a bosonic superpartner and viceversa [199]. In this vein, SUSY provides a framework for unifying particle physics and gravity at the Planck energy scale and gives an explanation of the hierarchy problem [200]. Despite the lack of direct experimental evidence of superpartner particles, some of its fundamental concepts have attracted attention across numerous fields of physics in the last decades such as nuclear [201] and atomic [202] physics, condensed-matter [203], cosmology [204], non-relativistic quantum mechanics [132], and classical [117, 123] and quantum [124, 205, 206] optics. In particular, in this chapter, we focus on supersymmetry in quantum mechanics and in optics and their connection. Supersymmetric quantum mechanics (SUSY QM), first proposed by Witten in the 80's [207], has become a field of investigation on its own [125–127, 132, 208], yielding new ways to find analytically solvable [209–211] and reflectionless one-dimensional potentials [212, 213]. Furthermore, SUSY QM has also been implemented to periodic and non-periodic lattice potentials [214–218], to non-linear systems [219, 220], and to systems with Parity-Time (PT) symmetry [221–223]. The generalization to two-dimensional potentials is not trivial and requires the use of high order supercharge operators [224, 225], a vector-form SUSY decomposition [226, 227], or intertwined Hamiltonians [228, 229].

In the middle of the 90's, Chumakov and Wolf proposed for the first time the mapping of the mathematical concepts of SUSY QM onto optics by exploiting the analogies between the Helmholtz and the Schrödinger equations [123]. Their idea started to grow fast within the optics community after the publication of *Supersymmetric Optical structures* by Miri *et. al.* [117], an overview of how SUSY transformations can be used to manipulate the modal content of a given optical structure and control its scattering properties. Since then, most of the ideas previously introduced in SUSY QM have been applied in optics to engineer novel photonic devices with non-trivial properties. In particular, in guided wave optics, SUSY is implemented through an appropriate manipulation in space of the transverse refractive index profile, which allows to systematically shape the modal content of highly multimode structures creating superpartner structures with global phase-matching conditions among their modes, except for some targeted modes that are eliminated. This property has been exploited for mode filtering and multiplexing purposes by properly engineering one-dimensional refractive index profiles along the transverse [133–136, 141, 230, 231] and propagation [142, 144] directions, and two-dimensional profiles with cylindrical symmetry [137, 138]. Note that inverse SUSY transformations have also been used to add modes with certain propagation constants [145, 147]. Besides, discrete SUSY (DSUSY) transformations have been applied to arrays of coupled waveguides [139, 143, 153, 154], to create band gaps in extremely

disordered potentials [151, 152, 232], to manipulate graph networks [233], to scale up the radiance of laser arrays [155–159, 234–237] and to explore the interplay between SUSY and topology [193, 238–240]. In addition, the ideas behind SUSY have also been extended to non-Hermitian settings [140, 241–243] and to the time-domain [244]. Another aspect of SUSY transformations that has been highly investigated is the fact that superpartner structures exhibit identical scattering properties [145, 146, 245], allowing to design transparent defects [147–150, 246–248].

3.2 Supersymmetric quantum mechanics

Unlike the Poincaré algebra, where symmetry generators satisfy commutation (bosonic) relations, the Super-Poincaré or SUSY algebra is characterized by anti-commutation (fermionic) relations [122]. In particular, in the quantum-mechanical formalism [132], SUSY algebra satisfies

$$\{\hat{Q}, \hat{Q}^\dagger\} = \hat{H}, \tag{3.1}$$

$$\{\hat{Q}, \hat{Q}\} = \{\hat{Q}^\dagger, \hat{Q}^\dagger\} = 0, \tag{3.2}$$

$$\left[\hat{H}, \hat{Q}\right] = \left[\hat{H}, \hat{Q}^\dagger\right] = 0, \tag{3.3}$$

where $\hat{Q}$ is the supercharge operator and $\hat{Q}^\dagger$ its Hermitian conjugate, satisfying $\hat{Q}^2 = (\hat{Q}^\dagger)^2 = 0$, and $\hat{H}$ is the super-Hamiltonian. In matrix form, the supercharge operators and the super-Hamiltonian read

$$\hat{Q} = \begin{pmatrix} 0 & 0 \\ \hat{A} & 0 \end{pmatrix}, \quad \hat{Q}^\dagger = \begin{pmatrix} 0 & \hat{A}^\dagger \\ 0 & 0 \end{pmatrix} \quad \text{and} \quad \hat{H} = \begin{pmatrix} \hat{A}^\dagger\hat{A} & 0 \\ 0 & \hat{A}\hat{A}^\dagger \end{pmatrix}. \tag{3.4}$$

where $\hat{A}$ and $\hat{A}^\dagger$ are the factorization operators and $\hat{\mathcal{H}}^{(1)} = \hat{A}^\dagger\hat{A}$ and $\hat{\mathcal{H}}^{(2)} = \hat{A}\hat{A}^\dagger$ are the superpartner Hamiltonians [249, 250]. Assuming that the superpartner Hamiltonian $\hat{\mathcal{H}}^{(1)}$ satisfies the eigenvalue equation $\hat{\mathcal{H}}^{(1)}\Psi_m^{(1)} = E_m^{(1)}\Psi_m^{(1)}$, where $\Psi_m^{(1)}$ is the eigenstate and $E_m^{(1)}$ the eigenvalue of state m, one can derive

$$\hat{A}\hat{\mathcal{H}}^{(1)}\Psi_m^{(1)} = \hat{A}E_m^{(1)}\Psi_m^{(1)}, \tag{3.5}$$

$$\hat{A}\hat{A}^\dagger\hat{A}\Psi_m^{(1)} = E_m^{(1)}\hat{A}\Psi_m^{(1)}, \tag{3.6}$$

$$\hat{\mathcal{H}}^{(2)}(\hat{A}\Psi_m^{(1)}) = E_m^{(1)}(\hat{A}\Psi_m^{(1)}), \tag{3.7}$$

obtaining that $\hat{A}\Psi_m^{(1)}$ is an eigenstate of $\hat{\mathcal{H}}^{(2)}$ with energy $E_m^{(1)}$, establishing SUSY isospectrality between $\hat{\mathcal{H}}^{(1)}$ and $\hat{\mathcal{H}}^{(2)}$. While for broken SUSY all the eigenvalues are shared between both superpartner Hamiltonians ($E_m^{(1)} = E_m^{(2)}$), as it is displayed in Fig. 3.1(a), for unbroken SUSY, the ground state eigenvalue of $\hat{\mathcal{H}}^{(1)}$ is annihilated ($\hat{A}\Psi_0^{(1)} = 0$) and

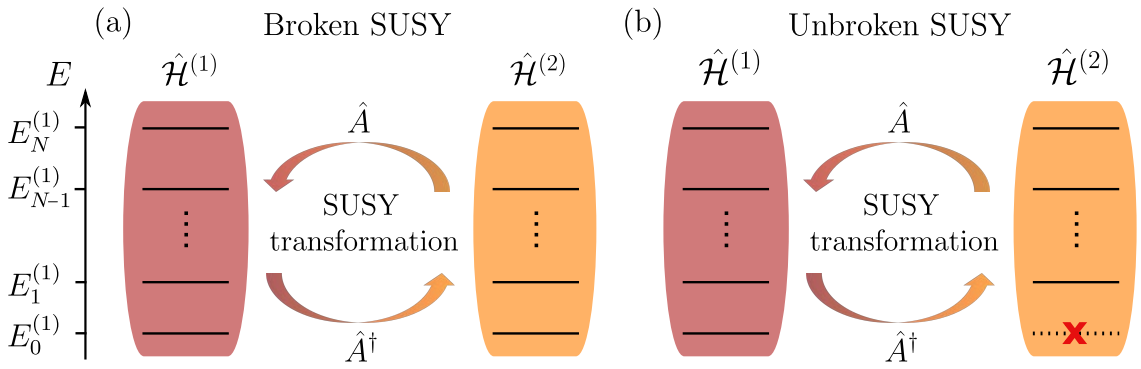

Figure 3.1: Schematic representation of the eigenvalue spectrum of the superpartner Hamiltonians $\hat{\mathcal{H}}^{(1)}$ and $\hat{\mathcal{H}}^{(2)}$ for the (a) broken and (b) unbroken SUSY regimes.

removed from the eigenvalue spectrum of $\hat{\mathcal{H}}^{(2)}$, as it is shown in Fig. 3.1(b). Therefore, in the unbroken SUSY regime, the eigenvalues satisfy

$$E_m^{(2)} = E_{m+1}^{(1)} \quad \text{and} \quad E_0^{(1)} = 0. \tag{3.8}$$

As an example of the factorization of the Hamiltonian, we consider the one-dimensional single-particle Hamiltonian, given by

$$\hat{\mathcal{H}} = -\frac{d^2}{dx^2} + V(x), \tag{3.9}$$

where $V(x)$ is the potential. The shape of the superpartner isospectral potentials $V^{(1)}$ and $V^{(2)}$ can be obtained using the factorization operators $\hat{A} = W(x) + d/dx$ and $\hat{A}^\dagger = W(x) - d/dx$, where $W(x)$ is the so-called superpotential. Applying $\hat{\mathcal{H}}^{(1)} = \hat{A}^\dagger \hat{A}$ and $\hat{\mathcal{H}}^{(2)} = \hat{A}\hat{A}^\dagger$ to $\Psi_m^{(1)}$ and $\Psi_m^{(2)}$, respectively, one obtains

$$\mathcal{H}^{(1)}\Psi_m^{(1)} = \left[-\frac{d^2}{dx^2} - \frac{dW(x)}{dx} + W^2(x)\right]\Psi_m^{(1)}, \tag{3.10}$$

$$\mathcal{H}^{(2)}\Psi_m^{(2)} = \left[-\frac{d^2}{dx^2} + \frac{dW(x)}{dx} + W^2(x)\right]\Psi_m^{(2)}, \tag{3.11}$$

with the superpartner potentials being

$$V^{(1)}(x) = W^2(x) - \frac{dW(x)}{dx} \quad \text{and} \quad V^{(2)}(x) = W^2(x) + \frac{dW(x)}{dx}, \tag{3.12}$$

and the superpotential $W(x)$, considering a nodeless ground state $\Psi_0^{(1)}$, reading

$$W(x) = -\frac{d}{dx}\ln\left[\Psi_0^{(1)}(x)\right]. \tag{3.13}$$

3.3 Supersymmetry in optics

The factorization process described in Section 3.2 can be adapted to optical waveguides. In particular, we introduce SUSY transformations considering a one-dimensional refractive index profile $n(x)$, in which Transverse Electric (TE) modes propagate along the z direction. Note that a similar derivation can be performed for Transverse Magnetic (TM) modes [136]. As discussed in Section 2.2 of Chapter 2, from the Helmholtz equation (2.35), one can derive the eigenvalue equation

$$\mathcal{H}e_m(x) = \mu_m e_m(x), \tag{3.14}$$

where $\mu_m = -\beta_m^2$ is the eigenvalue, β_m is the propagation constant and $e_m(x) \equiv e_{y,m}(x)$ the eigenfunction of mode m, and $\mathcal{H}$ is the Hamiltonian given by

$$\mathcal{H} = -\frac{d^2}{dx^2} - k_0^2 n^2(x), \tag{3.15}$$

where $k_0 = 2\pi/\lambda_0$ is the vacuum wavenumber. By comparing the Hamiltonians (3.9) and (3.15), one can see how $-k_0^2 n^2(x)$ is playing the role of the potential $V(x)$, as previously explained in Section 2.4 of Chapter 2. Thus, superpartner structures can be achieved by properly engineering the refractive index profiles. Note that, from here on, we order the modes with respect to its propagation constant β_m i.e., with the fundamental mode laying at the top of the eigenvalue spectrum, as it is represented in Fig. 3.2.

Considering the original index profile $n^{(1)}(x)$ supporting at least the fundamental TE_0 mode with a transverse field distribution $e_0^{(1)}(x)$ and a propagation constant $\beta_0^{(1)}$, SUSY can be established according to Eq. (3.4) by factorizing the Hamiltonian into

$$\mathcal{H}^{(1)} + \left(\beta_0^{(1)}\right)^2 = A^\dagger A \quad \text{and} \quad \mathcal{H}^{(2)} + \left(\beta_0^{(1)}\right)^2 = AA^\dagger, \tag{3.16}$$

where $A = W(x) + d/dx$ and $A^\dagger = W(x) - d/dx$ are the factorization operators and $W(x)$ the superpotential. Therefore, the eigenvalue equation (3.14) can be rewritten in terms of the factorization operators as

$$\mathcal{H}^{(1)} e_m^{(1)} = \left[\left(\beta_0^{(1)}\right)^2 - \left(W(x) - \frac{d}{dx}\right)\left(W(x) + \frac{d}{dx}\right)\right] e_m^{(1)}, \tag{3.17}$$

$$\mathcal{H}^{(2)} e_m^{(2)} = \left[\left(\beta_0^{(1)}\right)^2 - \left(W(x) + \frac{d}{dx}\right)\left(W(x) - \frac{d}{dx}\right)\right] e_m^{(2)}, \tag{3.18}$$

where $e_{m+1}^{(1)}(x) \propto A^\dagger e_m^{(2)}(x)$ and $e_m^{(2)}(x) \propto A e_{m+1}^{(1)}(x)$. Moreover, from Eqs. (3.17) and (3.18), one can derive the superpartner index profiles $n^{(1)}(x)$ and $n^{(2)}(x)$, reading

$$n^{(1)}(x) = \frac{1}{k_0^2}\sqrt{\left(\beta_0^{(1)}\right)^2 - W^2(x) + \frac{dW(x)}{dx}}, \tag{3.19}$$

$$n^{(2)}(x) = \frac{1}{k_0^2}\sqrt{\left(\beta_0^{(1)}\right)^2 - W^2(x) - \frac{dW(x)}{dx}}. \tag{3.20}$$

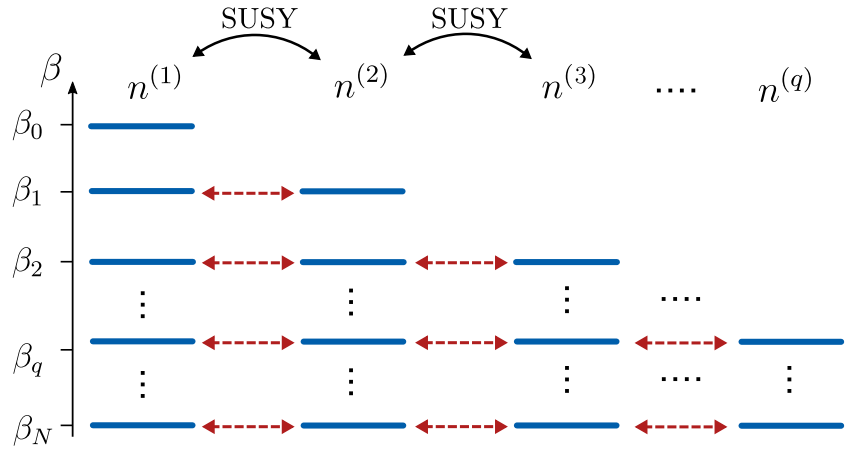

Figure 3.2: Schematic representation of the eigenvalue spectrum of a hierarchical sequence of superpartner refractive index profiles $\{n^{(1)}, n^{(2)}, \ldots, n^{(q)}\}$.

Finally, by imposing that for unbroken SUSY the ground state of $\mathcal{H}^{(1)}$ is annihilated i.e., $Ae_0^{(1)} = 0$, one obtains that the superpotential is given by

$$W(x) = -\frac{d}{dx} \ln \left[e_0^{(1)}(x) \right]. \tag{3.21}$$

Therefore, if one knows the fundamental mode wavefunction $e_0^{(1)}(x)$, the superpartner profile $n^{(2)}(x)$ can be derived. Besides, these SUSY transformations can be applied in an iterative manner q times. In this case, the superpartner Hamiltonians read

$$\mathcal{H}^{(q)} + (\beta_0^{(q)})^2 = \left(A^{(q)}\right)^\dagger A^{(q)} \quad \text{and} \quad \mathcal{H}^{(q+1)} + (\beta_0^{(q)})^2 = A^{(q)} \left(A^{(q)}\right)^\dagger, \tag{3.22}$$

where $A^{(q)} = W^{(q)}(x) + d/dx$, $\left(A^{(q)}\right)^\dagger = W^{(q)}(x) - d/dx$, $W^{(q)}(x) = -\partial_x \ln[e_0^{(q)}(x)]$, which correspond to a family of superpartner index profiles $\{n^{(1)}, n^{(2)}, \ldots, n^{(q)}\}$, satisfying

$$n^{(q+1)}(x) = \sqrt{[n^{(q)}(x)]^2 - \frac{2}{k_0^2} \frac{dW^{(q)}(x)}{dx}}, \tag{3.23}$$

and sharing a common set of eigenvalues as it is shown in Fig. 3.2.

3.3.1 Single waveguide

To illustrate how one-dimensional SUSY transformations are implemented, we examine first the simplest case of a single waveguide defined by a refractive index profile $n^{(1)}(x)$ supporting the fundamental $\mathrm{TE}_0^{(1)}$ and the first excited $\mathrm{TE}_1^{(1)}$ modes with propagation constants $\beta_0^{(1)}$ and $\beta_1^{(1)}$, respectively, whose superpartner is defined by a refractive index profile $n^{(2)}(x)$ only supporting the $\mathrm{TE}_0^{(2)}$ mode with propagation constant $\beta_0^{(2)} = \beta_1^{(1)}$.

As an example, we consider (i) a step-index profile, which is analytically solvable, and (ii) a super-Gaussian profile, which is numerically solvable.

First, let us consider the step-index waveguide represented in Fig. 3.3(a) consisting of a core of width d and refractive index n_{core} embedded in a medium of lower refractive index n_{clad}. Introducing the analytical field distributions of $e_0^{(1)}(x)$, given by Eqs. (2.40) and (2.41) in Chapter 2, into Eq. (3.21), one obtains the superpotential

$$W(x) = \begin{cases} k_0 \tan(k_{x,0}x), & |x| \leq d/2 \\ \pm\gamma_{x,0}, & |x| > d/2 \end{cases}, \tag{3.24}$$

where $k_{x,0}$ is the wavevector and $\gamma_{x,0}$ the extinction coefficient in the x direction, respectively. Moreover, introducing

$$\frac{dW(x)}{dx} = \begin{cases} k_0^2 \sec^2(k_{x,0}x), & |x| \leq d/2 \\ 0, & |x| > d/2 \end{cases}, \tag{3.25}$$

into Eq. (3.20), the analytical expression of the superpartner index profile reads

$$n^{(2)}(x) = \begin{cases} \sqrt{n_{\text{core}}^2 - 2\left(\frac{k_{x,0}}{k_0}\right)^2 \sec^2(k_{x,0}x)}, & |x| \leq d/2 \\ n_{\text{clad}}, & |x| > d/2 \end{cases}. \tag{3.26}$$

The superpartner index profile $n^{(2)}(x)$, the superpotential $W(x)$ and its derivative dW/dx, are represented in Figs. 3.3(b), (c) and (d), respectively. Note that the sharp features in the superpartner profile, which appear due to the discontinuity of the step-index profile at $x = \pm d/2$, can be reduced by smoothing the original profile. To this aim, we consider a super-Gaussian refractive index profile represented in Fig. 3.3(e), given by

$$\left[n^{(1)}(x)\right]^2 = n_{\text{clad}}^2 + (n_{\text{core}}^2 - n_{\text{clad}}^2) \exp\left[-\left(\frac{2x}{d}\right)^{2p}\right], \tag{3.27}$$

where $2p$ is an index that smooths the profile. Here, the fundamental mode wavefunction $e_0^{(1)}(x)$ has to be obtained numerically, e.g., using standard finite-difference methods [190]. As it can be seen in Fig. 3.3(f), the sharp dips in the superpartner index profile $n^{(2)}(x)$ have been considerably reduced.

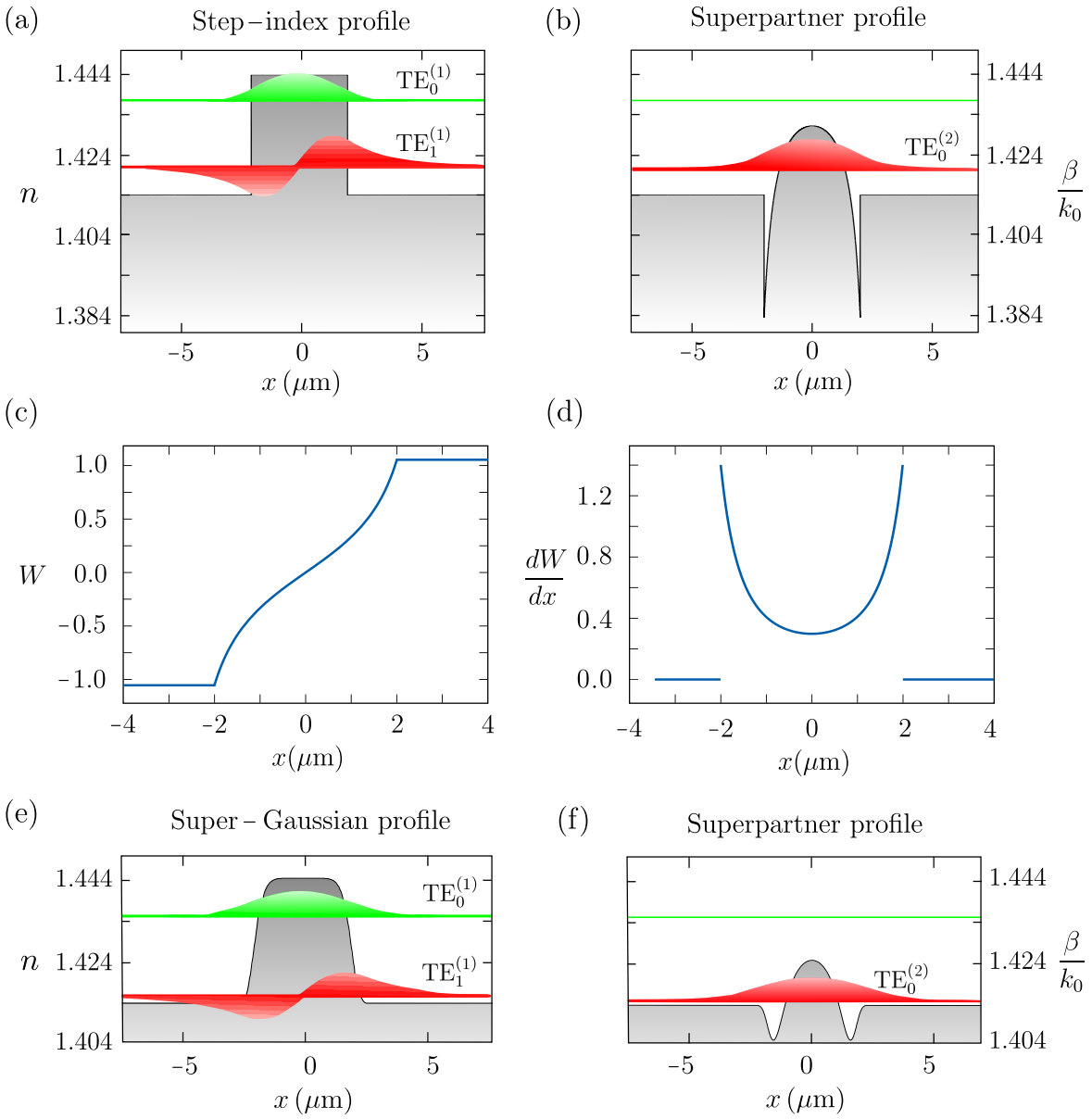

Figure 3.3: Refractive index and transverse mode profiles in (a) the step-index profile and (b) its superpartner profile. (c) Superpotential $W(x)$ and (d) its slope dW/dx corresponding to the step-index profile. Refractive index and transverse mode profiles in (e) the super-Gaussian profile and (f) its superpartner profile. The width of the waveguide is $d = 4\,\mu$m, $2p = 8$, $n_{\text{core}} = 1.444$, $n_{\text{clad}} = 1.414$ and the wavelength used is $\lambda_0 = 1.55\,\mu$m.

3.3.2 Array of waveguides

SUSY transformations are not restricted to single waveguides and can also be applied to arrays of waveguides just by considering the supermodes l of the entire structure satisfying the eigenvalue equation $\mathcal{H}e_l(x) = \mu_l e_l(x)$. In this case, the removal of the eigenvalue μ_0 corresponding to the fundamental supermode of the original structure, composed of N waveguides, generates a superpartner structure composed of $N-1$ waveguides. Note that, from here on, we name the superpartner lattices as SP_s, where s identifies the eigenvalue μ_s that is removed. To exemplify it, we consider a waveguide lattice described by a one-dimensional refractive index profile $n^{(1)}(x)$, we consider six identical step-index single-mode waveguides, see the lower panel of Fig. 3.4(a), supporting six $\mathrm{TE}_l^{(1)}$ supermodes with propagation constants $\beta_l^{(1)}$, as represented in the upper panel of Figure 3.4(a). By using the SUSY transformation given by Eq. (3.23), one obtains the

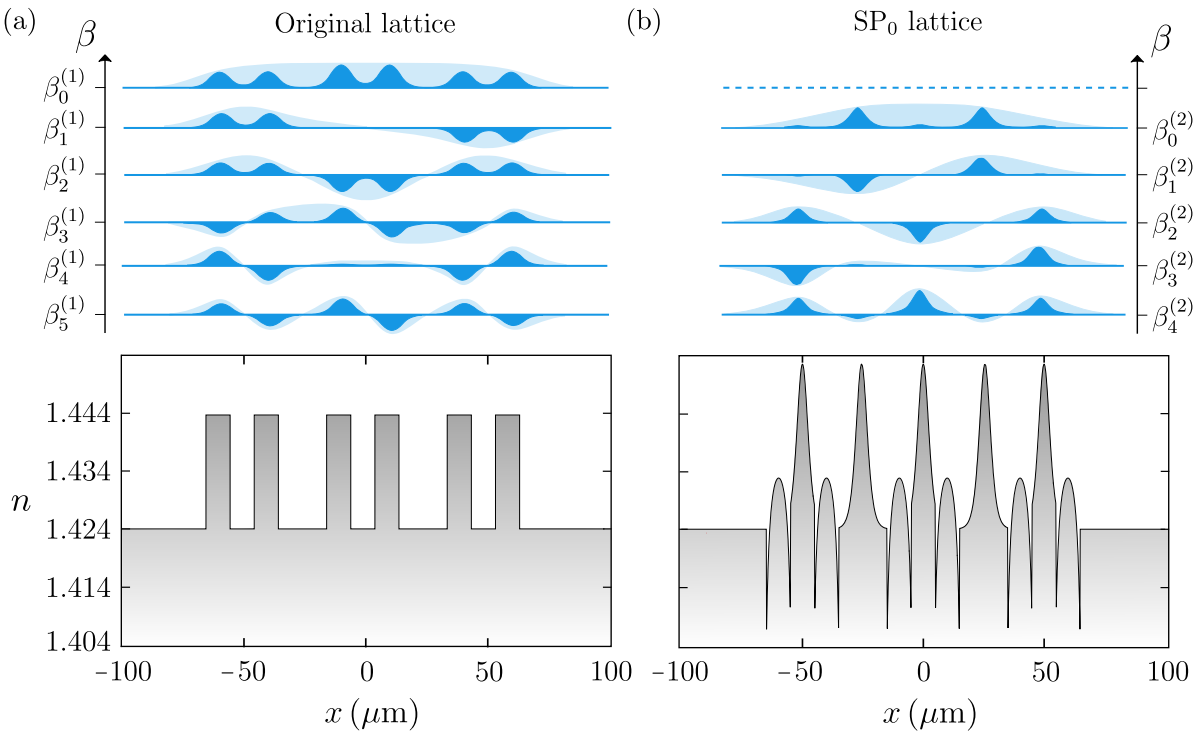

Figure 3.4: Eigenvalue spectrum and eigenstate profiles (upper panel) and refractive index distribution (lower panel) corresponding to (a) the original lattice and (b) the SP_0 lattice, obtained by removing the eigenvalue $\mu_0^{(1)}$ using standard SUSY factorization techniques. The original lattice is composed of six identical waveguides separated alternating distances $D_1 = 10\,\mu$m and $D_2 = 20\,\mu$m. The core width is $d = 10\,\mu$m, $n_{\mathrm{core}} = 1.444$, $n_{\mathrm{clad}} = 1.424$ and $\lambda_0 = 1.55\,\mu$m.

superpartner index profile $n^{(2)}(x)$ represented in the lower panel of Fig. 3.4(b), which sustains five $\mathrm{TE}_l^{(2)}$ supermodes with their propagation constants satisfying $\beta_l^{(2)} = \beta_{l+1}^{(1)}$, as it can be observed in the upper panel of Fig. 3.4(b).

From a technological perspective, the experimental implementation of superpartner index profiles has remained elusive so far due to the complexity of the spatial refractive index profiles, requiring fabrication methods with subwavelength scale control over the refractive index. In this regard, advanced femtosecond laser writing techniques [76, 102] or electron-beam lithography [251, 252] are promising techniques. Alternatively, the problem of implementing superpartner index profiles can be overcome in waveguide arrays described by the coupled-mode formalism introduced in Section 2.3 of Chapter 2, where one can fabricate the superpartner lattice [139, 146, 157, 193] just in terms of the detunings (controlled by the width/height of the waveguides) and the couplings (controlled by the separation between waveguides).

3.4 Discrete supersymmetry

In the coupled-mode regime introduced in Section 2.3 of Chapter 2, a chain of N single-mode evanescently-coupled waveguides can be described by

$$\mathcal{H}\boldsymbol{\psi}_l = \mu_l \boldsymbol{\psi}_l, \tag{3.28}$$

where $\boldsymbol{\psi}_l = (\tilde{a}_l^1, \ldots, \tilde{a}_l^N)^T$ is the eigenfunction of supermode l, with $\tilde{a}_l^j$ describing the complex modal field amplitude in waveguide j. Moreover, the Hamiltonian $\mathcal{H}$ of Eq. (3.28) is an $N \times N$ matrix with elements $\mathcal{H}_{i,j} = (\delta_{j-1,i} + \delta_{j+1,i})c_i + \Delta\beta_j \delta_{i,j}$, where c_j is the coupling strength between nearest-neighbours waveguides and $\Delta\beta_j$ the detuning between waveguides. In this regime, the problem of having two superpartner Hamiltonians $\mathcal{H}^{(1)}$ and $\mathcal{H}^{(2)}$ with the same eigenvalue spectrum $\mu_l^{(1)} = \mu_l^{(2)}$ can be addressed through the concept of similar matrices using symmetric or asymmetric methods [253]. Specifically, DSUSY transformations applied to tri-diagonal Hamiltonians preserve their form i.e., keep the nearest-neighbour couplings between waveguides but decouple the last waveguide ($c_{N-1} = 0$). Therefore, the superpartner Hamiltonian $\mathcal{H}^{(2)}$ is given by an $N \times N$ matrix that can be decomposed in two decoupled blocks, a one-dimensional one containing the eigenvalue $\mu_s^{(1)}$ and an $N-1$-dimensional one containing the rest of the eigenvalues, which are phase-matched with the original structure. Therefore, since one of the eigenvalues is decoupled from the rest of the system, these transformations resemble standard SUSY transformations and, from here on, we refer to the superpartner structure as the lattice composed of $N-1$ waveguides. In addition, the iterative application of DSUSY transformations reduces the overall size of the system, removing one waveguide in each iteration.

3.4.1 Cholesky factorization

The Cholesky factorization [253] is a symmetric method that resembles standard SUSY transformations in the sense that only the eigenvalue corresponding to the fundamental supermode of $\mathcal{H}^{(1)}$ can be detached from the eigenvalue spectrum of $\mathcal{H}^{(2)}$. This method decomposes the Hamiltonian into

$$\mathcal{H}^{(1)} - \mu_0^{(1)} I = A^* A \quad \text{and} \quad \mathcal{H}^{(2)} - \mu_0^{(1)} I = A A^*, \tag{3.29}$$

where A is a lower triangular matrix, A^* its conjugate transpose and I the N-dimensional identity matrix. As an example, we consider the lattice represented in the lower panel of Fig. 3.5(a) consisting of six identical waveguides with alternating couplings c_1 and c_2. As it is represented in the upper panel of Fig. 3.5(a), this lattice supports six $\mathrm{TE}_l^{(1)}$ supermodes. By applying the Cholesky factorization given by Eq. (3.29), the symmetric superpartner lattice SP_0 represented in the lower panel Fig. 3.5(b) is obtained. This superpartner structure is composed of five waveguides supporting five $\mathrm{TE}_l^{(2)}$ supermodes

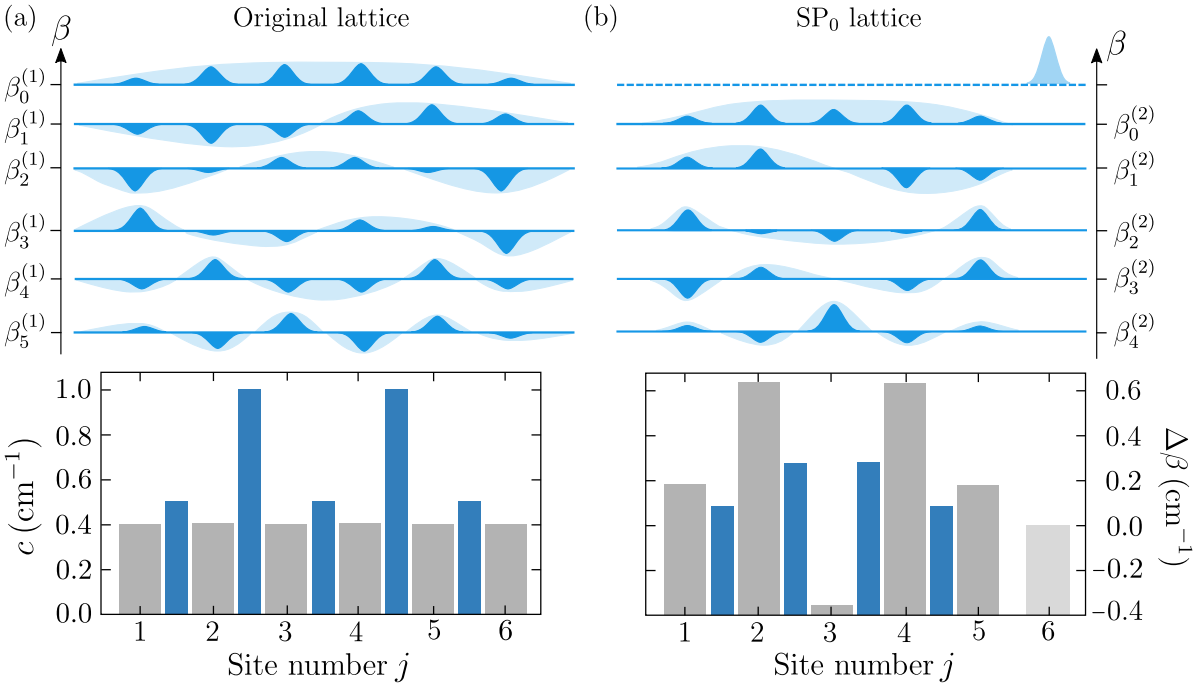

Figure 3.5: Eigenvalue spectrum and eigenstate profiles (upper panel) corresponding to (a) the original lattice and (b) the SP_0 lattice, obtained by removing the eigenvalue $\mu_0^{(1)}$ using the Cholesky factorization. Discrete representation (lower panel) in terms of the waveguide's detuning $\Delta\beta$ (grey bars) and couplings c (blue bars) of (a) the original lattice with $c_1 = 0.5$ cm^{-1} and $c_2 = 1.0$ cm^{-1}, and (b) the SP_0 lattice.

that are phase-matched with the ones of the original lattice, as it is displayed in the upper panel of Fig. 3.5(b). Moreover, there is an isolated waveguide where the supermode with eigenvalue $\mu_0^{(1)}$ if fully localized.

3.4.2 QR factorization

A more powerful decomposition technique that can be used to perform DSUSY transformations is the QR factorization [253]. The main advantage of this asymmetric method over the symmetric one is that it overcomes the limitation of removing only the fundamental supermode of the system while preserving the nearest-neighbour couplings configuration. With this method, the superpartner Hamiltonians can be factorized as

$$\mathcal{H}_s^{(1)} - \mu_s^{(1)} I = QR \quad \text{and} \quad \mathcal{H}_s^{(2)} - \mu_s^{(1)} I = RQ, \tag{3.30}$$

where $\mu_s^{(1)}$ is the eigenvalue ($s \geq 1$) that is detached from the eigenvalue spectrum of $\mathcal{H}^{(2)}$, as it is displayed in Fig. 3.6, Q is an orthogonal matrix, satisfying $Q^T Q = I$, and R is an upper triangular matrix. This factorization is unique only when $\mathcal{H}^{(1)}$ is invertible i.e., $\det(\mathcal{H}^{(1)}) = 0$, and requires the diagonal elements of R to be positive.

The QR factorization of Eq. (3.30) can be implemented using (i) the Gram–Schmidt method, which is easy to implement but numerically unstable, (ii) the Householder transformation, and (iii) the Givens rotation method, which is used in Chapter 6. Methods (ii) and (iii) are numerically stable and based on transforming an arbitrary linear system into a triangular system by systematically introducing zeros using unitary transformations. While the Householder transformation relies on using reflections to introduce zeros into the subdiagonal elements of $\mathcal{H}^{(1)}$ [253], the Givens rotation method does so

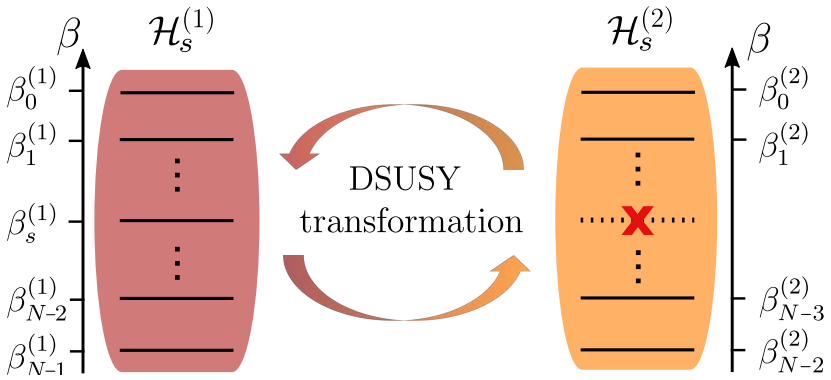

Figure 3.6: Schematic representation of the eigenvalue spectrum of the superpartner Hamiltonians $\mathcal{H}_s^{(1)}$ and $\mathcal{H}_s^{(2)}$, obtained by removing the eigenvalue $\mu_s^{(1)}$ using asymmetric DSUSY transformations.

by applying rotations g_j to each diagonal element of $\mathcal{H}^{(1)}$, such as

$$g_j \begin{pmatrix} \mathcal{H}_{j,j} \\ \mathcal{H}_{j+1,j} \end{pmatrix} = \begin{pmatrix} t_j & s_j \\ -s_j & t_j \end{pmatrix} \begin{pmatrix} \mathcal{H}_{j,j} \\ \mathcal{H}_{j+1,j} \end{pmatrix} = \begin{pmatrix} r_j \\ 0 \end{pmatrix}, \tag{3.31}$$

where

$$t_j = \frac{\mathcal{H}_{j,j}}{r_j}, \quad s_j = \frac{\mathcal{H}_{j+1,j}}{r_j} \quad \text{and} \quad r_j = \sqrt{|\mathcal{H}_{j,j}|^2 + |\mathcal{H}_{j+1,j}|^2}. \tag{3.32}$$

Therefore, the R matrix is obtained by introducing zeros at the tri-diagonal Hamiltonian $\mathcal{H}^{(1)}$ while the Q matrix is obtained by concatenating all the Givens rotation matrices $G_j = g_j \otimes I$, forming

$$R = \prod_{j=1}^{N-1} G_j \mathcal{H}_s^{(1)} \quad \text{and} \quad Q = \prod_{j=1}^{N-1} G_j^T. \tag{3.33}$$

The application of an asymmetric DSUSY transformation using the QR factorization is exemplified for the lattice represented in the lower panel of Fig. 3.7(a), which is composed of six identical waveguides supporting six $\text{TE}_l^{(1)}$ supermodes. The superpartner structure SP_2, obtained after decoupling the eigenvalue $\mu_2^{(1)}$ from the eigenvalue spectrum of $\mathcal{H}^{(2)}$ using the QR factorization given by Eq. (3.30), is shown in the lower panel of Fig. 3.7(b). Moreover, as it can be seen in the upper panel of Fig. 3.7(b), the SP_2 structure supports five $\text{TE}_l^{(2)}$ supermodes, which are phase-matched with the modes of the original structure except for the $\text{TE}_2^{(1)}$ which has no counterpart in the $N-1$ superpartner structure.

3.5 Two-dimensional supersymmetry

The extension of SUSY transformations to two-dimensional waveguides characterized by $n(x, y)$ is not trivial due to the coupling between the different components of the fields. Therefore, the implementation of two-dimensional SUSY transformations can only be achieved under some conditions such as cylindrical waveguides i.e., $n(r)$ [117, 137, 138], separable refractive index profiles i.e., $n(x, y) = n_x(x)n_y(y)$ [149, 151] or using Darboux transformations [231, 254]. Alternatively, DSUSY transformations can be easily applied to two-dimensional waveguide arrays described by the coupled-mode formalism [143, 152, 236, 237]. Nevertheless, one has to be aware that, in general, the Hamiltonian and its superpartner are no longer tri-diagonal matrices. Therefore, the off-diagonal terms appearing in the factorization process may correspond to long-range couplings [255] that are difficult to physically implement. Thus, one has to restrict the structures to those that have realistic solutions with implementable geometries. Here, the use of femtosecond laser written waveguides is of great interest due to its flexibility

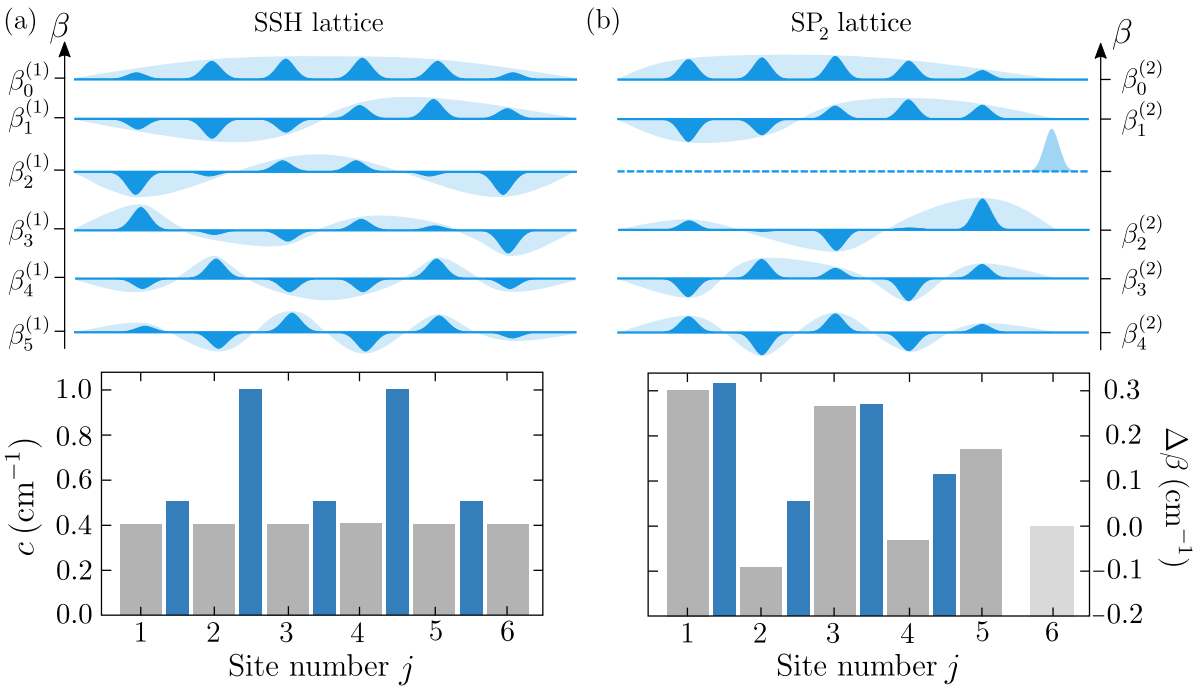

Figure 3.7: Eigenvalue spectrum and eigenstate profiles (upper panel) corresponding to the (a) original lattice and (b) SP_2 lattice, obtained by removing the eigenvalue $\mu_2^{(1)}$ using the QR factorization method. Discrete representation (lower panel) in terms of the waveguide's detuning $\Delta\beta$ (red bars) and couplings c (blue bars) of (c) the original lattice with $c_1 = 0.5\,\mathrm{cm}^{-1}$ and $c_2 = 1.0\,\mathrm{cm}^{-1}$, and (d) the SP_2 lattice.

to implement two-dimensional configurations [76]. To alleviate the restrictions of two-dimensional geometries, a new method based on implementing the notion of DSUSY to a quantum version of one-dimensional coupled bosonic oscillators has been recently proposed [237].

To illustrate two-dimensional DSUSY transformations, we consider four identical waveguides distributed in a rectangular geometry, as it is displayed in Fig. 3.8(a). The Hamiltonian of this system is given by

$$\mathcal{H} = \begin{pmatrix} 0 & c_{1,2} & c_{1,3} & 0 \\ c_{2,1} & 0 & 0 & c_{2,4} \\ c_{3,1} & 0 & 0 & c_{3,4} \\ 0 & c_{4,2} & c_{4,3} & 0 \end{pmatrix}. \tag{3.34}$$

The superpartner Hamiltonian obtained by removing $\mu_1^{(1)}$ using the QR factorization,

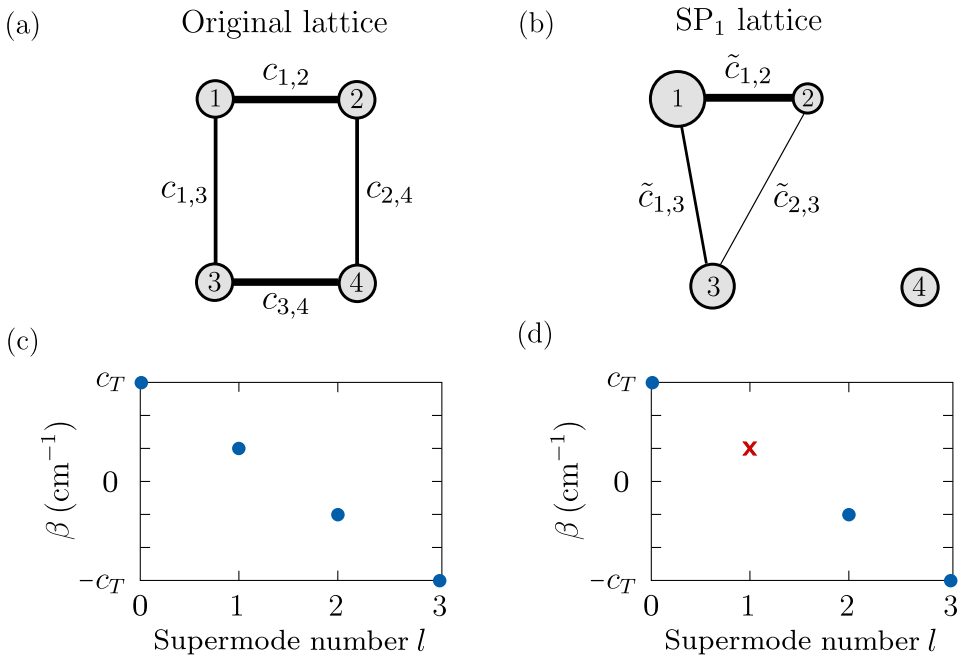

Figure 3.8: Schematic representation of (a) a two-dimensional array of optical waveguides, which are evanescently-coupled with couplings $c_v \equiv c_{1,2} = c_{3,4}$ and $c_h \equiv c_{1,3} = c_{2,4}$, and (b) its superpartner obtained by removing $\mu_1^{(1)}$ using the QR factorization. The width of the lines is proportional to the coupling strength and the size of the circles illustrate the detuning between waveguides. Eigenvalue spectrum corresponding to (c) the original and (d) the SP_1 lattices. The coupling strengths are $c_h = 1.0\,\mathrm{cm}^{-1}$, $c_v = 0.5\,\mathrm{cm}^{-1}$, and $c_T = c_v + c_h$.

given by Eq. (3.30), reads

$$\mathcal{H}^{(2)} = \begin{pmatrix} \Delta\beta_1 & \tilde{c}_{1,2} & \tilde{c}_{1,3} & 0 \\ \tilde{c}_{2,1} & \Delta\beta_2 & \tilde{c}_{2,3} & 0 \\ \tilde{c}_{3,1} & \tilde{c}_{3,2} & \Delta\beta_3 & 0 \\ 0 & 0 & 0 & 0 \end{pmatrix}. \tag{3.35}$$

Since the 4^{th} waveguide is completely detached from the rest of the system, see Fig. 3.8(b), the superpartner structure SP_1 becomes triangular and supports three supermodes whose eigenvalues are displayed in Fig. 3.8(d). Note that, although we have chosen a rectangular lattice as an example, this technique can be extended to systems with a higher number of waveguides and more complex geometries as long as the couplings that appear in the superpartner Hamiltonian are physically realistic. Moreover, by implementing these transformations in an iterative way, the geometry of the structure can be substantially changed while the properties of the eigenvalue spectrum are preserved, which could lead to novel two-dimensional non-trivial topological structures.

3.6 Conclusions

This chapter was aimed to introduce the reader to the concept of SUSY in Optics. In this context, we have started by briefly introducing the basic formalism of SUSY QM, illustrating how the Hamiltonian factorization process works for one-dimensional potentials, and we have mapped this process onto Optics, where superpartner structures can be synthesized by properly engineering the refractive index profile. Moreover, to familiarize the reader with the different SUSY transformations used along this thesis, we have started with the simplest case i.e., performing the SUSY transformation of a single optical waveguide structure. This transformation, in combination with spatial adiabatic passage techniques, is used in Chapter 4 to design an efficient and robust mode-division demultiplexing device. To continue, we have applied SUSY transformation of an array of evanescently-coupled waveguides. In this case, the adiabatic connection of superpartner structures along the propagation direction is used in Chapter 5 to design efficient and robust tapered waveguides, mode filters, beam splitters and interferometers. The chapter has continued with the introduction of DSUSY transformations, which can be applied to waveguide arrays, overcoming the restriction of standard SUSY techniques of removing only the eigenvalue associated to the fundamental mode. Moreover, this DSUSY transformations have also the advantage that can be experimentally implemented using standard fabrication techniques. In this regard, we use DSUSY transformations to induce topological phase transitions in Chapter 6. To end this chapter, we have discussed under which conditions SUSY transformation can be extended to two-dimensional waveguides and to arrays of waveguides arranged in two-dimensional configurations, which opens interesting perspectives for its application to manipulate two-dimensional systems with non-trivial topological properties. Finally, note that although we have focused on optical waveguide structures, the SUSY transformations presented in this chapter can be implemented in other platforms such as trapping potentials for neutral atoms [256] or acoustics [257], being a powerful mathematical tool to perform eigenvalue spectrum engineering that could lead to non-trivial phenomena.

4

Mode-division (de)multiplexing using adiabatic passage and supersymmetric waveguides

The development of mode-division multiplexing techniques is an important step to increase the information processing capacity in integrated photonic platforms. To this end, we propose an efficient and robust mode-division (de)multiplexing device based on the combination of spatial adiabatic passage and supersymmetric techniques. The proposed device consists of two identical step-index external waveguides coupled to a supersymmetric central one, which is engineered with a specific modal content that prevents the transfer of the fundamental transverse electric TE_0 spatial mode of the outer waveguides. Moreover, the separation between waveguides is modified along the propagation direction to optimize the adiabatic passage for the first excited TE_1 mode of the outer waveguides. Thus, by injecting a superposition of the two lowest TE modes into the left waveguide, the TE_0 mode remains in the input waveguide while the TE_1 mode is fully transferred to the right waveguide, hence, demultiplexing the modes. The combination of both techniques leads to a great improvement in terms of robustness and efficiency compared to conventional (de)multiplexing devices.

This chapter is organized as follows. First, in Section 4.1, we motivate the importance of developing mode-division multiplexing techniques. This is followed by the description of the device in Section 4.2 and the introduction of the supersymmetric and spatial adiabatic passage techniques used to engineer the device in Section 4.3. To continue, Section 4.4 is devoted to prove the efficiency and robustness of the device working as a demultiplexer. Finally, in Section 4.5, we conclude and propose possible extensions of the work.

4.1 Introduction

Integrated optical devices [28], exhibiting both high fidelity and high speed transmission, are expected to foster novel communication platforms [37, 38]. In this context, due to the increasing demand of high-capacity optical transmissions and the proximity of the capacity crunch [164, 258], a lot of efforts have been put during the last decades to further enhance the information transmission capacity [259, 260]. In this vein, multiplexing technologies [261], based on encoding information using different approaches including Space-Division Multiplexing [262], Mode-Division Multiplexing (MDM) [263], Wavelength-Division Multiplexing [264], and Polarization-Division Multiplexing [265], have emerged as an efficient solution. Here, we focus on MDM techniques, which use different spatial modes as degrees of freedom and can be implemented using multimode fibers and waveguides [266, 267]. In this regard, integrated MDM devices [268] have been designed using photonic lanterns [269], multimode interference devices [270, 271], asymmetric directional couplers [272–274], adiabatic couplers [275, 276], asymmetric Y-junctions [277, 278], microring-based devices [279, 280] and SUSY-based optical devices [137, 139, 141, 143].

The success of applying SUSY transformations to design mode-division demultiplexing devices relies on the possibility of generating superpartner phase-matched structures for an arbitrarily large number of modes, except for some targeted modes that can be removed from the spectrum of the system, as discussed in detail in Chapter 3. These SUSY techniques can be applied to guided wave optics through an appropriate manipulation of the refractive index profile, offering new ways of controlling the modal content of light beams in optical waveguides [117, 134, 140, 142, 142, 144, 230]. Thus, the application of SUSY techniques allows to systematically construct a superpartner profile with its modes sharing all the propagation constants with the original waveguide, except for the fundamental mode of the original waveguide that has no counterpart in the superpartner structure. By exploiting this property, SUSY-based optical devices constitute a promising alternative to standard MDM devices offering global phase-matching and efficient mode conversion in an integrated and scalable way [139], and being compatible with other existing multiplexing techniques. Here, to design a robust (de)multiplexing device, we combine SUSY transformations with Spatial Adiabatic Passage (SAP) techniques, known as a high-efficient and robust method to transfer light between systems of three evanescently-coupled waveguides [281, 282].

The idea of SAP [105], first proposed to transfer matter waves between spatially separated potential wells [283, 284] and later extended to transfer light beams between evanescently-coupled waveguides [162, 163], was inspired by the Stimulated Raman Adiabatic Passage (STIRAP) technique [88, 89]. The STIRAP technique consists of applying two temporally delayed laser pulses in a counter-intuitive sequence to effi-

ciently transfer the atomic population between the two ground states in a Λ-type three-level atomic system [160, 285]. Analogously, SAP can be achieved in systems of three evanescently-coupled optical waveguides by engineering the waveguide separation along the propagation direction introducing a spatial delay such that the light beam adiabatically follows a dark supermode of the system. Consequently, light is efficiently and robustly transferred between the outermost waveguides of the triple waveguide configuration. Besides, SAP of light has also been implemented in systems with a higher number of waveguides [286, 287], incorporating absorption and nonlinearity [288, 289], via a continuum [290, 291], and in digital systems [292, 293], leading to applications ranging from spectral filtering to quantum gates [106–108, 294, 295].

In this chapter, we combine SUSY and SAP techniques to design an efficient and robust device that can be used for (de)multiplexing spatial modes, to manipulate the modal content or to remove non-desired modes of an input field distribution [141]. In particular, we demonstrate that a system of three coupled waveguides, with two identical step-index external waveguides and a supersymmetric central one, engineered along the propagation direction to optimize SAP for the first excited mode of the step-index waveguides, can be used to demultiplex a superposition of the two lowest spatial modes. Besides, the same device can also be used for multiplexing by using the output ports as the input ones. Although the idea of SUSY has already been experimentally applied for MDM purposes [139], its combination with SAP techniques is proposed for the first time, leading to a great improvement in terms of robustness and efficiency.

4.2 Physical system

We consider a set of three planar evanescently-coupled waveguides consisting of a core of refractive index n_{core} embedded in a medium of lower refractive index n_{clad}. The central (C) waveguide is straight while the left (L) and right (R) waveguides are truncated circles of radius r, with their centers displaced δ from each other along the z direction, see Fig. 4.1(a). Regarding the refractive index profiles, two structures are investigated:

(i) The step-index (SI) structure formed by three identical step-index waveguides with refractive index $n_j^{(1)}(x)$ where $j = L, C, R$, see Fig. 4.1(b).

(ii) The SUSY structure consisting of two identical step-index waveguides with $n_L^{(1)}(x) = n_R^{(1)}(x)$ and a supersymmetric central one with $n_C^{(2)}(x)$, see Fig. 4.1(c).

Even though SUSY transformations are not restricted to specific refractive index contrasts and profiles [117], here we consider $n_{\text{core}} = 1.444$ and $n_{\text{clad}} = 1.414$, corresponding

to refractive indices of fused silica at telecom wavelength $\lambda_0 = 1.55\,\mu$m, which is the material used in the fabrication of discrete SUSY structures [139, 193]. In addition, the width d of the step-index waveguides is chosen to allow the propagation of the fundamental $\mathrm{TE}_0^{(1)}$ and the first excited $\mathrm{TE}_1^{(1)}$ modes while the superpartner waveguide only supports the $\mathrm{TE}_0^{(2)}$ mode, which has the same propagation constant as the $\mathrm{TE}_1^{(1)}$ mode.

As discussed in detail in Section 2.2 of Chapter 2, the TE component of the electric field in each isolated waveguide j, with an arbitrary one-dimensional refractive index profile $n_j(x)$, can be expressed as a superposition of modes as

$$E_y^j(x,z) = \sum_m a_m^j(z) e_m^j(x) \exp(-i\beta_m^j z), \tag{4.1}$$

where $k_0 = 2\pi/\lambda_0$ is the vacuum wavenumber, $a_m^j(z)$ is the amplitude, $e_m^j(x)$ is the transverse spatial distribution and β_m^j the propagation constant of mode m propagating in waveguide j. Moreover, these modes are solutions of the eigenvalue equation

$$\mathcal{H}_j e_m^j(x) = -\left(\beta_m^j\right)^2 e_m^j(x), \tag{4.2}$$

where $\mathcal{H}_j = -d^2/dx^2 - k_0^2 n_j^2(x)$ is the Hamiltonian of each isolated waveguide j. In particular, we apply a SUSY transformation to the central step-index refractive index profile and then, we engineer the separation between waveguides along the propagation direction in order to couple the waveguides in such a way that only the first excited $\mathrm{TE}_1^{(1)}$ mode of the step-index waveguides is transmitted between waveguides.

4.3 Theoretical background

As it has been discussed in detail in Section 2.3 of Chapter 2, in systems of weakly-coupled waveguides in which the transverse spatial distribution of the mode $e_m^j(x)$ remains constant and only its amplitude changes along the propagation direction, the Hamiltonian of the system can be defined in a discrete way. In this regime, the propagation of mode m in a system of three weakly-coupled waveguides can be defined by coupled-mode equations, which read [188]

$$i\frac{d}{dz}\begin{pmatrix} \tilde{a}_m^L \\ \tilde{a}_m^C \\ \tilde{a}_m^R \end{pmatrix} = \begin{pmatrix} \beta_m^L & c_m^{LC} & c_m^{LR} \\ c_m^{CL} & \beta_m^C & c_m^{CR} \\ c_m^{RL} & c_m^{RC} & \beta_m^R \end{pmatrix} \begin{pmatrix} \tilde{a}_m^L \\ \tilde{a}_m^C \\ \tilde{a}_m^R \end{pmatrix}, \tag{4.3}$$

where $\tilde{a}_m^j(z) = a_m^j(z)\exp(-i\beta_m^j z)$ is the complex modal field amplitude of mode m in waveguide j, and $c_m^{LC}(z)$, $c_m^{RC}(z)$ and $c_m^{LR}(z)$ are the coupling coefficients between mode m in the left $\leftrightarrow$ central, right $\leftrightarrow$ central and, left $\leftrightarrow$ right waveguides, respectively.

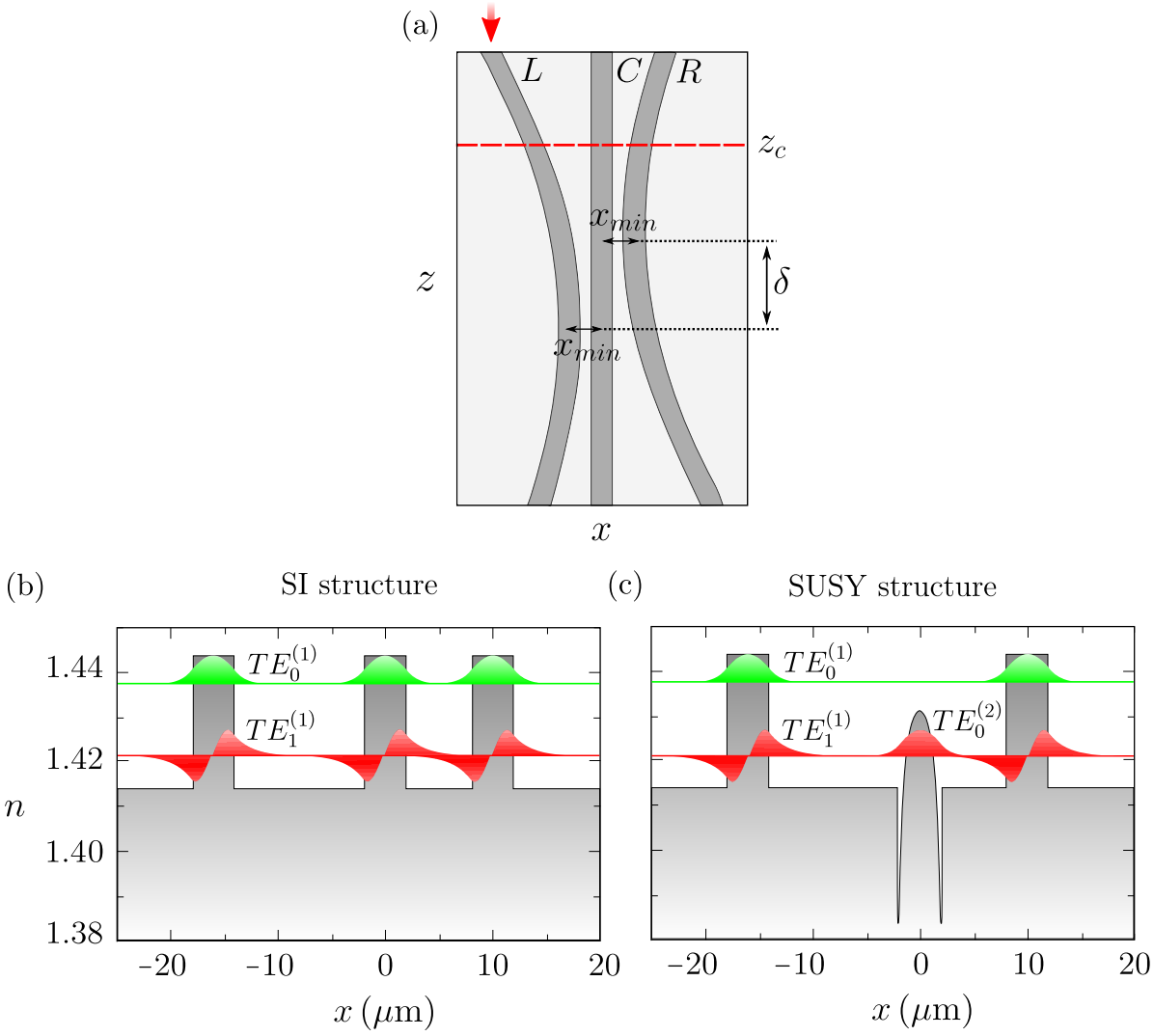

Figure 4.1: (a) Schematic representation of the proposed device viewed from above. The width of the waveguides cores is $d = 4\,\mu$m, the minimum separation between waveguides is $x_{min} = 7\,\mu$m, the radius of curvature of the external waveguides is $r = 3.5\,$m, the spatial delay between their centers is $\delta = 4\,$mm and the total length along z is $D = 18\,$mm. Refractive index distribution and transverse mode profiles supported for each isolated waveguide at z_c in (a) for (b) the SI structure and (c) the SUSY structure. The positions of the modes along the vertical axis correspond to β_m/k_0.

The coupling is due to evanescent fields, hence, depends on the separation between waveguides, and it is symmetric, i.e., $c_m^{ij} = c_m^{ji}$. Moreover, we assume that the left and right waveguides are not directly coupled ($c_m^{LR} = c_m^{RL} = 0$). Therefore, for the SI structure one has identical waveguides, hence, $\beta_m^{L(1)} = \beta_m^{C(1)} = \beta_m^{R(1)}$ for $m = 0, 1$. Furthermore, for the SUSY structure, one also has the same propagation constants for the fundamental mode of the step-index waveguide and the first excited mode of the superpartner waveguide i.e., $\beta_1^{L(1)} = \beta_0^{C(2)} = \beta_1^{R(1)}$. Therefore, when the modes are perfectly phase-matched, the coupled-mode equations read

$$i\frac{d}{dz}\begin{pmatrix} \tilde{a}_m^L \\ \tilde{a}_m^C \\ \tilde{a}_m^R \end{pmatrix} = \begin{pmatrix} 0 & c_m^{LC} & 0 \\ c_m^{LC} & 0 & c_m^{RC} \\ 0 & c_m^{RC} & 0 \end{pmatrix}\begin{pmatrix} \tilde{a}_m^L \\ \tilde{a}_m^C \\ \tilde{a}_m^R \end{pmatrix}. \tag{4.4}$$

For the SI structure, we have two independent sets of equations, one for each mode ($m = 0, 1$), while for the SUSY structure there is only one set of equations due to the coupling between the $\mathrm{TE}_1^{(1)}$ mode of the external waveguides with the $\mathrm{TE}_0^{(2)}$ mode of the central waveguide.

4.3.1 Spatial adiabatic passage technique

To achieve an efficient and robust transmission of the first excited TE mode between the outermost waveguides, we engineer the separation between waveguides along the propagation direction following a SAP protocol. Diagonalizing the matrix of the right hand side of Eq. (4.4), one obtains that one of the supermodes of the system only involves light in the left and right waveguides

$$\mathrm{Dark}(\Theta_m) = \begin{pmatrix} \cos(\Theta_m) \\ 0 \\ -\sin(\Theta_m) \end{pmatrix}, \tag{4.5}$$

where Θ_m is the mixing angle given by

$$\Theta_m(z) \equiv \arctan\left(\frac{c_m^{LC}(z)}{c_m^{RC}(z)}\right). \tag{4.6}$$

The supermode of Eq. (4.5) is analogous to the well known dark state of quantum optics [88]. If the input beam coincides with the dark supermode, its adiabatic modification allows for an efficient and robust transfer of the light beam between the outermost waveguides without light propagation into the central one, known as SAP of light [281]. In particular, we consider that light is injected into the left waveguide and the couplings are engineered following a counter-intuitive sequence along z. By counter-intuitive sequence we mean that, first, the right waveguide approaches to the central waveguide and

then, with a certain spatial delay, the left waveguide approaches to the central waveguide whereas the right separates from it, see Fig. 4.1(a). With this spatial configuration, the mixing angle Θ_m evolves from 0 to $\pi/2$ and light can be transferred from the left to the right waveguide. The variation of the couplings along z in the structure of Fig. 4.1(a) follows a Gaussian function of the form [282]

$$c_m^{LC,RC}(z) \approx c_m(x_{min},\lambda)\exp\left[\frac{-(z-D/2\pm\delta/2)^2}{2rb_m(\lambda)}\right], \tag{4.7}$$

where $2rb_m(\lambda)$ indicates the width of the Gaussian, $b_m(\lambda)$ is a decaying constant and

$$c_m(x_{min},\lambda) \equiv \tilde{c}_m(\lambda)\exp\left[\frac{-x_{min}}{b_m(\lambda)}\right], \tag{4.8}$$

gives the maximum value of the couplings. Note that, due to the fact that for higher λ the modes are less confined, the coupling coefficients increase linearly with the wavelength [295]. Besides, the global adiabaticity condition reads

$$\delta\sqrt{(c_m^{LC})^2+(c_m^{RC})^2} > K, \tag{4.9}$$

where K is a dimensionless constant that takes a value around 10 for optimal parameter values, such as the spatial delay between the couplings [160]. Thus, Eqs. (4.7) and (4.9) allow to select the appropriate geometrical parameter values D, δ and x_{min} to efficiently perform SAP of mode m.

4.3.2 Supersymmetric waveguides

To design the superpartner index profile $n_C^{(2)}(x)$ for the central waveguide only propagating the $\mathrm{TE}_0^{(2)}$ mode with the same propagation constant as the fundamental mode of the step-index waveguide ($\beta_0^{C(2)} = \beta_1^{C(1)}$), we perform a systematic deformation of the refractive index profile following the continuous SUSY techniques described in Section 3.3 of Chapter 3. From Eq. (4.2), the superpartner index profile can be derived by factorizing the Hamiltonian describing the central waveguide in terms of

$$\mathcal{H}_C^{(1)} + (\beta_0^{C(1)})^2 = A^\dagger A \quad \text{and} \quad \mathcal{H}_C^{(2)} + (\beta_0^{C(1)})^2 = AA^\dagger, \tag{4.10}$$

where $A = d/dx + W(x)$, and $A^\dagger = -d/dx + W(x)$ are the factorization operators and

$$W(x) = -\frac{\partial}{\partial x}\ln\left[e_0^{C(1)}(x)\right] \tag{4.11}$$

is the Superpotential of the central waveguide. By applying a SUSY transformation, the superpartner index profile $n_C^{(2)}(x)$ reads

$$n_C^{(2)}(x) = \sqrt{\left[n_C^{(1)}(x)\right]^2 - \frac{2}{k_0^2}\frac{dW(x)}{dx}}, \tag{4.12}$$

which for the step-index profile given by Eqs. (2.40) and (2.41) in Chapter 2, reads

$$n_C^{(2)}(x) = \begin{cases} \sqrt{n_{\text{core}}^2 - 2\left(\frac{k_{x,0}}{k_0}\right)^2 \sec^2(k_{x,0}x)}, & |x| \leq d/2 \\ n_{\text{clad}}, & |x| > d/2 \end{cases}, \tag{4.13}$$

where $k_{x,0}$ is the wavevector component of the fundamental mode in the x direction. The superpartner profile is represented in the central waveguide of Fig. 4.1(c).

4.4 Results and discussion

In this section we demonstrate that the combination of SAP and SUSY techniques allows for a very efficient and robust demultiplexing of transverse spatial modes. In particular, we show that, by injecting an equally weighted superposition of $\text{TE}_0^{(1)}$ and $\text{TE}_1^{(1)}$ modes in the left waveguide, the $\text{TE}_1^{(1)}$ mode is efficiently transferred to the right waveguide while the $\text{TE}_0^{(1)}$ mode remains in the left one. To guarantee an efficient and robust transfer of the $\text{TE}_1^{(1)}$ mode, we optimize the geometrical parameters to perform SAP of this mode in the SI structure. The coupling between waveguides is given by the overlap integral between the evanescent field of the modes. Therefore, since the coupling between fundamental modes is much weaker than for the first excited modes, the adiabaticity condition of Eq. (4.9) is not fulfilled for the former, hence, they are not efficiently transferred. On the contrary, although the coupling is slightly weaker between the $\text{TE}_1^{(1)}$ and the $\text{TE}_0^{(2)}$ modes of the SUSY structure than the coupling between the $\text{TE}_1^{(1)}$ modes of the SI structure, the adiabaticity condition is satisfied and the $\text{TE}_1^{(1)}$ mode will be efficiently transmitted.

In order to characterize the coupling coefficients along z, we numerically simulate the propagation of the $\text{TE}_1^{(1)}$ mode between two straight step-index waveguides separated different distances, x_{min}, as it is illustrated in Fig. 4.2(a). By measuring the spatial period of intensity oscillations given by the coupling length $L_c = \pi/2c_1$, an exponentially decaying curve can be fitted as represented in Fig. 4.2(b) and previously discussed in Section 2.3 of Chapter 2, obtaining the coupling coefficients $\tilde{c}_1^{(1)} \approx 263\,\text{mm}^{-1}$ and $b_1^{(1)} \approx 1.67\,\mu\text{m}$ Casting these values into Eq. (4.7), the optimized set of parameters to efficiently perform SAP of the $\text{TE}_1^{(1)}$ mode in the SI structure can be found. By properly adjusting the spatial delay between waveguides, as it is represented in Fig. 4.3(a), one obtains that the mixing angle Θ given by Eq. (4.6) evolves from 0 to $\pi/2$ as required for the SAP process, see Fig. 4.3(b). Moreover, by integrating Eq. (4.4) for these optimized parameters, we obtain that the $\text{TE}_1^{(1)}$ mode is fully transferred to the right waveguide following the dark supermode of the system, with almost no intensity in the central waveguide, as it can be observed in Fig. 4.3(c).

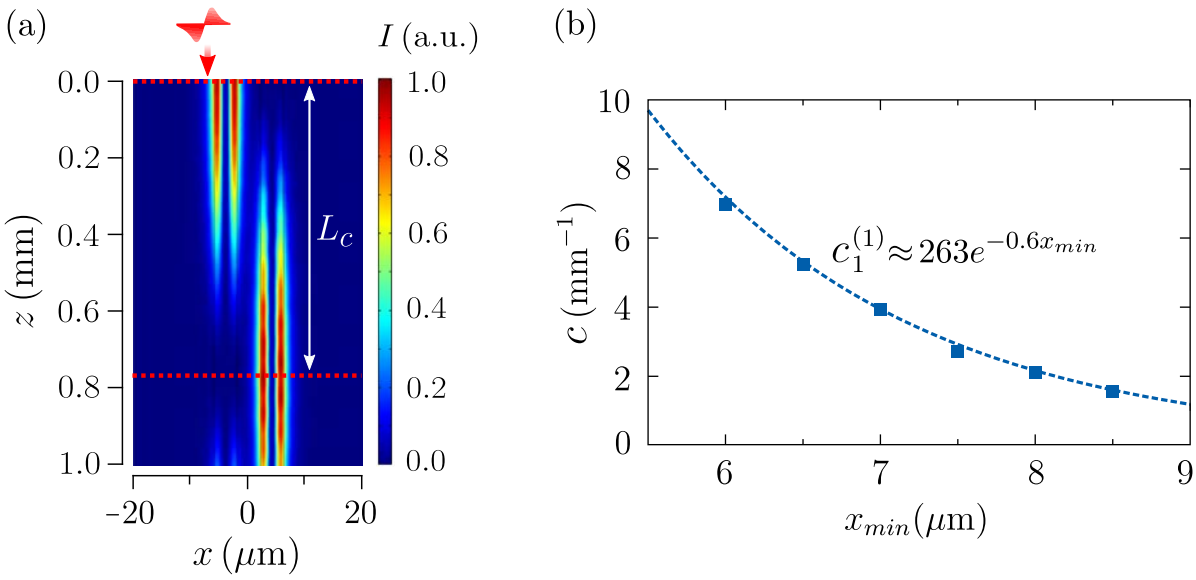

Figure 4.2: (a) Numerical simulation of light intensity propagation along z when the $\mathrm{TE}_1^{(1)}$ mode is injected in the left waveguide of a two straight step-index waveguide structure with $x_{min} = 8\,\mu$m. (b) Coupling coefficients calculated for $x_{min} = 6,\ 6.5,\ 7,\ 7.5,\ 8$ and $8.5\,\mu$m, $\lambda_0 = 1.55\,\mu$m and $d = 4\,\mu$m.

After verifying that the SAP of the first excited $\mathrm{TE}_1^{(1)}$ mode is efficiently performed in the SI structure, we check if these parameters are also valid for the SUSY structure. In this case, to verify that the couplings satisfy the adiabaticity condition of Eq. (4.9) using the SUSY structure, we perform the same analysis as before using a two-waveguide structure composed of a step-index $n^{(1)}(x)$ waveguide in the left and a supersymmetric $n^{(2)}(x)$ waveguide in the right, see Fig. 4.4(a). In this case, as displayed in Fig. 4.4(b), the obtained parameters are $\tilde{c}_1^{(2)} \approx 144\,\mathrm{mm}^{-1}$ and $b_1^{(2)} \approx 1.67\,\mu$m. As expected, the coupling coefficients in the SUSY structure are slightly weaker than in the SI structure. Nevertheless, if one introduces these parameters into Eq. (4.9), one obtains that they fulfill the adiabaticity condition. Therefore, since the modes are perfectly-phase matched and the adiabaticity condition is fulfilled, the optimized geometry for the SI structure also provides maximum $\mathrm{TE}_1^{(1)}$ mode transmission for the SUSY structure.

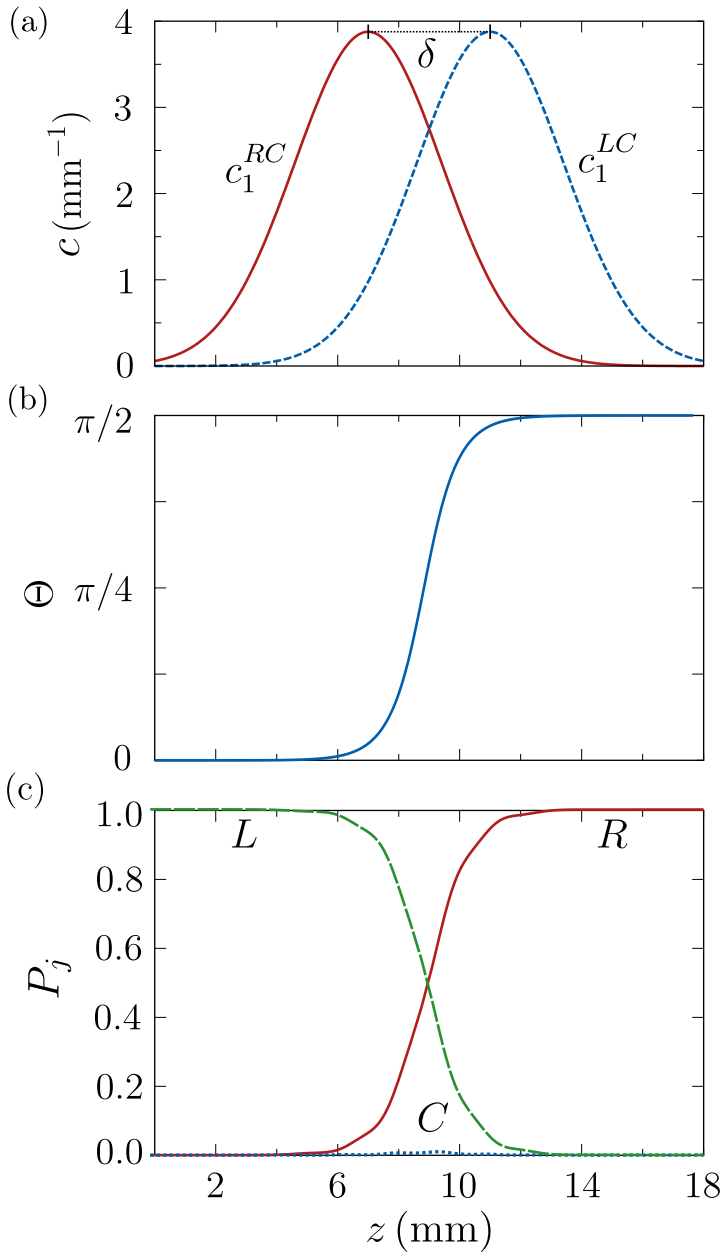

Figure 4.3: (a) Spatial sequence of the coupling coefficients for $m = 1$ in the designed device of Fig. 4.1(a) with the SI structure of Fig. 4.1(b). Spatial evolution of (b) the mixing angle Θ and (c) the $\mathrm{TE}_1^{(1)}$ mode power in each waveguide along the propagation direction predicted by the coupled-mode equations. The parameter values of the SI structure defined in Fig. 4.1(a) are $\lambda_0 = 1.55\,\mu\mathrm{m}$, $\tilde{c}_1^{(1)} = 263\,\mathrm{mm}^{-1}$, and $b_1^{(1)} = 1.66\,\mu\mathrm{m}$.

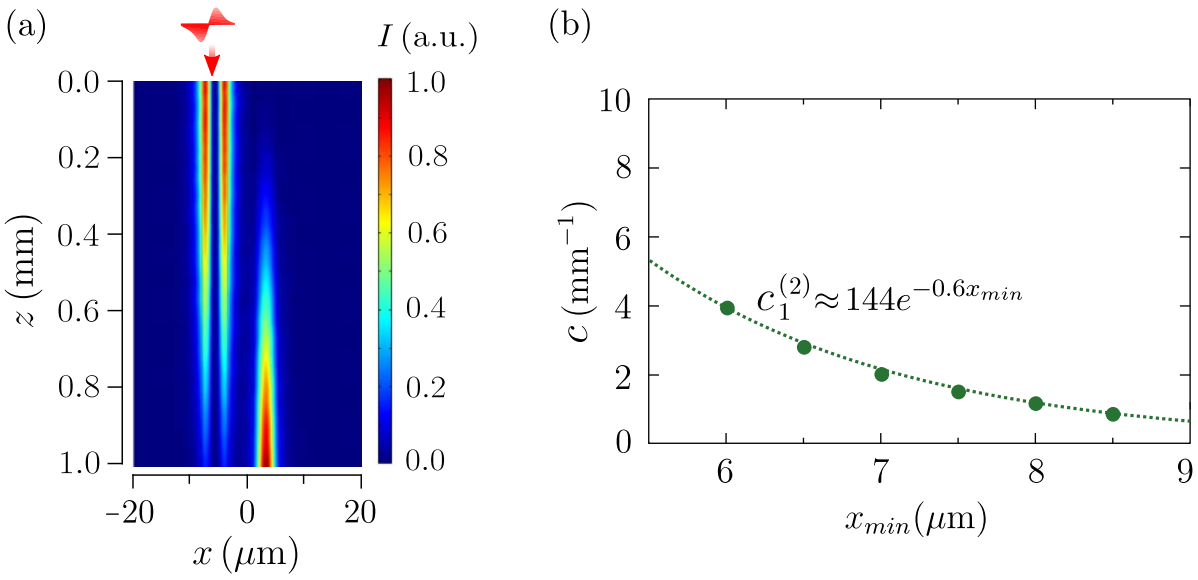

Figure 4.4: (a) Numerical simulation of light intensity propagation along z when the $TE_1^{(1)}$ mode is injected in the left waveguide of the structure composed of a step-index profile $n^{(1)}(x)$ (left) parallel to a supersymmetric profile $n^{(2)}(x)$ (right), with $x_{min} = 8\,\mu$m. (b) Coupling coefficients calculated for $x_{min} = 6,\ 6.5,\ 7,\ 7.5,\ 8$ and $8.5\,\mu$m, $\lambda_0 = 1.55\,\mu$m and $d = 4\,\mu$m.

Performing full numerical simulations using finite difference methods for the SI structure with the optimized geometry, we confirm the results of the coupled-mode equations, obtaining that 99.3% of the injected intensity of the $TE_1^{(1)}$ mode is transmitted to the right waveguide, see the right panel of Fig. 4.5(a). Alternatively, for the $TE_0^{(1)}$ mode, the injected intensity spreads among the three waveguides, see the left panel of Fig. 4.5(a), obtaining 11.2% in the right, 25.9% in the central and 62.8% in the left waveguides. To keep the $TE_0^{(1)}$ mode in the left waveguide and achieve efficient mode separation, we now consider the SUSY structure with the optimized geometry. In this case, 99.3% of the injected intensity of the $TE_1^{(1)}$ mode is still transmitted to the right waveguide while 99.8% of the injected intensity of the $TE_0^{(1)}$ mode now remains in the left waveguide, as it can be seen in the right and left panels of Fig. 4.5(b), respectively. Moreover, as the $TE_0^{(1)}$ and the $TE_1^{(1)}$ have different parity, the cross-talk between them is negligible. Thus, by injecting the superposition of both modes in the left waveguide of the SI structure, efficient demultiplexing is not achieved, as can be seen in Fig. 4.6(a). On the contrary, if we inject the superposition in the SUSY structure, the modes are efficiently demultiplexed as it can be seen in see Fig. 4.6(b).

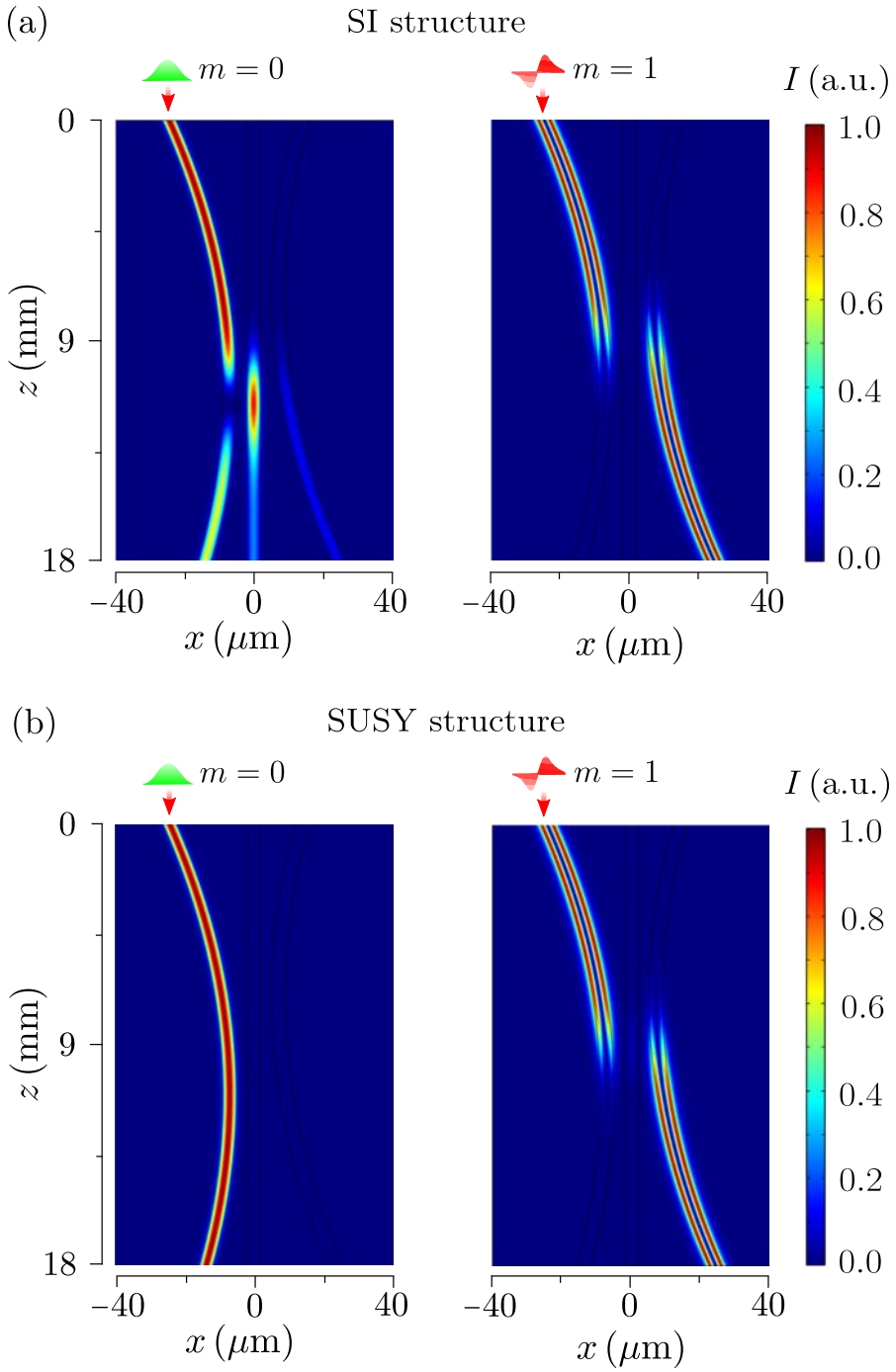

Figure 4.5: Numerical simulations of light intensity propagation ($\lambda_0 = 1.55\,\mu$m) along z when the fundamental (left panels) or the first excited mode (right panels) is injected in the left waveguide of the designed device of Fig. 4.1(a), with (a) the SI structure of Fig. 4.1(b) and (b) the SUSY structure of Fig. 4.1(c).

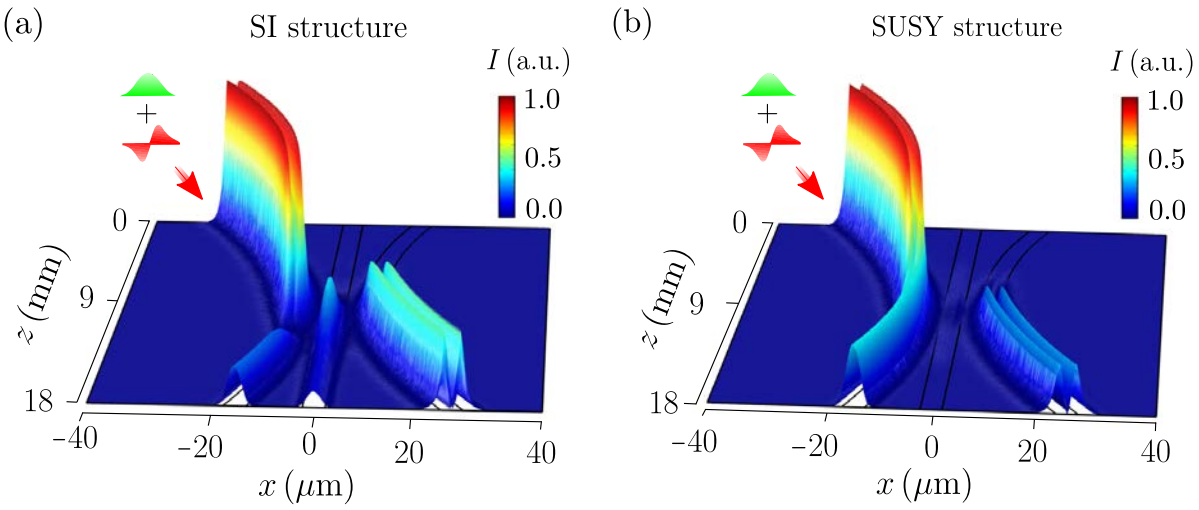

Figure 4.6: Numerical simulations of light intensity propagation ($\lambda_0 = 1.55\,\mu$m) along z when an equally weighted superposition of the fundamental and the first excited modes is injected in the left waveguide of the designed device of Fig. 4.1(a), with (a) the SI structure of Fig. 4.1(b) and (b) the SUSY structure of Fig. 4.1(c).

To investigate the efficiency and robustness of the proposed device for (de)multiplexing purposes, we introduce the Figure of Merit

$$\mathcal{F} = \frac{I^L_{0,out}}{I^L_{0,in}} \cdot \frac{I^R_{1,out}}{I^L_{1,in}} = \tilde{I}^L_0 \cdot \tilde{I}^R_1, \tag{4.14}$$

where $\tilde{I}^L_0$ is the fraction of intensity of the $\mathrm{TE}^{(1)}_0$ mode that remains in the left waveguide and $\tilde{I}^R_1$ is the fraction of intensity of the $\mathrm{TE}^{(1)}_1$ mode that is transmitted to the right waveguide. The maximum fidelity $\mathcal{F} = 0.99$ is achieved for the parameter values used so far to optimize SAP for the $\mathrm{TE}^{(1)}_1$ mode.

To prove the robustness of the device, we perform numerical simulations varying the geometrical parameters and light's wavelength. From these simulations, we find that the proposed device can be miniaturized down to $D_{min} = 10\,$mm and the spatial delay engineered within $3.5\,\mathrm{mm} \leq \delta \leq 4.5\,\mathrm{mm}$, maintaining a fidelity $\mathcal{F} = 0.99$. Moreover, fidelities $\mathcal{F} > 0.90$ are achieved for $2.0\,\mathrm{mm} < \delta < 6.0\,\mathrm{mm}$, as displayed in Fig. 4.7(a). Outside this range, the adiabaticity conditions are not fulfilled and light does not follow the dark supermode of the system anymore, spreading between waveguides, see Fig. 4.7(b). Note that, since the $\mathrm{TE}^{(1)}_0$ mode cannot be coupled to the central supersymmetric waveguide, it remains in the left waveguide even if the SAP conditions are not fulfilled.

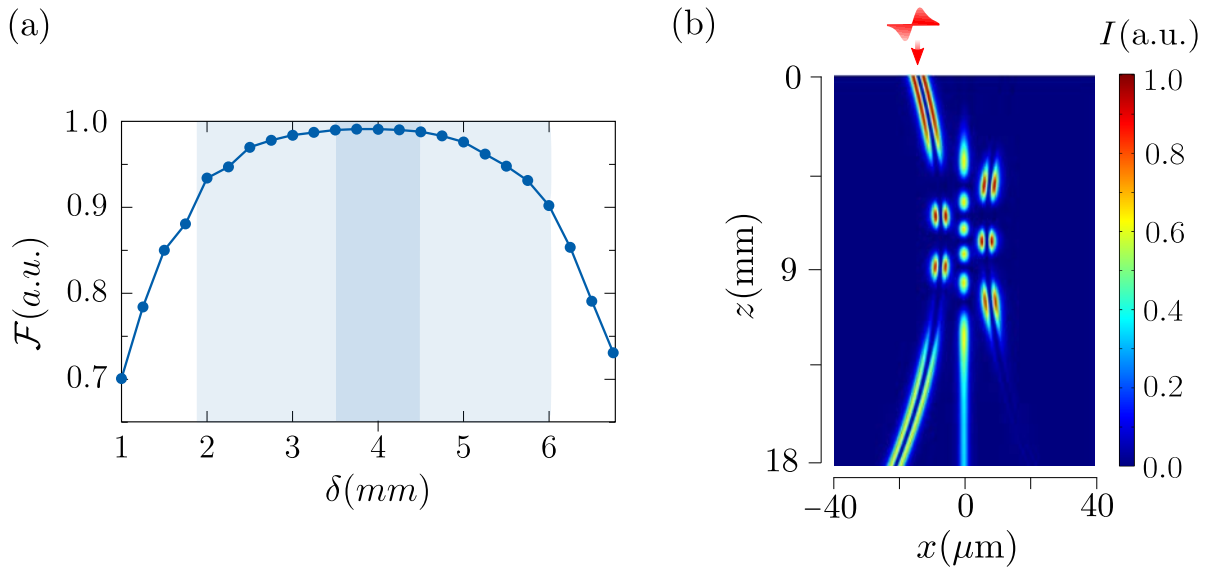

Figure 4.7: (a) Fidelity $\mathcal{F}$ in terms of the spatial delay δ calculated by injecting an equally weighted superposition of the fundamental and the first excited modes in the left waveguide of the SUSY structure of Fig. 4.1(c). The darker and lighter shaded regions indicate $\mathcal{F} > 0.99$ and $\mathcal{F} > 0.9$, respectively. (b) Numerical simulation of light intensity propagation along z when the $\mathrm{TE}_1^{(1)}$ mode is injected in the left waveguide of the SUSY structure of Fig. 4.1(c) without spatial delay ($\delta = 0$). Geometrical parameters as defined in Fig. 4.1(a) and $\lambda_0 = 1.55\,\mu$m.

Figure 4.8 shows the dependence of the fidelity with respect to the light's wavelength λ and the minimum separation between waveguide centers, x_{min}, assuming the refractive index profiles fixed and independent of the wavelength. Efficient demultiplexing ($\mathcal{F} > 0.90$) is achieved in a broad region of $\Delta\lambda \sim 0.5\,\mu$m and $\Delta x_{min} \sim 2\,\mu$m, reaching $\mathcal{F} = 0.99$ in some small regions. Although we have considered fixed refractive indices, the influence of dispersion remains negligible across $1.5\,\mu\text{m} \leq \lambda \leq 1.6\,\mu$m [139]. Besides, we have numerically checked that dispersion introduces deviations of the fidelities below 3% for the range $1.6\,\mu\text{m} < \lambda < 2\,\mu$m, while its impact becomes important for longer wavelengths. Note that, losses due to the bending of the waveguides associated to the adiabatic passage geometry [295] and the ones associated to SUSY mode conversion [139] are negligible. Thus, we only have the usual propagation losses, which depend on the characteristics of the specific waveguide. Therefore, from the results obtained in Fig. 4.8, we can conclude that the proposed device is an efficient and robust mode-division demultiplexing device. Furthermore, if one injects the fundamental and the first excited modes in the left and right waveguides of the output port, respectively, the same device operates as a multiplexer with the same fidelity and robustness.

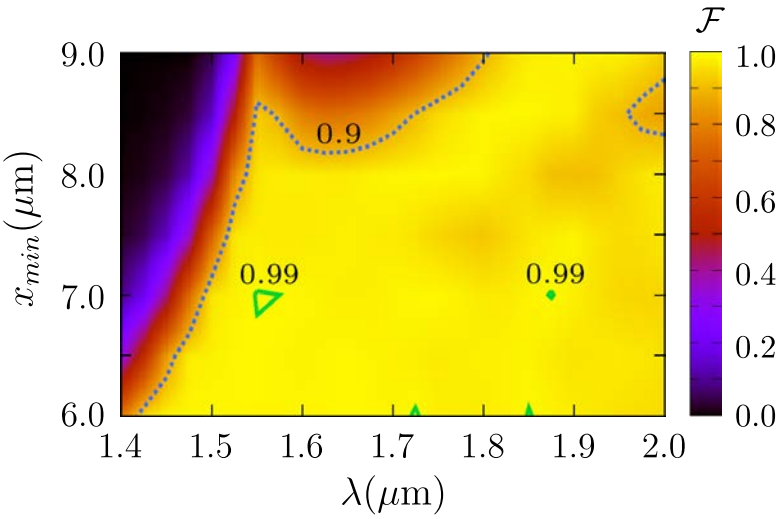

Figure 4.8: Demultiplexing fidelity calculated through numerical simulations when we inject an equally weighted superposition of the $\mathrm{TE}_0^{(1)}$ and the $\mathrm{TE}_1^{(1)}$ modes in the left waveguide for different wavelengths and different minimum separation between waveguides for the SAP device of Fig. 4.1(a) with the SUSY structure of Fig. 4.1(c).

To highlight the advantages of combining SUSY and SAP techniques, we compare the designed device with a device consisting of three straight waveguides with the SUSY structure of Fig. 4.1(c). Since it does not require adiabaticity, the straight SUSY structure can demultiplex modes in shorter distances than the here investigated device, as can be seen in Fig. 4.9(a), where the demultiplexing is achieved in $\widetilde{D} = 1\,\mathrm{mm}$, which is an order of magnitude less than our SAP device. Nevertheless, its efficiency rapidly decreases in front of small parameter variations, as can be observed in Fig. 4.9(b). In this case, the same level of fidelity as for the SAP geometry cannot be achieved since the process is not adiabatic and the regions with $\mathcal{F} > 0.90$ are drastically reduced to $\Delta\lambda < 0.05\,\mu\mathrm{m}$ and $\Delta x_{min} < 0.5\,\mu\mathrm{m}$, while for the SAP device we have obtained $\Delta\lambda \sim 0.5\,\mu\mathrm{m}$ and $\Delta x_{min} \sim 2\,\mu\mathrm{m}$. Thus, the introduction of the SAP geometry in the proposed device have clearly improved the robustness of the device.

Moreover, although we have designed the device to operate at telecom wavelengths, due to the high-fidelity mode conversion that SUSY offers over the telecommunication C-band [139], the device can be optimized to operate at different wavelengths by simply modifying the geometrical parameter values. In addition, as the proposed device is efficient for a broad wavelength range, it may also be used for demultiplexing light pulses and it is fully compatible with wavelength division multiplexing techniques [264].

As a proof of principle, we have focused on the simplest possible case for which only two TE spatial modes can propagate through the step-index planar waveguides. However, this configuration can be generalized to a higher number of TE modes as SUSY techniques offer global phase matching conditions among their modes, irrespective of the number of modes [135], to transverse magnetic modes [136] or even to modes propagating in optical fibers [137]. In the case of a higher number of TE modes, the index profile of the central waveguide could be engineered by applying SUSY transformations in a reiterative manner to select the modes to be transferred between the outermost waveguides and by coupling in series different devices to demultiplex the modes in an efficient and robust way. Note that, although demultiplexing between two modes could also be achieved using a central step-index waveguide designed in such a way that only one mode propagates with the same propagation constant as the first excited mode of the external waveguides, the extension to higher order modes cannot be performed without SUSY isospectrality.

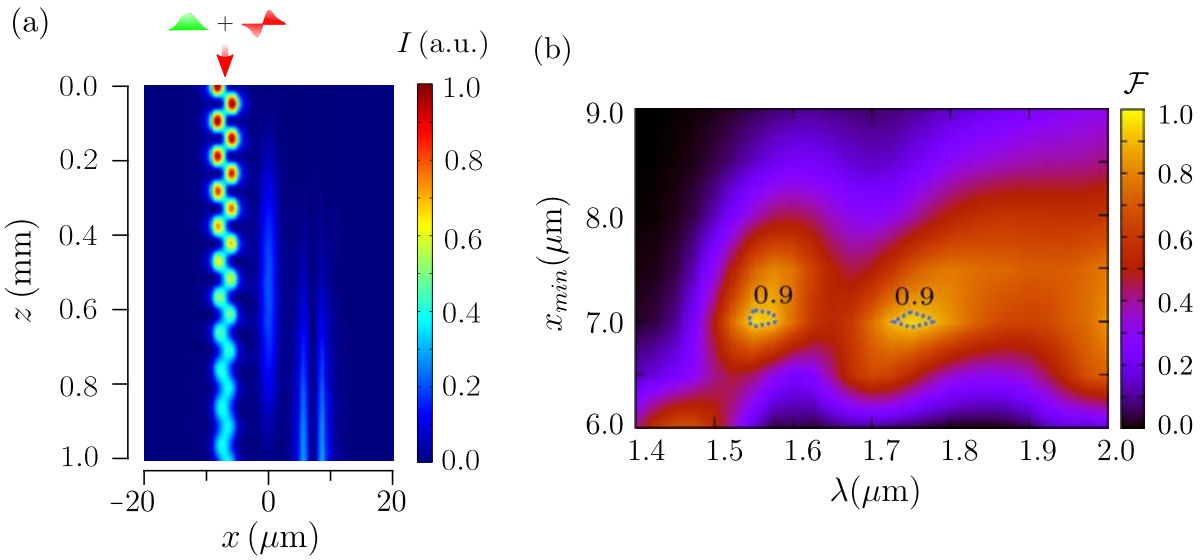

Figure 4.9: (a) Numerical simulations of light intensity propagation along z when an equally weighted superposition of the $\mathrm{TE}_0^{(1)}$ and the $\mathrm{TE}_1^{(1)}$ modes is injected in the left waveguide. (b) Demultiplexing fidelity for different wavelengths and different minimum separation between waveguides. The device is composed of three straight waveguides with the refractive index distribution of the SUSY structure of Fig 4.1(c). In (a), the parameter values considered are: $d = 4\,\mu$m, $x_{min} = 7\,\mu$m, $\widetilde{D} = 1\,$mm and $\lambda_0 = 1.55\,\mu$m.

4.5 Conclusions

In this chapter, we have demonstrated that it is possible to design an efficient and robust (de)multiplexing device by combining SUSY and SAP techniques. On the one hand, SUSY techniques have allowed to design the superpartner profile with the desired modal content. On the other hand, SAP techniques have provided robustness to the device. In particular, we have considered a triple-waveguide system with two curved step-index waveguides with their centers displaced from each other and a central straight waveguide characterized by a superpartner index profile. With this device, we have demonstrated that by injecting an equally weighted superposition of the $\mathrm{TE}_0^{(1)}$ and $\mathrm{TE}_1^{(1)}$ modes in the left waveguide, the $\mathrm{TE}_1^{(1)}$ mode is transferred to the right waveguide while the $\mathrm{TE}_0^{(1)}$ mode remains in the left one. Moreover, we have also tested the efficiency and robustness of the device obtaining demultiplexing fidelities $\mathcal{F} > 0.90$ in a broad region of $\Delta\lambda \sim 0.5\,\mu$m and $\Delta x_{min} \sim 2\,\mu$m, reaching $\mathcal{F} = 0.99$ for optimized values.

The proposed device offers a significant improvement in terms of robustness compared to previous approaches using SUSY for mode filtering [135, 139] and confirms that supersymmetric structures can be used for multiplexing/demultiplexing spatial modes, to manipulate and study the modal content of an input field distribution or to filter signals and remove the non-desired modes in an efficient and integrated way [137, 141, 142]. In addition, the high obtained fidelities open promising perspectives in the field of quantum integrated photonics to, for instance, prepare and manipulate quantum states with minimal errors or by taking profit of the high dimensional Hilbert space associated to spatial modes [296, 297].

5

Integrated photonic devices based on adiabatic transitions between supersymmetric structures

The development of new techniques to design efficient and robust integrated devices is crucial to consolidate the field of integrated photonics. To this aim, we introduce a new technique to connect superpartner profiles by adiabatically modifying the refractive index profile along the propagation direction. By doing so, if a superposition of transverse electric spatial modes is injected, the fundamental mode evolves adapting its shape and propagation constant without being coupled to other guided or radiation modes, while the rest of the modes are radiated during its propagation. Therefore, this technique offers a systematic way to manipulate the modal content in systems of optical waveguides, allowing to engineer efficient and robust photonic devices such as tapered waveguides, single-waveguide mode filters, beam splitters, and interferometers.

This chapter is organized as follows. First, we motivate the development of efficient and robust integrated photonic devices in Section 5.1. This is followed by Section 5.2, where we present the theoretical basis describing the transformation of a given refractive index profile along the propagation direction connecting two superpartner profiles, and we discuss the adiabaticity conditions that have to be fulfilled. To continue, in Section 5.3, we describe how one can design a tapered waveguide, a single-waveguide mode filter, a beam splitter and a Mach-Zehnder interferometer, by applying the previously described technique. Finally, we discuss the obtained numerical results in Section 5.4 and we conclude and adress future perspectives in Section 5.5.

5.1 Introduction

Photonic integrated devices, offering high fidelity, high speed transmissions, and scalability [28], are playing a fundamental role in the progress of modern technology [36, 39], becoming relevant in different areas such as communication networks [37, 38], lab-on-a-chip experiments [41, 298], and quantum technologies [42–44, 51]. In this regard, although the miniaturization process has been successfully achieved in integrated devices, the robustness of the devices is still a challenge in the field. Therefore, the development of new techniques to engineer devices with enhanced performances is of the main interest. In this vein, different approaches have been used to design tapered waveguides [299–301], photonic lanterns [269], adiabatic [275, 302] and directional [273, 276] couplers, mode filters [303], converters [304, 305], multiplexers [268], beam splitters [306, 307], symmetric [308] and asymmetric [309, 310] Y-junctions, and interferometers [311, 312]. To enhance the efficiency and robustness of these devices, a key factor is the control over the propagating modes such that they evolve adiabatically [313, 314].

As discussed in detail in Chapter 3, one of the emerging techniques in the field of integrated photonics is the application of Supersymmetry (SUSY), which allows to manipulate the modal content and engineer structures with global phase-matching conditions among their modes except some targeted ones that are removed [117]. So far, SUSY-based optical devices have been designed by evanescently-coupling the modes of superpartner structures [117, 137, 139–141]. Here, instead, we consider a structure where the transverse index profile is adiabatically modified along the propagation direction such that, at the input and output ports, one has superpartner index profiles [142]. Moreover, since the superpartner of a photonic lattice has one less waveguide than the original waveguide lattice [139], structures with different number of channels at the input and at the output ports can be implemented. Even more, as mode transformation losses are minimized due to the adiabaticity of the process and back reflections are negligible due to the phase-matching conditions of the modes at the interfaces, where consecutive transitions between superpartners are connected, the proposed technique constitutes an new efficient manner to engineer robust integrated photonic devices [142, 144].

In this chapter, we exemplify the potential of connecting superpartner index profiles in an adiabatic manner by designing four different devices. First, we adiabatically connect the superpartner profiles of a single-waveguide characterized by a refractive index profile $n^{(1)}(x)$, which supports three Transverse Electric (TE) spatial modes, with the superpartner index profiles $n^{(2)}(x)$ and $n^{(3)}(x)$, which support two and one TE modes, respectively. In particular, since the transition is adiabatic and the profile is engineered to remove high order modes, if a superposition of the three TE modes is injected into the structure, the fundamental TE mode will evolve adapting its shape and propagation constant without being coupled to other guided or radiation modes,

while the rest of the modes will be radiated. Thus, the device works will work as a filter of high order modes filter and as a tapered waveguide for the fundamental mode. This discussion is followed by the extension of this technique to a two-waveguide structure, whose superpartner is a one-waveguide structure. Therefore, if the lowest TE mode is injected using as the input port the superpartner profile that has one waveguide, it will coherently split at the output port that is composed of two waveguides, and thereby, the device will operate as a beam splitter. Note that, by exchanging the ports, the same device would operate as a beam recombiner. Finally, by joining the beam splitter with the beam recombiner, a Mach-Zehnder interferometer (MZI) could also be designed.

5.2 Theoretical model

The TE component of an electric field propagating along the z-direction given by Eq. (2.37) of Chapter 2, can be generalized to a medium with arbitrary index of refraction $n(x,z)$ as [27]

$$E_y(x,z) = \sum_m a_m(z) e_m(x,z) \exp\left[-i\int_0^z \beta_m(z)dz\right], \tag{5.1}$$

where $a_m(z)$ is the amplitude, $e_m(x,z)$ the transverse spatial distribution and $\beta_m(z)$ the propagation constant of mode m. Here, since the refractive index profile $n(x,z)$ changes along the propagation direction, so does the propagation constant $\beta_m(z)$ of the modes. Nevertheless, at any fixed position along the propagation direction, the problem can be defined by the eigenvalue equation

$$\mathcal{H} e_m(x) = -\beta_m^2 e_m(x), \tag{5.2}$$

where $\mathcal{H} = -d^2/dx^2 - k_0^2 n^2(x)$ is the Hamiltonian and $k_0 = 2\pi/\lambda_0$ is the vacuum wavenumber. As previously discussed in Section 3.3 of Chapter 3, the superpartner profile $n^{(q+1)}(x)$ of a given $n^{(q)}(x)$, obtained after applying q SUSY transformations, can be derived by factorizing the Hamiltonian in

$$\mathcal{H}^{(q)} + (\beta_0^{(q)})^2 = \left(A^{(q)}\right)^\dagger A^{(q)} \quad \text{and} \quad \mathcal{H}^{(q+1)} + (\beta_0^{(q)})^2 = A^{(q)}\left(A^{(q)}\right)^\dagger, \tag{5.3}$$

where $A^{(q)} = d/dx + W^{(q)}(x)$ and $A^{(q)\dagger} = -d/dx + W^{(q)}(x)$ are the factorization operators and $W^{(q)}(x) = -\partial_x \ln\left[e_0^{(q)}(x)\right]$ is the Superpotential. Moreover, as described in (3.32) in Chapter 3, the superpartner index profile reads

$$n^{(q+1)}(x) = \sqrt{\left[n^{(q)}(x)\right]^2 - \frac{2}{k_0^2}\frac{dW^{(q)}}{dx}}. \tag{5.4}$$

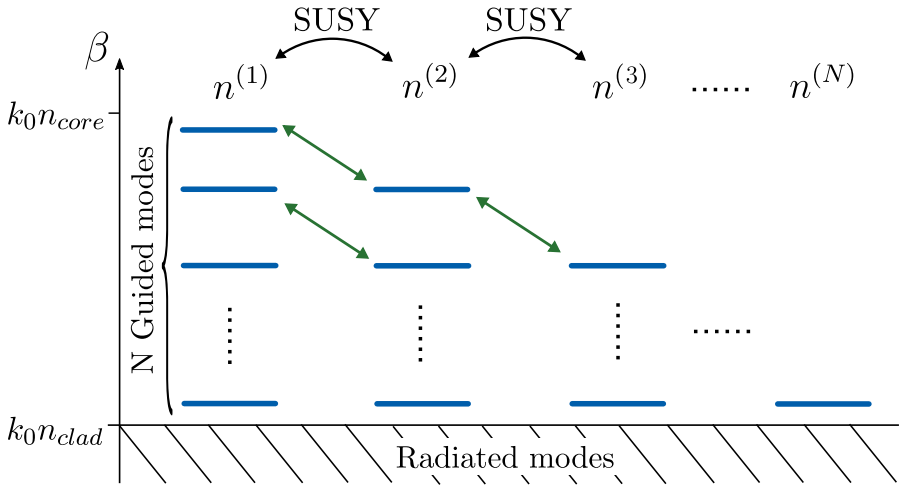

Figure 5.1: Schematic representation of a hierarchical sequence of superpartner structures characterized by the index profiles $\{n^{(1)}, n^{(2)}, \ldots, n^{(N)}\}$. The diagonal arrows indicate the evolution of the modes when the index profile is adiabatically modified along the propagation direction connecting the superpartner profiles.

These transformations allow the systematic design of superpartner profiles with desired modal content, as it is shown in Fig. 5.1. Here, to achieve a transition connecting superpartner profiles, we propose to smoothly modify the transverse refractive index profile along the propagation direction. To this aim, we introduce a continuous transformation function $g(z)$, valued between 0 and 1, from $z = L_q$ to $z = L_{q+1}$. To clarify the notation along the chapter, we introduce the subscript $g_{q\to q+1}(z)$ when we refer to a specific transition, whereas we omit it when referring to the transformation function in a general way i.e., $g(z)$. The index profile along the transition is then characterized by

$$n^{(q)\to(q+1)}(x,z) = \sqrt{[n^{(q)}(x)]^2 - g_{q\to q+1}(z)\frac{2}{k_0^2}\frac{dW^{(q)}}{dx}}. \tag{5.5}$$

To perform the adiabatic modification leading to the evolution of the propagating mode following the diagonal arrows of Fig. 5.1, the coupling to other guided or radiation modes should be avoided. This can be achieved by modifying $g(z)$ slowly enough such that the propagation constants do not cross each other. Specifically, the propagation constants and modes of the system should be continuous along the propagation direction, with well defined first and second derivatives along z [105]. From here on, to simplify the notation along the chapter, we use the bra-ket formulation from quantum mechanics where $|e_m\rangle$ accounts for the eigenfucntion of mode m and $\langle e_{m'}|\frac{de_m}{dz}\rangle$ denotes the corresponding overlap integral. To quantify how smooth this modification has to be

[313], the probability

$$p_{m\to m'} \leq \max \left| \frac{\langle e_{m'} | \frac{de_m}{dz} \rangle}{\beta_m(z) - \beta_{m'}(z)} \right|^2, \tag{5.6}$$

of exciting a mode $|e_{m'}\rangle$ while being in $|e_m\rangle$ has to be minimized. Specifically, to avoid coupling to any other guided mode m', the following adiabaticity condition

$$\left| \langle e_{m'} | \frac{de_m}{dz} \rangle \right| \ll |\beta_m(z) - \beta_{m'}(z)|. \tag{5.7}$$

should be satisfied. For symmetric variations of the refractive index profile along z, $\langle e_{m'} | \frac{de_m}{dz} \rangle = 0$ between modes with opposite parity. Besides, one also has to avoid the coupling with radiation modes and satisfying the adiabaticity condition

$$\left| \langle e_{rad} | \frac{de_m}{dz} \rangle \right| \ll |\beta_m(z) - k_0 n_{\text{clad}}|, \tag{5.8}$$

where $|e_{rad}\rangle$ accounts for a radiation mode and $k_0 n_{\text{clad}}$ sets the minimum propagation constant, below which, the modes are radiated.

5.3 Physical system

As a proof of concept, we focus on the application of adiabatic transitions connecting superpartner profiles of:

(i) a single-waveguide structure, which offer a systematic way to design tapered waveguides [299, 300] that can be used to propagate modes between waveguides with different widths [305], to avoid single-photon loss due to mode profile mismatch or to filter higher order modes by radiating them [315].

(ii) a two-waveguide structure, which allows to the design of beam splitters [307] resembling the behaviour of symmetric Y-junctions [308] and Mach-Zehnder interferometers [316] with potential applications for sensing [317].

To be specific, we consider $LiNbO_3$ waveguides [312, 318] with refractive indices $n_{\text{core}} = 2.111$ and $n_{\text{clad}} = 2.209$ at telecom wavelength ($\lambda = 1.55\,\mu$m), known for its high electro-optic coefficient [319]. Note that, from a technological perspective, the experimental realization of the proposed superpartner index profiles is difficult to achieve due to the high spatial resolution required both in the transverse and longitudinal directions. Nevertheless, as we have discussed in Chapter 3, promising techniques to this aim are femtosecond laser writing techniques [76, 102] or electron-beam lithography [251, 252]. Moreover, here, channel waveguide segmentation could be also an interesting approach to create an effective index profile that resembles the superpartner one [299, 320].

5.3.1 Single-waveguide structure

Here, we consider a waveguide defined by a super-Gaussian refractive index profile

$$\left[n^{(1)}(x)\right]^2 = n_{\text{clad}}^2 + (n_{\text{core}}^2 - n_{\text{clad}}^2)\exp\left[-\left(\frac{2x}{d}\right)^{2p}\right], \tag{5.9}$$

where $2p$ is an index that smooths the profile. The width d of the waveguide is selected to allow the propagation of the $\text{TE}_0^{(1)}$, $\text{TE}_1^{(1)}$ and $\text{TE}_2^{(1)}$ modes with propagation constants $\beta_0^{(1)}$, $\beta_1^{(1)}$, and $\beta_2^{(1)}$, respectively, see Fig. 5.2(a). The first superpartner profile $n^{(2)}(x)$, see Fig. 5.2(b), sustains the $\text{TE}_0^{(2)}$ and $\text{TE}_1^{(2)}$ modes with $\beta_0^{(2)} = \beta_1^{(1)}$ and $\beta_1^{(2)} = \beta_2^{(1)}$, respectively, and the second superpartner profile $n^{(3)}(x)$, see Fig. 5.2(c), only supports the $\text{TE}_0^{(3)}$ mode with $\beta_0^{(3)} = \beta_1^{(2)} = \beta_2^{(1)}$.

Considering the $n^{(1)\to(2)\to(3)}(x,z)$ structure with $n^{(1)}(x)$ as the input and $n^{(3)}(x)$ as the output ports, if the transverse refractive index profile is adiabatically modified along the propagation direction, the propagating modes will evolve adapting their shape and propagation constant as indicated by the arrows of Fig. 5.2. In particular, if the $\text{TE}_0^{(1)}$ mode is injected, it will be converted into the $\text{TE}_0^{(3)}$ mode at the output port and the device will work as a tapered waveguide. To optimize the device, the adiabaticity conditions of Eqs. (5.7) and (5.8) should be satisfied. For parity reasons, the $\text{TE}_0^{(1)}$ mode can only be coupled to the $\text{TE}_2^{(1)}$ mode, with the latest becoming a radiation mode after a short propagation distance. Hence, it is enough to fulfill Eq. (5.8) for the fundamental mode, avoiding the coupling with the radiation modes. This means that we need a transformation function $g(z)$ that behaves linearly at the beginning, where the

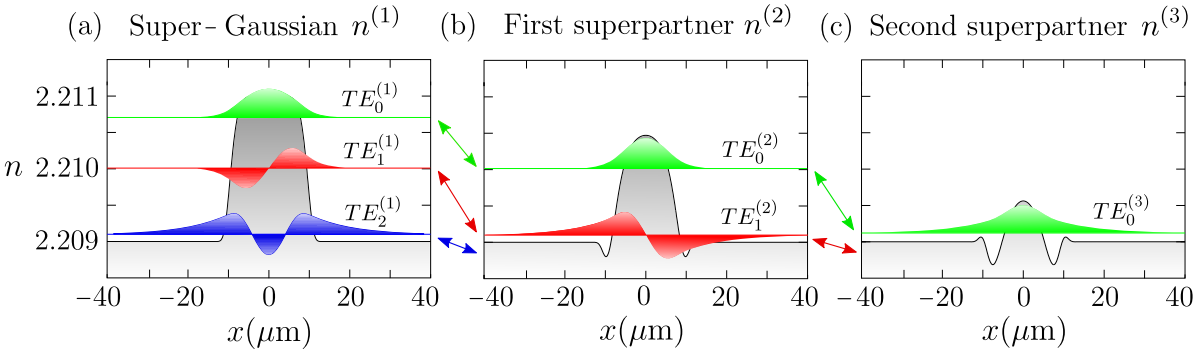

Figure 5.2: Refractive index distribution and transverse mode profiles of (a) a Super-Gaussian profile $n^{(1)}(x)$ with $d = 20\mu$m and $2p = 8$, (b) its first superpartner profile $n^{(2)}(x)$, and (c) its second superpartner profile $n^{(3)}(x)$. The positions of the modes along the vertical axis correspond to β_m/k_0 and the arrows indicate the evolution of the modes when the index profile is adiabatically modified along the propagation direction.

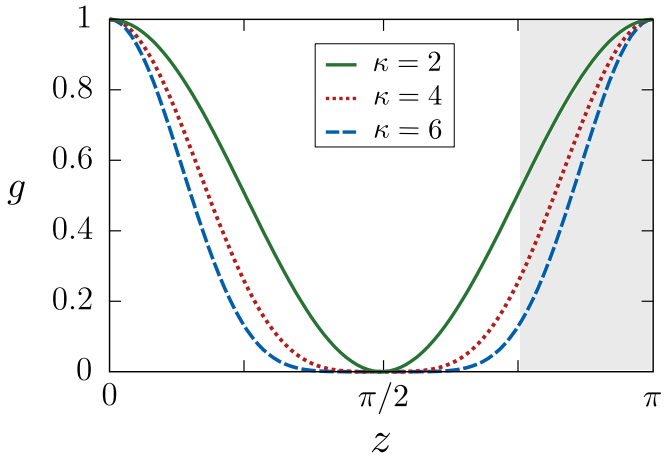

Figure 5.3: Continuous transformation function $g(z) = \cos^{\kappa}(z)$ for $\kappa = 2$ (green solid line), $\kappa = 4$ (red dotted line) and $\kappa = 6$ (blue dashed line), within the range $0 < z < \pi$. The shaded area delimits the range $3\pi/4 < z < \pi$.

gap between the propagation constants of the modes is constant, while it changes slowly as z approaches the end of the structure, where the gap between the fundamental and the radiation modes $|\beta_0(z) - k_0 n_{\text{clad}}|$ decreases. An analytic function satisfying these conditions is $g(z) \propto \cos^{\kappa}(z)$, which is represented in Fig. 5.3 for different values of κ. To be specific, we choose $\kappa = 2$ and $3\pi/4 < z < \pi$, illustrated by the green solid line and the shaded region in Fig. 5.3, which corresponds to a transformation function

$$g_{q\to q+1}(z) = 4\cos^2\left[A_q(z)\right] - B_q, \tag{5.10}$$

where $A_q(z)$ and B_q are used to bound the values of the function between 0 and 1. Specifically, for the $n^{(1)\to(2)}(x,z)$ transition occurring between $0 \le z \le L_2$, we use

$$A_1(z) = \frac{\pi}{12}\frac{z}{L_2} + \frac{3\pi}{4} \quad \text{and} \quad B_1 = 2, \tag{5.11}$$

which leads to

$$g_{1\to 2}(z) = 4\cos^2\left[\frac{\pi}{12}\frac{z}{L_2} + \frac{3\pi}{4}\right] + 2. \tag{5.12}$$

As desired, the $g_{1\to 2}(z)$ function is approximately linear function, as it can be seen in Fig. 5.4(a). On the other hand, for the $n^{(2)\to(3)}(x,z)$ transition occurring between $L_2 < z \le L_3$, we choose

$$A_2(z) = \frac{\pi}{6}\frac{(z-L_2)}{(L_3-L_2)} + \frac{5\pi}{6} \quad \text{and} \quad B_2 = 3, \tag{5.13}$$

and thereby,

$$g_{2\to 3}(z) = 4\cos^2\left[\frac{\pi}{6}\frac{(z-L_2)}{(L_3-L_2)} + \frac{5\pi}{6}\right] + 3, \tag{5.14}$$

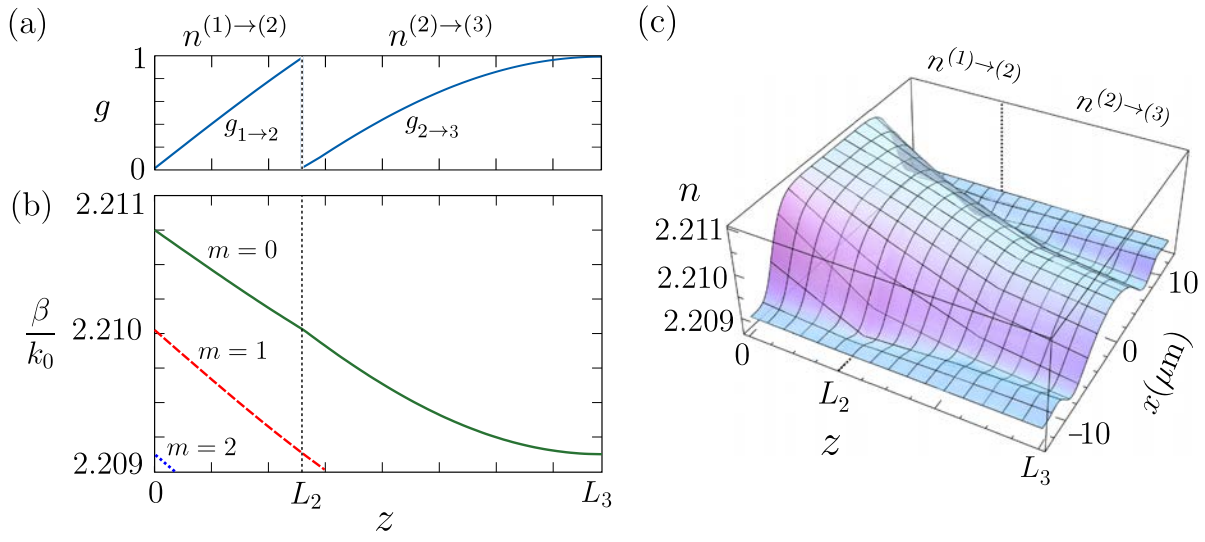

Figure 5.4: Evolution along the propagation direction of the (a) continuous transformation function $g(z)$, (b) propagation constants $\beta_m(z)$, and (c) refractive index profile, corresponding to the $n^{(1)\to(2)}(x,z)$ transition between $0 \leq z \leq L_2$ and $n^{(2)\to(3)}(x,z)$ transition between $L_2 \leq z \leq L_3$.

which becomes smoother as it approaches $z = L_3$, as it is displayed in Fig. 5.4(a). Note that the choice of the $g_{q\to q+1}(z)$ function is not unique. The evolution along the z-direction of the propagation constants and the refractive index profile are shown in Figs. 5.4(b) and (c), respectively. Furthermore, the $n^{(1)\to(2)\to(3)}(x,z)$ structure could also be used as a single-waveguide mode filter since the high order modes are not supported by the superpartner profile $n^{(3)}(x)$ and they would be radiated along the propagation. Specifically, if a superposition of the $\mathrm{TE}_0^{(1)}$, the $\mathrm{TE}_1^{(1)}$ and the $\mathrm{TE}_2^{(1)}$ modes is injected through the input port, the $\mathrm{TE}_1^{(1)}$ and the $\mathrm{TE}_2^{(1)}$ modes will be radiated during the $n^{(2)\to(3)}(x,z)$ and $n^{(1)\to(2)}(x,z)$ transitions, respectively, while the $\mathrm{TE}_0^{(1)}$ mode will be efficiently converted to the $\mathrm{TE}_0^{(3)}$ mode at the output port.

5.3.2 Two-waveguide structure

Here, we consider a two-waveguide structure with refractive index profile $\tilde{n}^{(1)}(x)$ characterized by two identical waveguides, each of them defined by a super-Gaussian profile (5.9), separated a distance D. The waveguides are single-mode in isolation and, when they are coupled, the entire structure supports the symmetric $\mathrm{TE}_s^{(1)}$ and the antisymmetric $\mathrm{TE}_a^{(1)}$ supermodes, with propagation constants $\tilde{\beta}_s^{(1)}$ and $\tilde{\beta}_a^{(1)}$, respectively, see Fig. 5.5(a). Therefore, by applying SUSY transformations, the superpartner profile $\tilde{n}^{(2)}(x)$ supporting only the $\mathrm{TE}_0^{(2)}$ mode with propagation constant $\tilde{\beta}_0^{(2)} = \tilde{\beta}_a^{(1)}$ is

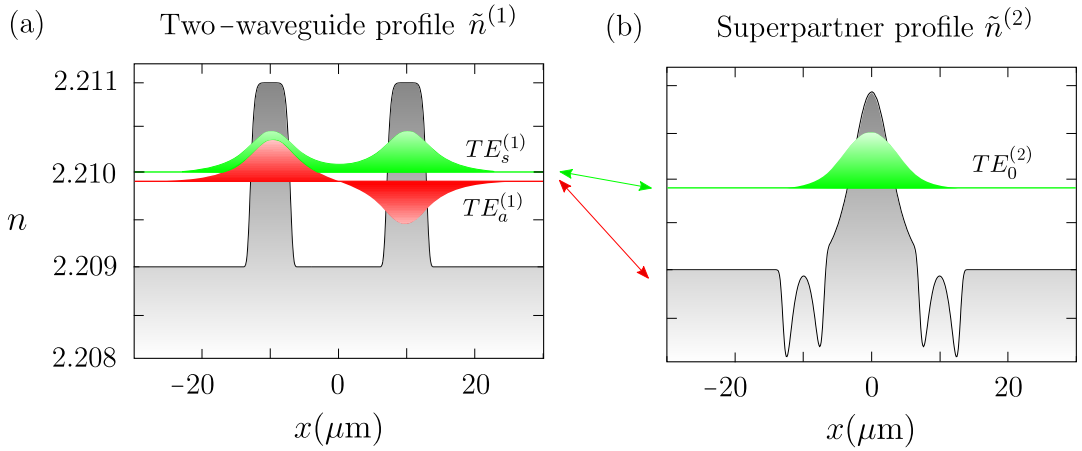

Figure 5.5: Refractive index profile and transverse mode profile of (a) a two-waveguide super-Gaussian profile $\tilde{n}^{(1)}(x)$ with $d = 8\,\mu$m and $D = 20\,\mu$m, and (b) its superpartner profile $\tilde{n}^{(2)}(x)$. The positions of the modes along the vertical axis correspond to β_m/k_0 and the diagonal arrows indicate the evolution of the modes when the index profile is modified adiabatically along the propagation direction.

obtained, as it is represented in Fig. 5.5(b). Note that, to avoid misleading, the main parameters corresponding to the two-waveguide structure are identified with a tilde.

Using the $\tilde{n}^{(2)\to(1)}(x,z)$ structure, with $\tilde{n}^{(2)}(x)$ as the input and $\tilde{n}^{(1)}(x)$ as the output ports, if the $\text{TE}_0^{(2)}$ mode is injected and the modification of the refractive index profile is performed adiabatically, the $\text{TE}_0^{(2)}$ mode will evolve following the green arrow of Fig. 5.5, becoming the $\text{TE}_s^{(1)}$ supermode at the output port. Thus, having the same power in each of the two waveguides of the output port, with the device behaving as a symmetric beam splitter. For parity reasons there is no coupling between the two guided modes, hence, it is enough to fulfill Eq. (5.8). Moreover, since the difference $|\beta_m(z) - k_0 n_{\text{clad}}|$ is approximately constant, a linear $\tilde{g}_{2\to1}(z)$ would satisfy the adiabaticity condition. The evolution of the propagation constants and the refractive index profile along the z-direction for the $\tilde{g}_{2\to1}(z)$ of Fig. 5.6(a), are shown in Figs. 5.6(b) and (c), respectively. Note that, by exchanging the input and output ports, the $\tilde{n}^{(1)\to(2)}(x,z)$ structure can be used to recombine two light beams into a single channel. In addition, the composition of the beam splitter, the two-waveguide profile and the beam recombiner, form a MZI represented in Fig. 5.7. Therefore, if one injects the $\text{TE}_0^{(2)}$ mode, it will coherently split after the $\tilde{n}^{(2)\to(1)}(x,z)$ region, becoming the $\text{TE}_s^{(1)}$ supermode, it will propagate without modifying its shape in $\tilde{n}^{(1)}(x)$, and it will recombine after $\tilde{n}^{(1)\to(2)}(x,z)$, obtaining the $\text{TE}_0^{(2)}$ mode at the output port. The evolution of the transformation function $\tilde{g}(z)$, the propagation constants and the index profile along the z-direction of the MZI are shown in Figs. 5.7(a), (b) and (c), respectively.

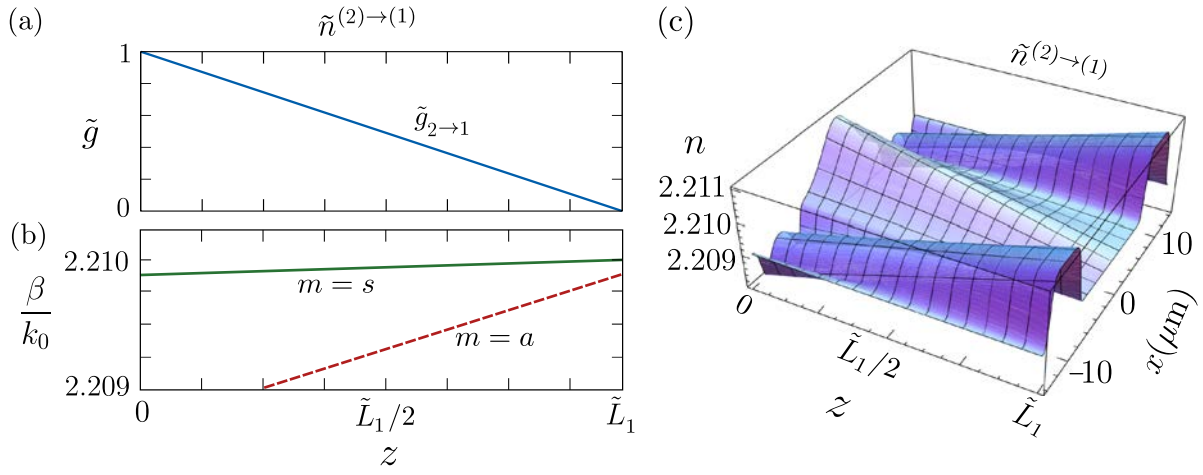

Figure 5.6: Evolution along the propagation direction of the (a) continuous transformation function $\tilde{g}_{2\to1}(z)$, (b) propagation constants $\beta_m(z)$, (c) the refractive index profile, corresponding to the $\tilde{n}^{(2)\to(1)}(x,z)$ transition between $0 \leq z \leq \tilde{L}_1$. Note that $m = s, a$ accounts for the symmetric and antisymmetric supermodes, respectively.

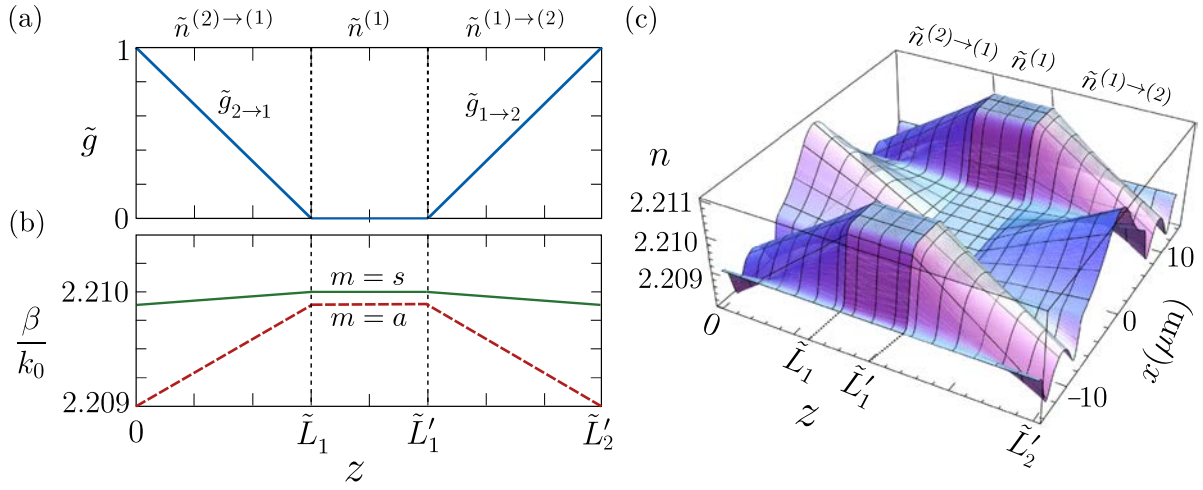

Figure 5.7: Evolution along the propagation direction of the (a) continuous transformation function $\tilde{g}(z)$, (b) propagation constants $\beta_m(z)$, and (c) refractive index profile, corresponding to the: $\tilde{n}^{(2)\to(1)}(x,z)$ transition between $0 \leq z \leq \tilde{L}_1$, $\tilde{n}^{(1)}(x,z)$ between $\tilde{L}_1 \leq z \leq \tilde{L}_1'$, and $\tilde{n}^{(1)\to(2)}(x,z)$ transition between $\tilde{L}_1' \leq z \leq \tilde{L}_2'$. Note that $m = s, a$ accounts for the symmetric and antisymmetric supermodes, respectively.

5.4 Numerical results

In this section, we demonstrate through numerical simulations using finite difference methods the efficiency and robustness of the devices. Moreover, we also test the MZI by simulating the application of a voltage in one of its arms, which changes the refractive index and give rise to a differential phase shift that modulates the output intensity. Specifically, the fidelity of each device is calculated using

$$\mathcal{F}_m = |\langle e_{out}|e_m\rangle|^2 , \tag{5.15}$$

where $|e_{out}\rangle$ is the transverse modal field distribution numerically obtained at the output port, and $|e_m\rangle$ is the theoretically expected transverse modal field distribution at this port. In addition, we also compute the transmitted power given by

$$T_m = \frac{P_m^{out}}{P_m^{in}} \cdot 100, \tag{5.16}$$

where P_m^{in} and P_m^{out} are the input and output powers of mode m, respectively, obtained by integrating the intensities within the waveguide cores.

5.4.1 Tapered waveguide

Here, we demonstrate the efficiency and robustness of the $n^{(1)\to(2)\to(3)}(x,z)$ structure, illustrated in Fig. 5.4(c), working as a tapered waveguide. The numerical simulations confirm that, since the adiabaticity condition is fulfilled, the $\mathrm{TE}_0^{(1)}$ mode is converted into the $\mathrm{TE}_0^{(3)}$ mode at the output port, while the $\mathrm{TE}_1^{(1)}$ and $\mathrm{TE}_2^{(1)}$ modes become radiation modes during the propagation, as can be seen in Figs. 5.8(a), (b) and (c), respectively. Besides, by injecting the $\mathrm{TE}_0^{(1)}$ mode at the telecom wavelength, we obtain fidelities $\mathcal{F}_0 > 0.99$ and $\mathcal{F}_0 > 0.999$ for devices with total length $L_3 > 1.2\,\mathrm{mm}$ and $L_3 > 1.8\,\mathrm{mm}$, respectively, see Fig. 5.9, with a transmitted power of $T_0 > 99\%$ for both cases. Instead, if one considers a linear $g(z)$ function rather than the optimized $g_{1\to2}(x)$ and $g_{2\to3}(x)$ transformation functions given by Eqs. (5.12) and (5.14), respectively, to achieve fidelities $\mathcal{F}_0 > 0.999$ one would require longer devices with $L_3 > 10\,\mathrm{mm}$. In addition, the robustness of the device is demonstrated obtaining $\mathcal{F}_0 > 0.99$ in a broad region of wavelengths $1.4\,\mu\mathrm{m} \leq \lambda \leq 1.7\,\mu\mathrm{m}$ for devices with $L_3 > 1.2\,\mathrm{mm}$, see Fig. 5.9, with back-reflections remaining under $-30\,\mathrm{dB}$. Note that, for lower wavelengths, the modes are more confined, less sensitive to the refractive index variations, and the fidelities are higher. The obtained results are similar to other approaches such as segmented waveguides [300], where fidelities between 0.78 and 0.98 and power transmissions above 98% are obtained. Thus, our proposal constitutes an efficient alternative to design tapered waveguides with a high mode overlap and minimum mode losses due to the adiabaticity of the process.

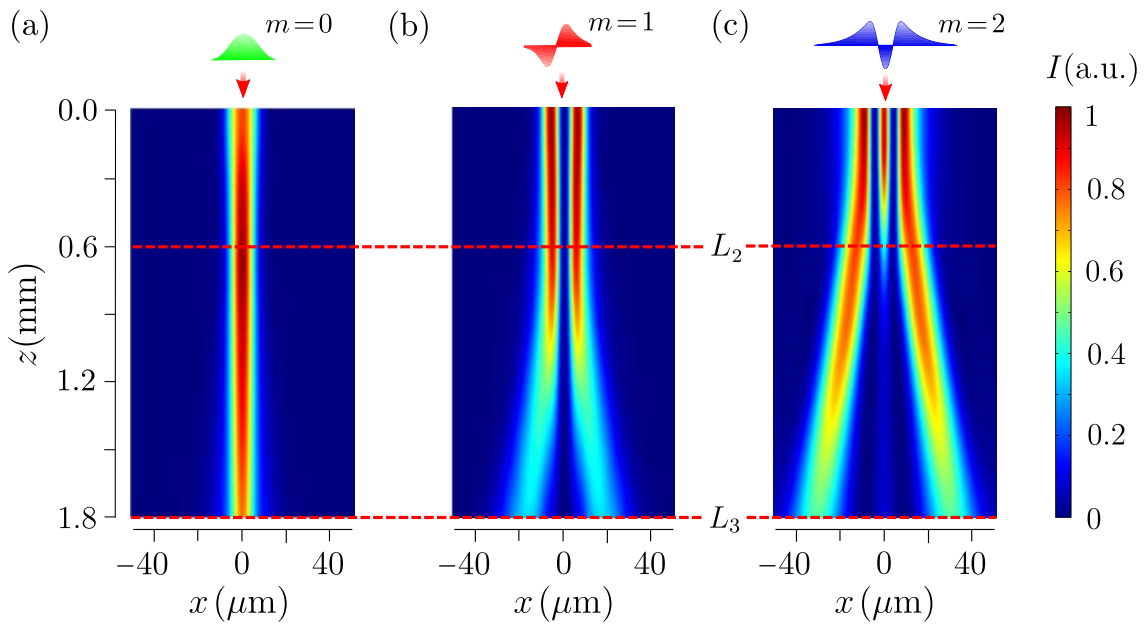

Figure 5.8: Numerical simulation of light intensity propagation ($\lambda = 1.55\,\mu$m) along the $n^{(1)\to(2)\to(3)}(x,z)$ structure of Fig. 5.4(c), when the (a) $\mathrm{TE}_0^{(1)}$, (b) $\mathrm{TE}_1^{(1)}$, and (c) $\mathrm{TE}_2^{(1)}$, mode is injected through the input port $n^{(1)}(x)$. The horizontal dashed line delimits the two transitions. The total length of the simulated device is $L_3 = 1.8\,$mm.

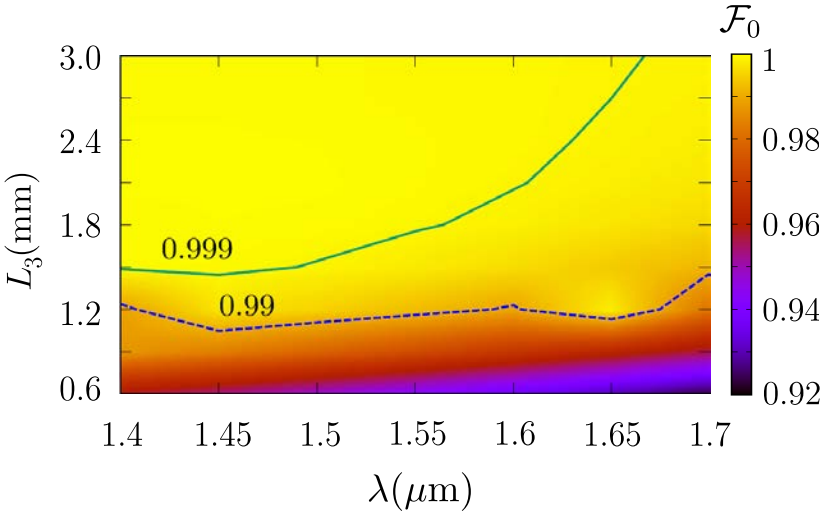

Figure 5.9: Numerically calculated fidelity of the tapered waveguide of Fig. 5.4(c) for the fundamental $\mathrm{TE}_0^{(1)}$ mode for different device lengths L_3 and light wavelengths λ.

Moreover, if only the $n^{(1)\to(2)}(x,z)$ transition is used, the device behaves as an efficient tapered waveguide for the $\mathrm{TE}_0^{(1)}$ and $\mathrm{TE}_1^{(1)}$ modes, obtaining $\mathcal{F}_0 > 0.99$ and $\mathcal{F}_1 = 0.96$, respectively, for $L_2 = 0.6\,\mathrm{mm}$. As the $\mathrm{TE}_1^{(1)}$ mode is less confined and $g_{1\to2}(z)$ has not been optimized to fulfill Eq. (5.8) for this mode, a longer device of $L_2 > 1.5\,\mathrm{mm}$ is required to obtain $\mathcal{F}_1 > 0.99$.

5.4.2 Single-waveguide mode filter

Here, we investigate the operation of the previous $n^{(1)\to(2)\to(3)}(x,z)$ structure as a mode filtering device. Specifically, the fidelity of the mode filter is given by

$$\mathcal{F}_{\mathrm{filter}} = \mathcal{F}_0(1-\mathcal{F}_1)(1-\mathcal{F}_2). \tag{5.17}$$

Fidelities $\mathcal{F}_0 = 0.999$, $\mathcal{F}_1 = 0.245$, and $\mathcal{F}_2 = 0.205$, are numerically obtained, yielding to $\mathcal{F}_{\mathrm{filter}} = 0.60$ using the previous used structure with $L_3 = 1.8\,\mathrm{mm}$. The fidelity of the mode filtering device can be increased to $\mathcal{F}_{\mathrm{filter}} > 0.9$ by re-scaling the structure from $L_3 = 1.8\,\mathrm{mm}$ to $L_3 = 3.9\,\mathrm{mm}$, or by adding $1.2\,\mathrm{mm}$ of the $n^{(3)}(x)$ profile after the $1.8\,\mathrm{mm}$ of the $n^{(1)\to(2)\to(3)}(x,z)$ structure. In terms of power, above $T_0 > 99\%$ of the $\mathrm{TE}_0^{(1)}$ mode is transmitted, and 94.5% and 98.5% of the $\mathrm{TE}_1^{(1)}$ and $\mathrm{TE}_2^{(1)}$ modes is radiated, respectively. The same fidelities could be achieved by optimizing $g(z)$ to faster radiate the unwanted modes. Note that the fidelities and transmitted powers are calculated using single mode excitation, as displayed in Fig. 5.8. Nevertheless, the

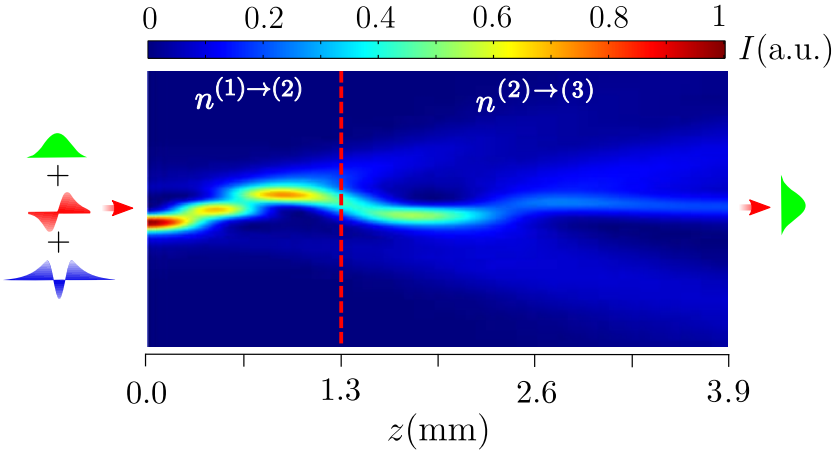

Figure 5.10: Numerical simulation of light intensity propagation ($\lambda = 1.55\,\mu\mathrm{m}$) along the $n^{(1)\to(2)\to(3)}(x,z)$ structure of Fig. 5.4(c), when an equally weighted superposition of the $\mathrm{TE}_0^{(1)}$, $\mathrm{TE}_1^{(1)}$, and $\mathrm{TE}_2^{(1)}$ modes is injected through the input port $n^{(1)}(x)$. The vertical dashed line delimits the two transitions. The width of the simulated device is $200\,\mu\mathrm{m}$ and the total length is $L_3 = 1.8\,\mathrm{mm}$.

device is still efficient when an equally weighted superposition of the $\mathrm{TE}_0^{(1)}$, $\mathrm{TE}_1^{(1)}$, and $\mathrm{TE}_2^{(1)}$ modes is injected as it can be seen in Fig. 5.10, with above 95% of the fundamental mode power being still transmitted.

The proposed device is more efficient than a standard taper designed by just decreasing the index contrast until a single-mode waveguide is obtained. Using the same optimized $g_{0\to1}(z)$ and $g_{1\to2}(z)$ functions given by Eqs. (5.12) and (5.14), respectively, $\mathcal{F}_{\mathrm{filter}} = 0.47$ is obtained for $L = 3.9\,\mathrm{mm}$, which is much lower than the obtained with the SUSY-based device. In terms of power, 99% is transmitted for the fundamental mode, and 77% and 97% is radiated for the first and second excited modes, respectively, which is lower than the obtained before. Furthermore, the obtained fidelities are higher than other filtering techniques, such as interference couplers [303] or segmented waveguides [321], with 63% and 80% of mode suppression, respectively. Finally, our proposal has the advantage over conventional tapers that both the waveguide size and the index contrast are modified in such a way that the desired mode profile is obtained at the output port, leading to higher fidelities.

5.4.3 Beam splitter

Here, we demonstrate the efficiency and robustness of the symmetric beam splitter, characterized by the index profile transition $\tilde{n}^{(2)\to(1)}(x,z)$, represented in Fig. 5.6(c). Figure 5.11(b) shows how when the $\mathrm{TE}_0^{(2)}$ mode injected through the input port $\tilde{n}^{(2)}(x)$, see Fig. 5.11(a), it is converted into the $\mathrm{TE}_s^{(1)}$ mode at the output port $\tilde{n}^{(1)}(x)$, see Fig. 5.11(c). In this case, the fidelity of the beam splitter is given by

$$\tilde{\mathcal{F}}_s = |\langle e_{out}|e_s^{(1)}\rangle|^2. \tag{5.18}$$

Using the previously discussed $\tilde{g}_{2\to1}(z)$ function and working at telecom wavelength, we find $\tilde{\mathcal{F}}_s > 0.99$ and $\tilde{\mathcal{F}}_s > 0.999$ for $\tilde{L}_1 > 6\,\mathrm{mm}$ and $\tilde{L}_1 > 8\,\mathrm{mm}$, respectively, with a transmitted power $\tilde{T}_s > 99\%$. Besides, $\tilde{\mathcal{F}}_s > 0.99$ are obtained in a wide region of wavelengths $1.4\,\mu\mathrm{m} \leq \lambda \leq 1.7\,\mu\mathrm{m}$ for $L_1 > 6\,\mathrm{mm}$, see Fig. 5.12, confirming the robustness of the device. The same fidelity and robustness is obtained for the device working as a beam recombiner. The robustness for a broad range of wavelengths is an advantage over standard beam splitters based on evanescently-coupled waveguides, and resembles a broadband beam splitter in which a transmission power of 97% is achieved for $1.5\,\mu\mathrm{m} \leq \lambda \leq 1.63\,\mu\mathrm{m}$ [322]. Moreover, the device also resembles a symmetric Y-junction [309] with similar transmitted powers for the same total length. Even more, a SUSY-based device resembling an asymmetric Y-junction, which allows mode-division demultiplexing [277], could also be designed using waveguides with different widths [144].

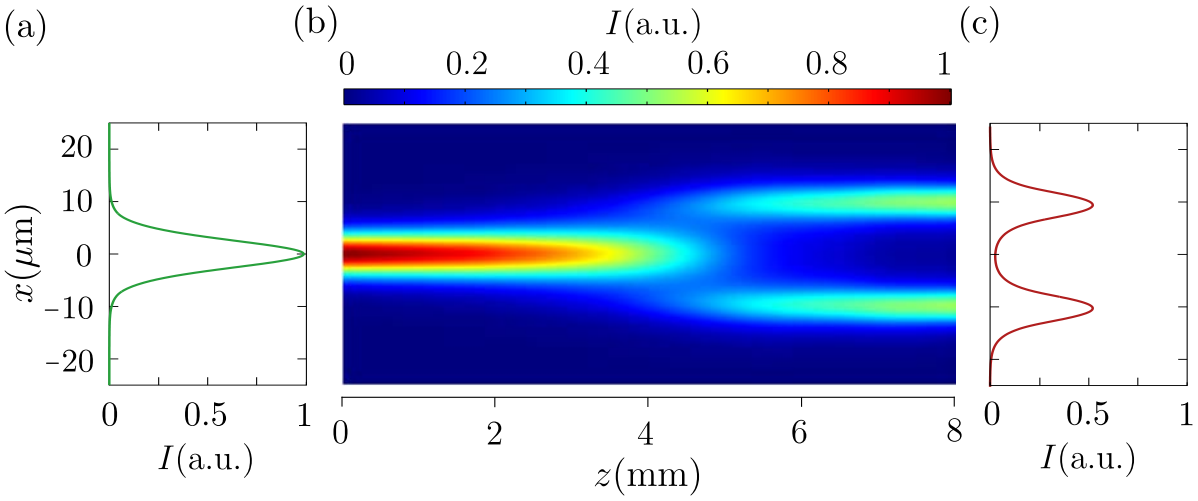

Figure 5.11: Numerical simulation of light intensity propagation ($\lambda = 1.55\,\mu$m) along the $\tilde{n}^{(2)\to(1)}(x,z)$ structure of Fig. 5.6(c), when the $\mathrm{TE}_0^{(2)}$ mode is injected through the input port $\tilde{n}^{(2)}(x)$. (a) Injected intensity corresponding to the $\mathrm{TE}_0^{(2)}$ mode, (b) intensity propagation, and (c) output intensity corresponding to the $\mathrm{TE}_s^{(1)}$ mode. The total length of the simulated device is $\tilde{L}_1 = 8\,$mm.

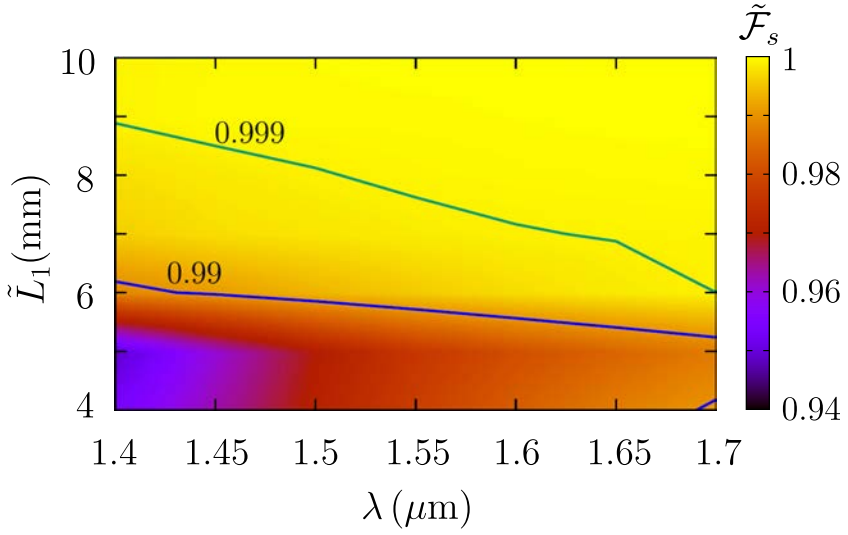

Figure 5.12: Numerically calculated fidelity of the beam splitter of Fig. 5.6(c) for the $\mathrm{TE}_0^{(2)}$ mode for different device lengths $\tilde{L}_1$ and light wavelengths λ.

5.4.4 Mach-Zehnder interferometer

Finally, we numerically test the performance of the MZI represented in Fig. 5.7(c). Applying a voltage to one of the arms, a change in the refractive index $\Delta\tilde{n}$ is introduced due to the linear electro-optical effect, which introduces a phase difference [318]

$$\Delta\phi = k_0 \Delta\tilde{L}_1 \Delta\tilde{n} = -k_0 \Delta\tilde{L}_1 [\tilde{n}^{(1)}(x)]^3 r_{33} \frac{V}{2h} \Gamma, \tag{5.19}$$

where $\Delta\tilde{L}_1 = \tilde{L}_1' - \tilde{L}_1$ is the electrode length, r_{33} is the electro-optical coefficient, V is the applied voltage, h is the distance between the electrodes and Γ is the overlap integral between the propagating and the applied electric fields. By injecting the $\mathrm{TE}_0^{(2)}$ mode through the input port, we can observe in Fig. 5.13(a) how, when no voltage is applied, the beams are recombined at the output port obtaining the $\mathrm{TE}_0^{(2)}$ mode with a fidelity $\tilde{\mathcal{F}}_0 = 0.998$ for $\tilde{L}_2' = 20\,\mathrm{mm}$. Instead, when $V = 5.63\,\mathrm{V}$ is applied, a phase difference $\Delta\phi = \pi/2$ is introduced, leading to a superposition of the symmetric $\mathrm{TE}_s^{(1)}$ and antisymmetric $\mathrm{TE}_a^{(1)}$ supermodes, which are partially radiated and recombined

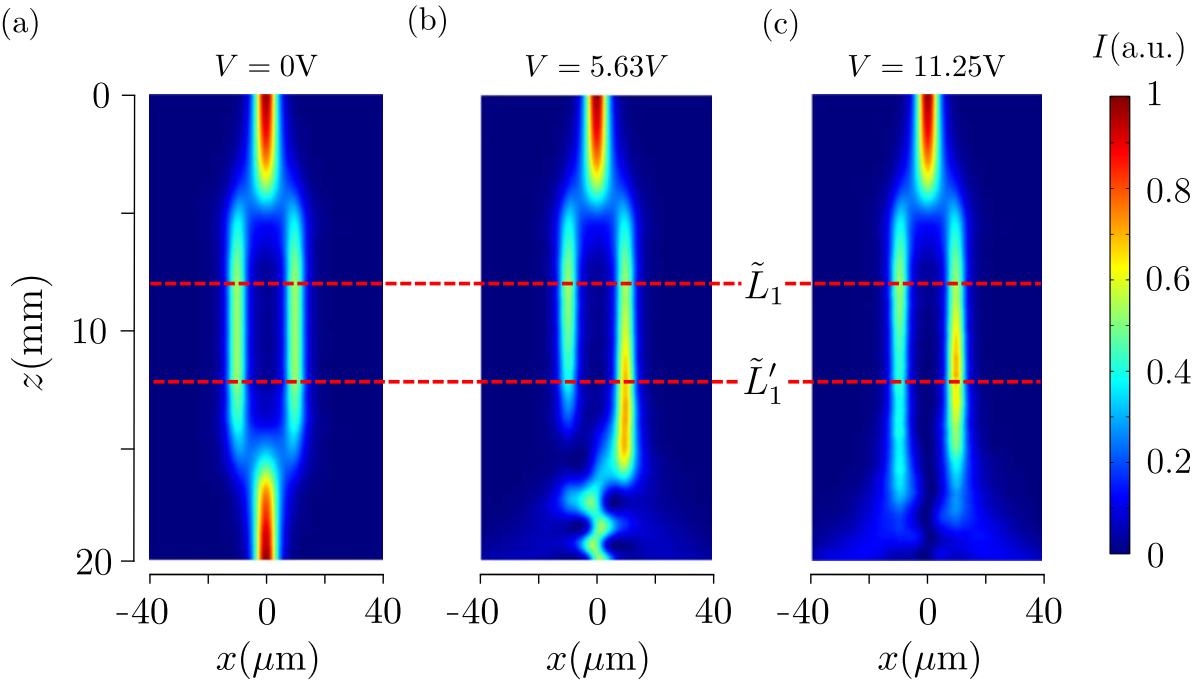

Figure 5.13: Numerical simulation of light intensity propagation ($\lambda = 1.55\,\mu\mathrm{m}$) along the MZI when the $\mathrm{TE}_0^{(2)}$ mode is injected through the input port $\tilde{n}^{(2)}(x)$, and a voltage (a) $V = 0$, (b) $V = 5.625\,\mathrm{V}$, and (c) $V = 11.25\,\mathrm{V}$, is applied to the right arm. The horizontal dashed lines delimit the three regions of the MZI. Parameters used: $\lambda = 1.55\,\mu\mathrm{m}$, $r_{33} = 30\,\mathrm{pm/V}$, $h = 8\,\mu\mathrm{m}$, $l = 4\,\mathrm{mm}$ and $\Gamma = 0.83$.

at the output port, see Fig. 5.13(b). Finally, when $V = 11.25\,\mathrm{V}$ is applied, a phase difference $\Delta\phi = \pi$ is introduced transforming the mode into the $\mathrm{TE}_a^{(1)}$ mode, which is radiated during the $\tilde{n}^{(1)\to(2)}(x,z)$ transition, see Fig. 5.13(c). The output intensities for these three different voltages are represented in Fig. 5.14(a). Besides, by computing the transmitted power $\tilde{T}_0$ of the $\mathrm{TE}_0^{(2)}$ mode, integrating the intensities in the waveguide core for different voltages, we find that the minimum transmitted power $\tilde{T}_{min} = 1.4\%$ occurs at $V = 11.25\,\mathrm{V}$, which is in good agreement with the expected behavior $\tilde{T} = \cos^2(\Delta\phi/2)$, see Fig. 5.14(b). Note that the SUSY-based MZI has a visibility of 98.6%, which could be improved by prolonging the output port $\tilde{n}^{(2)}(x)$.

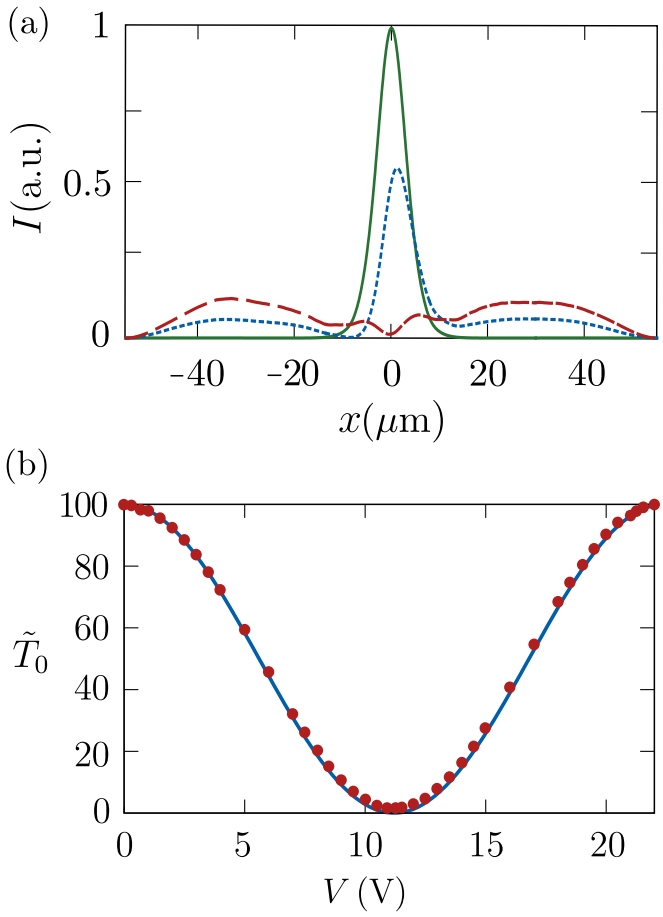

Figure 5.14: (a) Output intensities obtained after the $\mathrm{TE}_0^{(2)}$ mode has propagated through the MZI as shown in Fig. 5.13, and a voltage $V = 0$ (green solid line), $V = 5.625\,\mathrm{V}$ (blue dotted line), and $V = 11.25\,\mathrm{V}$ (red dashed line), is applied to the right arm. (b) Numerically computed transmission (dots) and theoretical expected curve (solid line) for the MZI as a function of the applied voltage V. Parameters used: $\lambda = 1.55\,\mu\mathrm{m}$, $r_{33} = 30\,\mathrm{pm/V}$, $h = 8\,\mu m$, $l = 4\,\mathrm{mm}$ and $\Gamma = 0.83$.

5.5 Conclusions

In this chapter, we have introduced transitions connecting superpartner profiles in systems of optical waveguides by modifying the transverse refractive index profile along the propagation direction. Specifically, this has been achieved by defining a continuous transformation function that connects the superpartner structures, which has allowed to manipulate the modal content in an adiabatic fashion. In particular, we have demonstrated that these transitions offer a systematic way to design efficient and robust (i) tapered waveguides and mode filters by using a single-waveguide structure, and (ii) beam splitters and MZI's by using a two-waveguide structure. Numerically calculated fidelities above 0.999 have been achieved in a broad region of wavelengths for $L > 1.8\,\text{mm}$ tapered waveguides and $L > 8\,\text{mm}$ symmetric beam splitters, respectively. Moreover, we have also designed a single-waveguide mode filter with fidelities above 0.9 and a MZI with a visibility of 98.6%. Due to the high efficiency and robustness of the proposed devices, we conclude that adiabatic transitions connecting superpartner profiles constitute a novel powerful technique to design integrated photonic devices.

As a proof of principle, we have focused on transitions applied to single- and two-waveguide structures. However, more complex structures could be designed by increasing the number of waveguides, using waveguides with different widths [144], using optical fibers [137] or combining the transitions along the propagation direction with SUSY transformations along the transverse direction. Finally, we would like to remark that such transitions are not restricted to optical systems and could be extended to the general formalism of SUSY quantum mechanics and applied to, for instance, trapping potentials for neutral atoms, modifying its shape in time instead of space [256].

6

Topological state engineering via supersymmetric transformations

The quest to explore new techniques for the manipulation of topological states provides a deeper understanding of topological physics, and it is essential for identifying new ways to harness their unique features. Here, we examine the potential of supersymmetric (SUSY) transformations to systematically address, alter and reconfigure the topological properties of a system. To this end, we theoretically and experimentally study the changes that topologically protected states in photonic lattices undergo as SUSY transformations are applied to their host system. In particular, we show how SUSY-induced phase transitions can selectively suspend and re-establish topological protection of specific states. Furthermore, we reveal how understanding the interplay between internal symmetries and symmetry constraints of SUSY transformations provides a road-map to directly access the desirable topological properties of a system. Our findings pave the way for establishing SUSY-inspired techniques as a powerful and versatile tool for topological state engineering.

This chapter is organized as follows. In Section 6.1, we motivate the interest in applying SUSY transformations to a system supporting topologically protected states. This is followed by Section 6.2, where we introduce the Su-Schrieffer-Heeger (SSH) model. To continue, we describe the experimental set-up used to inscribe one-dimensional lattices of femtosecond laser written waveguides and how to design supersymmetric topological photonic structures and engineer its topological properties in Section 6.3. Moreover, in Section 6.4 we provide the experimental verification of the predicted results. Finally, we conclude and discuss future perspectives in Section 6.5. The work included in this chapter was carried out thanks to different short stays at Prof. Szameit group in the Universität Rostock, during which I was involved both in the development of the theory and the realization of the experiments.

6.1 Introduction

Physical laws are intrinsically connected to symmetries, which can be mainly classified in space-time symmetries, involving transformations in space and time, and internal symmetries [323]. Unlike any other symmetry, Supersymmetry (SUSY), originally developed as an extension of the Poincaré Group [199], offers a loophole to the Coleman-Mandula theorem [324], allowing the interplay of space-time and internal symmetries in a non-trivial way [325]. Despite the lack of direct experimental evidence of SUSY in high-energy physics, some of its fundamental concepts have been extended to numerous fields [123, 132, 203, 204]. In particular, SUSY provides an effective theory to describe quantum phase transitions occurring at the boundary of topological superconductors [326], where topologically protected edge states [327, 328] characterized by topological invariants [165, 329] emerge. Discovered with the integer quantum Hall effect [167, 168], topological insulators led to a breakthrough in condensed-matter [171]. Moreover, the study of topological phases has been extended to other fields such as solid-state physics [330], atomic physics [331], acoustics [332], electronics [333], mechanics [334], magnetism [335], ultracold atoms [336] or photonics [170, 337–340].

In this chapter, we explore the interplay between SUSY and topology – two seemingly independent fundamental concepts in physics - and demonstrate theoretically and experimentally its deep connection [193]. To this aim, SUSY transformations are applied to manipulate topological properties strongly connected to internal symmetries of the systems, inducing topological phase transitions. Specifically, a new method for topological state engineering, e.g., to selectively suspend and re-establish the topological protection of a targeted state, is presented. Moreover, it is shown how closely this behavior is linked to symmetry constraints of SUSY transformations [238, 240], enabling these symmetries to be fully or partially preserved, or cancelled in their entirety. As SUSY transformations are tailored to their specific purpose, they imprint their characteristic signature on the topological invariants, as well as the related topological protection.

To explore the fruitful interplay between SUSY and topology, we employ femtosecond laser written photonic lattices [76, 102]. In recent years, the field of photonics has shed light on a plethora of phenomena stemming from topological phases [338, 339], sparkling numerous sophisticated applications such as scatter free light transport, due to the unidirectional nature of the edge states [109–112], which can be used for efficient routing and switching applications [174–177]. Within the field of topological photonics (see [170] for a recent review), photonic lattices have been consolidated as a versatile experimental platform [172, 173, 341, 342]. In a similar vein, SUSY notions have been introduced to photonics [117] leading to many applications (as discussed in detail in Section 3.1 of Chapter 3) ranging from mode filtering [137, 139, 141] to creating topologically protected mig-gap states starting from trivial configurations [239]. Here,

to elucidate how SUSY enables the manipulation of topological properties, we apply Discrete SUSY (DSUSY) transformations to photonic lattices embodying the simplest system with non-trivial topological properties, the Su-Schrieffer-Heeger (SSH) model [178, 343]. The SSH model, which is one of the most important models in condensed-matter physics for illustrating topological physics [344, 345], has also been extensively studied and implemented using optical waveguides [346–350]. Along these lines, we show how SUSY allows the systematic breaking and recovery of symmetries of the system, constituting a powerful tool to tailor topological transitions and to manipulate the topological properties of a system. In addition, the proposed method for topological state engineering is not restricted to photonic lattices and can be extended to other systems described by a tight-binding Hamiltonian, e.g., coupled cavities [159], ultra-cold atoms [344] or acoustic and mechanical systems [257].

6.2 Theory

6.2.1 The Su-Schrieffer-Heeger (SSH) model

The SSH model is characterized by a one-dimensional lattice consisting of $N/2$ unit cells hosting two sites, one on sublattice A and one on sublattice B, and staggered couplings c_1 and c_2, as it is displayed in Fig. 6.1(a). The coupling within the sites of the unit cell is c_1 while the coupling between unit cells is c_2. Here, the SSH model is discussed considering N evanescently-coupled single-mode waveguides whose couplings can be tuned by changing the separation between waveguides. For the waveguide lattices here employed, light propagation along the z-direction can be defined using coupled-mode equations introduced in Section 2.3 of Chapter 2, which are given by

$$i\frac{d}{dz}\boldsymbol{\psi} = \mathcal{H}\boldsymbol{\psi}, \tag{6.1}$$

where $\boldsymbol{\psi} = (\tilde{a}^1, \ldots, \tilde{a}^N)^T$, with $\tilde{a}^j$ describing the complex modal field amplitude in waveguide j, and the Hamiltonian is given by the $N \times N$ tri-diagonal matrix

$$\mathcal{H} = \begin{pmatrix} \beta_1 & c_1 & 0 & \ldots & 0 \\ c_1 & \beta_2 & c_2 & \ddots & \vdots \\ 0 & c_2 & \ddots & \ddots & 0 \\ \vdots & \ddots & \ddots & \ddots & \ddots \\ 0 & \ldots & 0 & \ddots & \beta_N \end{pmatrix}, \tag{6.2}$$

where the propagation constants β_j occupy the diagonal elements and the coupling strengths between adjacent waveguides the off-diagonal ones. Note that, depending

on the number N of waveguides, the lattice terminates with c_1 or c_2. In addition, the properties of the model can be described in terms of the bulk, which is the long central part of the chain and determines the most important physical properties of the system, and the edges. By applying periodic boundary conditions, the system becomes translationally invariant and it can be Fourier transformed, with the Bloch Hamiltonian in momentum space reading [343]

$$\mathcal{H}(k) = \begin{pmatrix} 0 & c_1 + c_2 e^{ik} \\ c_1 + c_2 e^{-ik} & 0 \end{pmatrix}, \tag{6.3}$$

where k is the Bloch wavenumber within the first Brillouin zone. Diagonalizing (6.3), one obtains the bulk dispersion relation

$$E(k) = \pm\sqrt{c_1^2 + c_2^2 + 2c_1 c_2 \cos(k)}. \tag{6.4}$$

If one of the coupling parameters is zero or there is staggering $c_1 \neq c_2$, we have an insulator that is characterized by a gapped band structure, see Figs. 6.1(b) and (c), respectively. Instead, the band gap closes for $c_1 = c_2$, as it can be observed in Fig. 6.1(d). Note that, although the band structure is the same for $|c_1| > |c_2|$ and $|c_1| < |c_2|$, its topological properties are different. The Hamiltonian (6.3) can be rewritten as

$$\mathcal{H}(k) = h_x(k)\sigma_x + h_y(k)\sigma_y + h_z(k)\sigma_z, \tag{6.5}$$

where

$$h_x(k) = c_1 + c_2 \cos(k), \quad h_y(k) = c_2 \sin(k) \quad \text{and} \quad h_z(k) = 0, \tag{6.6}$$

and the Pauli matrices are given by

$$\sigma_x = \begin{pmatrix} 0 & 1 \\ 1 & 0 \end{pmatrix}, \quad \sigma_y = \begin{pmatrix} 0 & -i \\ i & 0 \end{pmatrix} \quad \text{and} \quad \sigma_z = \begin{pmatrix} 1 & 0 \\ 0 & -1 \end{pmatrix}. \tag{6.7}$$

The trajectories of $\vec{h}(k)$ on the $h_x - h_y$ plane form a closed loop due to the periodicity of the Brillouin zone [343]. For $|c_1| > |c_2|$ ($|c_1| > |c_2|$) the loop is localized outside (around) the origin, as it can be seen in Fig. 6.1(e) (Fig. 6.1(g)). Thus, to go from one situation to the other, one has to cross the origin at least once, see Fig. 6.1(f), closing the energy gap and inducing a topological phase transition. The topological invariant distinguishing when the trajectory winds or not around the origin is the Winding number $\mathcal{W} = \mathcal{Z}/\pi$, which is related with the Zak phase [351]

$$\mathcal{Z} = i \oint_{BZ} \psi^*(k) \frac{\partial}{\partial k} \psi(k) dk, \tag{6.8}$$

where $\psi(k)$ is the eigenstate in k-space. Whereas an infinite lattice is invariant under the exchange of the couplings, the presence of edges in a finite SSH chain gives rise to

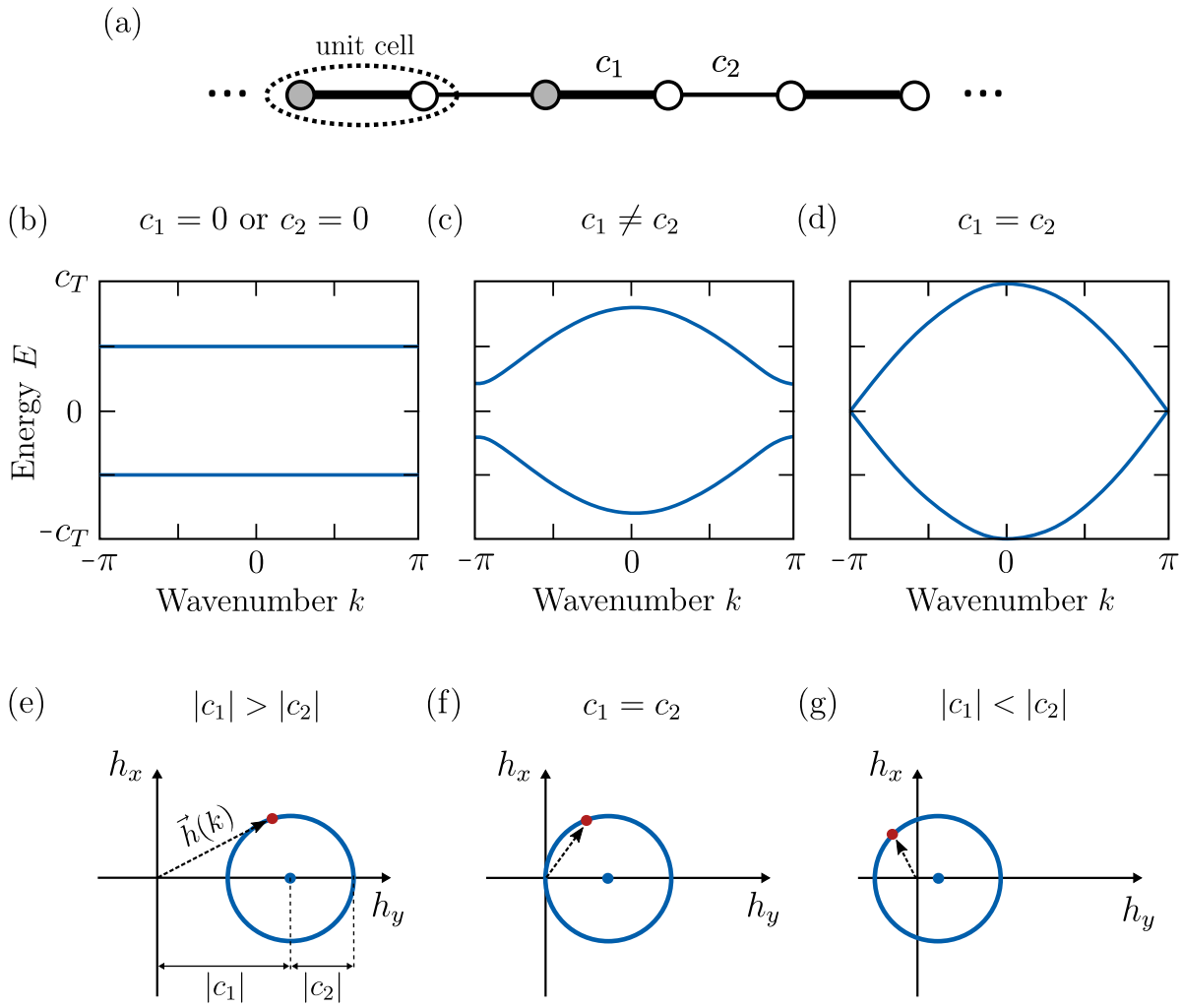

Figure 6.1: (a) Visual representation of the SSH chain formed by N unit cells, with each unit cell hosting two sites, one on sublattice A (grey circles) and one on sublattice B (white circles). The coupling within the sites of the unit cell is given by c_1 while the coupling between unit cells is given by c_2. Dispersion relation obtained from the bulk Hamiltonian plotted for (b) $c_1 = 0$ or $c_2 = 0$, (c) $c_1 \neq c_2$ and (d) $c_1 = c_2$. Trajectories of $\vec{h}(k)$ on the $h_x - h_y$ plane for (e) $|c_1| > |c_2|$, (f) $c_1 = c_2$, and (g) $|c_1| < |c_2|$.

topological edge states at the end of a region with non-zero Zak phase, which can be described by the bulk-edge correspondence [352, 353]. Establishing that $c_1 < c_2$, if one side of the lattice terminates with the weak coupling c_1, one has $\mathcal{W} = 1$ and that side hosts a topological edge state, as it is shown in Fig. 6.2(a). On the other hand, if that side terminates with the strong coupling c_2, one has $\mathcal{W} = 0$ and does not support an edge state, as it is displayed in Fig. 6.2(b).

Furthermore, the full Hamiltonian satisfies the eigenvalue equation

$$\mathcal{H}\boldsymbol{\psi}_l = \mu_l \boldsymbol{\psi}_l, \tag{6.9}$$

where $\boldsymbol{\psi}_l = (\tilde{a}_l^1, \ldots, \tilde{a}_l^N)^T$ is the eigenstate and μ_l the eigenvalue of supermode l. The eigenvalue spectrum has a topologically protected zero-energy eigenstate within the gap when the lattice terminates with the weak coupling, while it does not appear when the lattice terminates with the strong coupling, as it can be seen in Figs. 6.2(c) and (d), respectively. Note that, the edge states are exponentially localized in one side of the lattice and are characterized by a staggered profile, while the rest of the states spread across the bulk of the lattice. This behaviour can be observed in Fig. 6.2(e), where apart from the bulk states, the structure supports one edge state, and in Fig. 6.2(f) where all the states spread across the bulk.

Symmetries of the SSH model

Topological systems can be classified regarding symmetries [354, 355]. In particular, the SSH model can be characterized with two main symmetries: the chiral symmetry and the particle hole symmetry. On the one hand, the chiral or sublattice symmetry, is defined by the unitary and Hermitian operator Γ, which anti-commutes with the Hamiltonian $\mathcal{H}$, hence, $\{\mathcal{H}, \Gamma\} = 0$. On the other hand, the particle hole symmetry is defined by an anti-unitary operator P, which also anti-commutes with the Hamiltonian $\mathcal{H}$, having $\{\mathcal{H}, P\} = 0$. The application of these operators to the Hamiltonian leads to

$$\Gamma\mathcal{H}\Gamma^\dagger = -\mathcal{H}, \tag{6.10}$$

$$P\mathcal{H}P^{-1} = -\mathcal{H}. \tag{6.11}$$

Moreover, the chiral operator Γ can be expressed in terms of the z Pauli matrix as

$$\Gamma = \sigma_z \oplus \sigma_z \oplus \ldots \oplus \sigma_z = \oplus_{i=1}^{N/2} \sigma_z, \tag{6.12}$$

where i is the index of the unit cell. Thus, the chiral operator Γ can be rewritten as an $N \times N$ matrix of the form

$$\Gamma = \begin{pmatrix} 1 & 0 & 0 & \ldots & 0 \\ 0 & -1 & 0 & \ddots & \vdots \\ 0 & 0 & \ddots & \ddots & 0 \\ \vdots & \ddots & \ddots & 1 & 0 \\ 0 & \ldots & 0 & 0 & -1 \end{pmatrix}. \tag{6.13}$$

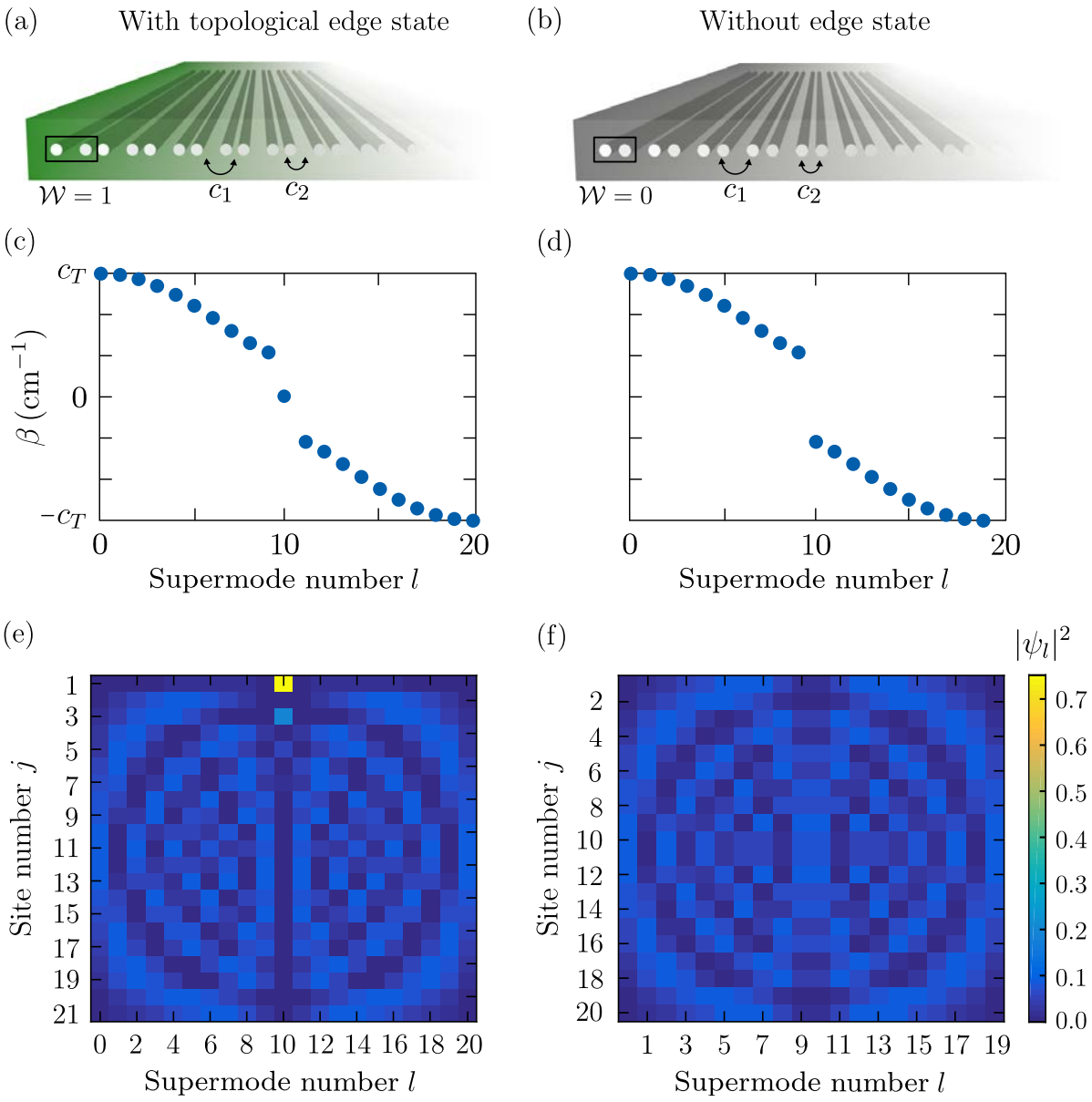

Figure 6.2: Representation of a SSH-like lattice implemented using optical waveguides, which are evanescently-coupled with alternating couplings c_1 and c_2 ($c_1 < c_2$). Depending on the termination of the lattice, the structure has (a) Winding number $\mathcal{W} = 1$ and supports a topological edge state on that edge or (b) $\mathcal{W} = 0$ and does not support an edge state on that edge. Eigenvalue spectrum corresponding to the lattice supporting (c) one topologically protected edge state and (d) no edge states. The energy gap is $2|c_1 - c_2|$ and $c_T = c_1 + c_2$. Amplitude of the eigenstates of the SSH lattice supporting (e) one topologically protected edge state and (d) no edge states. The lattices are composed of $N = 21$ waveguides for (c) and (e) and $N = 20$ waveguides for (d) and (f).

The chiral operator is local, acting only within the unit cell, and follows the same algebra as σ_z, satisfying $\Gamma^\dagger\Gamma = \Gamma^2 = 1$. In the momentum space, where the Hamiltonian $\mathcal{H}(k)$ is defined by a 2×2 matrix, chiral symmetry implies

$$\sigma_z \mathcal{H}(k) \sigma_z = 0. \tag{6.14}$$

Besides, since chiral and PHS exist for this model, time reversal symmetry also exists by combining the two previous operators [343]

$$\Gamma P \mathcal{H} P^{-1} \Gamma^\dagger = \mathcal{H}. \tag{6.15}$$

The chiral symmetry of the system entails that the energy spectrum of the system is symmetric around zero, guaranteeing that all the states with positive energy have a counterpart with the same negative energy. This can be easily verified by applying the chiral operator Γ to the eigenvalue equation (6.9), obtaining

$$\mathcal{H}(\Gamma \boldsymbol{\psi}_l) = -\Gamma \mathcal{H} \boldsymbol{\psi}_l = -\Gamma \mu_l \boldsymbol{\psi}_l = -\mu_l (\Gamma \boldsymbol{\psi}_l). \tag{6.16}$$

Thus, one can see that for any eigenstate $\boldsymbol{\psi}_l$ with eigenvalue $\mu_l \neq 0$, a symmetric eigenstate $\Gamma\boldsymbol{\psi}_l$ with energy $-\mu_l$ exists, implying that they can be host in both sublattices [343]. On the contrary, the states with zero energy eigenvalue ($\mu_l = 0$) are localized within one sublattice, being protected by the chiral symmetry and thereby, becoming robust against disorder maintaining the underlying symmetry of the system.

6.2.2 Discrete SUSY transformations

As we have seen with more detail in Section 3.4 of Chapter 3, DSUSY connects two superpartner Hamiltonians $\mathcal{H}^{(1)}$ and $\mathcal{H}^{(2)}$, sharing a common set of eigenvalues except for the eigenvalue $\mu_l^{(1)}$ of $\mathcal{H}^{(1)}$, which is removed from the spectrum of $\mathcal{H}^{(2)}$. Using the QR factorization technique, the superpartner Hamiltonians are given by

$$\mathcal{H}_s^{(1)} = \mathcal{H} - \mu_s I = QR \quad \text{and} \quad \mathcal{H}_s^{(2)} = RQ, \tag{6.17}$$

where Q is an orthogonal matrix ($Q^T Q = I$), R is an upper triangular matrix, and I is the $N \times N$ identity matrix. Note that, in general, the QR factorization is not unique and could lead to different solutions sharing the same eigenvalue spectrum [253]. In particular we use the Givens rotation method, based on applying rotations $G_j = g_j \otimes I$ to the tri-diagonal Hamiltonian $\mathcal{H}_s^{(1)}$, where

$$g_j = t_j \sigma_0 + i s_j \sigma_y, \tag{6.18}$$

and σ_0 is the 2×2 identity matrix. In addition, the R and Q matrices can be calculated as

$$R = \prod_{j=1}^{N-1} G_j \mathcal{H}_s^{(1)} \quad \text{and} \quad Q = \prod_{j=1}^{N-1} G_j^T. \tag{6.19}$$

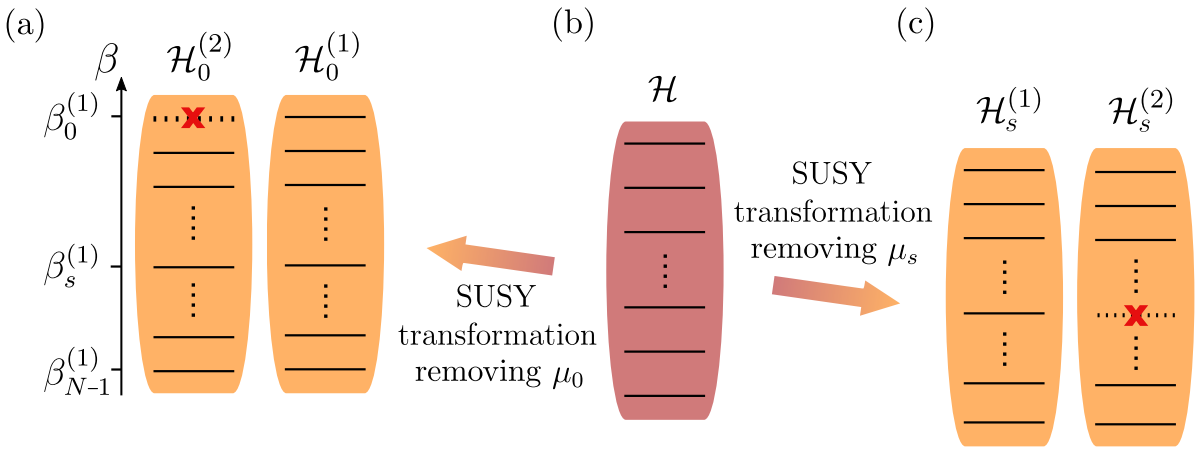

Figure 6.3: Schematic representation of the eigenvalue spectrum of the (a) superpartner Hamiltonians $\{\mathcal{H}_0^{(1)}, \mathcal{H}_0^{(2)}\}$, (b) original Hamiltonian $\mathcal{H}$, and (c) superpartner Hamiltonians $\{\mathcal{H}_s^{(1)}, \mathcal{H}_s^{(2)}\}$. The sets of superpartner Hamiltonians are obtained by removing the eigenvalues μ_0 and μ_s using SUSY transformations, respectively.

The superpartner Hamiltonian $\mathcal{H}_s^{(2)}$ shares a common set of eigenvalues with $\mathcal{H}_s^{(1)}$, except for μ_s that has been removed from the spectrum, as it is shown in Fig. 6.3(c). The corresponding eigenvalue μ_s is removed because its eigenstate $\boldsymbol{\psi}_s$ is completely localized in the fully decoupled N^{th} waveguide and, as such, does not have any influence on the dynamics of the remaining system of $N-1$ waveguides. Note that the standard SUSY transformation annihilating the fundamental state can still be carried out with this method, as it is illustrated in Fig. 6.3(a). By applying these transformations in an iterative way, superpartner structures with desired eigenvalue spectra can be engineered by removing the desired number of eigenvalues, and reducing the overall system size. A question that naturally arises and yet to this date has remained unexplored, is the impact of targeting a state with non-trivial topological properties, such as the topological edge states of the SSH model. Does its removal irrevocably change the topological properties of the system?

Symmetry preservation in SUSY transformations

Discrete SUSY transformations applied to the Hamiltonian can be expressed in terms of a transformation matrix V as

$$V\mathcal{H}_s^{(1)}V^{-1} = VQRV^{-1} = RQ = \mathcal{H}_s^{(2)}, \tag{6.20}$$

where $V = Q^{-1}$. If both $\mathcal{H}_s^{(1)}$ and V possess some symmetry, e.g., chiral symmetry satisfying the anti-commutation relation $\{\mathcal{H}_s^{(1)}, \Gamma\} = \{V, \Gamma\} = 0$, then, this symmetry is

transferred to the superpartner Hamiltonian

$$\mathcal{H}_s^{(2)} = V\mathcal{H}_s^{(1)}V^{-1} = -V\Gamma\mathcal{H}_s^{(1)}\Gamma^\dagger V^{-1} = -\Gamma\mathcal{H}_s^{(2)}\Gamma^\dagger. \tag{6.21}$$

On the other hand, if the transformation matrix V does not obey this symmetry, it is not reproduced in the superpartner Hamiltonian $\mathcal{H}_s^{(2)}$ either. Exploiting this connection between symmetry constraints of SUSY transformations and symmetries of the system, superpartner Hamiltonians with modified topological properties can be engineered. Thus, establishing a new method for topological state engineering by combining SUSY isospectrality and the breaking of symmetries of the system.

6.3 Supersymmetric topological photonic structures

To explore the interplay between topological non-trivial systems and SUSY transformations, we engineer supersymmetric structures of the SSH lattice and evaluate its different topological properties. To elucidate this, a SSH-type lattice composed of N (even) waveguides with the weak coupling c_1 at both terminations and thus, supporting two topologically protected zero-energy edge states, is considered as the starting point, as it is displayed in Figs. 6.4(b) and (e). As a proof of concept, two distinct superpartner structures are investigated:

(i) the superpartner SP_0 lattice obtained by removing the eigenvalue μ_0 corresponding to a bulk state, as it is represented in Figs. 6.4(a) and (d),

(ii) the superpartner $\mathrm{SP}_{N/2}$ lattice obtained by removing the eigenvalue $\mu_{N/2}$ corresponding to a topological edge state, as it is displayed in Figs. 6.4(c) and (f).

Note that, due to the symmetry of the eigenvalue spectrum, equivalent results would be obtained by removing μ_{N-1} and $\mu_{N/2-1}$, respectively. Subsequently, the degree of protection of the superpartner topological states is probed analytically with respect to their symmetries, as well as by gauging their robustness against chiral disorder.

First, let us focus on the SP_0 lattice displayed in Fig. 6.4(d) (see the entire lattice in Figs. 6.11(b) and (d)). Considering that the removal of any bulk state of the system per definition breaks the inversion symmetry of the eigenvalue spectrum, see Fig. 6.4(a), one would expect that the topological protection of the edge states is necessarily destroyed. Nevertheless, the chiral symmetry of the system is partially respected by the SUSY transformation, preserving the topological protection of one edge state. This can be explained by separating the Hamiltonian $\mathcal{H}_0^{(2)}$ into $\mathcal{H}_{0,L}^{(2)}$ and $\mathcal{H}_{0,R}^{(2)}$, corresponding to the left and right parts of the lattice, respectively. On the one hand, the chiral symmetry

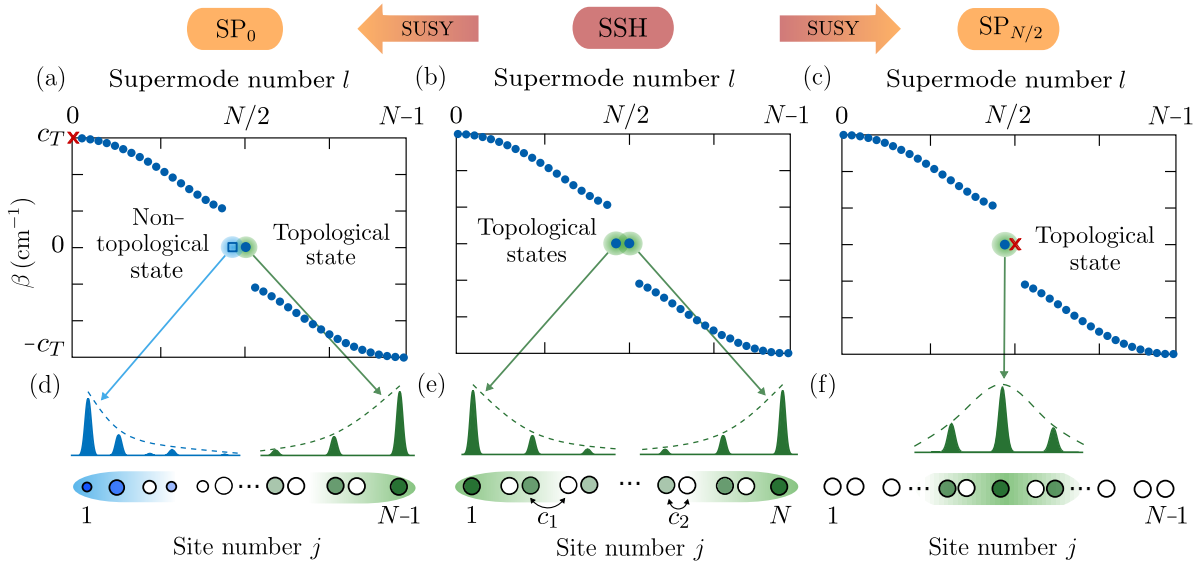

Figure 6.4: Eigenvalue spectrum of the (b) SSH and two superpartner lattices, obtained by removing (a) a bulk state ($m = 0$) and (c) an edge-state ($m = N/2$), respectively. The energy gap is $2|c_1 - c_2|$ and $c_T = c_1 + c_2$. Sketch of the (d) SP_0, (e) SSH and (f) $SP_{N/2}$ lattices. Detuning (coupling) is indicated by the size (spacing) of (between) the circles. The intensity of the color inside each waveguide is proportional to the amplitude of the edge/interface states, which is also illustrated above the lattices.

of $\mathcal{H}^{(2)}_{0,R}$ is preserved, satisfying

$$\Gamma \mathcal{H}^{(2)}_{0,R} \Gamma^{\dagger} = -\mathcal{H}^{(2)}_{0,R}, \tag{6.22}$$

hence, the topological protection of the right edge-state is maintained. On the contrary, the chiral symmetry of $\mathcal{H}^{(2)}_{0,L}$ is destroyed by the appearance of nonzero diagonal elements and the symmetry protection of the left edge state removed. Moreover, although the left edge-state loses its topological protection, its zero-energy eigenvalue is still pinned to zero due to SUSY isospectrality. Specifically, the SP_0 lattice exhibits an exponentially decaying detuning on the left side of the lattice, which is responsible for the edge state localization, while still resembles the SSH model towards the right part of the lattice, where the topological edge state is located. Note that, by applying another SUSY transformation removing μ_{N-1}, the inversion symmetry of the system is reestablished, and the topological protection of the left edge state can be restored. Moreover, by removing high-order ($0 < m < N/2$) bulk states of the spectrum, the detuned region can be extended across the lattice to facilitate an enhanced coupling with the right edge state, which can even lose its topological protection due to the effect of the detuning. Finally, by applying multiple SUSY transformations symmetrically, gaps can be carved

out in the eigenvalue spectrum while preserving the topological protection of the zero-energy states. In short, we transform a lattice supporting two topological edge states to a phase-matched lattice supporting one topological edge state, and one state that has lost its topological protection becoming sensitive to the underlying disorder.

Now, let us analyse the $\mathrm{SP}_{N/2}$ lattice displayed in Fig. 6.4(f) (see the entire lattice in Figs. 6.12(b) and (d)). Since we are removing the zero energy eigenvalue $\mu_{N/2}$, see Fig. 6.4(c), the diagonal elements of the superpartner Hamiltonians $\mathcal{H}^{(1)}_{N/2}$ and $\mathcal{H}^{(2)}_{N/2}$ remain zero, and thereby, the superpartner lattice is composed of waveguides with zero detuning. Here, the transformation matrix possesses chiral symmetry, which is transferred to the superpartner Hamiltonian, and thereby,

$$\Gamma \mathcal{H}^{(2)}_{N/2} \Gamma^{\dagger} = -\mathcal{H}^{(2)}_{N/2}. \tag{6.23}$$

Therefore, the symmetries of the system are preserved and the topological properties of the remaining zero-energy eigenstate stand. By applying SUSY transformations, two different superpartner lattices supporting one topological state $\boldsymbol{\psi}_{N/2-1}$, which can be an interface or an edge state, can be obtained due to the non-unicity of the QR factorization process [253]. For the interface state solution, the $\mathrm{SP}_{N/2}$ structure resembles two SSH chains with different terminations at the interface and strong coupling at the outer edges. The topological interface state, whose position in the lattice can be controlled by changing the dimerization $|c_1 - c_2|$, is located between the two SSH lattices and decays exponentially into the bulk, as it is illustrated in Fig. 6.4(f). For the edge state solution, the $\mathrm{SP'}_{N/2}$ lattice resembles the SSH model, see Fig. 6.4(e), with interchanged couplings and the N^{th} waveguide removed, except for a localized deviation in the couplings with respect to c_1 and c_2 near the leading edge. Here, the SUSY transformation constitutes a topological phase transition in the sense that couplings are interchanged and one waveguide removed, annihilating one of the edge states. Note that, by applying another SUSY transformation, the remaining zero-energy eigenvalue can be removed and the system would become topologically trivial. To sum up, by annihilating zero-energy eigenvalues, SUSY transformations induce topological phase transitions, leading to the displacement, and destruction of topological states. Besides, the protocol could be implemented the other way around by applying inverse SUSY transformations [147] i.e., starting with the topologically trivial SSH model, whose eigenvalue spectrum does not support any zero-energy state as it is displayed in Fig. 6.5(a), and adding a zero-energy eigenvalue to the spectrum as it is represented in Fig. 6.5(b). In this case, since the removal or addition of a zero-energy eigenvalue does not break the chiral symmetry of the system, the symmetry will be transferred to the superpartner structure and the introduced zero-energy state will be topologically protected.

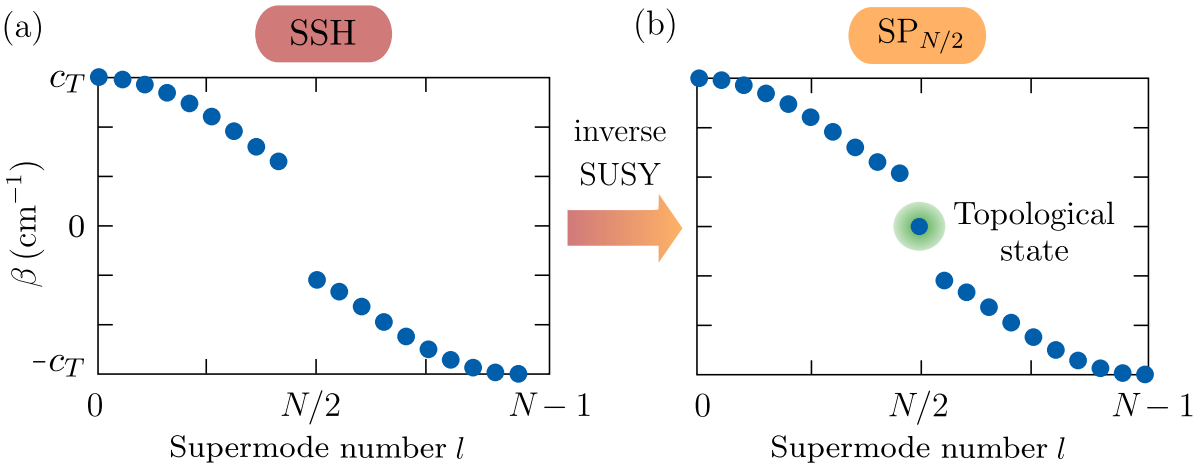

Figure 6.5: Eigenvalue spectrum of (a) the trivial SSH lattice and (b) the superpartner lattice obtained by adding a zero-energy state ($m = N/2$). The energy gap is $2|c_1 - c_2|$ and $c_T = c_1 + c_2$.

To summarize, the effects that DSUSY transformations induce on a system supporting two topologically protected zero-energy states are the following:

(i) the removal of a bulk state that is energetically far from the energy gap i.e., l is close to 0 or $N-1$, leads to a superpartner structure that supports one topological and one non-topological zero-energy states,

(ii) the suppression of a bulk state that is energetically close to the energy gap (l close to $N/2$), may destroy the topological protection of both zero-energy states of the superpartner structure,

(iii) the elimination of a zero-energy state ($l = N/2$ or $N/2-1$), produces a superpartner structure that supports one topologically protected zero-energy state.

Finally, note that, if one removes bulk states of the system in a symmetric way, e.g., $l = 0$ and $l' = N-1$, both zero-energy states will hold their topological properties since chiral symmetry is preserved. Instead, if the bulk states of the system are removed in an asymmetric way e.g., $l = 2$ and $l' = N-10$, both zero-energy states will loss their topological protection due to the breaking of the chiral symmetry of the system.

6.3.1 Experimental set-up

In order to experimentally corroborate the previous theoretical findings, we employ the femtosecond direct laser writing technology [76], to inscribe waveguide arrays in 10 cm fused-silica glass (Corning 7980). This method is based on focusing femtosecond pulses, creating a microplasma due to a nonlinear absorption process that induces a change in the molecular structure, as it is illustrated in Fig. 6.6(a). In particular, for fused silica the density is locally increased due to the partial breaking of the molecular ring structure of SiO_2, yielding to an increase of the refractive index [356]. To be specific, the laser system used to inscribe the waveguides consists of a Coherent RegA 9000 amplifier seeded with a Coherent Vitara S Ti:Sa laser with an energy of 250 nJ at 800 nm, 100 kHz repetition rate, and a pulse width of approximately 130 fs. By moving the sample along the propagation direction with a high-precision positioning stage (Aerotech ALS 180) with speeds between 91 to 103 mm min^{-1}, the refractive index change at the focal point is around 7×10^{-4}, creating waveguides with a mode field diameter of about 10.4 μm $\times$ 8 μm at 633 nm. The propagation losses and birefringence are estimated to be 0.2 dB cm^{-1} and 1×10^{-7}, respectively.

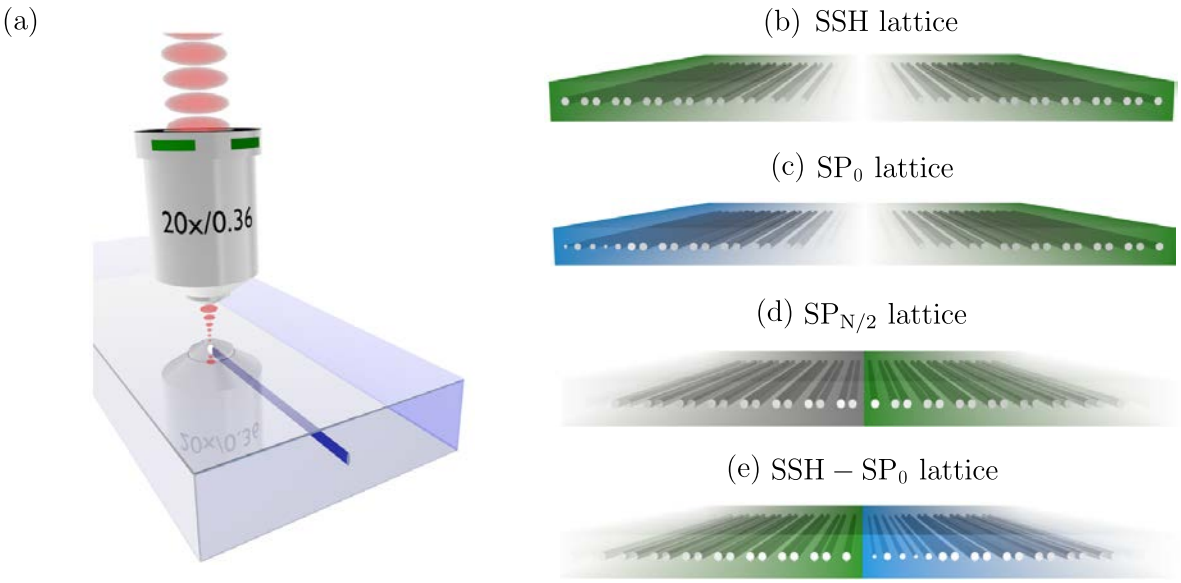

Figure 6.6: (a) Illustration of the waveguide laser writing process (image courtesy of M. Kremer). Representation of (b) the original SSH lattice, (c) the superpartner $SP_{N/2}$ lattice, (d) the superpartner SP_0 lattice, and (e) the SSH lattice weakly coupled to the SP_0 lattice.

To our aim, four different samples are fabricated

(i) the original SSH lattice represented in Fig. 6.6(b),

(ii) the superpartner $SP_{N/2}$ lattice displayed in Fig. 6.6(c),

(iii) the superpartner SP_0 lattice depicted in Fig. 6.6(d),

(iv) the SSH lattice weakly coupled to the SP_0 lattice illustrated in Fig. 6.6(e).

For the implementation of the SUSY structures, the coupling as well as the detuning needs to be tuned individually. This can be achieved with our method, which allows to independently tune the coupling c and detuning $\Delta\beta$ by changing the separation between waveguides d and the inscription velocity v, respectively [139]. The relation between distance and coupling is retrieved from directional couplers, by measuring the spatial period of intensity oscillation i.e., the coupling length L_c, which is connected with the coupling strength c by $c = \pi/2L_c$ (as discussed in detail in Section 2.3 of Chapter 2). In addition, the relation between the writing speed and the detuning is calculated by measuring the intensity contrast

$$V = \frac{\max(I_1) - \min(I_1)}{\max(I_1)}, \tag{6.24}$$

where I_1 is the light intensity in the first waveguide. In this case, the coupling and detuning are given by [139]

$$c = \frac{\pi\sqrt{V}}{2\tilde{L}_c} \quad \text{and} \quad \Delta\beta = \frac{\pi\sqrt{1-V}}{2\tilde{L}_c}, \tag{6.25}$$

respectively. The calibration graphs of the relation between coupling, separation distance and writing velocity are plotted in Figs. 6.7(a) and (b), respectively, while the relation between detuning and writing velocity is shown in Fig. 6.7(c). The coupling is well fitted by an exponential function of the distance between waveguides, while the detuning depends linearly on the writing speed. The exponential and linear fits are

$$c\ (d) = \kappa_1 \exp(-\kappa_2 d), \tag{6.26}$$

$$\Delta\beta\ (v) = \kappa_3 v + \kappa_4, \tag{6.27}$$

where $\kappa_1 = 10.93\,\mathrm{cm}^{-1}$, $\kappa_2 = 0.121\,\mu\mathrm{m}^{-1}$, $\kappa_3 = -0.8327\,\mathrm{min\,cm}^{-2}$ and $\kappa_4 = 8.376\,\mathrm{cm}^{-1}$. Note that the coupling is virtually unaffected by changes in the writing speed, as shown in Fig. 6.7(b), and thereby, an independent tuning of the coupling and the detuning can be achieved for a wide parameter values range.

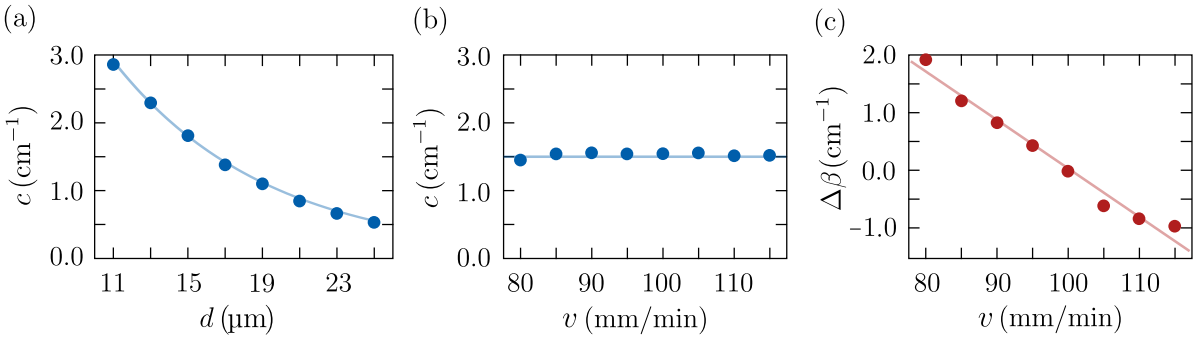

Figure 6.7: Coupling coefficient c dependence with respect to (a) the waveguide separation d, calibrated using pairs of evanescently-coupled waveguides with different separation, and, (b) the writing speed v, calibrated using pairs of evanescently-coupled waveguides written with different velocities. (c) Detuning $\Delta\beta$ dependence with respect to the writing velocity. The dots correspond to the experimentally obtained values while the lines are the (a) exponential and (b)-(c) linear fits. The experimental error associated to the couplings and detunings is $\pm 0.05\,\mathrm{cm}^{-1}$ and $\pm 0.1\,\mathrm{cm}^{-1}$, respectively.

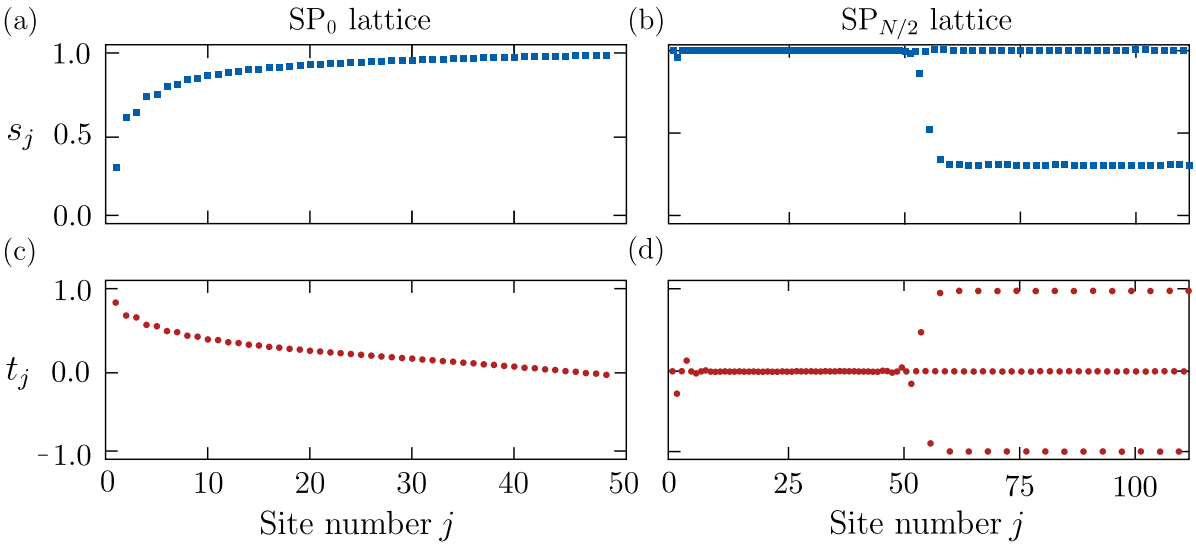

Figure 6.8: Representation of s_j and t_j of the Givens rotation matrices $g_j = t_j\sigma_0 + is_j\sigma_y$, where σ_0 is the two-dimensional identity matrix, σ_y the y-Pauli matrix and j the site number. (a) and (c) shows the s_j and t_j elements, respectively, corresponding to the SP_1 lattice, while (b) and (d) display the elements associated with the $\mathrm{SP}_{N/2}$ lattice. The original SSH lattice used to construct the SP_1 ($\mathrm{SP}_{N/2}$) lattice is composed of $N = 50$ ($N = 110$) waveguides, $c_1 = 0.5\,\mathrm{cm}^{-1}$ and $c_2 = 1.0\,\mathrm{cm}^{-1}$ ($c_2 = 1.8\,\mathrm{cm}^{-1}$).

6.3.2 Design of the superpartner structures

To design the superpartner structures we use the Givens rotation method previously introduced in Section 6.2. Specifically, the parameters t_j and s_j of Eq. (6.18), which are represented in Fig. 6.8 for the SP_0 and $SP_{N/2}$ lattices, are directly related with the structure of the couplings and detunings of the superpartner lattices and connected to the topological transitions. Note that, to design the structures, there are some constraints from the fabrication process that needs to be taken into account.

To design the SP_1 structure, we consider an original SSH lattice with $c_1 = 0.5\,\mathrm{cm}^{-1}$, $c_2 = 1.0\,\mathrm{cm}^{-1}$ and $N = 50$ waveguides, which supports two topologically protected edge states, as it is represented in Figs. 6.9(a) and (c). Here, we have the experimental restriction to adjust the detuning $\Delta\beta$ below 2 cm^{-1} in order to guarantee that the coupling stays constant when changing the detuning. This could not be fulfilled when using higher contrast between c_1 and c_2 for the SSH lattice. By applying the Givens rotation method, we can observe in Fig. 6.8(a) and (c) how $s_j \to 1$ and $t_j \to 0$ as j increases, respectively. Thus, $g_j \to i\sigma_y$ towards the right part of the lattice, where the superpartner still resembles the SSH model, while $g_j \sim t_j\sigma_0$ is the dominant term throughout the left side of the lattice, inducing a small deviation in the couplings with respect to the

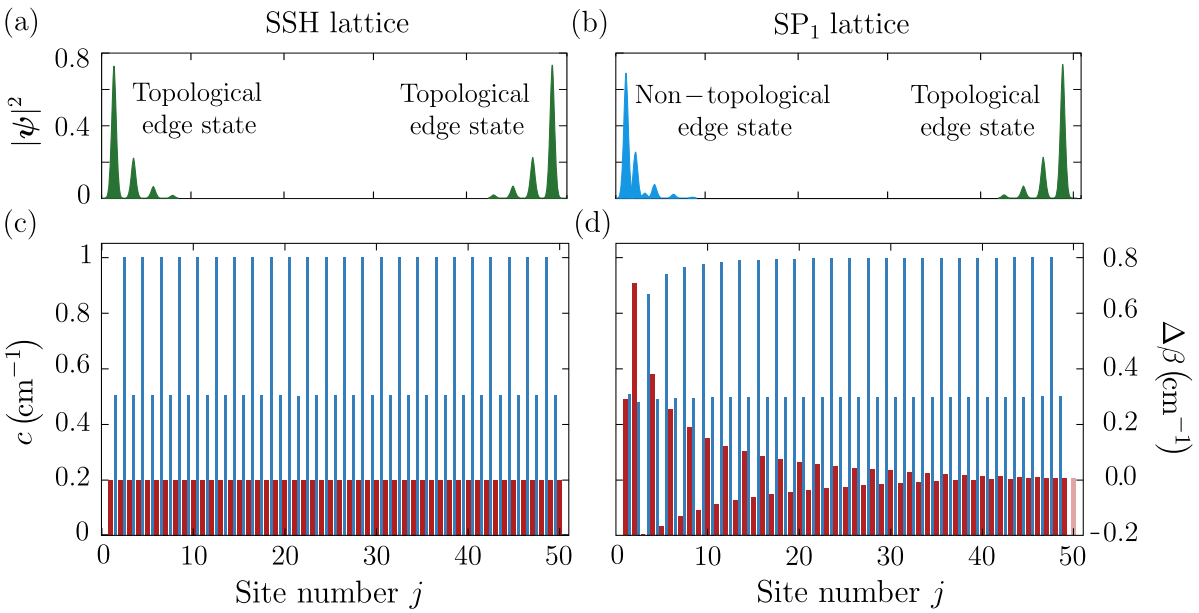

Figure 6.9: Eigenstate amplitudes of the edge states for the (a) SSH and (b) SP_0 lattices. Discrete representation in terms of the detunings $\Delta\beta$ (red bars) and couplings c (blue bars) of the (c) SSH, and (d) SP_0 lattices. The original SSH lattice is composed of $N = 50$ waveguides, $c_1 = 0.5\,\mathrm{cm}^{-1}$ and $c_2 = 1.0\,\mathrm{cm}^{-1}$.

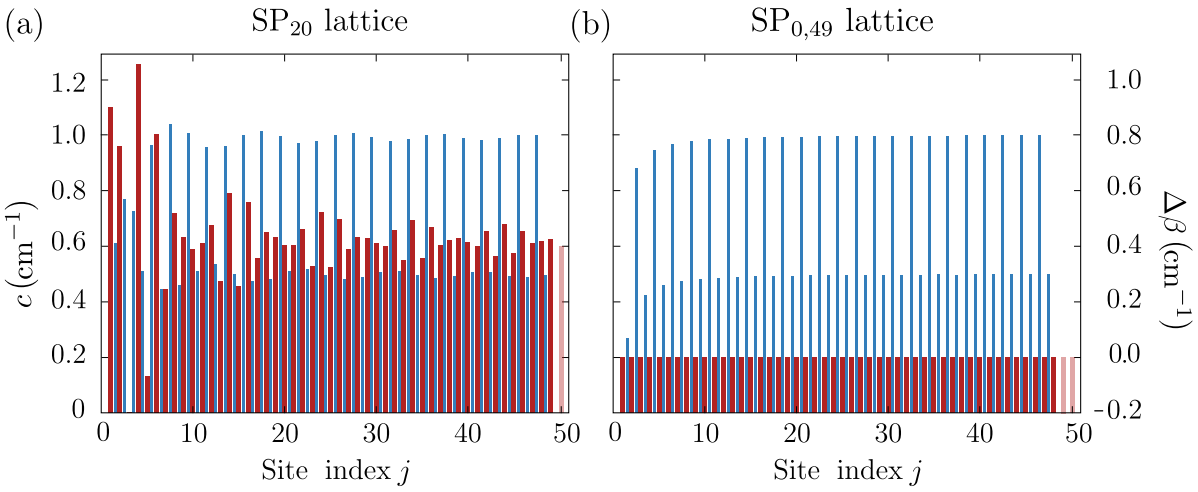

Figure 6.10: Discrete representation in terms of the detunings $\Delta\beta$ (red bars) and couplings c (blue bars) of the (a) SP_{20} lattice obtained after removing μ_{20}, and (b) the $SP_{0,49}$ lattice obtained after removing μ_0 and μ_{49}. The original SSH lattice is represented in Fig. 6.9(c).

original SSH lattice and introducing an exponentially decaying detuning. Note that the shape of t_j and s_j is reflected in the SP_0 structure displayed in Fig. 6.9(d). Besides, the detuning of the left part of the lattice is the responsible for the confinement of the non-topological edge state represented in Fig. 6.9(b), whose profile is clearly different from the staggered profile of the topological edge states. Remember that topological edge states are localized only in one of the sublattices, a condition that is not fulfilled in this case. This occurs because the appearance of detunings in the left side of the lattice, corresponding to the diagonal terms of the Hamiltonian, breaks down the chiral symmetry of the system. Besides, if one removes a bulk state that is close to the energy gap (l close to $N/2$), the detunings become more asymmetric and spread towards the right part of the lattice, as it can be seen in Fig. 6.10(a). In this case, if one apply DSUSY transformations in an iterative way removing different eigenvalues from just one side ($0 < l < N/2$) of the eigenvalue spectrum, the topological protection of the right edge state will also be destroyed due to the effect of the detunings. On the other hand, if the eigenvalues are removed in a symmetric way, e.g., $l = 0$ and $l' = N - 1$, the $SP_{l,l'}$ lattice composed of $N - 2$ waveguides would not have any detuning, see Fig. 6.10(b). Thus, preserving the chiral symmetry of the system that protects the edge states.

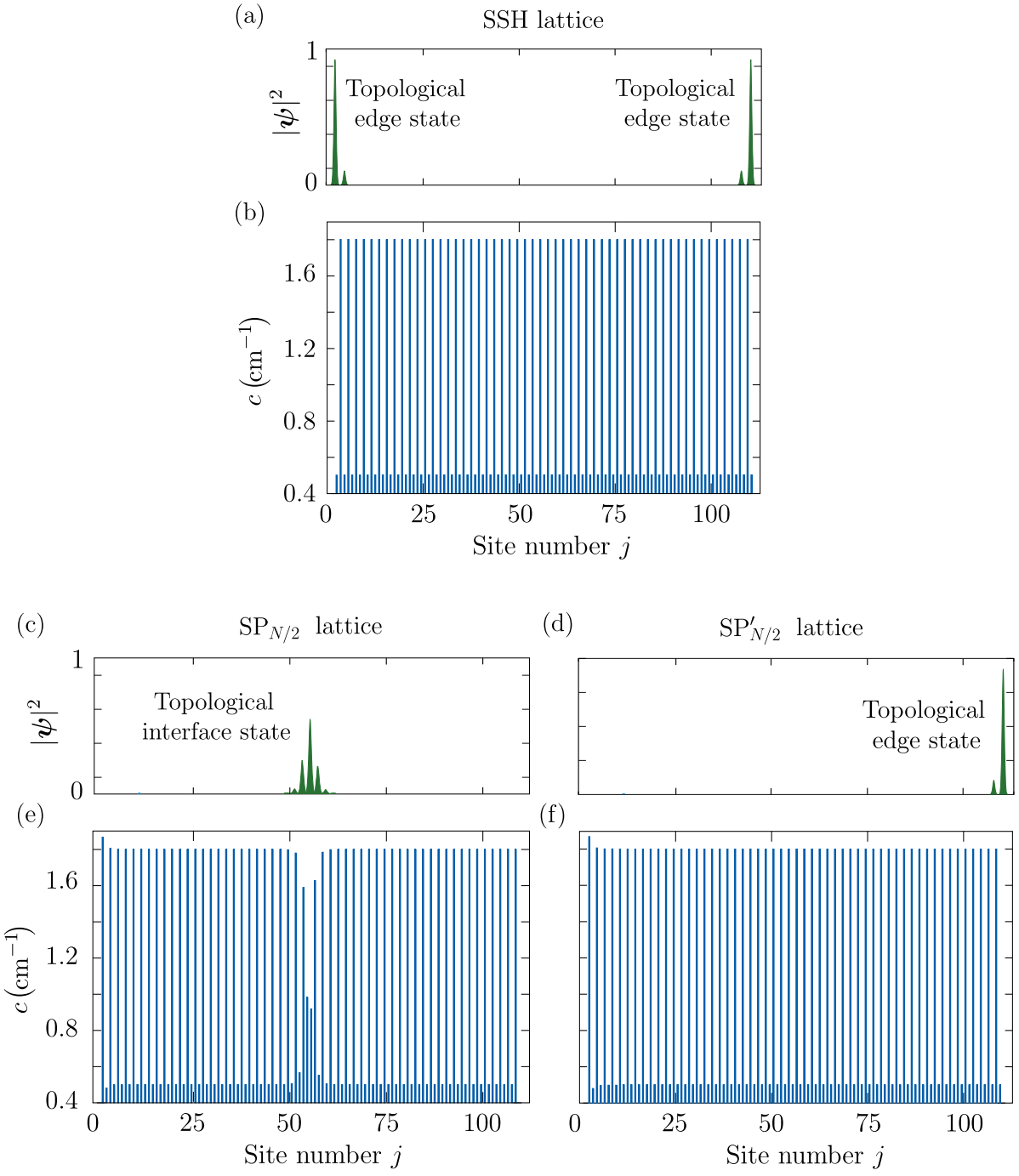

Figure 6.11: Eigenstate amplitudes of the edge and interface states for the (a) SSH, (c) $\mathrm{SP}_{N/2}$ and (d) SP'$_{N/2}$ lattices. Discrete representation in terms of the couplings c of the (b) SSH, (e) $\mathrm{SP}_{N/2}$ and (f) SP'$_{N/2}$ lattices. The original SSH lattice is composed of $N = 110$ waveguides, $c_1 = 0.5\,\mathrm{cm}^{-1}$ and $c_2 = 1.8\,\mathrm{cm}^{-1}$.

To design the $\mathrm{SP}_{N/2}$ structure, the original SSH lattice represented in Fig. 6.11(b) with $c_1 = 0.5\,\mathrm{cm}^{-1}$, $c_2 = 1.8\,\mathrm{cm}^{-1}$ is considered. Here, since no detuning is needed, we introduce a higher contrast between the couplings c_1 and c_2 of the original SSH lattice in order to have more confined edge states. By comparing Fig. 6.9(a) and Fig. 6.11(a), one can clearly see how the edge state confinement is directly related to the difference between couplings. Now, by applying the Givens rotation method, one can observe in Figs. 6.8(b) and (d), how $s_j \to 1$ and $t_j \to 0$ for $j < j_{\mathrm{interface}}$, and thereby, $g_j \to i\sigma_y$, interchanging the couplings c_1 and c_2 of the original SSH lattice. In addition, around $j_{\mathrm{interface}}$, there is a transition to a more complex behavior $g_{j,\mathrm{even}} \to i\sigma_y$, and $g_{j,\mathrm{odd}} \to \pm\sigma_0 + i\sigma_y c_2/c_1$, which leads to a recovering of the original SSH configuration. As it can be seen in Fig. 6.11(c), the generated structure supports an interface state with a staggered profile. Note that, although the pattern of Fig. 6.8(d) suggests that the lattice should have detunings, the diagonal terms appearing at $\mathcal{H}^{(2)}_{N/2}$ are of the same order than the subtracted eigenvalue, which is $\mu_{N/2} \sim 10^{-16}\mathrm{cm}^{-1}$, and does not have any influence on the dynamics of the system. Note that, in this case, a degenerate solution exists when one performs the QR factorization. In particular, the $\mathrm{SP'}_{N/2}$ lattice resembles the SSH model with interchanged couplings and $N-1$ waveguides, with $g_j \to i\sigma_y$ constituting a topological phase transition, as it is represented in Fig. 6.11(f).

6.3.3 Robustness of the topological states

To numerically prove the topological protection of the states, we introduce chiral disorder of the form

$$\tilde{c}_1^q = c_1 + \Delta c \quad \text{and} \quad \tilde{c}_2^q = c_2 - \Delta c, \tag{6.28}$$

where $\Delta c = \xi_q \tilde{K} = \xi_q K |c_1 - c_2|/2$. The disorder is quantified in terms of the disorder strength K, the dimerization $|c_1 - c_2|$, and a random number $-1 \leq \xi_q \leq 1$ affecting the couplings of each unit cell q. To demonstrate the robustness, we compute the deviation of the eigenvalues and eigenstates with respect to the case without disorder

$$|\Delta\mu_l| = |\mu_l - \mu_l(K=0)| \quad \text{and} \quad |\Delta\boldsymbol{\psi}_l|^2 = |\boldsymbol{\psi}_l - \boldsymbol{\psi}_l(K=0)|^2. \tag{6.29}$$

Due to their symmetries, the zero-energy eigenvalues, corresponding to the topological edge states, should be robust against this kind of disorder, while the other states should exhibit an eigenvalue deviation.

For the SP_0 lattice of Fig. 6.9(d), by introducing up to 25% of disorder with respect to $|c_1 - c_2|$, we can observe in Fig. 6.12(a) how there is no deviation of the eigenvalue $\mu_{N/2}$ corresponding to the topological edge state. Instead, if we take a look at the deviation of the eigenvalue $\mu_{N/2-1}$ corresponding to the non-topological edge state, we can confirm that the state is not topologically protected since the deviation of its eigenvalue

with respect to the non-disordered case increases linearly with the amount of disorder. Besides, the deviation of the topological edge state eigenvalue $\mu_{N/2}$ is reduced as N increases, whereas the eigenvalue deviation of the non-topological edge state $\Delta\mu_{N/2-1}$ is not affected by the size of the system. Regarding the changes in the eigenstate shapes shown in Fig. 6.12(b), we can observe how the non-topological edge state suffers more deviations than the topological one. In both cases, the change in the eigenstate shapes are small, and the states remain localized at the corresponding edges of the SP_0 lattice. Moreover, if we look at the $\mathrm{SP}_{N/2}$ lattice of Fig. 6.11(d), we obtain that by introducing up to 25% of disorder, there is no deviation of the zero-energy eigenvalue $\mu_{N/2-1}$ corresponding to the topological interface state, see Fig. 6.12(a). In this case, the slightly higher deviation of the interface shape with respect to the edge states shape may be produced due to the fact that the interface state spreads along more waveguides. Thus, the disorder introduced to the system has more impact on the modification of its shape, while it does not affect its eigenvalue which is symmetrically protected. Note that, if any other kind of disorder not preserving the chiral symmetry of the system is introduced, the topological states are no longer protected and their zero-energy eigenvalues suffer deviations of the same order as those of the non-topological states.

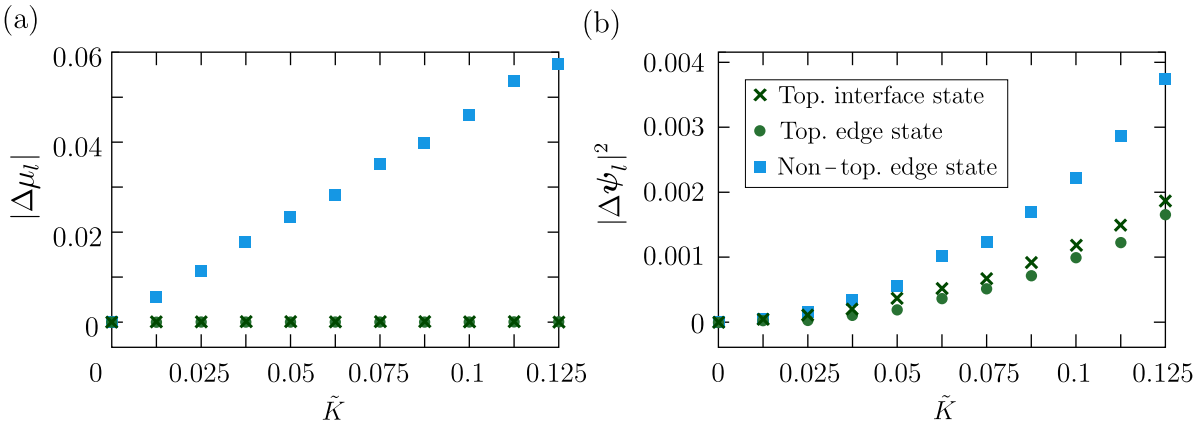

Figure 6.12: Robustness against chiral disorder. Deviation of the (a) eigenvalues μ_l and (b) eigenstate shapes $\boldsymbol{\psi}_l$ with respect to the ones of the original lattice ($K = 0$) when chiral disorder is introduced into the system, for: the non-topological edge state $l = 24$ (squares), the topological edge state $l = 25$ (circles), and the topological interface state $l = 54$ (crosses). The introduced chiral disorder is of the form $\Delta c = \tilde{K}\xi_q$, where $\tilde{K} = K|c_1 - c_2|/2$ being K the disorder strength, $|c_1 - c_2|$ the dimerization, and $-1 \leq \xi_q \leq 1$ a random number that affects the couplings of unit cell q. The total deviation is averaged over 5000 different simulations with different random disorder. All the simulations were carried out using the lattices of Figs. 6.9(c)-(d) and Fig. 6.11(d).

6.4 Experimental verification

In this section, we verify the existence and the different properties of the topological and non-topological states described in Section 6.3. On the one hand, by launching a single site excitation using a 10× microscope objective (0.25NA) with light from a Helium-Neon laser at 633 nm (Melles-Griot), light evolution of the different states along the different structures is directly measured. This can be done because color centers are formed during the fabrication process, which enables a direct observation of the propagation dynamics by using fluorescence microscopy [76]. Moreover, the resulting light at the output facet of the sample is imaged onto a CCD camera (BASLER Aviator) with another 10× microscope objective. Note that, the recorded images are post processed to reduce noise, distortions and the influence of background light. On the other hand, by using a white light source, the wavelength of the injected light is continuously tuned to evaluate the robustness and different origins of the edge states. In this case, the intensities at the output facet at different wavelengths are measured by using a white light source (NKT SuperK EXTREME) combined with a narrow wavelength filter (Photon ETC LLTF-SR-VIS-HP8). Moreover, the recorded images are post processed to reduce noise and subsequently integrated over a strip along the direction perpendicular to the lattice orientation for each wavelength. The resulting intensity distributions for the different wavelengths are then normalized to the maximum value to increase the visibility. Finally, by placing the SSH lattice in close proximity to the SP_0 lattice, evanescent coupling is introduced between the topological edge state in the former, and the non-topological edge state in the latter. The contrast of the resulting sinusoidal intensity oscillations serves as a direct indicator for any detuning between them.

The first step to verify the previous theoretical predictions is to prove the existence of the topological edge states of the SSH lattice shown in Fig. 6.9(c). To this end, we excite the right edge state by injecting light into the N^{th} waveguide, as depicted in Fig. 6.13(b). As a single-site excitation is made, and the theoretically expected edge state is exponentially localized within the waveguides N, $N-2$ and $N-4$, see Fig. 6.9(a), other bulk states of the system are also excited and the injected intensity slightly spreads during the propagation. However, one can clearly observe how the output measured intensity distribution is in accordance with the predicted mode profile, showing the expected SSH edge state. Besides, since the SSH lattice is symmetric, a mirrored propagation image would be obtained by injecting light into the first waveguide, exciting the left topological edge state. The next step is to demonstrate the presence of the interface state of the $SP_{N/2}$ lattice described in Fig. 6.11(d). Although the expected theoretical interface state spans approximately five odd waveguides, as depicted in Fig. 6.11(b), it is nevertheless populated by a single site excitation at the interface waveguide, as displayed in Fig. 6.13(c). Moreover, as can be observed from the output intensity pattern, most of the light is

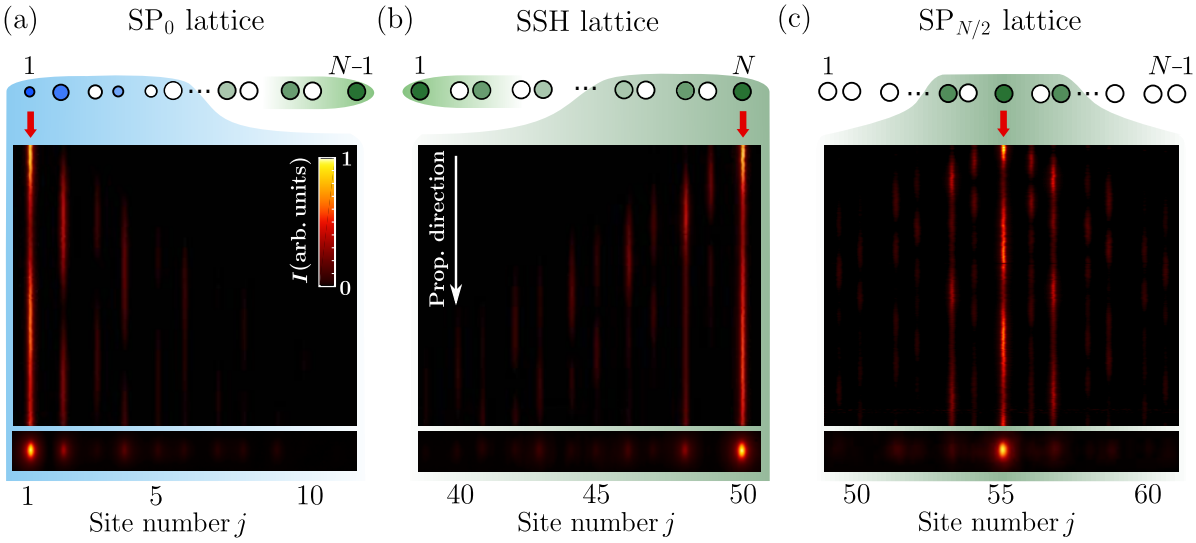

Figure 6.13: Experimentally observed light evolution along the propagation direction (top) and output intensities (bottom) for the (a) non-topological edge state, (b) topological edge state and (c) topological interface state. The total length of the sample is $L = 10\,\text{cm}$ and the wavelength used to excite the waveguides is $\lambda = 633\,\text{nm}$. The SP$_0$, SSH, and SP$_{N/2}$ lattices, which are sketched above the propagation images, are composed of 49, 50 and 109 waveguides, respectively. The values of couplings and detunings used to fabricate the SSH, SP$_0$, and SP$_{N/2}$ lattices are shown in Figs. 6.9(c) and (d) and Fig. 6.11(d), respectively.

localized at the interface waveguide itself. Note that, for the solution corresponding to the SP$_{N/2}$ structure supporting only one edge state, light evolution and output intensity would resemble the previously obtained for the SSH lattice. The next stage is to prove the existence of the non-topological edge state of the SP$_0$ lattice described in Fig. 6.9(d), which has lost its topological protection due to the breaking of chiral symmetry of one part of the system. To do that, the first waveguide of the SP$_0$ lattice is excited, as it is displayed in Fig. 6.13(a). While the localization is still visible, it may be noted that the intensity distribution at the output facet for the non-topological edge state does not have the staggered profile that characterizes the topological edge states. Instead, the non-topological edge state is mainly localized due to the high detuning in the first and second waveguides of the lattice, as it is depicted in Fig. 6.13(a). These differences are in agreement with the theoretical edge state profiles previously depicted in Fig. 6.9(b). Besides, since this edge state is solely mediated by the detuning, it is less robust against perturbations than the topological state as we have numerically verified.

Furthermore, to verify the different origin of the edge states of the SP$_0$ lattice, we

excite both edges with different wavelengths and observe the output intensities after 10 cm of propagation, see Fig. 6.14. The first observation is that, in spite of their different topological nature, both edge states remain localized at the corresponding edges. However, since the non-topological edge state is supported by the detuning, its degree of localization strongly decreases towards longer wavelengths as can be seen in Fig. 6.14(a). This occurs because the coupling substantially increases while the detuning decreases, and thereby, the former becomes the dominant term. On the contrary, it gets fully localized into a single waveguide for shorter wavelengths, where the detuning is the dominant term. This confirms that this edge state is localized due to the detuning, and thereby, it is less robust since it does not have a topological origin. The second observation is that the topological state strictly maintains its characteristic staggered intensity structure across the investigated spectral range as it is shown in Fig. 6.14(b). The slight delocalization at short wavelengths occurs as both couplings decrease and their absolute difference $|c_1 - c_2|$ becomes too small to strongly confine the state at the edge.

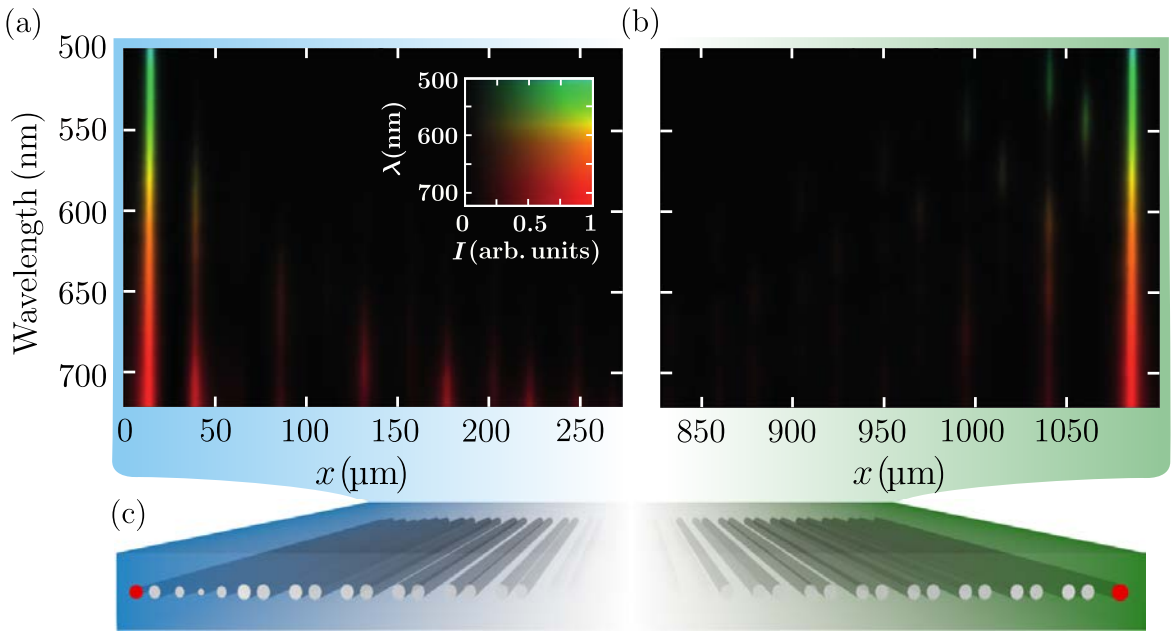

Figure 6.14: Experimentally observed output intensities for different wavelengths (500 nm $\leq \lambda \leq$ 720 nm) obtained by exciting the (a) non-topological and (b) the topological edge states of the SP_0 lattice, schematically represented in (c). The red dots indicate the excited waveguides. The relation between the wavelength used and its intensity measured at the output is represented in the inset. The total length of the sample is $L = 10$ cm and the SP_0 lattice is composed of 49 waveguides.

The last step is to verify that the non-topological edge state does indeed possess a zero-energy eigenvalue, as expected from SUSY transformation. To this aim, we weakly couple the non-topological edge state with the topological state, as displayed in Fig. 6.15(c). Here, if the two states have the same energy, one would expect their coupling with a full exchange of power. On the contrary, if the two states have different energies, one would expect only a partial exchange of power. In Figs. 6.15(a) and (b), we show the light evolution along the propagation direction when we excite either the waveguide supporting the topological state or the non-topological edge state, respectively. Moreover, in Figs. 6.15(c) and (d), one can see how the topological edge state is coupled to the non-topological one and viceversa. Specifically, one can observe how light is completely outcoupled from the excited waveguide, indicating that both edge states share the same propagation constant. Note that the intensity oscillations are in good agreement with the tight-binding simulations, shown by the dashed lines of Figs. 6.15(c) and (d).

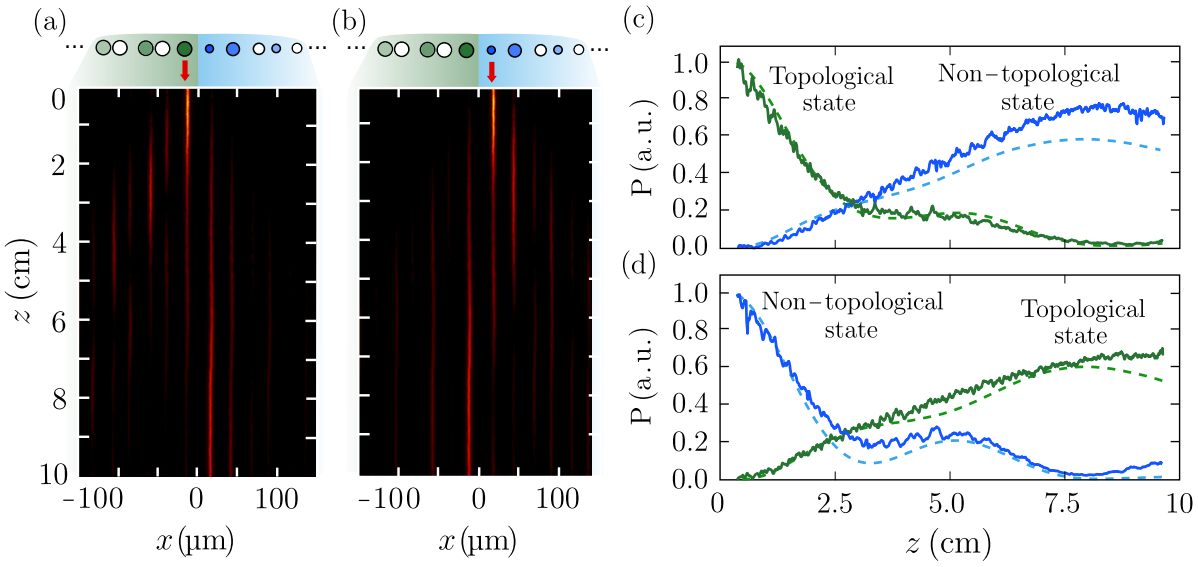

Figure 6.15: Experimentally observed light evolution along the propagation direction when the waveguides supporting (a) the topological and (b) the non-topological edge states of the coupled structure, schematically displayed above, are excited. Power oscillations when the waveguide supporting (c) the topological (green line) and (d) the non-topological (blue line) edge state, is excited. The solid lines correspond to the experimental results while the dashed lines correspond to the tight-binding numerical simulations. The total length of the sample is $L = 10\,\text{cm}$, the wavelength used to excite the waveguides is $\lambda = 633$ nm and the lattice is composed of $N = 99$ waveguides.

Moreover, an additional check that both edge states share the same energy independently of the wavelength is made exciting them with a white light source, as displayed in Fig. 6.16(a). By increasing the wavelength, the coupling increases, leading to a reduced effective length scale of the chip. Looking at the output intensities, the full exchange of intensity between waveguides can be observed, confirming that both superpartners share the same eigenvalue spectrum.

Finally, the resulting patterns are compared to tight-binding simulations, obtained by numerically integrating Eq. (6.1) with the corresponding Hamiltonian for each structure. The results are displayed in Fig. 6.17, showing an overall good agreement between the experiments and the simulations and confirming the validity of the theoretical description. Note that a quantitative discrepancy in Fig. 6.17(c), due to locally increased coupling caused by tightly spaced waveguides at the interface, can be observed. Nevertheless, the qualitative behavior is well reproduced.

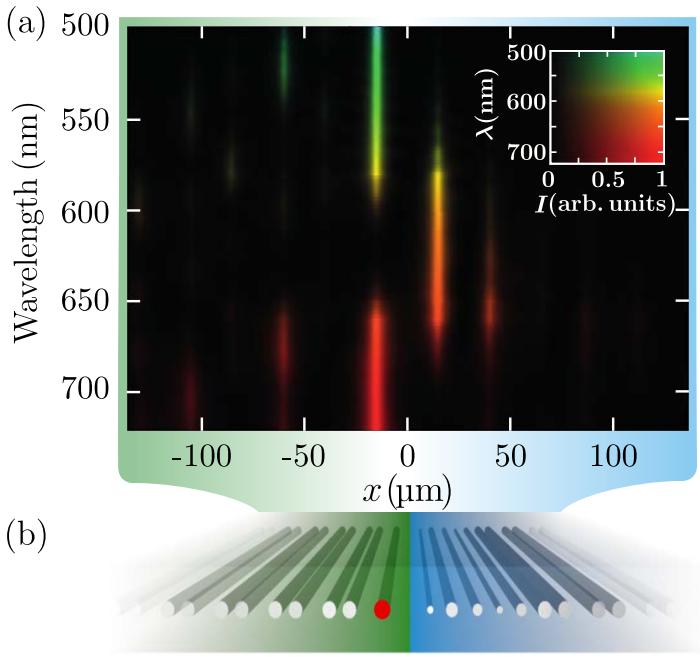

Figure 6.16: (a) Experimentally observed output intensities for different wavelengths obtained by exciting the topological edge state of the coupled lattice, indicated with the red dot in (b). (b) Schematic representation of the SSH lattice (left) weakly coupled to the SP1 lattice (right). The relation between the wavelength used and its intensity measured at the output is represented in the inset. The total length of the sample is $L = 10\,\mathrm{cm}$, the wavelength range used to excite the waveguides is $500\,\mathrm{nm} \leq \lambda \leq 720\,\mathrm{nm}$ and the lattice is composed of $N = 99$ waveguides.

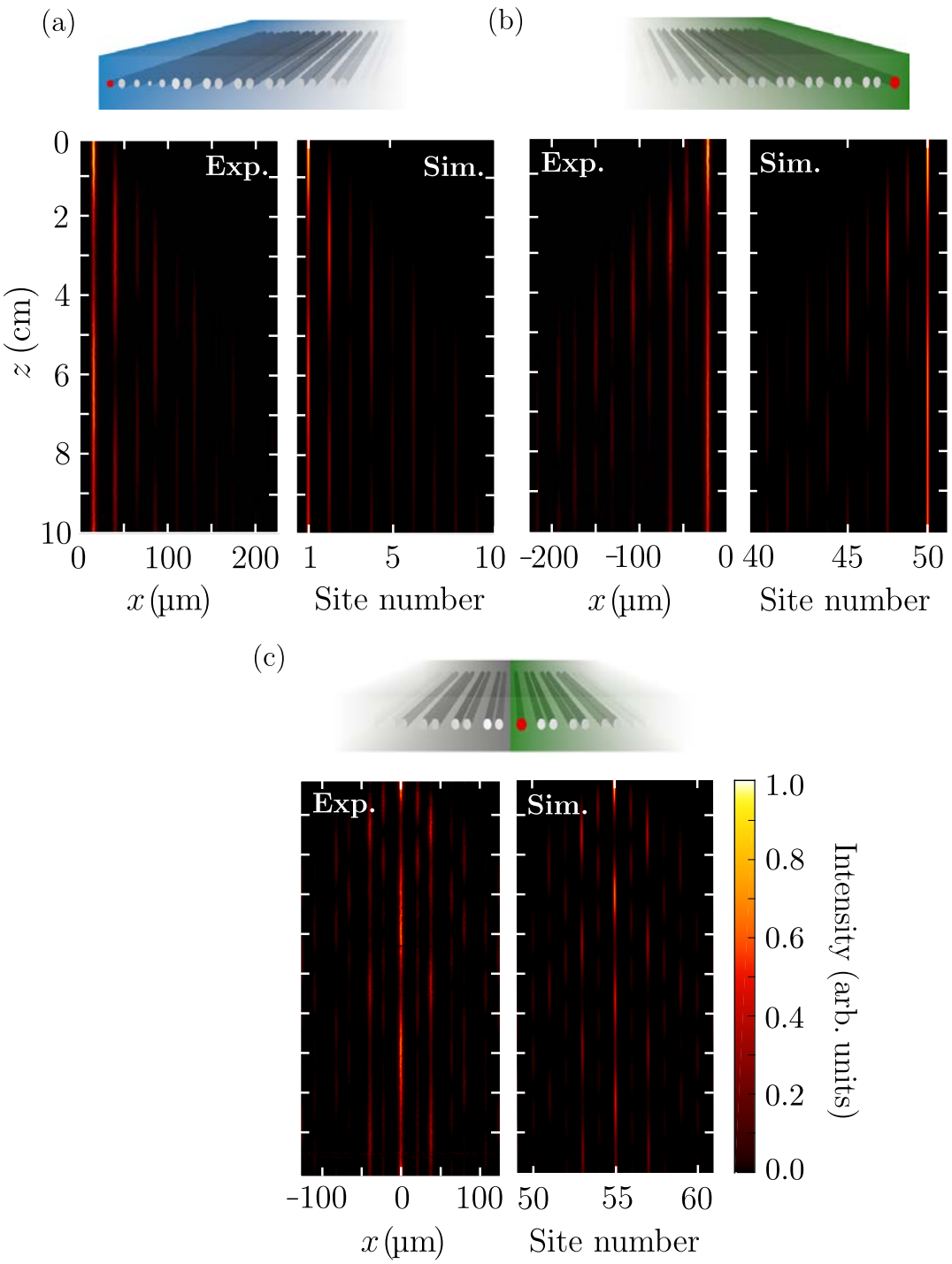
(a)
(b)
(c)
Exp.
Sim.
Exp.
Sim.
Exp.
Sim.
0
2
4
6
8
10
z (cm)
0
100
200
x (µm)
1
5
10
Site number
-200
-100
0
x (µm)
40
45
50
Site number
-100
0
100
x (µm)
50
55
60
Site number
1.0
0.8
0.6
0.4
0.2
0.0
Intensity (arb. units)

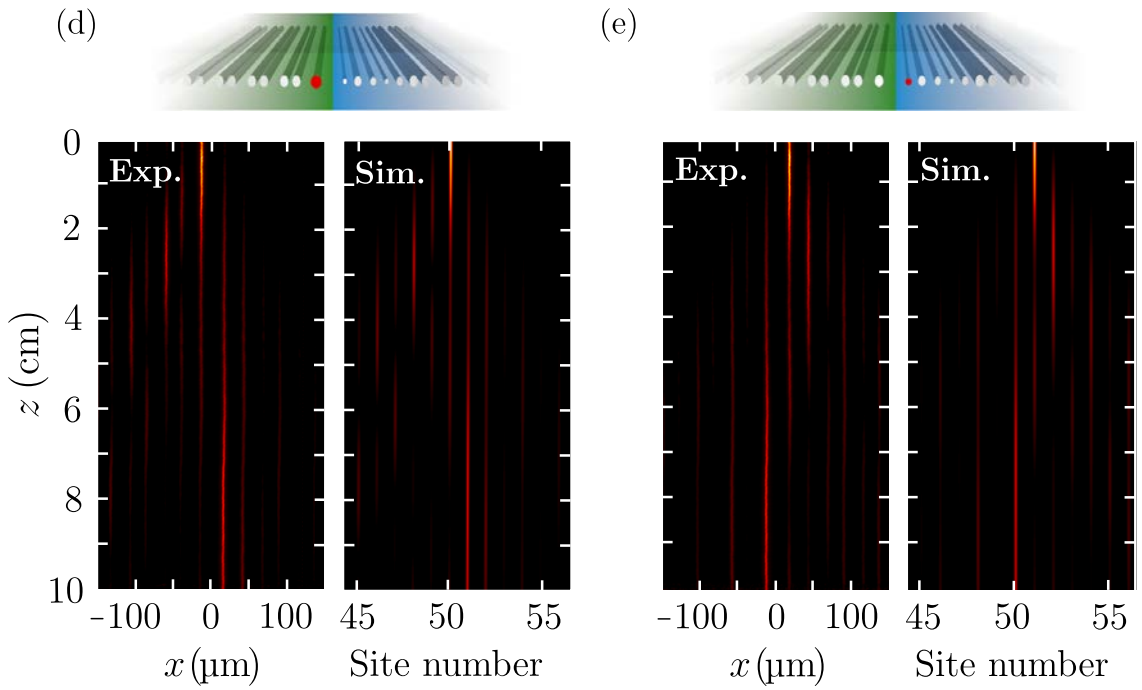

Figure 6.17: Intensity distribution, extracted by means of fluorescence microscopy (left) and tight-binding binding simulations (right), for the (a) SP_0 lattice, (b) SSH lattice, (c) $SP_{N/2}$ lattice, and (d)-(e) coupled SSH and SP_0 lattices. The corresponding lattices are shown schematically above the propagation pictures. The red dots of each structure indicate the excited waveguide. In (a) and (e) the non-topological edge state propagation, in (b) and (d) the topological edge state propagation, and in (c) the topological interface state propagation are shown. All the simulations have a correction of $\Delta c = -0.05$ cm^{-1} with respect to the lattices represented in Fig. 6.9(c)-(d), to adjust the results to the experimental values.

6.5 Conclusions

In this chapter, we have explored theoretically and experimentally the interplay between topological non-trivial systems and SUSY transformations. For this, we have considered one of the most prominent models for illustrating topological physics, the SSH model, and we have demonstrated how topological phase transitions can be induced by SUSY transformations. Specifically, we have explained how SUSY transformations can suspend and reestablish the topological protection of a state. Moreover, we have also shown how SUSY transformations can be used to annihilate topological states as well as to displace them from the edge to the bulk of the lattice. Specifically, we have exemplified it by transforming a lattice supporting two topological edge states to a lattice supporting (i) one topological edge or interface state, and, (ii) one topological and one non-topological edge states. Besides a throughout theoretical analysis, our findings have been experimentally verified by using femtosecond laser written waveguides.

Clearly, we have shown how SUSY techniques constitute a powerful tool to design structures with desirable topological properties, which could be extended to higher dimensions and chiral edge states in future works. Our work not only has shed light to the connection between topology and SUSY transformations, it also has shown how to harvest it to specifically tailor topological phase transitions. This is potentially of high importance for the design of topological non-trivial structures, leading to a deeper understanding of how both fields are intertwined, which might spark further developments in this field. Moreover, iterative SUSY transformations could also serve to remove any number of states from the system and reduce its overall size while preserving the desired part of the spectrum and the system's topological properties. Besides, inverse SUSY transformations [145, 147] could be used to introduce zero-energy states, which would be topologically protected when these transformations are applied to systems having topology protecting symmetries. Finally, note that the method for topological state engineering presented here can be extended to any platform allowing independent control of the coupling and detuning of the sites such as coupled cavities [159], ultra-cold atoms trapped in lattice potentials [344] or acoustic and mechanical systems [257].

7

Artificial gauge field switching using orbital angular momentum modes in optical waveguides

The discovery of artificial gauge fields, providing control over the dynamics of uncharged particles that otherwise elude the influence of standard electromagnetic fields, has revolutionized the field of quantum simulation. In this vein, developing new techniques to induce those artificial fields is essential to boost quantum simulation in photonic structures. Here, we demonstrate the generation of an artificial gauge field in a photonic lattice by modifying the input state, overcoming the need to modify the geometry or imposing the presence of real external fields. Specifically, we show that an effective magnetic flux naturally appears when light beams carrying orbital angular momentum are injected into waveguide lattices with certain configurations. Moreover, to validate the existence of this flux, we experimentally measure an effect that derives its origin solely from the presence of a magnetic flux, the Aharonov-Bohm caging effect. Our findings verify the possibility of switching artificial gauge fields just by changing the input state, paving the way to access different topological regimes in one single structure and representing an important step forward for optical quantum simulation.

This chapter is organized as follows. In Section 7.1, we motivate the interest in inducing artificial gauge fields in an active way by changing the input state of a light beam, rather than by properly engineering the geometry of the structure. This is followed by Section 7.2, where we introduce the diamond-chain photonic lattice, its band structure and the different basis rotations required to understand the appearance of the artificial magnetic flux. The chapter continues with the description of the experimental setup and the experimental verification of the Aharonov-Bohm caging effect in Section 7.3. Finally, in Section 7.4 we conclude and discuss future perspectives. The work included in this chapter was carried out in collaboration with Prof. von Freymann group from the Universität Kaiserlautern and Prof. Szameit group from the Universität Rostock.

7.1 Introduction

Photonic platforms have been shown to provide an ideal playground for quantum simulation [65], where many efforts have been devoted to implement topologically non-trivial phenomena [170, 337–340] such as topological insulators [171–173] or topological edge states [174–177]. Some of these non-trivial topological phases can be accessed via the introduction of Artificial Gauge Fields (AGF) [357, 358], controlling the dynamics of uncharged particles that otherwise elude the influence of standard electromagnetic fields. In this context, developing new techniques to induce AGF [359–362] is essential to boost quantum simulation in photonic structures. Typically, these AGF are introduced either by geometry manipulation [172, 362] or by time-dependent modulation [363–365]. While in Wu *et al.* [366] wavepackets carrying OAM were used to create edge states in crystalline topological insulators, here, we experimentally demonstrate that an AGF in the form of an effective magnetic flux can be induced using light beams carrying orbital angular momentum (OAM) [185].

Light beams carrying OAM are characterized by a helical phase front $\exp(i\ell\phi)$, where ℓ is the topological charge accounting for the amount $\ell\hbar$ of OAM carried per photon. In particular, light carrying OAM was first proposed by Allen *et. al.* in 1992 [367] and, since then, it has attracted a lot of attention in classical and quantum optical communications [179–186]. In this regard, OAM modes have been used to increase the transmission capacity in optical fibers [266, 368, 369], for space-division multiplexing [370–373], for optical tweezers [374, 375], to create synthetic lattices [376] or in stimulated emission depletion microscopy [377] and lithography [378] (see [185] for a recent review). In particular, these OAM states can be generated using q-plates [379], spiral-phase plates [380], Spatial Light Modulators (SLM) [381], micro-ring resonators [382], phase and waveguide arrays [383, 384] or directly implementing a geometric phase control inside a laser cavity [385].

In this chapter, we inject OAM modes in cylindrical optical waveguides arranged in a diamond-chain configuration to create an effective magnetic flux in a diamond-chain configuration [195, 196], whose presence is demonstrated by measuring the induced Aharonov-Bohm (AB) caging effect [386]. Originally studied in the context of two-dimensional electronic systems [92], the AB caging is a single-particle localization effect arising as a consequence of the interplay between the lattice geometry and the magnetic flux. More precisely, it is due to a constant magnetic flux that modifies the phase relations of wave packets, resulting in a destructive interference effect that binds the modes. Thus, it enables one to halt all propagation by controlling the flux. This phenomenon, which can be interpreted in terms of quantum interference [387, 388], has been predicted to occur [389–393] and experimentally verified [394, 395] in photonic structures implementing AGF. Unlike the previous photonic experimental proposals based on geometry

manipulations [394, 395], here we show how non-zero energy flat bands, which are required for the caging effect, can be achieved naturally and deliberately by injecting light carrying OAM, instead of fabricating a new sample. Therefore, our proposal enables to study the effect of AGF in photonic lattices just by selecting the topological charge of the input beam. In this context, our proposal differs from related works where the intrinsic angular momentum, i.e., the polarization of the input beam, instead of the extrinsic one, i.e., the OAM, has been used as the AGF switching mechanism [396]. Moreover, this method allows to access different topological regimes without the need of fabricating different structures or employing high intensities, as it is the case for topological phase transitions realized via nonlinear optics [397].

7.2 Physical system

We consider an array of evanescently-coupled optical waveguides arranged in a diamond-chain configuration, as it is displayed in Fig. 7.1(a). Specifically, the chain can be divided in N unit cells, with each unit cell j being composed of three waveguides $(S_j = A_j, B_j, C_j)$ forming a triangle with a central angle θ. Moreover, as introduced in Section 2.2 of Chapter 2, cylindrical waveguides sustain OAM modes of the form [189]

$$E_{S_j}^{\pm\ell}(r_{S_j}, \phi_{S_j}, z) = e_{S_j}^{\ell}(r_{S_j}) \exp(\pm i\ell(\phi_{S_j} - \phi_0)) \exp(-i\beta_{S_j}^{\ell} z), \tag{7.1}$$

where S_j accounts for the waveguide S in unit cell j, $\ell = 0, 1, 2, \ldots$ is the topological charge, $\pm$ accounts for positive and negative circulations of the phase front, (r_{S_j}, ϕ_{S_j}) are the polar coordinates with respect to the center of each waveguide S_j in the transverse plane, z is the propagation direction, ϕ_0 is an arbitrary phase origin, and $\beta_{S_j}^{\ell}$ is the propagation constant of mode ℓ in waveguide S_j. In particular, we restrict our implementation to $\ell = 0$ and $\ell = 1$ modes propagating in identical waveguides. The restriction on the number of guided modes is achieved by properly engineering the refractive index contrast and the width of the step-index waveguides, which consist of a core of refractive index n_{core} embedded in a cladding of lower refractive index n_{clad}, as it is illustrated in Fig. 7.1(b). The transverse field distribution of the modes $e_{S_j}^{\ell}(r_{S_j})$ can be obtained by solving Helmholtz equation in cylindrical coordinates (2.45) introduced in Chapter 2, which reads [189]

$$e_{S_j}^{\ell}(r_{S_j}) \propto \begin{cases} J_\ell(k_{S_j}^{\ell} r_{S_j}) & \text{if } \mathrm{r_{S_j}} \leq \mathrm{R} \\ K_\ell(\gamma_{S_j}^{\ell} r_{S_j}) & \text{if } \mathrm{r_{S_i}} > \mathrm{R} \end{cases}, \tag{7.2}$$

where J_ℓ is the Bessel function of the first kind and order ℓ, K_ℓ is the modified Bessel function of the second kind and order ℓ, $(k_{S_j}^{\ell})^2 = n_{core}^2 k_0^2 - (\beta_{S_j}^{\ell})^2$ and $(\gamma_{S_j}^{\ell})^2 = (\beta_{S_j}^{\ell})^2 - n_{clad}^2 k_0^2$ are the wavevector and the extinction coefficient, respectively, $k_0 = 2\pi/\lambda_0$ is the vacuum's wavenumber and λ_0 the vacuum's wavelength.

7.2.1 Unit cell structure and coupling amplitudes

To introduce the coupling amplitudes between modes $c_{\ell,\ell'}$ we focus on a unit cell of the diamond-chain. Moreover, since modes with different ℓ are not coupled between them due to its different propagation constant, we can analyse the coupling in the $\ell = 0$ and $\ell = 1$ subsets independently. Assuming $\theta > \pi/3$, the coupling between modes propagating in B_j with modes propagating in C_j can be neglected for both ℓ due to the exponential decaying of the evanescent field of the modes [398], as it will be discussed in detail in Section 7.2.3. Instead, the coupling between the other sites is different depending on the considered mode. While between fundamental modes ($\ell = 0$) there is only one coupling amplitude $c_{0,0} \equiv c_0$, between OAM modes ($\ell \neq 0$) there are two coupling amplitudes $c_{\ell,\ell} \equiv c_1$ and $c_{\ell,-\ell} \equiv c_2 \exp(i2\ell\phi_0)$ between modes with equal or opposite circulations, respectively [399].

For $\ell = 0$, there is only one coupling amplitude $c_{0,0} \equiv c_0$ occurring between modes propagating in A_j with modes propagating in C_j and B_j, as it is represented by the green arrows in Fig. 7.1(c). In this case, the system is described by a 3×3 Hamiltonian

$$\mathcal{H}_0 = \begin{pmatrix} \beta^0_{C_j} & c_0 & 0 \\ c_0 & \beta^0_{A_j} & c_0 \\ 0 & c_0 & \beta^0_{B_j} \end{pmatrix}, \tag{7.3}$$

where $\beta^0_{S_j}$ is the propagation constant of mode $\ell = 0$ in waveguide S_j. Note that, since we consider identical waveguides, $\beta^0_{S_j} \equiv \beta_0$. On the other hand, for $\ell = 1$, there are two different coupling amplitudes between modes with equal and opposite circulations

$$c_{1,1} \equiv c_1 \quad \text{and} \quad c_{1,-1} \equiv c_2 e^{i2\phi_0} = c_2 e^{-i2\theta}, \tag{7.4}$$

respectively [399]. While $c_{1,1} \equiv c_1$ irrespective of the direction (see black solid arrows in Fig. 7.1(d)), $c_{1,-1}$ changes depending on the phase origin ϕ_0. To be precise, we set ϕ_0 along the $A_j \leftrightarrow C_j$ direction such that the coupling amplitude $c_{1,-1}$ is real i.e., $c_{1,-1} \equiv c_2$, in that direction, while it is complex i.e., $c_{1,-1} \equiv c_2 e^{-i2\theta}$ in the $A_j \leftrightarrow B_j$ direction, as represented by the blue dashed and red dotted arrows in Fig. 7.1(d), respectively. Therefore, when dealing with OAM modes, complex coupling amplitudes between modes with different circulations appear naturally in some directions. In this case, the system is described by a 6×6 Hamiltonian of the form

$$\mathcal{H}_1 = \begin{pmatrix} \beta^+_{C_j} & 0 & c_1 & c_2 & 0 & 0 \\ 0 & \beta^-_{C_j} & c_2 & c_1 & 0 & 0 \\ c_1 & c_2 & \beta^+_{A_j} & 0 & c_1 & c_2 e^{-i2\theta} \\ c_2 & c_1 & 0 & \beta^-_{A_j} & c_2 e^{i2\theta} & c_1 \\ 0 & 0 & c_1 & c_2 e^{-i2\theta} & \beta^+_{B_j} & 0 \\ 0 & 0 & c_2 e^{i2\theta} & c_1 & 0 & \beta^-_{B_j} \end{pmatrix}, \tag{7.5}$$

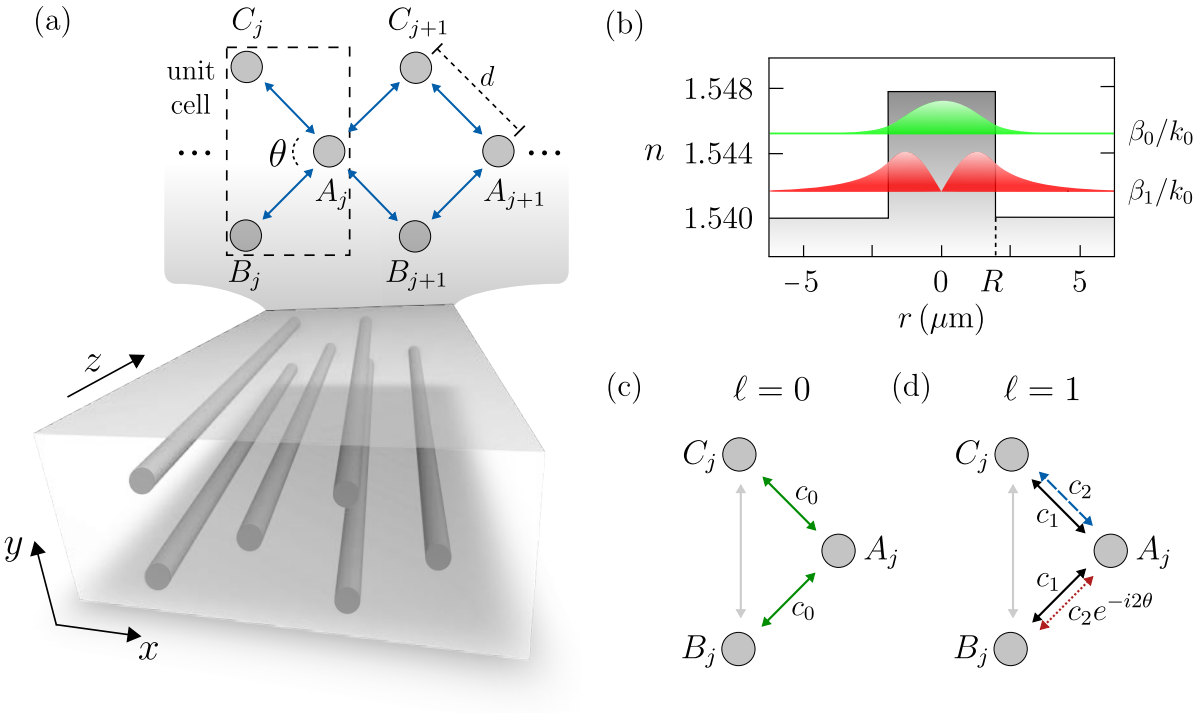

Figure 7.1: (a) Schematic representation of the structure composed of identical cylindrical waveguides arranged in a diamond-chain configuration. Each unit cell j hosts three waveguides $S_j \equiv A_j, B_j, C_j$ forming a triangle with central angle θ. The distances between waveguide centers are $d_{A_j \leftrightarrow B_j} = d_{A_j \leftrightarrow C_j} \equiv d$, $d_{B_j \leftrightarrow C_j} = 2d\sin(\theta/2)$ and $d_{A_j \leftrightarrow A_{j+1}} = 2d\cos(\theta/2)$. The blue arrows indicate the directions of the couplings. (b) Refractive index profile of the waveguides, defined by $n_{\mathrm{core}} = 1.548$, $n_{\mathrm{clad}} = 1.540$ and waveguide radius $R = 1.9\,\mu$m and field intensity profile of $\ell = 0$ (green) and $\ell = 1$ (red) modes, where β_ℓ is the propagation constant of mode ℓ, $k_0 = 2\pi/\lambda_0$ the vacuum wavenumber and λ_0 the light's wavelength in vacuum. (c) Coupling amplitudes in a unit cell j of the photonic lattice. The coupling amplitudes between $\ell = 0$ modes are represented by the green arrows, the coupling amplitudes between $\ell = 1$ modes with equal circulations $c_{1,1} \equiv c_1$ are represented by the black solid arrows, the coupling amplitudes between $\ell = 1$ modes with opposite circulations $c_{1,-1} \equiv c_2$ are represented by the blue dashed arrow, and $c_{1,-1} \equiv c_2 \exp(2i\phi_0) = c_2 \exp(-i2\theta)$, represented by the red dotted arrow, for the phase origin ϕ_0 fixed along the $A_j \leftrightarrow C_j$ direction. The grey arrow indicates the coupling between B_j and C_j that can be neglected for $\theta > \pi/3$.

where $\beta_{S_j}^{\pm}$ is the propagation constant of mode $\ell = 1$ with positive and negative circulations in waveguide S_j. Note that, since we consider identical waveguides and $\beta_{S_j}^{+\ell} = \beta_{S_j}^{-\ell}$, all the propagation constants of $\ell = 1$ modes are the same i.e., $\beta_{S_j}^{\pm 1} \equiv \beta_1$. In particular, in our implementation, we fix $\theta = \pi/2$ such that a relative phase difference of π between the $c_{1,-1}$ couplings in the $A_j \leftrightarrow C_j$ and $A_j \leftrightarrow B_j$ directions appears. This phase difference is responsible of introducing a π flux in the plaquettes, opening an energy gap between the dispersive bands of the system and inducing magnetic-like effects. To properly understand the band structure of the system, let us first characterize the coupling strengths c_0, c_1 and c_2.

Coupling characterization

We momentarily consider a unit cell with the in-line configuration ($\theta = \pi$) that simplifies the characterization of c_0, c_1 and c_2. Particularly, we numerically simulate the propagation of modes injected in the central waveguide A for a different separation d between waveguides, we then measure the coupling length L_ℓ, which is directly connected to the coupling strength as previously explained in Section 2.3 of Chapter 2, and, finally we fit the results into a exponential decaying function of the form

$$c_\ell(d) \equiv K_\ell \exp(-\kappa_\ell d), \tag{7.6}$$

where K_ℓ and κ_ℓ are constants. On the one hand, by injecting the $\ell = 0$ mode in the central waveguide A, as it can be seen in Fig. 7.2(a), one can extract the coupling strength $c_0 = \pi/4L_0$ for a fixed separation d between waveguides. By repeating this process for different separations, see crosses in Fig. 7.3(a), one can fit the values into (7.6) and obtain the specific values $K_0 = 387\,\mathrm{mm}^{-1}$ and $\kappa_0 = 1.17\,\mu\mathrm{m}^{-1}$, characterizing $c_0(d)$. On the other hand, the calculation of c_1 and c_2 cannot be directly performed injecting $\ell = 1$ modes with positive and negative circulations in waveguide A, since modes with positive and negative circulations propagating in different waveguides are coupled between them, requiring a basis rotation to decouple them. Note that, to simplify the notation along the chapter, we use the bracket notation i.e., $|S^{\pm\ell}\rangle$, where the superscripts $\pm$ accounts for positive or negative circulations of mode ℓ in waveguide S. In particular, the symmetric $|A_S\rangle$ and antisymmetric $|A_A\rangle$ supermodes, given by

$$|A_S\rangle = \frac{1}{\sqrt{2}}(|A^+\rangle + |A^-\rangle) \quad \text{and} \quad |A_A\rangle = \frac{1}{\sqrt{2}}(|A^+\rangle - |A^-\rangle), \tag{7.7}$$

are only coupled to [400]

$$|K_S\rangle = \frac{1}{\sqrt{2}}\left(|C_S\rangle + |B_S\rangle\right) \quad \text{and} \quad |K_A\rangle = \frac{1}{\sqrt{2}}\left(|C_A\rangle + |B_A\rangle\right), \tag{7.8}$$

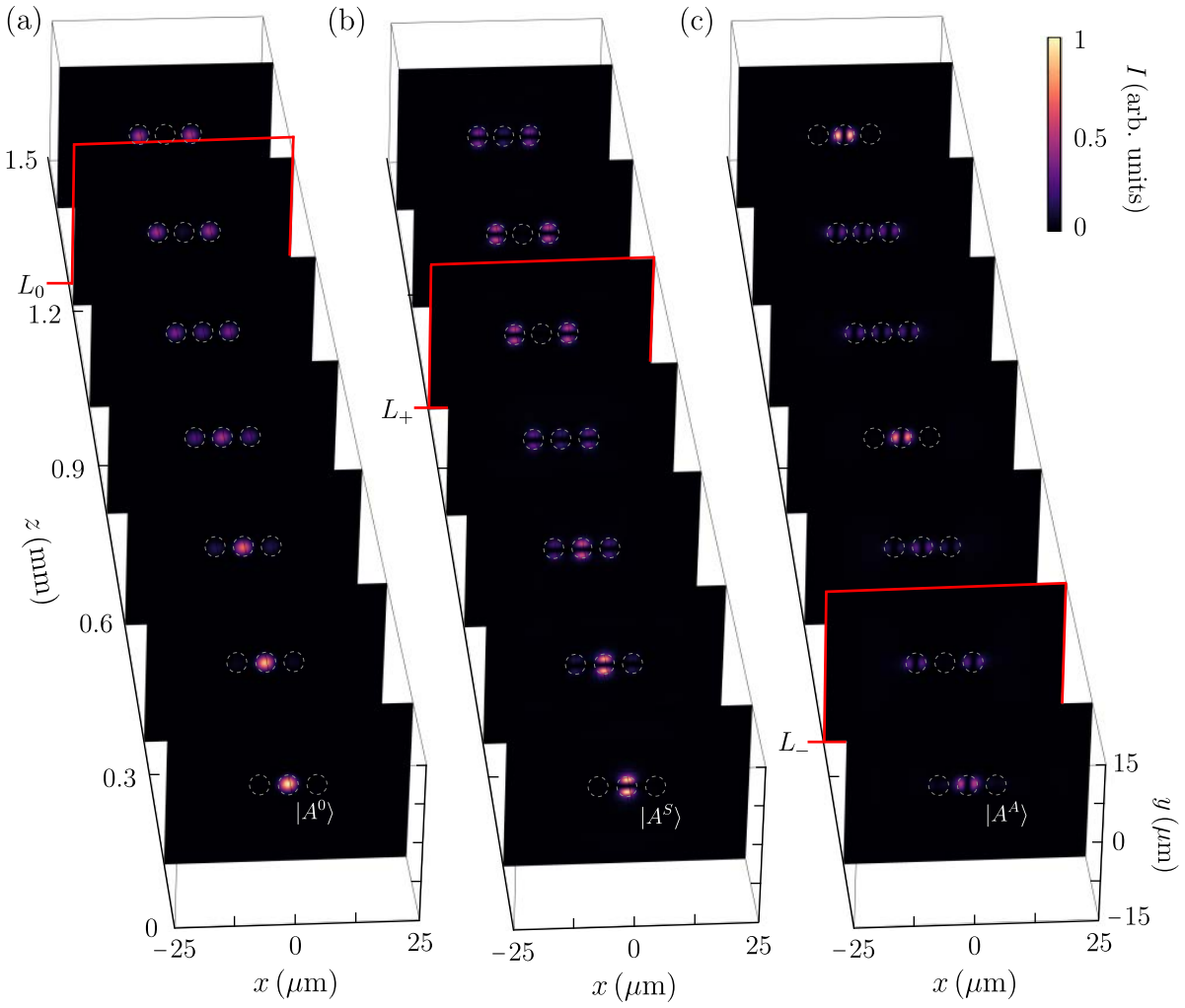

Figure 7.2: Numerically simulated light evolution along the propagation direction when we inject (a) the $|A^0\rangle$ mode, (b) the symmetric $|A_S\rangle = (|A^+\rangle + |A^-\rangle)/\sqrt{2}$ supermode and (c) the antisymmetric $|A_A\rangle = (|A^+\rangle - |A^-\rangle)/\sqrt{2}$ supermode, in central site A. The parameters used in the simulations are $n_{\text{core}} = 1.548$, $n_{\text{clad}} = 1.540$, waveguide radius $R = 1.9\,\mu$m, separation $d = 5.5\,\mu$m and wavelength $\lambda_0 = 700\,$nm.

respectively, with coupling strengths

$$c_S = \sqrt{2}(c_1 + c_2) \quad \text{and} \quad c_A = \sqrt{2}|c_1 - c_2|. \tag{7.9}$$

Therefore, by injecting the symmetric and antisymmetric supermodes in waveguide A, one can measure the beating lengths

$$L_S = \frac{\pi}{2c_S} \quad \text{and} \quad L_A = \frac{\pi}{2c_A}, \tag{7.10}$$

as it can be observed in Figs. 7.2(b) and (c), respectively. By repeating these measurements for different separation between waveguides, one can extract the coupling strengths c_1 and c_2, see circles and squares in Fig. 7.3(a), respectively, obtaining $K_1 = 19.39\,\mathrm{mm}^{-1}$, $\kappa_1 = 0.52\,\mu\mathrm{m}^{-1}$, $K_2 = 56.25\,\mathrm{mm}^{-1}$ and $\kappa_2 = 0.59\,\mu\mathrm{m}^{-1}$. Note that, the fact that $|c_2| > |c_1|$ can be intuitively understood by realizing that the phases between modes propagating with opposite (equal) circulations flow in the same (opposite) direction at the region between waveguides where the overlap between modes occurs [400]. Moreover, once $c_1(d)$ and $c_2(d)$ are known, the ratio $c_2(d)/c_1(d)$, which is a fundamental parameter to understand the flattening of the dispersive energy bands and the associated AB caging phenomena, can be computed, as it is represented in Fig. 7.3(b).

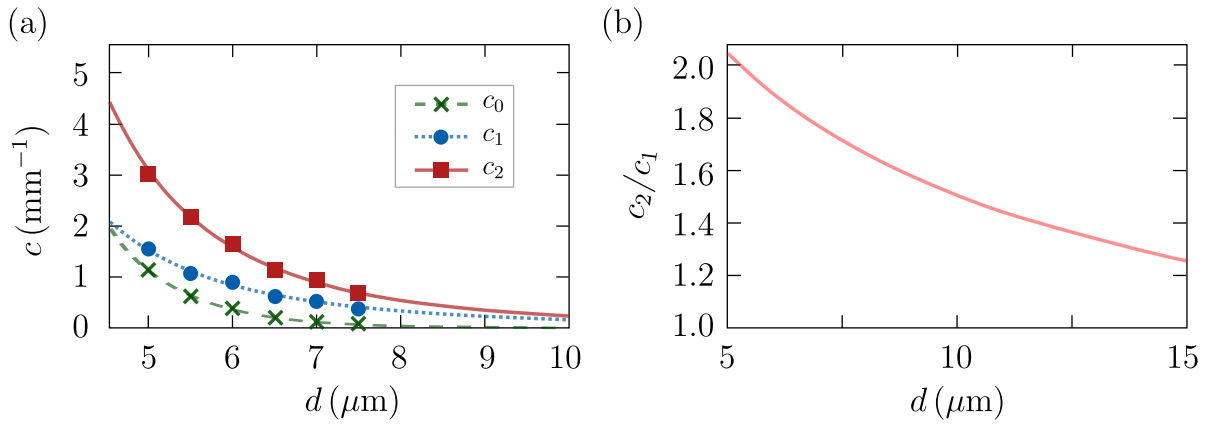

Figure 7.3: (a) Numerically calculated coupling strengths for separation $d = 5,\ 5.5,\ 6,\ 6.5,\ 7$ and $7.5\,\mu\mathrm{m}$ using $\lambda_0 = 700\,\mathrm{nm}$. In particular, c_0 (crosses) accounts for the coupling between $\ell = 0$ modes, and c_1 (circles) and c_2 (squares) account for the coupling between $\ell = 1$ modes with equal or opposite circulations, respectively. The dashed, dotted and solid lines correspond to the exponential fitting of $c_0(d) \approx K_0 \exp(-\kappa_0 d)$, $c_1(d) \approx K_1 \exp(-\kappa_1 d)$ and $c_2(d) \approx K_2 \exp(-\kappa_2 d)$, respectively, where $K_0 = 387\,\mathrm{mm}^{-1}$, $\kappa_0 = 1.17\,\mu\mathrm{m}^{-1}$, $K_1 = 19.39\,\mathrm{mm}^{-1}$, $\kappa_1 = 0.52\,\mu\mathrm{m}^{-1}$, $K_2 = 56.25\,\mathrm{mm}^{-1}$ and $\kappa_2 = 0.59\,\mu\mathrm{m}^{-1}$. (b) Numerically calculated c_2/c_1 with respect to the separation d using the exponential fits calculated in (a).

7.2.2 Band-structure

After the coupling characterization, we consider again the entire diamond-chain lattice represented in Fig. 7.1(a), specifically, with a central angle $\theta = \pi/2$. Assuming periodic boundary conditions, the momentum space Hamiltonian $\mathcal{H}_0(k)$ for $\ell = 0$ modes reads

$$\mathcal{H}_0 = c_0 \begin{pmatrix} 0 & 1+e^{-ik} & e^{-ik} \\ 1+e^{ik} & 0 & 0 \\ e^{ik} & 0 & 0 \end{pmatrix}, \tag{7.11}$$

whose eigenvalues corresponding to the energy bands of the bulk are given by [390]

$$E_0^0(k) = 0, \tag{7.12}$$

$$E_+^0(k) = 2c_0\sqrt{1+\cos(k\sqrt{2}d)}, \tag{7.13}$$

$$E_-^0(k) = -2c_0\sqrt{1+\cos(k\sqrt{2}d)}, \tag{7.14}$$

where k is the quasi-momentum and $\sqrt{2}d$ is the lattice constant. Therefore, the band structure consists of one zero-energy flat band, represented by the red solid line in Fig. 7.4(a), and two dispersive bands, represented by the green dotted lines in Fig. 7.4(a). On the other hand, the momentum space Hamiltonian $\mathcal{H}_1(k)$ for $\ell = 1$ is given by

$$\begin{pmatrix} 0 & 0 & c_1(1+e^{-ik}) & c_2(-1+e^{-ik}) & c_1(1+e^{-ik}) & c_2(1-e^{-ik}) \\ 0 & 0 & c_2(-1+e^{-ik}) & c_1(1+e^{-ik}) & c_2(1-e^{-ik}) & c_1(1+e^{-ik}) \\ c_1(1+e^{ik}) & c_2(-1+e^{ik}) & 0 & 0 & 0 & 0 \\ c_2(-1+e^{ik}) & c_1(1+e^{ik}) & 0 & 0 & 0 & 0 \\ c_1(1+e^{ik}) & c_2(1-e^{ik}) & 0 & 0 & 0 & 0 \\ c_2(1-e^{ik}) & c_1(1+e^{ik}) & 0 & 0 & 0 & 0 \end{pmatrix}. \tag{7.15}$$

Note that $\mathcal{H}_1(k)$ possesses chiral symmetry i.e., $\Gamma\mathcal{H}_1\Gamma^\dagger = -\mathcal{H}_1$, where Γ is an unitary and Hermitian operator [195]. For $\ell = 1$, the band structure is composed of six energy bands i.e., three bands with a two-fold degeneracy (positive and negative circulations), given by [195]

$$E_0^1(k) = 0, \tag{7.16}$$

$$E_+^1(k) = 2\sqrt{(c_1^2+c_2^2)+(c_1^2-c_2^2)\cos(k\sqrt{2}d)}, \tag{7.17}$$

$$E_-^1(k) = -2\sqrt{(c_1^2+c_2^2)+(c_1^2-c_2^2)\cos(k\sqrt{2}d)}, \tag{7.18}$$

Thus, the band structure consists of two zero-energy flat bands, represented by the red solid line in Fig. 7.4(b), and four dispersive bands, represented by the blue dashed lines in Fig. 7.4(b).

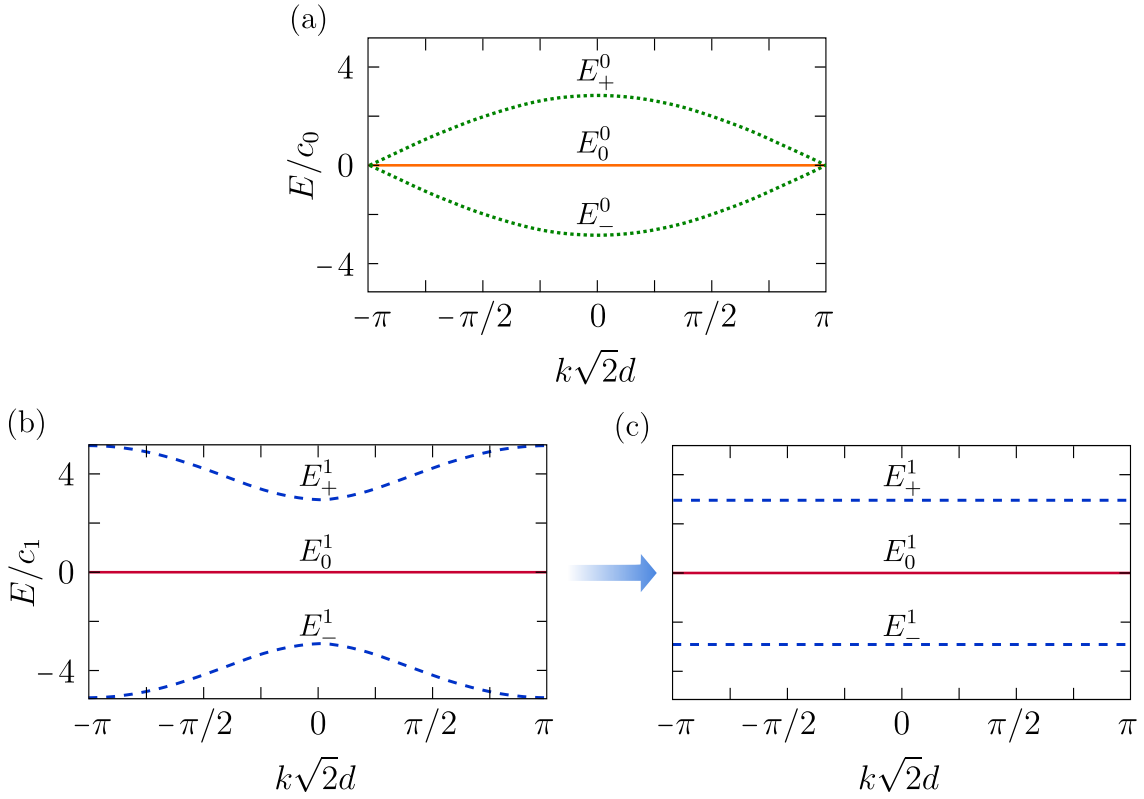

Figure 7.4: Band structure of the diamond-chain lattice for (a) $\ell = 0$, consisting of two dispersive bands $E^0_-(k)$ and $E^0_+(k)$ (green dotted lines) and one zero-energy flat band $E^0_0(k)$ (orange solid line), and $\ell = 1$ when (b) $c_2/c_1 = 2$ and (c) $c_2/c_1 = 1.25$. In (b) and (c) each band has a two-fold degeneracy, i.e., $E^1_-(k) \equiv E_1(k) = E_2(k)$ (blue dashed line), $E^1_0 \equiv E_3(k) = E_4(k)$ (red solid line) and $E^1_+(k) \equiv E_5(k) = E_6(k)$ (dashed line).

The main difference between the energy bands in both cases is the existence of an energy gap for $\ell = 1$, which is absent for $\ell = 0$, indicating the presence of a flux throughout the plaquettes of the lattice for $\ell = 1$. Moreover, while the zero-energy band $E^1_0(k)$ is flat regardless of the values of c_1 and c_2, the non-zero energy bands flatten $E^1_\pm \to \pm 2\sqrt{2}c_1$ in the $c_2/c_1 \to 1$ limit, as it is represented in Fig. 7.4(c). Note that, as it can be seen in Fig. 7.3(b), this limit can be achieved for large separation d between waveguides. Moreover, the supermodes associated to the non-zero energy flat bands are localized in A_j, B_j, B_{j+1}, C_j and C_{j+1} waveguides, hence, if one excites A_j with a $\ell = 1$ mode, the injected intensity will oscillate between the central and the four surrounding waveguides producing the AB caging effect. To properly understand the gap opening due to the presence of a π-flux as well as to derive the supermodes associated to the non-zero energy flat bands, some basis rotations have to be performed [195].

Basis rotations for $\ell = 1$ modes

Let us consider the diamond chain for the $\ell = 1$ manifold with coupling strengths c_1, c_2 and $-c_2$, represented by the black solid, blue dashed and red dotted arrows in Fig. 7.5(a), respectively. By performing the following basis rotation [195]

$$|D_j^{\pm}\rangle = \frac{1}{\sqrt{2}}\left(|C_j^{+}\rangle \pm |B_j^{+}\rangle\right) \quad \text{and} \quad |F_j^{\pm}\rangle = \frac{1}{\sqrt{2}}\left(|C_j^{-}\rangle \pm |B_j^{-}\rangle\right), \tag{7.19}$$

the original chain with two OAM modes (positive and negative circulations) per waveguide splits into two identical and decoupled sub-chains, depicted in Figs. 7.5(b) and (c), which sustain one mode per waveguide and with a π-flux throughout the plaquettes.

In the sub-chain of Fig. 7.5(b) (Fig. 7.5(c)), $|D_j^{+}\rangle$ and $|F_j^{-}\rangle$ ($|D_j^{-}\rangle$ and $|F_j^{+}\rangle$) are coupled to the $|A_j^{+}\rangle$ ($|A_j^{-}\rangle$) with coupling strengths $\sqrt{2}c_1$, $\sqrt{2}c_2$ and $-\sqrt{2}c_2$, as it is represented by the black solid, blue dashed and red dotted arrows, respectively. This basis rotation breaks the degeneracy of the energy bands of the original lattice and allows to understand the gap opening due to the existence of a π-flux in the plaquettes. Moreover, in order to get more insight into the topology of the system and the origin of the non-zero energy flat-bands, we perform a second basis rotation [195]

$$|G_j^{+}\rangle = \frac{1}{\sqrt{c_1^2 + c_2^2}}\left(c_1|D_j^{+}\rangle + c_2|F_j^{-}\rangle\right), \tag{7.20}$$

$$|G_j^{-}\rangle = \frac{1}{\sqrt{c_1^2 + c_2^2}}\left(c_2|D_j^{+}\rangle - c_1|F_j^{-}\rangle\right). \tag{7.21}$$

By doing so, the sub-chain of Fig. 7.5(b) can be mapped into a modified SSH chain with alternating strong ($\Omega_1 \equiv \sqrt{2}\sqrt{c_1^2 + c_2^2}$) and weak ($\Omega_3 \equiv \sqrt{2}(c_1^2 + c_2^2)/\sqrt{c_1^2 + c_2^2}$) couplings, and extra dangling states coupled by $\Omega_2 \equiv 2\sqrt{2}c_1c_2/\sqrt{c_1^2 + c_2^2}$, as represented by the green solid, purple dashed and orange dotted arrows in Fig. 7.5(d), respectively. In the $c_2/c_1 \to 1$ limit, $\Omega_3 \to 0$ and the chain is decoupled into trimers whose (non-zero energy) eigenmodes read

$$|E_{j,1}^{\pm}\rangle = \frac{1}{2}\left(|G_j^{+}\rangle \pm \sqrt{2}|A_j^{+}\rangle + |G_{j+1}^{-}\rangle\right). \tag{7.22}$$

Specifically, $|E_{j,1}^{\pm}\rangle$ can be rewritten in the original basis as

$$\begin{aligned} |E_{j,1}^{\pm}\rangle &= \frac{1}{2}\left(|C_j^{+}\rangle + |B_j^{+}\rangle + |C_{j+1}^{+}\rangle + |B_{j+1}^{+}\rangle\right) \\ &+ \frac{1}{2}\left(|C_j^{-}\rangle - |B_j^{-}\rangle - |C_{j+1}^{-}\rangle + |B_{j+1}^{-}\rangle\right) \pm \frac{1}{\sqrt{2}}|A_j^{+}\rangle. \end{aligned} \tag{7.23}$$

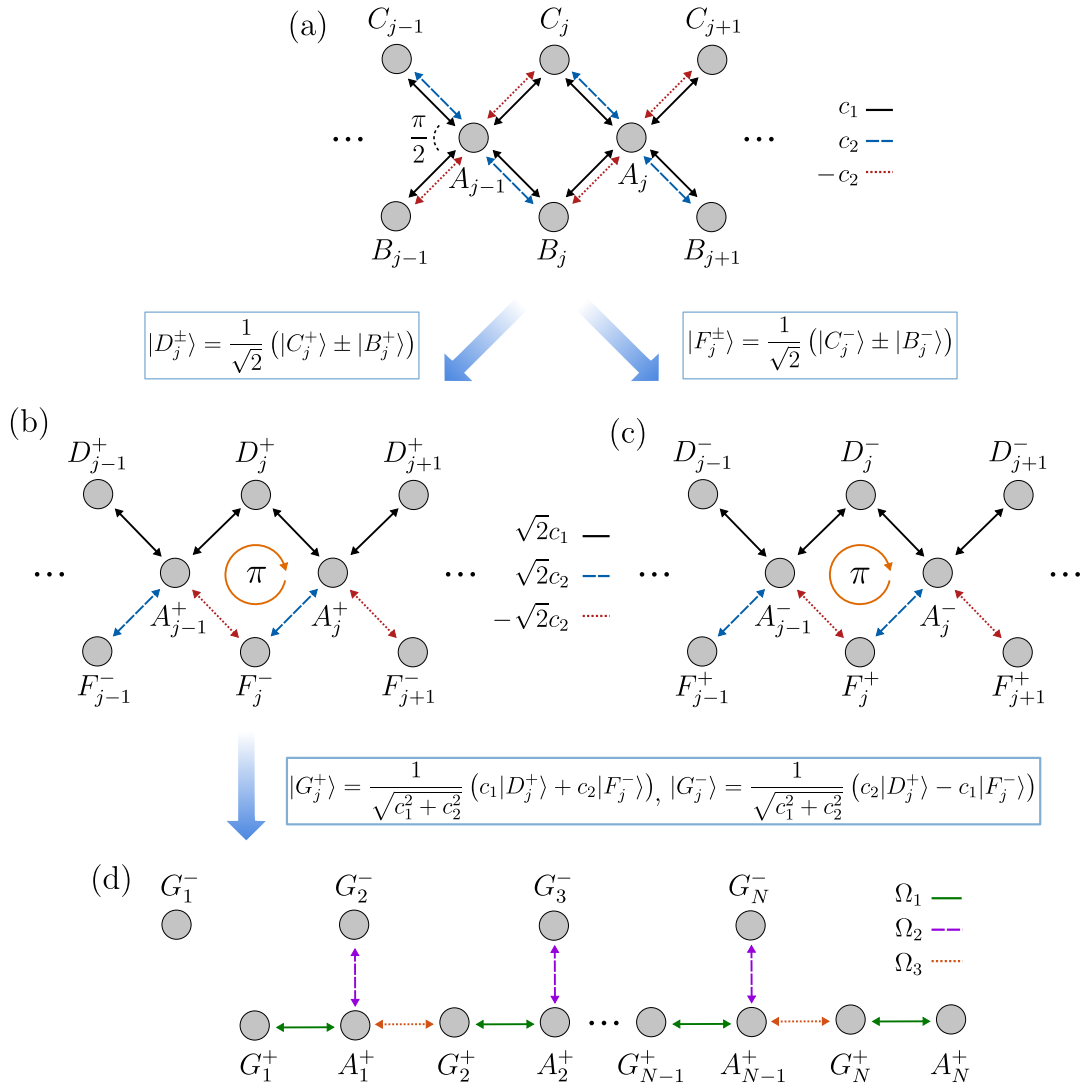

Figure 7.5: (a) Schematic representation of the photonic lattice arranged in a diamond chain configuration with central angle $\theta = \pi/2$, supporting two $\ell = 1$ modes per waveguide. The coupling amplitudes between modes with equal and opposite circulations are given by $c_{1,1} = c_1$ and $c_{1,-1} = \pm c_2$, respectively. Specifically, c_1, c_2 and $-c_2$ are represented by the black solid, blue dashed and red dotted arrows, respectively. (b)-(c) Schematic representation of the decoupled diamond chain lattices obtained performing a basis rotation into $|D_j^{\pm}\rangle$ and $|F_j^{\pm}\rangle$. In this new basis there is only one mode per waveguide and a π-flux is present in the plaquettes. The coupling amplitudes $\sqrt{2}c_1$, $\sqrt{2}c_2$ and $-\sqrt{2}c_2$ are represented by the black solid, blue dashed and red dotted arrows, respectively. (d) Schematic representation of the modified SSH chain obtained performing a second basis rotation for the positive circulation sub-chain. The coupling amplitudes $\Omega_1 \equiv \sqrt{2}\sqrt{c_1^2 + c_2^2}$, $\Omega_2 \equiv 2\sqrt{2}c_1c_2/\sqrt{c_1^2 + c_2^2}$ and $\Omega_3 \equiv \sqrt{2}(c_1^2 + c_2^2)/\sqrt{c_1^2 + c_2^2}$ are represented by the green solid, purple dashed and orange dotted arrows, respectively.

Note that an analogous derivation can be performed for the sub-chain of Fig. 7.5(c) by substituting F_j by D_j in Eqs. (7.20) and (7.21), which leads to $|E^{\pm}_{j,2}\rangle$ given by Eq. (7.23) with exchanged circulations i.e., $+ \leftrightarrow -$. These non-zero energy flat-band supermodes are localized in the j and $j+1$ unit cells and can be rewritten as

$$|A^{+}_{j}\rangle = \frac{1}{\sqrt{2}}\left(|E^{+}_{j,1}\rangle - |E^{-}_{j,1}\rangle\right) \quad \text{and} \quad |A^{-}_{j}\rangle = \frac{1}{\sqrt{2}}\left(|E^{+}_{j,2}\rangle - |E^{-}_{j,2}\rangle\right), \tag{7.24}$$

respectively. Therefore, since $|A^{+}_{j}\rangle$ and $|A^{-}_{j}\rangle$ belong to different decoupled sub-chains, any superposition of $\ell = 1$ OAM modes with positive and negative circulations injected in A_j is trapped in the cage formed by $A_j, B_j, C_j, B_{j+1}, C_{j+1}$ as it evolves along the propagation direction, producing the AB caging effect.

7.2.3 Light dynamics

For the evanescently-coupled waveguides with a small refractive index contrast here employed, the spin-orbit interaction can be neglected [368, 401]. Therefore, as discussed in detail in Section 2.3 of Chapter 2, light dynamics along the z direction can be described by coupled-mode equations of the form

$$i\frac{d}{dz}\boldsymbol{\psi} = \mathcal{H}\boldsymbol{\psi}. \tag{7.25}$$

where $\boldsymbol{\psi} = (\tilde{c}^{\pm\ell}_1, \tilde{a}^{\pm\ell}_1, \tilde{b}^{\pm\ell}_1, \ldots, \tilde{c}^{\pm\ell}_N, \tilde{a}^{\pm\ell}_N, \tilde{b}^{\pm\ell}_N,)^T$, with $\tilde{a}^{\pm\ell}_j$, $\tilde{b}^{\pm\ell}_1$ and $\tilde{c}^{\pm\ell}_1$ describing the complex field amplitude of mode ℓ with positive or negative circulation in waveguides A_j, B_j and C_j, respectively, and $\mathcal{H}$ is the Hamiltonian of the system. In particular, for $\ell = 0$, coupled-mode equations can be decomposed as

$$i\frac{d\tilde{a}^{0}_{j}}{dz} = \beta^{0}_{A_j}\tilde{a}^{0}_{j} + c_0\left(\tilde{b}^{0}_{j} + \tilde{b}^{0}_{j+1} + \tilde{c}^{0}_{j} + \tilde{c}^{0}_{j+1}\right), \tag{7.26}$$

$$i\frac{d\tilde{b}^{0}_{j}}{dz} = \beta^{0}_{B_j}\tilde{b}^{0}_{j} + c_0\left(\tilde{a}^{0}_{j} + \tilde{a}^{0}_{j+1}\right), \tag{7.27}$$

$$i\frac{d\tilde{c}^{0}_{j}}{dz} = \beta^{0}_{C_j}\tilde{c}^{0}_{j} + c_0\left(\tilde{a}^{0}_{j} + \tilde{a}^{0}_{j+1}\right). \tag{7.28}$$

On the other hand, coupled-mode equations for $\ell = 1$ can be decomposed as

$$i\frac{d\tilde{a}^{\pm}_{j}}{dz} = \beta^{1}_{A_j}\tilde{a}^{\pm}_{j} + c_1\left(\tilde{b}^{\pm}_{j} + \tilde{b}^{\pm}_{j+1} + \tilde{c}^{\pm}_{j} + \tilde{c}^{\pm}_{j+1}\right) + c_2\left(\tilde{b}^{\mp}_{j+1} - \tilde{b}^{\mp}_{j} + \tilde{c}^{\mp}_{j} - \tilde{c}^{\mp}_{j+1}\right), \tag{7.29}$$

$$i\frac{d\tilde{b}^{\pm}_{j}}{dz} = \beta^{1}_{B_j}\tilde{b}^{\pm}_{j} + c_1\left(\tilde{a}^{\pm}_{j} + \tilde{a}^{\pm}_{j+1}\right) + c_2\left(\tilde{a}^{\mp}_{j+1} - \tilde{a}^{\mp}_{j}\right), \tag{7.30}$$

$$i\frac{d\tilde{c}^{\pm}_{j}}{dz} = \beta^{1}_{C_j}\tilde{c}^{\pm}_{j} + c_1\left(\tilde{a}^{\pm}_{j} + \tilde{a}^{\pm}_{j+1}\right) + c_2\left(\tilde{a}^{\mp}_{j} - \tilde{a}^{\mp}_{j+1}\right). \tag{7.31}$$

Nearest neighbor vs. Next-nearest neighbor couplings for $\ell = 1$ modes

The nearest neighbor (NN) couplings occur between $A_j \leftrightarrow B_j$, $A_j \leftrightarrow B_{j+1}$, $A_j \leftrightarrow C_j$ and $A_j \leftrightarrow C_{j+1}$, as it is illustrated in Fig. 7.6(a), while the next-nearest neighbor (NNN) couplings occur between $A_j \leftrightarrow A_{j\pm1}$, $B_j \leftrightarrow B_{j\pm1}$, $C_j \leftrightarrow C_{j\pm1}$ and $B_j \leftrightarrow C_j$ as it is illustrated in Fig. 7.6(b). Moreover, although the coupling strengths c_1 and c_2 between NN waveguides has the dependence of the separation between waveguides, d, illustrated in Fig. 7.3(a) of the main text, the coupling strengths $\tilde{c}_1$ and $\tilde{c}_2$ between NNN waveguides cannot be directly retrieved from the values corresponding to their separation $\sqrt{2}d$ in Fig. 7.3(a). The reason is that the NN waveguide laying between the NNN waveguides has to be taken into account when calculating the overlap integral between the modes, reducing the effective NNN coupling strengths [398], which are ~ 10 times weaker than the NN ones. Therefore, the NNN couplings can be safely neglected. This fact can be easily verified by comparing the light dynamics described by the coupled-mode (CM) equations (7.29)-(7.31) considering only NN couplings (see Fig. 7.7(a)) or also including NNN couplings (see Fig. 7.7(b)), with the numerical simulations performed using finite-difference methods (FDM) that take into account all the possible couplings. We can observe in Fig. 7.7 how NN couplings already give a good approximation of light dynamics, validating our assumption.

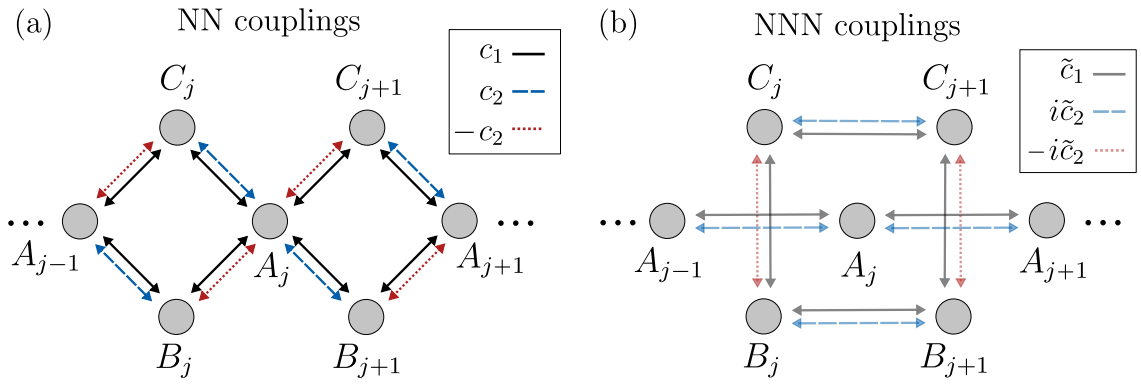

Figure 7.6: Schematic representation of the (a) nearest-neighbor (NN) couplings between $\ell = 1$ modes with equal $c_{1,1} = c_1$ and opposite $c_{1,-1} = \pm c_2$ circulations, represented by the black solid, blue dashed and red dotted arrows, respectively, and (b) Next-Nearest Neighbor (NNN) couplings between $\ell = 1$ modes with equal $\tilde{c}_{1,1} = \tilde{c}_1$ and opposite $\tilde{c}_{1,-1} = \pm\tilde{c}_2$ circulations, represented by the light black solid, light blue dashed and light red dotted arrows, respectively.

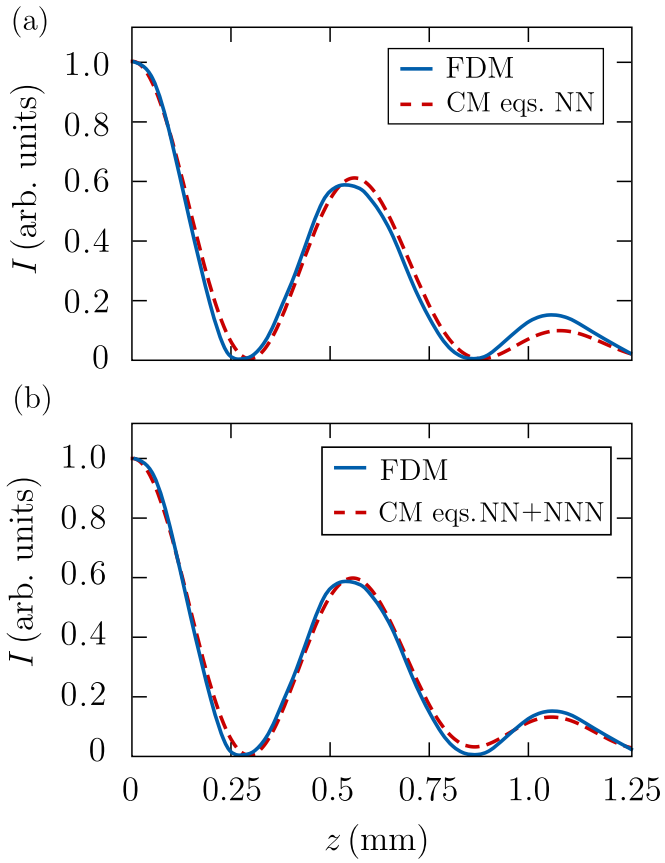

Figure 7.7: Numerically calculated intensity propagating in waveguide A_j when the $\ell = 1$ mode is injected in waveguide A_j. The blue solid lines correspond to the full numerical simulations performed using finite difference method (FDM) calculations that take into account all the real couplings while the red dashed lines correspond to the coupled-mode (CM) equations considering (a) NN couplings, (b) NN and NNN couplings. All the simulations were performed using $d = 5.3\,\mu$m, $R = 1.9\,\mu$m, $n_{\text{core}} = 1.548$, $n_{\text{clad}} = 1.540$ and $\lambda_0 = 700\,$nm.

7.2.4 Robustness of the Aharonov-Bohm caging effect

To test the robustness of the AB caging effect, we have numerically analyzed the deviations induced by changes in the separation between waveguides, d and the refractive index contrast $\Delta n = n_{\text{core}} - n_{\text{clad}}$. Specifically, we have analyzed (i) uniform deviations and (ii) random deviations, of the distances and the refractive index contrast.

Uniform deviations

Small deviations in the separation between waveguides induce small changes in the positions and values of the minima and maxima of the caging. For instance, if the separation between waveguide centers varies by $\Delta d = \pm 0.2\,\mu$m as considered in Fig. 7.8(a), the position of the first maximum z_1 is displaced by $\Delta z_1 = \pm 0.04\,$mm and its value, I_1, changes by $\Delta I_1 = \pm 0.03$. The reason why the effect is robust against these variations relies on the fact that c_2/c_1 only changes by ± 0.05, and thereby, the band structure remains almost unaltered. Moreover, uniform variations in the refractive index contrast have a similar effect and the AB caging effect remains robust. In particular, we can observe in Fig. 7.8(b) how for $\Delta n = \pm 0.001$ deviations, the first maximum is displaced by $\Delta z_1 = \pm 0.05\,$mm and its value changes by $\Delta I_1 = \pm 0.09$. Note that, the larger decrease for $n_{\text{core}} = 1.547$ occurs because $\beta_1/k_0 \approx k_0 n_{\text{clad}}$, inducing losses as the mode is only weakly-bound to the waveguide.

Random deviations

Small random deviations of the distances between waveguides induce similar changes in the positions and values of the maxima than uniform deviations. In particular, as illustrated in Fig. 7.8(c), for an average of five different random deviations $d_j \pm 0.2\,\mu$m in the x- and y- directions, the position of the first maximum z_1 is displaced by $\Delta z_1 = \pm 0.03\,$mm and its peak value, I_1, changes by $\Delta I_1 = \pm 0.03$. Therefore, the effect is still robust against random Δd variations. Instead, the effect is no longer robust against random Δn_j variations because it implies different mode propagation constants between different waveguides, decreasing the coupling between modes. In particular, as illustrated in Fig. 7.8(d), we can see how for an average of five different random deviations $n_{\text{core},j} \pm 0.001$, the first maximum displaces its position z_1 by a similar value than before, $\Delta z_1 = \pm 0.04\,$mm, and its value I_1 changes by $\Delta I_1 = \pm 0.1$. However, one can observe how after the first peak one does not reach the zero minimum due to the detuning between waveguides and the second oscillation is clearly different from the case without disorder. For this reason, we restrict our experimental observations to the central waveguides (A_3 and A_4) where the deviations in the index contrast due to fabrication are the lowest.

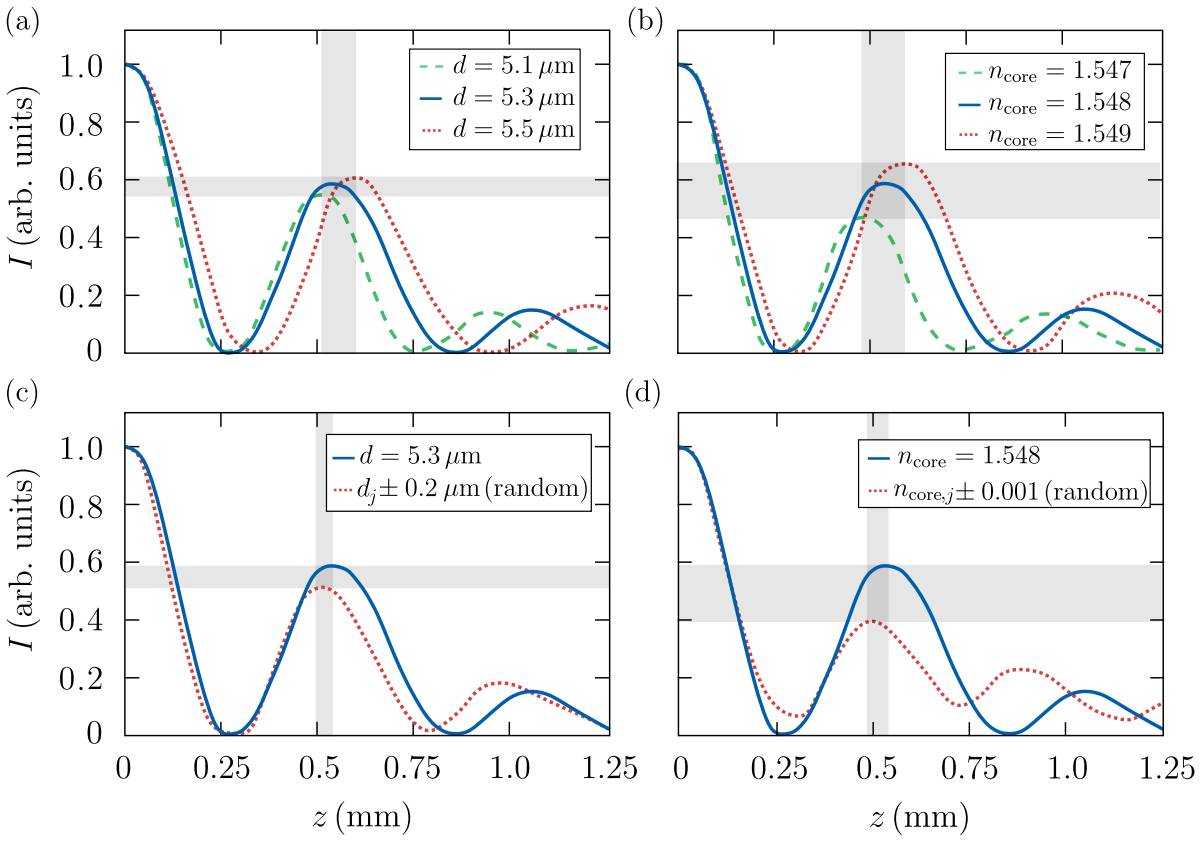

Figure 7.8: Numerically calculated intensity propagating in waveguide A_4 using finite-difference methods for (a) $d = 5.1\,\mu$m (green dashed line), $d = 5.3\,\mu$m (blue solid line) and $d = 5.5\,\mu$m (red dotted line) and $n_{\text{core}} = 1.548$, (b) $n_{\text{core}} = 1.547$ (green dashed line), $n_{\text{core}} = 1.548$ (blue solid line) and $n_{\text{core}} = 1.549$ (red dotted line) and $d = 5.3\,\mu$m, (c) $d = 5.3\,\mu$m (blue solid line) and an average of five random variations of $d_j \pm 0.2\,\mu$m (red dotted line) and $n_{\text{core}} = 1.548$, (d) $n_{\text{core}} = 1.548$ (blue solid line) and an average of five random variations of $n_{\text{core},j} \pm 0.001$ (red dotted line) and $d = 5.3\,\mu$m. The rest of the parameters are $R = 1.9\,\mu$m, $n_{\text{clad}} = 1.540$ and $\lambda_0 = 700\,$nm. The vertical shaded regions indicate the deviation with respect to the position of the first maximum Δz_1 and the horizontal shaded regions the deviation of its value ΔI_1.

7.3 Experimental verification

7.3.1 Sample fabrication

To experimentally demonstrate the generation of AGF in photonic lattices by changing the input state, we fabricate several samples of direct laser written optical waveguides [187] inscribed using a commercial Nanoscribe system and the photo-resist IP-Dip, as it is represented in Fig. 7.9(a). In particular, the waveguides have a radius of $R = 1.9\,\mu$m, a refractive index contrast of $\Delta n = n_{\text{core}} - n_{\text{clad}} \approx 0.008$ obtained by writing with more laser power the core (60%) than the cladding (35%) [402], with center-to-center distance of $d = 5.5\,\mu$m and a total number of $N = 7$ unit cells, as it is shown in Fig. 7.9(b). Moreover, in order to be able to observe light evolution along the propagation direction, we fabricate samples with different total lengths corresponding to $z = 250$, 500, 750 and $1000\,\mu$m, from which we extract the output intensities.

During the writing process, the laser intensity towards the edges of the sample decreased due to vignetting of the writing objective lens. At the same time, the proximity effect [403] had less influence at the edges of the sample than in the center. Therefore, both processes led to a non-uniform refractive index profile of the sample, with higher index in the center and lower index at the edges [404]. As a result, the waveguides that were written with high laser power, were less prone to refractive index changes by vignetting and proximity effect than the material surrounding the waveguides. Therefore, the measurements were performed on the central waveguides (A_3 and A_4).

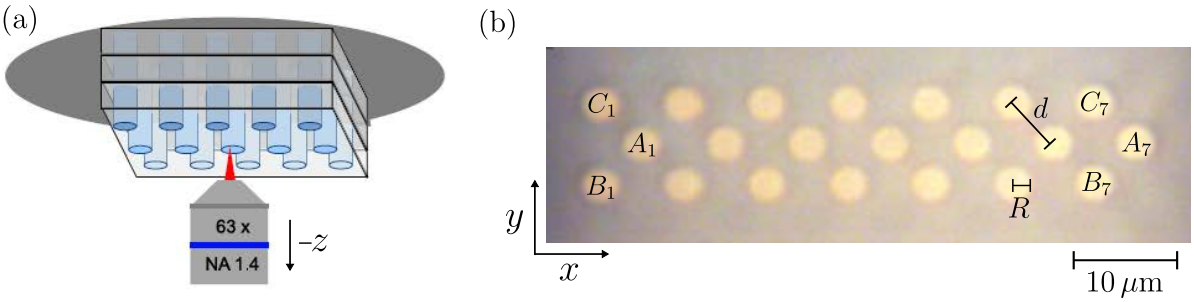

Figure 7.9: (a) Illustration of the waveguide laser writing process (image courtesy of C. Jörg). (b) Microscopy image of the waveguide lattice composed of waveguides with radius $R = 1.9\,\mu$m, center-to-center distance $d = 5.5\,\mu$m and $N = 7$ unit cells.

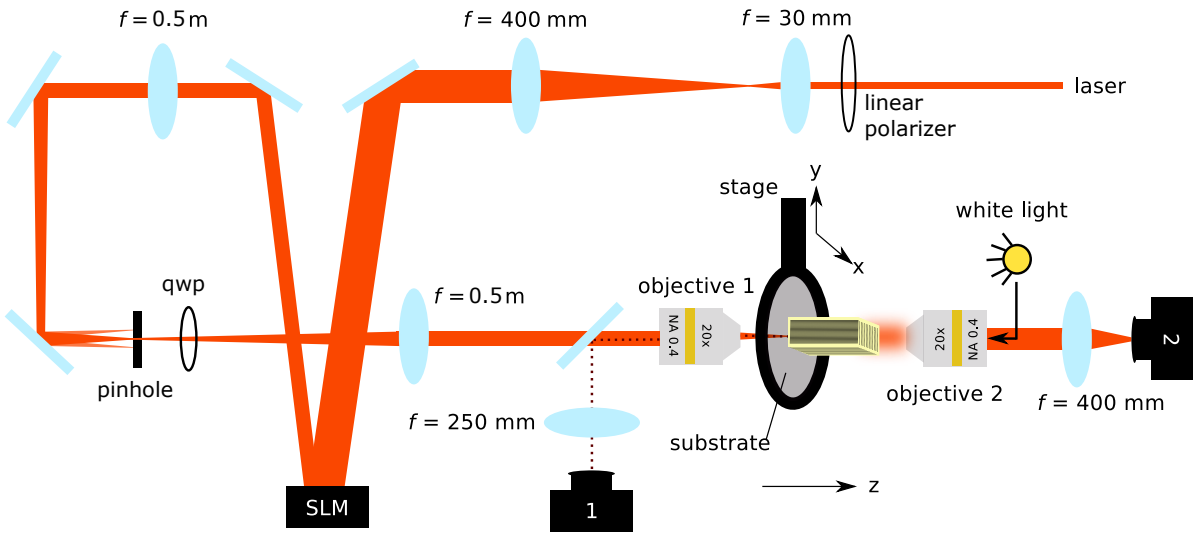

Figure 7.10: Laser light from a white light laser (NKT photonics) is sent through a VARIA filter box to select a wavelength of $\lambda_0 = 700\,\mathrm{nm}$. The beam is linearly polarized, expanded and sent onto a spatial light modulator (SLM). We load a hologram onto the SLM that consists of a phase-only vortex, with an added blazed grating to shift the pattern to the first diffraction order. Other orders are blocked by a pinhole. The beam is circularly polarized by a quarter wave-plate and imaged onto objective lens 1, which Fourier transforms the phase hologram to create a donut-shaped intensity profile with $\ell = 1$ and positive/negative circulations, or a Gaussian-shaped intensity profile with $\ell = 0$ and constant phase. The reflection of the input mode is imaged via a beamsplitter onto camera 1. Using white light from a common torch lamp allows to additionally image the sample input facet onto camera 1 at the same time, to overlap the input mode with the waveguide position. The sample can be moved in the x- and y-directions by linear actuators (Zaber, smallest realistic step size 100 nm). The output intensity at the sample output facet is imaged by objective lens 2 onto camera 2.

7.3.2 Experimental observation of Aharonov-Bohm caging

To experimentally demonstrate AB caging using OAM modes, we excite a central waveguide A_j using modes with $\ell = 0$ or $\ell = 1$ and compare the resulting dynamics. In particular, the modes are excited using a white light laser, which is sent through a filter to select the wavelength and onto an SLM, where an hologram consisting of a phase-only vortex is loaded to generate a donut-shaped intensity profile with $\ell = 1$ and positive/negative circulations or a Gaussian-shaped intensity profile with $\ell = 0$ and constant phase. The full measurement set-up is displayed in Fig. 7.10. First, we inject a mode with $\ell = 1$ and negative circulation in waveguide A_4 as it is displayed in Fig. 7.11(a). As expected from the AB caging effect, the injected mode spreads to the four surrounding waveguides at $z = 250\,\mu$m and recombines in the central waveguide at $z = 500\,\mu$m, as it can be seen in Figs. 7.11(b) and (c), respectively. This spreading and recombination effect occurs a second time at $z = 750\,\mu$m and $z = 1000\,\mu$m, as it can be seen in Figs. 7.11(d) and (e), respectively. Note that the input and output intensities were measured with camera 1 and 2 of Fig. 7.10, respectively. Besides, the recorded images were post processed to reduce noise by overlapping the pictures with a mask of the waveguide structure, separating the intensity within the waveguides and the surroundings and subtracting the noise level of the surrounding. Note that the experimental results are in agreement with finite differences method (FDM) simulations once a small correction in the separation distance of $\Delta d = d_{\text{exp}} - d_{\text{sim}} = 0.2\,\mu$m is introduced, as it is represented in Figs. 7.11(f)-(j). This difference Δd may be originated from slight variations of the position in the writing process ($\pm 0.05\,\mu$m) or/and small changes in the refractive index contrast. Even though we implement the model with $c_2/c_1 \approx 2$ due to experimental restrictions in the total size of the samples, we are able to measure two full oscillations of the AB caging effect. Nevertheless, since the dispersive bands are not totally flat, light propagates into waveguides A_3 and A_5 during the second oscillation and part of the intensity escapes from the cage, as it can be seen in Figs. 7.11(d) and (e).

Note that, the donut mode with positive or negative circulations injected in waveguide A_j is an eigenmode of the waveguide in isolation. Therefore, according to the tight-binding model, when these donut modes are injected in a waveguide A_j of the diamond-chain lattice they should always recombine to waveguide A_j in the same shape. However, one observes in Figs. 7.11(b)-(e) that although we try to excite the donut mode with a negative circulation (see the input beam in Fig. 7.11(a)), the propagating mode has a lobe-shaped intensity corresponding to a superposition of donut modes with positive and negative circulations. This lobe-shaped mode, which is a superposition of donut modes with positive and negative circulations, appears due to the nonsymmetric presence of the NNN waveguides and a slight ellipticity of the fabricated waveguides. In particular

considering perfectly cylindrical waveguides, we can observe how in the first recombination the mode still looks like a donut mode in the simulations (see Fig. 7.11(h)), rather than the lobe-shaped mode that seems to appear in the experiment (see Fig. 7.11(c)), while in the second recombination we obtain the lobe-shaped mode in both cases (see Fig. 7.11(e) and (j)).

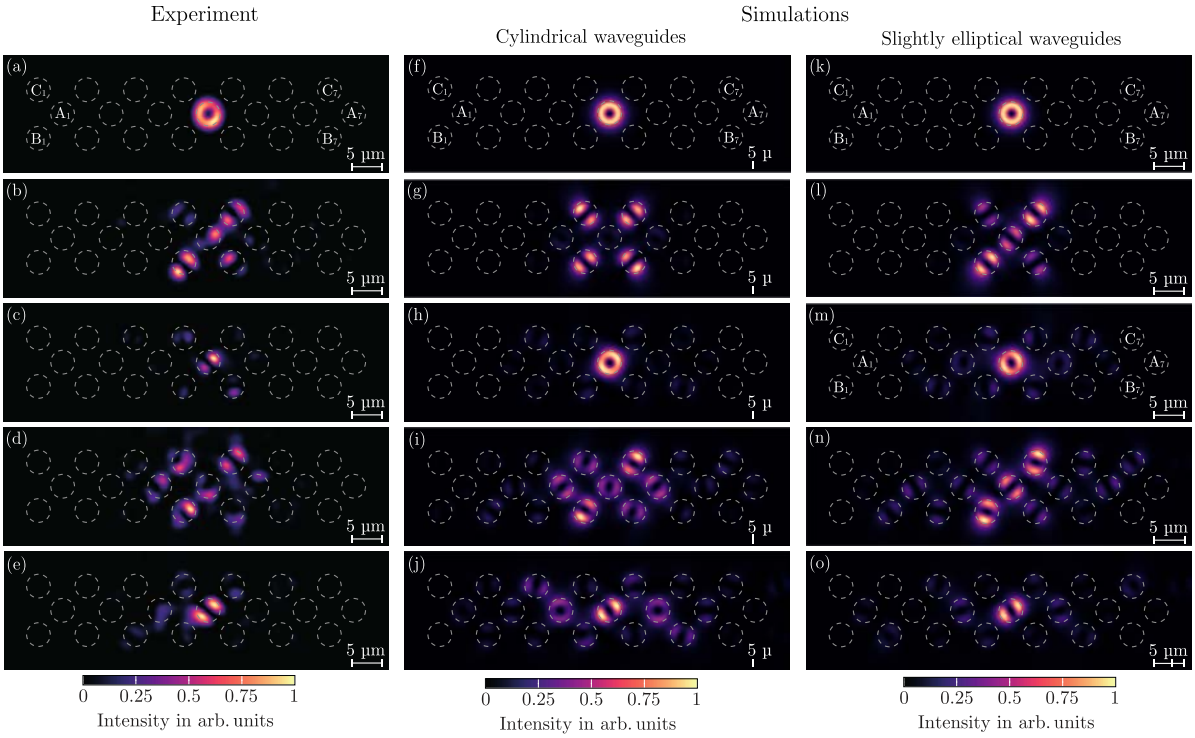

Figure 7.11: Experimentally observed input and output intensities, obtained by exciting waveguide A_4 using the OAM mode with $\ell = 1$ and negative circulation, at (a) $z = 0\,\mu$m, (b) $z = 250\,\mu$m, (c) $z = 500\,\mu$m, (d) $z = 750\,\mu$m and (e) $z = 1000\,\mu$m. Note that the image in (a) is taken before entering the sample. Input and output intensities numerically obtained considering cylindrical waveguides at (f) $z = 0\,\mu$m, (g) $z = 250\,\mu$m, (h) $z = 500\,\mu$m, (i) $z = 750\,\mu$m and (j) $z = 1000\,\mu$m, and considering slightly elliptical waveguides at (k) $z = 0\,\mu$m, (l) $z = 250\,\mu$m, (m) $z = 500\,\mu$m, (m) $z = 750\,\mu$m and (o) $z = 1000\,\mu$m. The lattice is composed of 7 unit cells, i.e., 21 waveguides with radius $R = 1.9\,\mu$m, nearest-neighbor separation $d_{\text{exp}} = 5.5\,\mu$m and $\lambda_0 = 700\,$nm. The experimental results are in agreement with the simulations once a small correction of $\Delta d = d_{\text{exp}} - d_{\text{sim}} = 0.2\,\mu$m is introduced. Moreover, in (k)-(o) the waveguides are slightly elliptical, i.e. the diameter of the waveguide is slightly bigger in the y- direction than in the x- direction by $\Delta R = 0.1\,\mu$m. The intensity distribution is normalized to the maximum intensity value of each figure to increase the visibility.

The changing from the donut mode into the lobe-shaped mode in the lattice is due to the non-symmetric presence of the NNN waveguides (they are present to the left and right of the chain, but not to the top and bottom), which slightly breaks the degeneracy of the modes. In addition, the faster appearance of the lobe-shaped mode in the experiment respect to the simulations is due to a slight ellipticity of the fabricated waveguides. This has been checked by sending a donut mode in a single waveguide without neighbors and observing that the mode is also transformed into a lobe-shaped mode, which rotates when rotating the sample. Introducing this ellipticity in the diamond-chain lattice, we can observe how the lobe-shaped mode is obtained faster Figs. 7.11(k)-(o), in better agreement with the experimental results of Figs. 7.11(a)-(e). Therefore, confirming that our experimental measurements are influenced by the slight ellipticity of the waveguides. Nevertheless, since the propagation of $\ell = 1$ modes with positive and negative circulations results in the same flux, the observed AB caging is

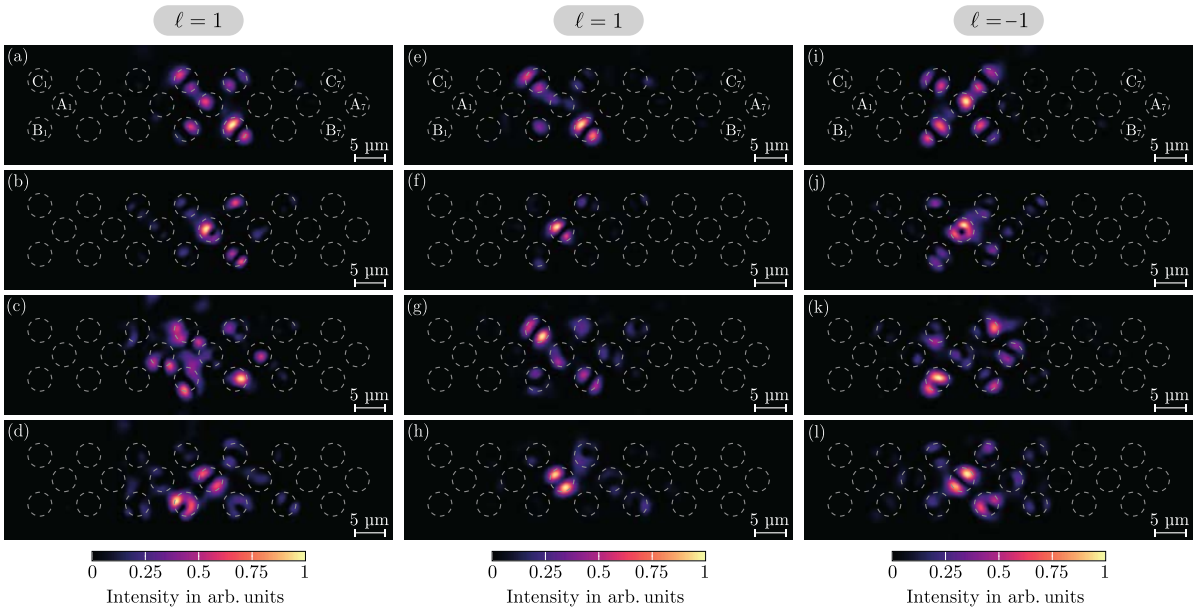

Figure 7.12: Experimentally observed output intensities, obtained by exciting (left column) waveguide A_4 using the OAM mode with $\ell = 1$ and positive circulation, at (a) $z = 250\,\mu$m, (b) $z = 500\,\mu$m, (c) $z = 750\,\mu$m and (d) $z = 1000\,\mu$m, (central column) waveguide A_3 using the OAM mode with $\ell = 1$ and positive circulation, at (e) $z = 250\,\mu$m, (f) $z = 500\,\mu$m, (g) $z = 750\,\mu$m and (h) $z = 1000\,\mu$m, (right column) waveguide A_3 using the OAM mode with $\ell = 1$ and negative circulation at (i) $z = 250\,\mu$m, (j) $z = 500\,\mu$m, (k) $z = 750\,\mu$m and (l) $z = 1000\,\mu$m. The lattice is composed of 7 unit cells, i.e., 21 waveguides with $R = 1.9\,\mu$m, $d_{\text{exp}} = 5.5\,\mu$m and $\lambda_0 = 700\,$nm. The intensity distribution is normalized to the maximum intensity value of each figure.

exactly the same for any superposition of both circulations i.e., a lobe-shaped mode [195]. In fact, if we keep exciting waveguide A_4 but changing to a positive circulation, see Fig. 7.12(a), or we excite waveguide A_3 with positive and negative circulations, see Figs. 7.12(b) and (c), respectively, the AB caging effect is still present. In contrast, when the $\ell = 0$ mode is injected in A_4, see Fig. 7.13(a), it just spreads transversely as

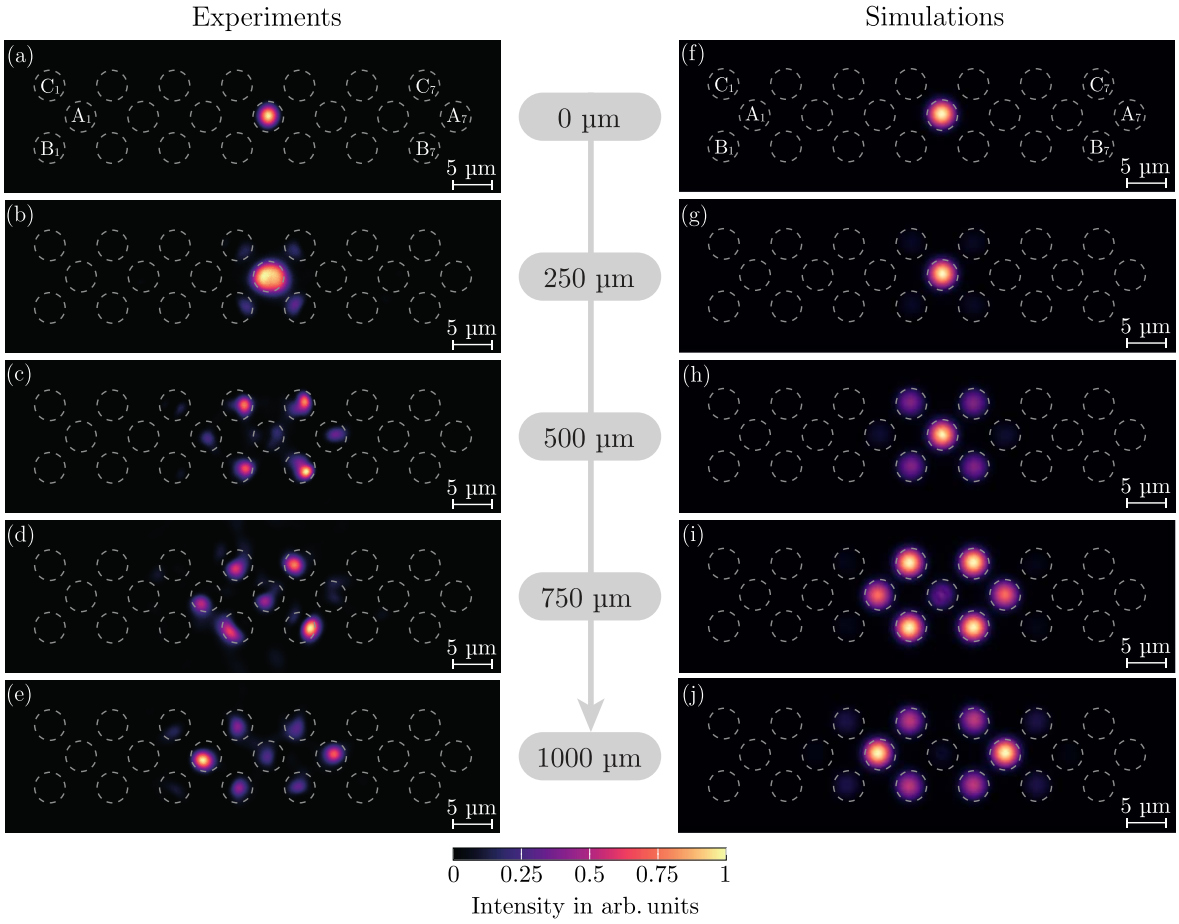

Figure 7.13: Input and output intensities experimentally measured by exciting the A_4 waveguide using the mode with $\ell = 0$ at (a) $z = 0\,\mu$m, (b) $z = 250\,\mu$m, (c) $z = 500\,\mu$m, (d) $z = 750\,\mu$m and (e) $z = 1000\,\mu$m. Note that the image in (a) is taken without the sample in the measurement set-up. Input and output intensities numerically obtained using FDM techniques at (f) $z = 0\,\mu$m, (g) $z = 250\,\mu$m, (h) $z = 500\,\mu$m, (i) $z = 750\,\mu$m and (j) $z = 1000\,\mu$m. The lattice is composed of 7 unit cells, i.e., 21 waveguides with $R = 1.9\,\mu$m, $d_{\text{exp}} = 5.5\,\mu$m and $\lambda_0 = 700\,$nm. The simulations have been made with $d_{\text{sim}} = 5.3\,\mu$m . The intensity distribution is normalized to the maximum intensity value of each figure.

it evolves along the propagation direction and no caging is observed in Figs. 7.13(a)-(e). As before, the experimental results propagating the $\ell = 0$ mode, with the same correction of $\Delta d = d_{\text{exp}} - d_{\text{sim}} = 0.2\,\mu$m, are in agreement with the numerical results shown in Figs. 7.13(f)-(j).

To compare the experimental observations with the numerical simulations in a quantitative way, we extract the intensities at the output ports by integrating over a circle that covers almost the whole mode at the position of each waveguide i.e., the circles are as big as possible such that they touch at the diagonals. In particular, the intensities extracted at the output port from the A_4 waveguide and its associated cage formed by A_4, B_4, C_4, B_5 and C_5 are shown in Fig. 7.14. On the one hand, in Fig. 7.14(a), one can observe how the experimentally measured maxima of intensity in A_4 associated to the caging phenomenon occur around $z = 500\,\mu$m and $z = 1000\,\mu$m, in agreement with FDM simulations. Besides, one can observe how the minima of the experimental results do not reach the zero value, remaining above 10% of the injected power, and the second maximum peak is slightly above the expected one. This fact may be due to small variations between waveguides leading to small variation between the propagation constants of the modes. On the other hand, in Fig. 7.14(b), one can observe the standard decay of the intensity in A_4 when the $\ell = 0$ mode is injected.

Moreover, to investigate the dynamics for longer distances, we use the coupled-mode equations given by Eqs. (7.26)-(7.28) for the $\ell = 0$ mode and Eqs. (7.29)-(7.31) for the $\ell = 1$ modes. In Fig. 7.14(c), one can observe how, for $\ell = 1$, the first and second maxima of intensity in A_4 have around 60% and 10% of the injected intensity, respectively, which can be increased by reducing the difference between c_1 and c_2 (see Fig. 7.3(b)). For example, for $c_2/c_1 \approx 1.25$ i.e., $d = 15\,\mu$m the first and second maxima increase up to 97% and 80%, respectively, achieving 100% in the flat-band limit. However, larger separations between waveguides require longer samples, which were not feasible in our experiments due to restriction in the total length [404]. Finally, for $\ell = 0$, the intensity in A_4 decays exponentially independently of the waveguide separation, as it can be seen in Fig. 7.14(d), confirming the different origins of the oscillations. An interesting approach to observe light dynamics for longer distances using a short sample could be the use of state-recycling methods [405], in which the output state is introduced again in the prepared sample. By using this technique, one could overcome the total length limitation.

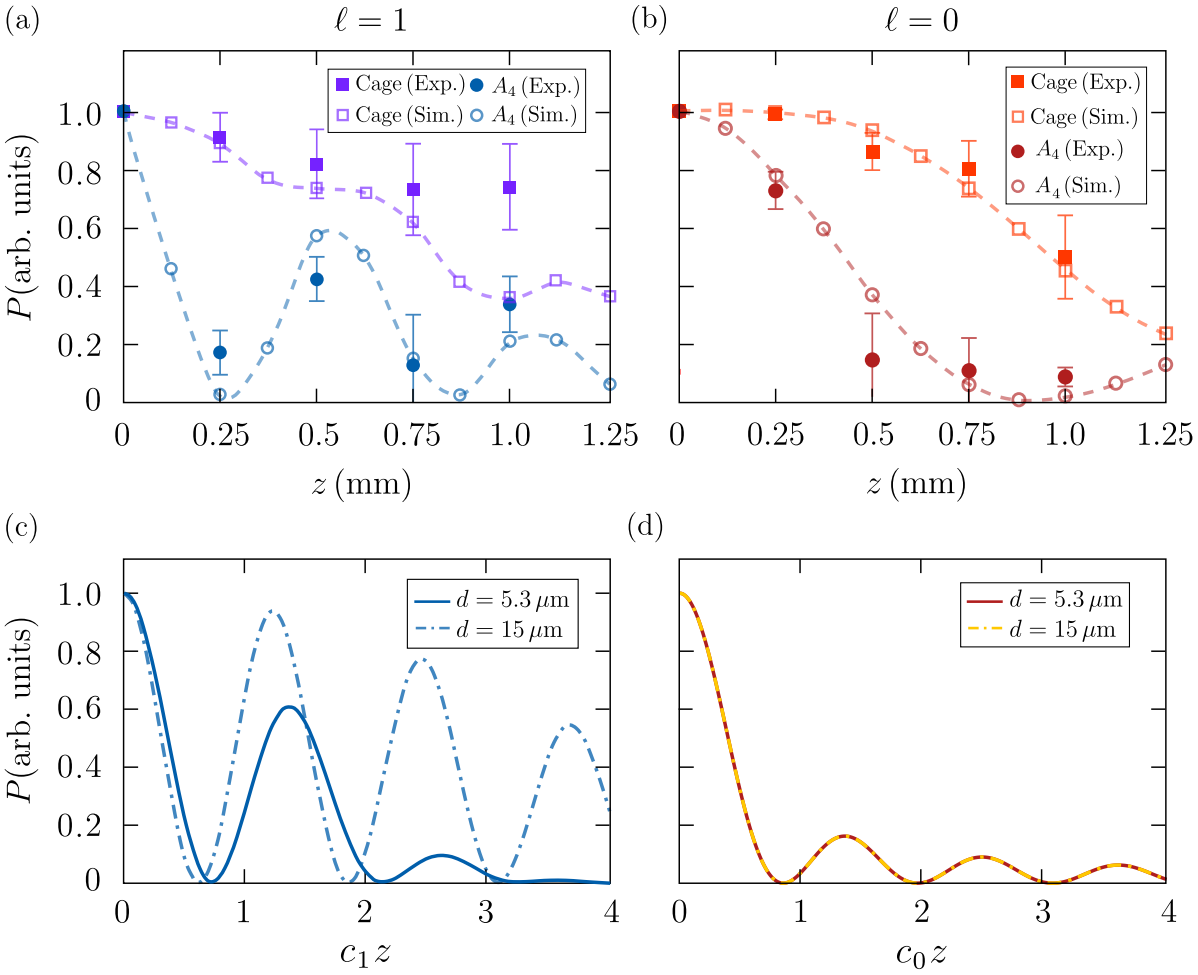

Figure 7.14: Intensity extracted from waveguide A_4 (circles) and from the cage formed by A_4, B_4, C_4, B_5 and C_5 (squares) normalized to the intensity extracted from the entire lattice as a function of the propagation distance z when the (a) $\ell = 1$ mode and (b) $\ell = 0$ mode is injected in waveguide A_4. The results shown in (a) are an average of the intensities extracted for $\ell = 1$ with positive and negative circulations. The solid (empty) circles and squares correspond to the experimental (simulated) extracted intensities, while the lines correspond to the best-fitting curve of the simulated results using FDM numerical techniques. The error bars associated to the experimental data are estimated taking into account a refractive index error of $\Delta n = \pm 0.001$ in the fabrication process. Numerically calculated intensity propagating in waveguide A_4 using coupled-mode equations as a function of z when the (c) $\ell = 1$ mode and (d) $\ell = 0$ mode is injected in waveguide A_4. The solid lines correspond to the case with $d_{\text{sim}} = 5.3\,\mu$m i.e., $c_2/c_1 \approx 2$ while the dashed lines correspond to $d_{\text{sim}} = 15\,\mu$m i.e., $c_2/c_1 \approx 1.25$.

7.4 Conclusions

In this chapter, we have demonstrated theoretically and experimentally that an artificial gauge field of the form of an effective magnetic flux can be induced in a photonic lattice by exploiting the OAM carried by light beams. Specifically, we have shown the appearance of this synthetic flux by experimentally measuring the photonic analogue of the AB caging effect in an arrangement of direct laser written cylindrical waveguides distributed in a diamond-chain configuration. Using this structure, we have presented how an energy gap is opened between the dispersive bands of the system when light carrying OAM is injected, analogous to the effect produced by an AGF [390]. Moreover, we have shown how non-zero energy flat-bands, which yield the AB caging effect, can be achieved by properly tuning the geometry of the unit cells and the separation between waveguides. The agreement between the dynamics shown by the coupled-mode equations, the FDM simulations and the experiments have confirmed the validity of the presented model.

Clearly, the possibility of inducing AGF in an active way by changing the topological charge of the input state constitutes a step-forward in the field of quantum simulation allowing to explore different topological regimes in a single structure. In addition, the inherently infinite dimensionality of OAM modes [185] might pave the way towards combining integrated spatial multiplexing [370] with topological protection [170]. Moreover, the method demonstrated here to induce AGF using OAM states is not restricted to photonic lattices and it could be extended to other platforms like, for instance, polariton micropillars in quantum wells [406], photonic crystals [407] or ultracold atoms in optical lattices [195, 196], being thus of interest for different research areas.

8 Conclusions and outlook

In this last chapter, we summarize the main results and we discuss future perspectives of the research lines that have been addressed along the thesis.

The common element binding this thesis is the use of coupled optical waveguides as a tool to (i) design novel photonic devices with advanced functionalities using quantum techniques, and (ii) simulate, both theoretically and experimentally, the physics of relevant quantum systems. In particular, we have exploited the similarity between the Helmholtz and the Schrödinger equations, which allows to mimic the temporal dynamics of a single particle trapped in a lattice potential with the spatial evolution of a light beam propagating in an array of optical waveguides [75], to investigate the combination of supersymmetry (SUSY) with adiabatic passage techniques [141, 142] and with non-trivial topological geometries [193] in systems of coupled optical waveguides. Moreover, by exploiting these quantum-optical analogies, we have also investigate the generation of artificial gauge fields in systems of coupled optical waveguides [386], .

To start, in Chapter 2, we have introduced the physics describing light propagation in optical waveguides to set the general background of the physical system used along the thesis. First, we have presented the basic waveguide geometries and, starting from Maxwell's equations describing electromagnetic waves propagating in homogeneous and inhomogeneous dielectric media, we have derived the Helmholtz equation governing light propagation in optical waveguides. Moreover, we have also discussed systems of evanescently-coupled optical waveguides and we have presented the coupled-mode theory describing light dynamics in such systems. To end this first chapter, we have reviewed the quantum-optical analogies used in this thesis to investigate coherent quantum effects stemming from other fields of physics such as atomic or condensed-matter physics.

To continue with the theoretical background, in Chapter 3 we have addressed the concept of SUSY in optics. In particular, we have started by introducing the mathematical formalism of SUSY in quantum mechanics (QM) and, by harnessing the quantum-

optical analogies announced in Chapter 2, we have extended SUSY transformations to optical waveguides. To be precise, we have started with the simplest analytically solvable case, which is the SUSY transformation of an isolated step-index waveguide. This transformation, in combination with Spatial Adiabatic Passage (SAP) techniques [105], has been used in Chapter 4 to design a robust mode-division (de)multiplexing device. To continue, we have applied a SUSY transformation to an array of coupled waveguides. In this case, the adiabatic connection of superpartner refractive index profiles along the propagation direction has served in Chapter 5 to design efficient and robust photonic integrated devices. Finally, we have discussed the discrete version of SUSY transformations i.e., DSUSY, which can be applied to one-dimensional and two-dimensional waveguide arrays. Specifically, DSUSY transformations have been considered in Chapter 6 to explore the interplay between SUSY and topology, offering a powerful tool to modify the topological protection of some targeted states [193]. In a similar vein, the interplay of SUSY with Parity-Time (PT) symmetry or non-linear physics are promising lines of research. The former has already provided a few novel applications in photonics [140, 241, 242] and it seems a fertile ground to further dip in. On the contrary, the latter has been explored in QM [219, 220] but it remains absent in optics. Moreover, note that the introduction of non-linear effects could also allow to simulate interactions such as the ones appearing in many-body quantum physics, opening new lines of research.

After introducing the theoretical background in Chapters 2 and 3, we have presented in Chapter 4 a mode-division (de)multiplexing (MDM) device based on the application of SUSY and SAP techniques to a system of three evanescently-coupled waveguides. On the one hand, we have used SUSY transformations to engineer the refractive index of the central waveguide such that it can not sustain the lowest Transverse Electric (TE) mode of the adjacent waveguides, while it preserves the phase-matching conditions among the other modes. On the other hand, we have engineered the waveguide separation along the propagation direction following the SAP protocol such that the first excited mode is robustly and efficiently transferred between the outermost waveguides [105]. Therefore, by injecting an equally weighted superposition of the fundamental and the first excited modes in the left waveguide, we have been able to efficiently transfer the first excited mode to the right waveguide while keeping the fundamental mode in the left waveguide. The combination of SUSY and SAP techniques has revealed a significant improvement of the efficiency and robustness of the MDM process with respect to standard devices, hence, constituting an alternative approach for the increasing demand of high-capacity optical transmissions [164]. Moreover, the high demultiplexing fidelities ($\mathcal{F} > 0.90$) obtained for a broad wavelength range, open the possibility of using the proposed device for demultiplexing light pulses, to combine it with wavelength division multiplexing schemes or even to use it to manipulate quantum states and engineer novel waveguides architectures for coherent information transfer [408, 409].

Keeping on the idea of applying quantum engineering protocols to design novel photonic devices with enhanced performances, in Chapter 5 we have proposed to connect, in an adiabatic fashion, superpartner structures along the propagation direction. By doing so, we have incorporated a new degree of freedom to manipulate the modal content of optical waveguides [142]. As a proof of principle, we have focused on both a single- and a two- waveguide structure. On the one hand, by adiabatically connecting the superpartner profiles of a single-waveguide, we have engineered a tapered waveguide in which the fundamental TE mode has propagated adapting its shape and propagation constant without being coupled to other guided or radiated modes. Moreover, the same waveguide has worked as a mode filter, radiating the rest of the modes before arriving at the output port. On the other hand, we have created a beam splitter by adiabatically joining a two-waveguide structure with its single-waveguide superpartner. In this case, we have shown how if one injects the fundamental TE mode of the superpartner profile, it adiabatically evolves until it becomes the symmetric supermode of a two-waveguide system, hence, coherently splitting its intensity between the two waveguides of the output port. Moreover, by concatenating the beam splitter with a recombiner, we have designed a MZI based on adiabatic transitions connecting superpartner index profiles. Remarkably, high fidelities $\mathcal{F} > 0.90$ have been obtained in a broad region of parameters for all the proposed devices, evidencing the capabilities of the proposed technique. Furthermore, note that more complex structures could be designed by: (i) increasing the number of waveguides to generate a 1-to-N power splitter, (ii) using waveguides with different widths to design asymmetric Y-junctions that could be used for MDM purposes, or (iii) combining the transitions along the propagation direction with SUSY transformations along the transverse direction, to gain more degrees of freedom for modal content manipulation. A second extension of Chapter 5 could be the adiabatic connection of two discrete superpartner structures along the propagation direction, yielding novel possibilities such as exciting supermodes at will just by exciting a single waveguide, which is initially decoupled from the rest of the system.

Whilst in Chapters 4 and 5 we have focused on the development of novel photonic devices by exploiting the combination of SUSY and adiabatic techniques, in Chapters 6 and 7 we have moved to the field of photonic simulators using coupled optical waveguides. In particular, in Chapter 6, we have explored theoretically and experimentally, using femtosecond laser written waveguides, the interplay between SUSY and topology, two seemingly independent fundamental concepts in physics. In this vein, we have demonstrated how SUSY transformations could induce topological phase transitions, unmasking the links between topological behavior and symmetry constraints of SUSY transformations [238, 240]. Particularly, we have shown how SUSY transformations could fully preserve, partially preserve, or totally suppress the protecting symmetries of a targeted system, shedding light on how both fields are connected. As an exam-

ple, we have considered the simplest system with non-trivial topological properties, the Su-Schrieffer-Heeger (SSH) model [178], and we have demonstrated how the topological protection of a state can be suspended and reestablished by applying DSUSY transformations. To be more precise, we have transformed a lattice supporting two topological edge states to a lattice supporting (i) one topological edge state, (ii) one topological interface state, or (iii) one topological and one non-topological edge states. Note that these transformations could be applied in an iterative way to remove any number of states from a given system, reducing its overall size while preserving its topological properties. Moreover, the proposed technique could be naturally extended to two-dimensional systems or to other physical platforms such as coupled cavities [159], ultra-cold atoms [344] or acoustics and mechanical systems [257], boosting the design of structures with desirable topological properties. Even more, one could explore quantum state transfer protocols to efficiently transmit the topological edge states discussed in Chapter 6 between the outermost sites of the lattice [409, 410]. Another natural continuation of Chapter 6 would be to investigate the effect of DSUSY transformations applied to two-dimensional waveguide arrays, which could be used to manipulate topological chiral edge states and enhance novel ways of transmitting information in a robust manner.

Moreover, to access these non-trivial topological phases, a key step is the introduction of Artificial Gauge Fields (AGF) controlling the dynamics of uncharged particles that otherwise elude the influence of standard electromagnetic fields. To this end, in Chapter 7, we have focused on the generation of AGF by breaking the time-reversal symmetry using light beams carrying Orbital Angular Momentum (OAM) [185], in line with the proposal of Pelegrí *et al.* based on ultracold atoms carrying OAM [195, 196]. To be concrete, we have experimentally verified the generation of an AGF in the form of a synthetic magnetic flux using direct laser written cylindrical waveguides distributed in a diamond-chain configuration. Moreover, to validate the presence of that flux, we have measured the Aharonov-Bohm (AB) caging effect, a localization phenomenon of wavepackets that derives its origin solely from the presence of the flux. In addition, we have theoretically described how non-zero energy flat bands, which are responsible for the caging effect, can be achieved by injecting light beams carrying OAM, verifying the possibility of switching on and off AGF just by changing the topological charge of the input state. Thus, we have proposed a technique that paves the way to access different topological regimes in one single structure, which represents an important step forward to enhance the possibilities of quantum simulation in photonic structures. The proposed method could be applied to other platforms such as polariton micropillars in quantum wells [406], photonic crystals [407] or ultracold atoms in optical lattices [195], and could also be extended to different geometrical configurations and higher order OAM modes.

Bibliography

[1] G. Sarton, *Ancient Science Through the Golden Age of Greece* (Dover Publications, 1993).

[2] H. E. Burton, "The optics of Euclid," J. Opt. Soc. Am. **35**, 357 (1945).

[3] O. Darrigol, *A History of Optics from Greek Antiquity to the Nineteenth Century* (OUP Oxford, 2012).

[4] M. Guarnieri, "Two millennia of light: The long path to maxwell's waves," IEEE Ind. Electron. Mag. **9**, 54 (2015).

[5] D. Lindberg and D. Lindberg, *Theories of Vision from Al-kindi to Kepler* (University of Chicago Press, 1981).

[6] J. Kepler, W. von Dyck, M. Caspar, F. Hammer, *et al.*, *Astronomiae pars optica* (C. H. Beck, 1937).

[7] C. Huygens, *Traité de la lumière* (Pierre van der Aa, 1690).

[8] I. Newton, *Opticks* (Dover Press, 1704).

[9] A. Roy, "Great experiments in physics," Resonance **4**, 6 (1999).

[10] J. Maxwell, *A Treatise on Electricity and Magnetism* (Dover Publications, 1954).

[11] M. Planck, "Ueber das gesetz der energieverteilung im normalspectrum," Ann. Phys. **309**, 553 (1901).

[12] A. Einstein, "Über einen die erzeugung und verwandlung des lichtes betreffenden heuristischen gesichtspunkt," Ann. Phys. **322**, 132 (1905).

[13] R. Baierlein, *Newton to Einstein: The Trail of Light* (Cambridge University Press, 1992).

[14] E. C. Watson, "The first reported observations on emission spectra," Am. J. Phys. **20**, 569 (1952).

[15] N. Bohr, "On the constitution of atoms and molecules I," Philos. Mag. **26**, 1 (1913).

[16] M. Born and P. Jordan, "Zur quantenmechanik," Z. Phys **34**, 858 (1925).

[17] E. Schrödinger, "Quantisierung als eigenwertproblem," Ann. Phys. **384**, 361 (1926).

[18] L. de Broglie, "Recherches sur la théorie des quanta," Ann. Phys. **10**, 22 (1925).

[19] W. Heisenberg, "Über den anschaulichen inhalt der quantentheoretischen kinematik und mechanik," Z. Phys **43**, 172 (1927).

[20] M. Scully and M. Zubairy, *Quantum Optics* (Cambridge University Press, 1997).

[21] A. Celi, A. Sanpera, V. Ahufinger, and M. Lewenstein, "Quantum optics and frontiers of physics: the third quantum revolution," Phys. Scr. **92**, 013003 (2016).

[22] T. H. Maiman, "Stimulated optical radiation in ruby," Nature **187**, 493 (1960).

[23] C. Webb and J. Jones, *Handbook of Laser Technology and Applications: Applications* (Institute of Physics, 2004).

[24] S. E. Miller, "Integrated optics: An introduction," BSTJ **48**, 2059 (1969).

[25] J. Millman and C. C. Halkias, *Integrated Electronics: Analog and Digital Circuits and Systems* (Mcgraw-Hill, 1972).

[26] K. Kao and G. Hockham, "Dielectric-fibre surface waveguides for optical frequencies," Proc. Inst. Electr. Eng. **113**, 1151 (1966).

[27] A. Snyder and J. Love, *Optical Waveguide Theory* (Springer, 1983).

[28] G. Lifante, *Integrated Photonics: Fundamentals* (Wiley-Blackwell, 2003).

[29] N. K. Efremidis, J. Hudock, D. N. Christodoulides, J. W. Fleischer, *et al.*, "Two-dimensional optical lattice solitons," Phys. Rev. Lett. **91**, 213906 (2003).

[30] J. W. Fleischer, M. Segev, N. K. Efremidis, and D. N. Christodoulides, "Observation of two-dimensional discrete solitons in optically induced nonlinear photonic lattices," Nature **422**, 147 (2003).

[31] T. Pertsch, U. Peschel, F. Lederer, J. Burghoff, *et al.*, "Discrete diffraction in two-dimensional arrays of coupled waveguides in silica," Opt. Lett. **29**, 468 (2004).

[32] K. Itoh, W. Watanabe, S. Nolte, and C. B. Schaffer, "Ultrafast processes for bulk modification of transparent materials," MRS Bulletin **31**, 620 (2006).

[33] X. C. Tong, *Advanced Materials for Integrated Optical Waveguides*, 1st ed. (Springer International Publishing, 2014).

[34] S. Bogdanov, M. Shalaginov, A. Boltasseva, and V. M. Shalaev, "Material platforms for integrated quantum photonics," Opt. Mater. Express **7**, 111 (2017).

[35] M. Krasnodebski, "Throwing light on photonics: The genealogy of a technological paradigm," Centaurus **60**, 3 (2018).

[36] L. Thylén and L. Wosinski, "Integrated photonics in the 21st century," Photonics Res. **2**, 75 (2014).

[37] R. W. Tkach, "Scaling optical communications for the next decade and beyond," Bell Labs Tech. J. **14**, 3 (2010).

[38] E. Agrell, M. Karlsson, A. R. Chraplyvy, D. J. Richardson, *et al.*, "Roadmap of optical communications," J. Opt. **18**, 063002 (2016).

[39] J. Wang and Y. Long, "On-chip silicon photonic signaling and processing: a review," Sci. Bull. **63**, 1267 (2018).

[40] N. Thomas-Peter, N. K. Langford, A. Datta, L. Zhang, *et al.*, "Integrated photonic sensing," New J. Phys. **13**, 055024 (2011).

[41] P. Kozma, F. Kehl, E. Ehrentreich-Förster, C. Stamm, and F. F. Bier, "Integrated planar optical waveguide interferometer biosensors: A comparative review," Biosens. Bioelectron. **58**, 287 (2014).

[42] J. L. O'Brien, A. Furusawa, and J. Vučković, "Photonic quantum technologies," Nat. Photonics **3**, 687 (2009).

[43] A. Politi, J. Matthews, M. Thompson, and J. O'Brien, "Integrated quantum photonics," IEEE J. Quantum Electron. **15**, 1673 (2009).

[44] T. Meany, M. Gräfe, R. Heilmann, A. Pérez-Leija, S. Gross, *et al.*, "Laser written circuits for quantum photonics," Laser Photonics Rev. **9**, 363 (2015).

[45] J. Wang, F. Sciarrino, A. Laing, and M. G. Thompson, "Integrated photonic quantum technologies," Nat. Photonics **14**, 273 (2019).

[46] N. Gisin, G. Ribordy, W. Tittel, and H. Zbinden, "Quantum cryptography," Rev. Mod. Phys. **74**, 145 (2002).

[47] J. Silverstone, D. Bonneau, J. O Brien, and M. Thompson, "Silicon quantum photonics," IEEE J. Quantum Electron. **22**, 390 (2016).

[48] P. Sibson, C. Erven, M. Godfrey, S. Miki, *et al.*, "Chip-based quantum key distribution," Nat. Commun. **8**, 13984 (2017).

[49] A. Orieux and E. Diamanti, "Recent advances on integrated quantum communications," J. Opt. **18**, 083002 (2016).

[50] M. Herrero-Collantes and J. C. Garcia-Escartin, "Quantum random number generators," Rev. Mod. Phys. **89**, 015004 (2017).

[51] P. Kumar, P. Kwiat, A. Migdall, S. W. Nam, *et al.*, "Photonic technologies for quantum information processing," Quantum Inf. Process. **3**, 215 (2004).

[52] O. Alibart, V. D'Auria, M. De Micheli, F. Doutre, *et al.*, "Quantum photonics at telecom wavelengths based on lithium niobate waveguides," J. Opt. **18**, 104001 (2016).

[53] F. Flamini, N. Spagnolo, and F. Sciarrino, "Photonic quantum information processing: a review," Rep. Prog. Phys. **82**, 016001 (2019).

[54] J. B. Spring, B. J. Metcalf, P. C. Humphreys, W. S. Kolthammer, *et al.*, "Boson sampling on a photonic chip," Science **339**, 798 (2013).

[55] M. Tillmann, B. Dakić, R. Heilmann, S. Nolte, *et al.*, "Experimental boson sampling," Nat. Photonics **7**, 540 (2013).

[56] D. J. Brod, E. F. Galvão, A. Crespi, R. Osellame, *et al.*, "Photonic implementation of boson sampling: a review," Adv. Photonics **1**, 1 (2019).

[57] L. Sansoni, F. Sciarrino, G. Vallone, P. Mataloni, *et al.*, "Two-particle bosonic-fermionic quantum walk via integrated photonics," Phys. Rev. Lett. **108**, 010502 (2012).

[58] M. Gräfe, R. Heilmann, M. Lebugle, D. Guzman-Silva, *et al.*, "Integrated photonic quantum walks," J. Opt. **18**, 103002 (2016).

[59] M. Gräfe and A. Szameit, "Integrated photonic quantum walks," J. Opt. B **53**, 073001 (2020).

[60] E. Knill, R. Laflamme, and G. J. Milburn, "A scheme for efficient quantum computation with linear optics," Nature **409**, 46 (2001).

[61] P. Kok, K. Nemoto, T. C. Ralph, J. P. Dowling, and G. J. Milburn, "Linear optical quantum computing with photonic qubits," Rev. Mod. Phys. **79**, 135 (2007).

[62] M. G. Thompson, A. Politi, J. C. Matthews, and J. L. O'Brien, "Integrated waveguide circuits for optical quantum computing," IET circuits **5**, 94 (2011).

[63] A. Acín, I. Bloch, H. Buhrman, T. Calarco, *et al.*, "The quantum technologies roadmap: a european community view," New J. Phys. **20**, 080201 (2018).

[64] I. Buluta and F. Nori, "Quantum simulators," Science **326**, 108 (2009).

[65] A. Aspuru-Guzik and P. Walther, "Photonic quantum simulators," Nat. Phys. **8**, 285 (2012).

[66] I. Georgescu, S. Ashhab, and F. Nori, "Quantum simulation," Rev. Mod. Phys. **86**, 153 (2014).

[67] D. Dragoman and M. Dragoman, *Quantum-Classical Analogies* (Springer-Verlag Berlin Heidelberg, 2004).

[68] M. Lewenstein, A. Sanpera, V. Ahufinger, B. Damski, and *et. al.*, "Ultracold atomic gases in optical lattices: mimicking condensed matter physics and beyond," Adv. Phys. **56**, 243 (2007).

[69] R. Blatt and C. F. Roos, "Quantum simulations with trapped ions," Nat. Phys. **8**, 277 (2012).

[70] A. A. Houck, H. E. Türeci, and J. Koch, "On-chip quantum simulation with superconducting circuits," Nat. Phys. **8**, 292 (2012).

[71] N. Chiodo, G. Della Valle, R. Osellame, S. Longhi, *et al.*, "Imaging of bloch oscillations in erbium-doped curved waveguide arrays," Opt. Lett. **31**, 1651 (2006).

[72] G. Della Valle, S. Longhi, P. Laporta, P. Biagioni, *et al.*, "Discrete diffraction in waveguide arrays: A quantitative analysis by tunneling optical microscopy," Appl. Phys. Lett. **90**, 261118 (2007).

[73] F. Dreisow, M. Heinrich, A. Szameit, S. Doering, *et al.*, "Spectral resolved dynamic localization in curved fs laser written waveguide arrays," Opt. Express **16**, 3474 (2008).

[74] I. L. Garanovich, S. Longhi, A. A. Sukhorukov, and Y. S. Kivshar, "Light propagation and localization in modulated photonic lattices and waveguides," Phys. Rep. **518**, 1 (2012).

[75] S. Longhi, "Quantum-optical analogies using photonic structures," Laser Photonics Rev. **3**, 243 (2009).

[76] A. Szameit and S. Nolte, "Discrete optics in femtosecond-laser-written photonic structures," J. Phys. B **43**, 163001 (2010).

[77] F. Lederer, G. I. Stegeman, D. N. Christodoulides, G. Assanto, *et al.*, "Discrete solitons in optics," Phys. Rep. **463**, 1 (2008).

[78] T. Pertsch, P. Dannberg, W. Elflein, A. Bräuer, and F. Lederer, "Optical Bloch oscillations in temperature tuned waveguide arrays," Phys. Rev. Lett. **83**, 4752 (1999).

[79] R. Morandotti, U. Peschel, J. S. Aitchison, H. S. Eisenberg, and Y. Silberberg, "Experimental observation of linear and nonlinear optical bloch oscillations," Phys. Rev. Lett. **83**, 4756 (1999).

[80] R. Khomeriki and S. Ruffo, "Nonadiabatic landau-zener tunneling in waveguide arrays with a step in the refractive index," Phys. Rev. Lett. **94**, 113904 (2005).

[81] H. Trompeter, T. Pertsch, F. Lederer, D. Michaelis, *et al.*, "Visual observation of zener tunneling," Phys. Rev. Lett. **96**, 023901 (2006).

[82] H. S. Eisenberg, Y. Silberberg, R. Morandotti, and J. S. Aitchison, "Diffraction management," Phys. Rev. Lett. **85**, 1863 (2000).

[83] G. Lenz, R. Parker, M. Wanke, and C. de Sterke, "Dynamical localization and ac bloch oscillations in periodic optical waveguide arrays," Opt. Commun. **218**, 87 (2003).

[84] T. Schwartz, G. Bartal, S. Fishman, and M. Segev, "Transport and anderson localization in disordered two-dimensional photonic lattices," Nature **446**, 52 (2007).

[85] Y. Lahini, A. Avidan, F. Pozzi, M. Sorel, *et al.*, "Anderson localization and nonlinearity in one-dimensional disordered photonic lattices," Phys. Rev. Lett. **100**, 013906 (2008).

[86] S. Longhi, "Landau–zener dynamics in a curved optical directional coupler," J. Opt. B **7**, L9 (2005).

[87] S. Longhi, "Dynamics of driven two-level systems with permanent dipole moments: an optical realization," J. Phys. B **39**, 1985 (2006).

[88] N. V. Vitanov, A. A. Rangelov, B. W. Shore, and K. Bergmann, "Stimulated raman adiabatic passage in physics, chemistry, and beyond," Rev. Mod. Phys. **89**, 015006 (2017).

[89] K. Bergmann, H.-C. Naegerl, C. D. Panda, G. Gabrielse, *et al.*, "Roadmap on stirap applications," J. Phys. B **52**, 202001 (2019).

[90] D. D. Smith, H. Chang, K. A. Fuller, A. T. Rosenberger, and R. W. Boyd, "Coupled-resonator-induced transparency," Phys. Rev. A **69**, 063804 (2004).

[91] Q. Xu, S. Sandhu, M. L. Povinelli, J. Shakya, *et al.*, "Experimental realization of an on-chip all-optical analogue to electromagnetically induced transparency," Phys. Rev. Lett. **96**, 123901 (2006).

[92] Y. Aharonov and D. Bohm, "Significance of electromagnetic potentials in the quantum theory," Phys. Rev. **115**, 485 (1959).

[93] M. Berry, "The adiabatic phase and Pancharatnam's phase for polarized light," J. Mod. Opt. **34**, 1401 (1987).

[94] I. Vorobeichik, E. Narevicius, G. Rosenblum, M. Orenstein, and N. Moiseyev, "Electromagnetic realization of orders-of-magnitude tunneling enhancement in a double well system," Phys. Rev. Lett. **90**, 176806 (2003).

[95] S. Longhi, "Coherent destruction of tunneling in waveguide directional couplers," Phys. Rev. A **71**, 065801 (2005).

[96] K. Yamane, M. Ito, and M. Kitano, "Quantum zeno effect in optical fibers," Opt. Commun. **192**, 299 (2001).

[97] S. Longhi, "Nonexponential decay via tunneling in tight-binding lattices and the optical zeno effect," Phys. Rev. Lett. **97**, 110402 (2006).

[98] A. G. Kofman and G. Kurizki, "Universal dynamical control of quantum mechanical decay: Modulation of the coupling to the continuum," Phys. Rev. Lett. **87**, 270405 (2001).

[99] S. Longhi, "Quantum simulation of decoherence in optical waveguide lattices," Opt. Lett. **38**, 4884 (2013).

[100] J. Fu, Z. Si, S. Tang, and J. Deng, "Classical simulation of quantum entanglement using optical transverse modes in multimode waveguides," Phys. Rev. A **70**, 042313 (2004).

[101] I. Pitsios, L. Banchi, A. S. Rab, M. Bentivegna, *et al.*, "Photonic simulation of entanglement growth and engineering after a spin chain quench," Nat. Commun. **8**, 1 (2017).

[102] R. Osellame, G. Della Valle, N. Chiodo, S. Taccheo, *et al.*, "Lasing in femtosecond laser written optical waveguides," Appl. Phys. A **93**, 17 (2008).

[103] F. C. D. N. Rodríguez-Lara, B Mand Soto-Eguibar, "Quantum optics as a tool for photonic lattice design," Phys. Scr. **90**, 068014 (2015).

[104] R. El-Ganainy, A. Eisfeld, M. Levy, and D. N. Christodoulides, "On-chip nonreciprocal optical devices based on quantum inspired photonic lattices," Appl. Phys. Lett. **103**, 161105 (2013).

[105] R. Menchon-Enrich, A. Benseny, V. Ahufinger, A. D. Greentree, *et al.*, "Spatial adiabatic passage: a review of recent progress," Rep. Prog. Phys. **79**, 074401 (2016).

[106] F. Dreisow, M. Ornigotti, A. Szameit, M. Heinrich, *et al.*, "Polychromatic beam splitting by fractional stimulated raman adiabatic passage," Appl. Phys. Lett. **95**, 261102 (2009).

[107] C. W. Wu, A. S. Solntsev, D. N. Neshev, and A. A. Sukhorukov, "Photon pair generation and pump filtering in nonlinear adiabatic waveguiding structures," Opt. Lett. **39**, 953 (2014).

[108] S. Longhi, "Topological pumping of edge states via adiabatic passage," Phys. Rev. B **99**, 155150 (2019).

[109] F. D. M. Haldane and S. Raghu, "Possible realization of directional optical waveguides in photonic crystals with broken time-reversal symmetry," Phys. Rev. Lett. **100**, 013904 (2008).

[110] S. Raghu and F. D. M. Haldane, "Analogs of quantum-Hall-effect edge states in photonic crystals," Phys. Rev. A **78**, 033834 (2008).

[111] Z. Wang, Y. D. Chong, J. D. Joannopoulos, and M. Soljačić, "Reflection-free one-way edge modes in a gyromagnetic photonic crystal," Phys. Rev. Lett. **100**, 013905 (2008).

[112] Z. Wang, Y. Chong, J. D. Joannopoulos, and M. Soljačić, "Observation of unidirectional backscattering-immune topological electromagnetic states," Nature **461**, 772 (2009).

[113] J.-L. Tambasco, G. Corrielli, R. J. Chapman, A. Crespi, and R. P.-A. Zilberberg, Oded; Osellame, "Quantum interference of topological states of light," Sci. Adv. **4**, eaat3187 (2018).

[114] D. N. Christodoulides, F. Lederer, and Y. Silberberg, "Discretizing light behaviour in linear and nonlinear waveguide lattices," Nature **424**, 817 (2003).

[115] L. Yuan, Q. Lin, M. Xiao, and S. Fan, "Synthetic dimension in photonics," Optica **5**, 1396 (2018).

[116] T. Ozawa and H. M. Price, "Topological quantum matter in synthetic dimensions," Nat. Rev. Phys. **1**, 349 (2019).

[117] M.-A. Miri, M. Heinrich, R. El-Ganainy, and D. N. Christodoulides, "Supersymmetric optical structures," Phys. Rev. Lett. **110**, 233902 (2013).

[118] D. Christodoulides and J. Yang, *Parity-time Symmetry and Its Applications* (Springer Singapore, 2018).

[119] R. El-Ganainy, M. Khajavikhan, D. N. Christodoulides, and S. K. Ozdemir, "The dawn of non-Hermitian optics," Commun. Phys. **2**, 37 (2019).

[120] P. Ramond, "Dual theory for free fermions," Phys. Rev. D **3**, 2415 (1971).

[121] A. Neveu and J. H. Schwarz, "Factorizable dual model of pions," Nucl. Phys. B **31**, 86 (1971).

[122] Y. A. Gol'fand and E. P. Likhtman, "Extension of the algebra of Poincare group generators and violation of P invariance," JETP Lett. **13**, 323 (1971).

[123] S. M. Chumakov and K. B. Wolf, "Supersymmetry in Helmholtz optics," Phys. Lett. A **193**, 51 (1994).

[124] Y.-S. Ling and W. Zhang, "Supersymmetry and its application in quantum optics," Phys. Lett. A **193**, 47 (1994).

[125] F. Cooper and B. Freedman, "Aspects of supersymmetric quantum mechanics," Ann. Phys. **146**, 262 (1983).

[126] B. Friedman and F. Cooper, "A review of supersymmetric quantum mechanics," Physica D **15**, 138 (1985).

[127] C. V. Sukumar, "Supersymmetric quantum mechanics of one-dimensional systems," J. Phys. A **18**, 2917 (1985).

[128] C. M. Bender and S. Boettcher, "Real spectra in non-hermitian hamiltonians having PT symmetry," Phys. Rev. Lett. **80**, 5243 (1998).

[129] K. G. Makris, R. El-Ganainy, D. N. Christodoulides, and Z. H. Musslimani, "Beam dynamics in $\mathcal{PT}$ symmetric optical lattices," Phys. Rev. Lett. **100**, 103904 (2008).

[130] R. G. L. Feng, Liangand El-Ganainy, "Non-hermitian photonics based on parity–time symmetry," Nat. Photonics **11**, 752 (2017).

[131] R. El-Ganainy, K. G. Makris, M. Khajavikhan, Z. H. Musslimani, *et al.*, "Non-hermitian physics and pt symmetry," Nat. Phys. **14**, 11 (2018).

[132] F. Cooper, A. Khare, and U. Sukhatme, "Supersymmetry and quantum mechanics," Phys. Rep. **251**, 267 (1995).

[133] H. P. Laba and V. M. Tkachuk, "Quantum-mechanical analogy and supersymmetry of electromagnetic wave modes in planar waveguides," Phys. Rev. A **89**, 033826 (2014).

[134] M.-A. Miri, M. Heinrich, and D. N. Christodoulides, "Supersymmetric optical waveguides," Proc. SPIE Int. Soc. Opt. Eng. **8980**, 89801F (2014).

[135] M.-A. Miri, M. Heinrich, and D. N. Christodoulides, "Supersymmetry-generated complex optical potentials with real spectra," Phys. Rev. A **87**, 043819 (2013).

[136] M.-A. Miri, *Parity-time and supersymmetry in optics*, Ph.D. thesis, Electronic Theses and Dissertations (2014).

[137] A. Macho, R. Llorente, and C. García-Meca, "Supersymmetric transformations in optical fibers," Phys. Rev. Appl. **9**, 014024 (2018).

[138] A. Macho, *Multi-Core Fiber and Optical Supersymmetry: Theory and Applications*, Ph.D. thesis, Universitat Politècnica de València (2019).

[139] M. Heinrich, M.-A. Miri, S. Stützer, R. El-Ganainy, *et al.*, "Supersymmetric mode converters," Nat. Commun. **5**, 3698 (2014).

[140] M. Principe, G. Castaldi, M. Consales, A. Cusano, and V. Galdi, "Supersymmetry-inspired non-hermitian optical couplers," Sci. Rep. **5**, 8568 (2015).

[141] G. Queraltó, V. Ahufinger, and J. Mompart, "Mode-division (de)multiplexing using adiabatic passage and supersymmetric waveguides," Opt. Express **25**, 27396 (2017).

[142] G. Queraltó, V. Ahufinger, and J. Mompart, "Integrated photonic devices based on adiabatic transitions between supersymmetric structures," Opt. Express **26**, 33797 (2018).

[143] W. Walasik, B. Midya, L. Feng, and N. M. Litchinitser, "Supersymmetry-guided method for mode selection and optimization in coupled systems," Opt. Lett. **43**, 3758 (2018).

[144] W. Walasik, N. Chandra, B. Midya, L. Feng, and N. M. Litchinitser, "Mode-sorter design using continuous supersymmetric transformation," Opt. Express **27**, 22429 (2019).

[145] M.-A. Miri, M. Heinrich, and D. N. Christodoulides, "SUSY-inspired one-dimensional transformation optics," Optica **1**, 89 (2014).

[146] M. Heinrich, M.-A. Miri, S. Stützer, S. Nolte, *et al.*, "Observation of supersymmetric scattering in photonic lattices," Opt. Lett. **39**, 6130 (2014).

[147] S. Longhi, "Invisibility in non-hermitian tight-binding lattices," Phys. Rev. A **82**, 32111 (2010).

[148] S. Longhi and G. Della Valle, "Transparency at the interface between two isospectral crystals," EPL **102**, 40008 (2013).

[149] S. Longhi, "Supersymmetric transparent optical intersections," Opt. Lett. **40**, 463 (2015).

[150] S. Longhi, "Reflectionless and invisible potentials in photonic lattices," Opt. Lett. **42**, 3229 (2017).

[151] S. Yu, X. Piao, J. Hong, and N. Park, "Bloch-like waves in random-walk potentials based on supersymmetry," Nat. Commun. **6**, 8269 (2015).

[152] S. Yu, X. Piao, J. Hong, and N. Park, "Metadisorder for designer light in random systems," Sci. Adv. **2**, e1501851 (2016).

[153] A. Zúñiga-Segundo, B. M. Rodríguez-Lara, D. J. Fernández C., and H. M. Moya-Cessa, "Jacobi photonic lattices and their SUSY partners," Opt. Express **22**, 987 (2014).

[154] M. H. Teimourpour, D. N. Christodoulides, and R. El-Ganainy, "Optical revivals in nonuniform supersymmetric photonic arrays," Opt. Lett. **41**, 372 (2016).

[155] R. El-Ganainy, M. Ge, Liand Khajavikhan, and D. N. Christodoulides, "Supersymmetric laser arrays," Phys. Rev. A **92**, 033818 (2015).

[156] M. H. Teimourpour, L. Ge, D. N. Christodoulides, and R. El-Ganainy, "Non-hermitian engineering of single mode two dimensional laser arrays," Sci. Rep. **6**, 33253 (2016).

[157] M. P. Hokmabadi, N. S. Nye, R. El-Ganainy, D. N. Christodoulides, and M. Khajavikhan, "Supersymmetric laser arrays," Science **363**, 623 (2019).

[158] T. Kottos, "Single-mode lasing by selective mode pairing," Science **363**, 586 (2019).

[159] J. Ding and M.-A. Miri, "Mode discrimination in dissipatively coupled laser arrays," Opt. Lett. **44**, 5021 (2019).

[160] K. Bergmann, H. Theuer, and B. W. Shore, "Coherent population transfer among quantum states of atoms and molecules," Rev. Mod. Phys. **70**, 1003 (1998).

[161] M. Born and V. Fock, "Beweis des adiabatensatzes," Z. Phys. **51**, 165 (1928).

[162] S. Longhi, "Optical realization of multilevel adiabatic population transfer in curved waveguide arrays," Phys. Lett. A **359**, 166 (2006).

[163] E. Paspalakis, "Adiabatic three-waveguide directional coupler," Opt. Commun. **258**, 30 (2006).

[164] D. J. Richardson, "New optical fibres for high-capacity optical communications," Philos. Trans. Royal Soc. A **374**, 20140441 (2016).

[165] C.-K. Chiu, J. C. Y. Teo, A. P. Schynder, and S. Ryu, "Classification of topological quantum matter with symmetries," Rev. Mod. Phys. **88**, 035005 (2016).

[166] J. Wang and S.-C. Zhang, "Topological states of condensed matter," Nat. Materials **16**, 1062 (2017).

[167] K. Klitzing, G. Dorda, and M. Pepper, "New method for high-accuracy determination of the fine-structure constant based on quantized Hall resistance," Phys. Rev. Lett. **45**, 494 (1980).

[168] D. Thouless, M. Kohmoto, M. Nightingale, and M. den Nijs, "Quantized Hall conductance in a two-dimensional periodic potential," Phys. Rev. Lett. **49**, 405 (1982).

[169] D.-W. Zhang, Y.-Q. Zhu, Y. X. Zhao, H. Yan, and S.-L. Zhu, "Topological quantum matter with cold atoms," Adv. Phys. **67**, 253 (2018).

[170] T. Ozawa, H. M. Price, A. Amo, N. Goldman, *et al.*, "Topological photonics," Rev. Mod. Phys. **91**, 015006 (2019).

[171] M. Hasan and C. Kane, "Colloquium: Topological insulators," Rev. Mod. Phys. **82**, 3045 (2010).

[172] M. C. Rechtsman, J. M. Zeuner, Y. Plotnik, Y. Lumer, *et al.*, "Photonic floquet topological insulators," Nature **496**, 196 (2013).

[173] A. B. Khanikaev, S. Hossein Mousavi, W.-K. Tse, M. Kargarian, *et al.*, "Photonic topological insulators," Nat. Mater. **12**, 233 (2013).

[174] M. Hafezi, E. A. Demler, M. D. Lukin, and J. M. Taylor, "Robust optical delay lines with topological protection," Nat. Phys. **7**, 907 (2011).

[175] T. Kitagawa, E. Berg, M. Rudner, and E. Demler, "Topological characterization of periodically driven quantum systems," Phys. Rev. B **82**, 235114 (2010).

[176] T. Kitagawa, M. A. Broome, A. Fedrizzi, M. S. Rudner, *et al.*, "Observation of topologically protected bound states in photonic quantum walks," Nat. Commun. **3**, 882 (2012).

[177] M. C. Rechtsman, Y. Lumer, Y. Plotnik, A. Perez-Leija, *et al.*, "Topological protection of photonic path entanglement," Optica **3**, 925 (2016).

[178] W. P. Su, J. R. Schrieffer, and A. J. Heeger, "Solitons in polyacetylene," Phys. Rev. Lett. **42**, 1698 (1979).

[179] G. Molina-Terriza, J. P. Torres, and L. Torner, "Twisted photons," Nat. Phys. **3**, 305 (2007).

[180] A. M. Yao and M. J. Padgett, "Orbital angular momentum: origins, behavior and applications," Adv. Opt. Photonics **3**, 161 (2011).

[181] A. E. Willner, H. Huang, Y. Yan, Y. Ren, *et al.*, "Optical communications using orbital angular momentum beams," Adv. Opt. Photonics **7**, 66 (2015).

[182] J. Wang, "Advances in communications using optical vortices," Photonics Res. **4**, B14 (2016).

[183] M. J. Padgett, "Orbital angular momentum 25 years on," Opt. Express **25**, 11265 (2017).

[184] H. Rubinsztein-Dunlop, A. Forbes, M. V. Berry, M. R. Dennis, *et al.*, "Roadmap on structured light," J. Opt. **19**, 013001 (2017).

[185] Y. Shen, X. Wang, Z. Xie, C. Min, *et al.*, "Optical vortices 30 years on: OAM manipulation from topological charge to multiple singularities," Light Sci. Appl. **8**, 90 (2019).

[186] D. Cozzolino, B. Da Lio, D. Bacco, and L. K. Oxenløwe, "High-dimensional quantum communication: Benefits, progress, and future challenges," Adv. Quantum Tech. **2**, 1900038 (2019).

[187] J. K. Hohmann, M. Renner, E. H. Waller, and G. von Freymann, "Three-dimensional μ-printing: An enabling technology," Adv. Opt. Materials **3**, 1488 (2015).

[188] C.-L. Chen, *Foundations for guided-wave optics* (Wiley-Interscience, 2007).

[189] B. E. A. Saleh and M. C. Teich, *Fundamentals of photonics* (Wiley, 1991).

[190] U. S. Inan and R. A. Marshall, *Numerical Electromagnetics: The FDTD Method* (Cambridge University Press, 2011).

[191] S. Longhi, "Equivalence principle and quantum mechanics: quantum simulation with entangled photons," Opt. Lett. **43**, 226 (2018).

[192] G. Della Valle, R. Osellame, and P. Laporta, "Micromachining of photonic devices by femtosecond laser pulses," J. Opt. **11**, 013001 (2009).

[193] G. Queraltó, M. Kremer, L. Maczewsky, M. Heinrich, *et al.*, "Topological state engineering via supersymmetric transformations," Commun. Phys. **3**, 49 (2020).

[194] G. Nienhuis, "Analogies between optical and quantum mechanical angular momentum," Philos. Trans. R. Soc. A **375**, 20150443 (2017).

[195] G. Pelegrí, A. M. Marques, R. G. Dias, A. J. Daley, *et al.*, "Topological edge states and Aharanov-Bohm caging with ultracold atoms carrying orbital angular momentum," Phys. Rev. A **99**, 023613 (2019).

[196] G. Pelegrí, A. M. Marques, R. G. Dias, A. J. Daley, *et al.*, "Topological edge states with ultracold atoms carrying orbital angular momentum in a diamond chain," Phys. Rev. A **99**, 023612 (2019).

[197] D. V. Volkov and V. P. Akulov, "Is the neutrino a goldstone particle?" Phys. Lett. B **46**, 109 (1973).

[198] J. Wess and B. Zumino, "Supergauge transformations in four dimensions," Nucl. Phys. B **70**, 39 (1974).

[199] G. Kane and M. A. Shifman, *The Supersymmetric World: The Beginnings of the Theory* (World Scientific, 2001).

[200] P. M. R. Binetruy, *Supersymmetry: theory, experiment, and cosmology* (Oxford University Press, 2007).

[201] L. F. Urrutia and E. Hernández, "Long-range behavior of nuclear forces as a manifestation of supersymmetry in nature," Phys. Rev. Lett. **51**, 755 (1983).

[202] V. A. Kostelecky and M. M. Nieto, "Evidence for a phenomenological supersymmetry in atomic physics," Phys. Rev. Lett. **54**, 851 (1985).

[203] N. Sourlas, "Introduction to supersymmetry in condensed matter physics," Physica D **15**, 115 (1985).

[204] M. Dine, *Supersymmetry and string theory: beyond the standard model* (Cambridge University Press, 2007).

[205] B. M. Rodríguez-Lara, "Intensity-dependent quantum rabi model: spectrum, supersymmetric partner, and optical simulation," J. Opt. B **31**, 1719 (2014).

[206] M. Tomka, M. Pletyukhov, and V. Gritsev, "Supersymmetry in quantum optics and in spin-orbit coupled systems," Sci. Rep. **5**, 13097 (2015).

[207] E. Witten, "Dynamical breaking of supersymmetry," Nucl. Phys. B **188**, 0 (1981).

[208] A. Khare, "Supersymmetry in quantum mechanics," Pramana **49**, 41 (1997).

[209] C. A. Blockley and G. E. Stedman, "Simple supersymmetry: I. basic examples," Eur. J. Phys. **6**, 218 (1985).

[210] R. Dutt, "Supersymmetry, shape invariance, and exactly solvable potentials," Am. J. Phys. **56**, 163 (1988).

[211] A. Arai, "Exactly solvable supersymmetric quantum mechanics," J. Math. Anal. Appl. **158**, 63 (1991).

[212] S. P. Maydanyuk, "SUSY-hierarchy of one-dimensional reflectionless potentials," Ann. Phys. **316**, 440 (2005).

[213] A. del Campo, M. G. Boshier, and A. Saxena, "Bent waveguides for matter-waves: supersymmetric potentials and reflectionless geometries," Sci. Rep. **4**, 5274 (2014).

[214] G. Dunne and J. Mannix, "Supersymmetry breaking with periodic potentials," Phys. Lett. B **428**, 115 (1998).

[215] G. Dunne and J. Feinberg, "Self-isospectral periodic potentials and supersymmetric quantum mechanics," Phys. Rev. D **57**, 1271 (1998).

[216] U. Sukhatme and A. Khare, "Supersymmetry and solvable periodic potentials," Phys. At. Nucl. **65**, 1122 (2002).

[217] D. J. Fernández C., B. Mielnik, O. Rosas-Ortiz, and B. F. Samsonov, "The phenomenon of darboux displacements," Phys. Lett. A **294**, 168 (2002).

[218] T. Iadecola and T. H. Hsieh, "Floquet supersymmetry," Phys. Rev. Lett. **120**, 210603 (2018).

[219] A. A. Andrianov and M. V. Ioffe, "Nonlinear supersymmetric quantum mechanics: concepts and realizations," J. Phys. A **45**, 503001 (2012).

[220] R. Hayward and F. Biancalana, "Constructing new nonlinear evolution equations with supersymmetry," J. Phys. A **51**, 275202 (2018).

[221] D. Bazeia, A. Das, L. Greenwood, and L. Losano, "The structure of supersymmetry in PT symmetric quantum mechanics," Phys. Lett. B **673**, 283 (2009).

[222] P. G. Kevrekidis, J. Cuevas–Maraver, A. Saxena, F. Cooper, and A. Khare, "Interplay between parity-time symmetry, supersymmetry, and nonlinearity: An analytically tractable case example," Phys. Rev. E **92**, 042901 (2015).

[223] F. Cooper, A. Khare, A. Comech, B. Mihaila, *et al.*, "Stability of exact solutions of the nonlinear Schrödinger equation in an external potential having supersymmetry and parity-time symmetry," J. Phys. A **50**, 015301 (2017).

[224] A. A. Izquierdo, M. A. G. Leon, M. T. Mayado, and J. M. Guilarte, "On two-dimensional superpotentials: from classical Hamilton–Jacobi theory to 2D supersymmetric quantum mechanics," J. Phys. A **37**, 10323 (2004).

[225] M. Ioffe, J. Mateos Guilarte, and P. Valinevich, "Two-dimensional supersymmetry: From SUSY quantum mechanics to integrable classical models," Ann. Phys. **321**, 2552 (2006).

[226] A. A. Andrianov, N. V. Borisov, and M. V. Ioffe, "Factorization method and darboux transformation for multidimensional hamiltonians," Theor. Math. Phys **61**, 1078 (1984).

[227] F. Cannata, M. Ioffe, and D. Nishnianidze, "Two-dimensional susy-pseudo-hermiticity without separation of variables," Phys. Lett. A **310**, 344 (2003).

[228] S. Kuru, A. Teğğmen, and A. Verçin, "Intertwined isospectral potentials in an arbitrary dimension," J. Math. Phys. **42**, 3344 (2001).

[229] J. F. Cariñena, A. Ramos, and D. J. Fernández C., "Group theoretical approach to the intertwined hamiltonians," Ann. Phys. **292**, 42 (2001).

[230] G. González, "Dirac equation and optical wave propagation in one dimension," Phys. Status Solidi , 1700357 (2017).

[231] A. Contreras-Astorga and V. Jakubský, "Photonic systems with two-dimensional landscapes of complex refractive index via time-dependent supersymmetry," Phys. Rev. A **99**, 053812 (2019).

[232] S. Yu, X. Piao, and N. Park, "Controlling random waves with digital building blocks based on supersymmetry," Phys. Rev. Appl. **8**, 054010 (2017).

[233] S. Yu, X. Piao, J. Hong, and N. Park, "Interdimensional optical isospectrality inspired by graph networks," Optica **3**, 836 (2016).

[234] J. Bai and D. S. Citrin, "Supersymmetric optimization of second-harmonic generation in mid-infrared quantum cascade lasers," Opt. Express **14**, 4043 (2006).

[235] B. Midya, H. Z. Xingdu, Q. Pei Miao, W. Walasik, *et al.*, "Supersymmetric microring laser arrays," Photonics Res. **7**, 363 (2019).

[236] D. A. Smirnova, P. Padmanabhan, and D. Leykam, "Parity anomaly laser," Opt. Lett. **44**, 1120 (2019).

[237] Q. Zhong, S. Nelson, M. Khajavikhan, D. Christodoulides, and R. El-Ganainy, "Bosonic discrete supersymmetry for quasi-two-dimensional optical arrays," Photonics Res. **7**, 1240 (2019).

[238] M. I. Afzal and Y. T. Lee, "Supersymmetrical bounding of asymmetric states and quantum phase transitions by anti-crossing of symmetric states," Sci. Rep. **6**, 39016 (2016).

[239] B. Midya, W. Walasik, N. M. Litchinitser, and L. Feng, "Supercharge optical arrays," Opt. Lett. **43**, 4927 (2018).

[240] S. Barkhofen, L. Lorz, T. Nitsche, C. Silberhorn, and H. Schomerus, "Supersymmetric polarization anomaly in photonic discrete-time quantum walks," Phys. Rev. Lett. **121**, 260501 (2018).

[241] R. El-Ganainy, K. G. Makris, and D. N. Christodoulides, "Local PT invariance and supersymmetric parametric oscillators," Phys. Rev. A **86**, 033813 (2012).

[242] B. Midya, "Supersymmetry-generated one-way-invisible PT-symmetric optical crystals," Phys. Rev. A **89**, 032116 (2014).

[243] F. Correa, V. Jakubský, and M. S. Plyushchay, "PT-symmetric invisible defects and confluent darboux-crum transformations," Phys. Rev. A **92**, 023839 (2015).

[244] C. García-Meca, A. Ortiz, and R. Sáez, "Supersymmetry in the time domain and its applications in optics." Nat. Commun. **11**, 813 (2020).

[245] A. Brandstötter, K. G. Makris, and S. Rotter, "Scattering-free pulse propagation through invisible non-hermitian media," Phys. Rev. B **99**, 115402 (2019).

[246] S. Longhi, "Bloch oscillations in tight-binding lattices with defects," Phys. Rev. B **81**, 195118 (2010).

[247] S. Longhi and G. Della Valle, "Invisible defects in complex crystals," Ann. Phys. **334**, 35 (2013).

[248] S. Longhi, "Supersymmetric bragg gratings," J. Opt. **17**, 045803 (2015).

[249] L. Infeld and T. E. Hull, "The factorization method," Rev. Mod. Phys. **23**, 21 (1951).

[250] G. E. Stedman, "Simple supersymmetry: II. Factorisation method in quantum mechanics," Eur. J. Phys. **6**, 225 (1985).

[251] C. Yifang, "Nanofabrication by electron beam lithography and its applications: A review," Microelectron. Eng. **135**, 57 (2015).

[252] N. Jiang, "On the spatial resolution limit of direct-write electron beam lithography," Microelectron. Eng. **168**, 41 (2017).

[253] L. Hogben, *Handbook of Linear Algebra* (Chapman & Hall/CRC, 2007).

[254] S. Dehdashti, R. Li, X. Liu, M. Raoofi, and H. Chen, "Role of intertwined hamiltonian in two dimensional classical optics," Laser Phys. **25**, 075201 (2015).

[255] A. Szameit, T. Pertsch, S. Nolte, A. Tünnermann, and F. Lederer, "Long-range interaction in waveguide lattices," Phys. Rev. A **77**, 043804 (2008).

[256] M. Lahrz, C. Weitenberg, and L. Mathey, "Implementing supersymmetric dynamics in ultracold-atom systems," Phys. Rev. A **96**, 043624 (2017).

[257] G. Ma, M. Xiao, and C. T. Chan, "Topological phases in acoustic and mechanical systems," Nat. Rev. Phys. **1**, 281 (2019).

[258] N. Zhao, X. Li, G. Li, and J. M. Kahn, "Capacity limits of spatially multiplexed free-space communication," Nat. Photonics **9**, 822 (2015).

[259] D. J. Richardson, J. M. Fini, and L. E. Nelson, "Space-division multiplexing in optical fibres," Nat. Photonics **7**, 354 (2013).

[260] D. Dai and J. E. Bowers, "Silicon-based on-chip multiplexing technologies and devices for Peta-bit optical interconnects," Nanophotonics **3**, 4 (2014).

[261] P. J. Winzer, "Making spatial multiplexing a reality," Nat. Photonics **8**, 345 (2014).

[262] G. Li, N. Bai, N. Zhao, and C. Xia, "Space-division multiplexing: the next frontier in optical communication," Adv. Opt. Photonics **6**, 413 (2014).

[263] B. Stern, X. Zhu, C. P. Chen, L. D. Tzuang, *et al.*, "On-chip mode-division multiplexing switch," Optica **2**, 530 (2015).

[264] H. Jia, T. Zhou, L. Zhang, J. Ding, *et al.*, "Optical switch compatible with wavelength division multiplexing and mode division multiplexing for photonic networks-on-chip," Opt. Express **25**, 20698 (2017).

[265] J. Wang, S. He, and D. Dai, "On-chip silicon 8-channel hybrid (de)multiplexer enabling simultaneous mode- and polarization-division-multiplexing," Laser Photonics Rev. **8**, L18 (2014).

[266] N. Bozinovic, Y. Yue, Y. Ren, M. Tur, *et al.*, "Terabit-scale orbital angular momentum mode division multiplexing in fibers," Science **340**, 1545 (2013).

[267] C. Xia, M. A. Eftekhar, R. A. Correa, J. E. Antonio-Lopez, *et al.*, "Supermodes in coupled multi-core waveguide structures," IEEE J. Quantum Electron. **22**, 4401212 (2016).

[268] D. Dai, "Silicon nanophotonic integrated devices for on-chip multiplexing and switching," J. Light. Technol. **35**, 572 (2016).

[269] T. A. Birks, I. Gris-Sánchez, S. Yerolatsitis, S. G. Leon-Saval, and R. R. Thomson, "The photonic lantern," Adv. Opt. Photonics **7**, 107 (2015).

[270] D. M. Mackie, "Multimode interference devices with input-output ports on the sides," Appl. Opt. **45**, 4933 (2006).

[271] D. A. B. Miller, "Reconfigurable add-drop multiplexer for spatial modes," Opt. Express **21**, 20220 (2013).

[272] Y. Ding, J. Xu, F. Da Ros, B. Huang, *et al.*, "On-chip two-mode division multiplexing using tapered directional coupler-based mode multiplexer and demultiplexer," Opt. Express **21**, 10376 (2013).

[273] Z. Zhang, X. Hu, and J. Wang, "On-chip optical mode exchange using tapered directional coupler," Sci. Rep. **5**, 16072 (2015).

[274] L.-W. Luo, N. Ophir, C. P. Chen, L. H. Gabrielli, *et al.*, "WDM-compatible mode-division multiplexing on a silicon chip," Nat. Commun. **5**, 3069 (2014).

[275] J. Xing, Z. Li, X. Xiao, J. Yu, and Y. Yu, "Two-mode multiplexer and demultiplexer based on adiabatic couplers," Opt. Lett. **38**, 3468 (2013).

[276] Y. Luo, Y. Yo, M. Ye, C. Sun, and X. Zhang, "Integrated dual-mode 3dB power coupler based on tapered directional coupler," Sci. Rep. **6**, 23516 (2016).

[277] J. B. Driscoll, R. R. Grote, B. Souhan, J. I. Dadap, *et al.*, "Asymmetric Y junctions in silicon waveguides for on-chip mode-division multiplexing," Opt. Lett. **38**, 1854 (2013).

[278] W. Chen, P. Wang, T. Yang, G. Wang, *et al.*, "Silicon three-mode (de)multiplexer based on cascaded asymmetric Y junctions," Opt. Lett. **41**, 2851 (2016).

[279] W. Bogaerts, P. De Heyn, T. Van Vaerenbergh, K. De Vos, *et al.*, "Silicon microring resonators," Laser Photonics Rev. **6**, 47 (2012).

[280] B. A. Dorin and W. N. Ye, "Two-mode division multiplexing in a silicon-on-insulator ring resonator," Opt. Express **22**, 4547 (2014).

[281] S. Longhi, G. Della Valle, M. Ornigotti, and P. Laporta, "Coherent tunneling by adiabatic passage in an optical waveguide system," Phys. Rev. B **76**, 201101 (2007).

[282] R. Menchon-Enrich, A. Llobera, V. J. Cadarso, J. Mompart, and V. Ahufinger, "Adiabatic passage of light in CMOS-compatible silicon oxide integrated rib waveguides," IEEE Photonic Tech. Lett. **24**, 536 (2012).

[283] K. Eckert, M. Lewenstein, R. Corbalán, G. Birkl, *et al.*, "Three-level atom optics via the tunneling interaction," Phys. Rev. A **70**, 23606 (2004).

[284] A. D. Greentree, J. H. Cole, A. R. Hamilton, and L. C. L. Hollenberg, "Coherent electronic transfer in quantum dot systems using adiabatic passage," Phys. Rev. B **70**, 235317 (2004).

[285] N. V. Vitanov, T. Halfmann, B. W. Shore, and K. Bergmann, "Laser-induced population transfer by adiabatic passage techniques," Ann. Rev. Phys. Chem. **52**, 763 (2001).

[286] G. Della Valle, M. Ornigotti, T. Toney Fernandez, P. Laporta, *et al.*, "Adiabatic light transfer via dressed states in optical waveguide arrays," Appl. Phys. Lett. **92**, 011106 (2008).

[287] C. Ciret, V. Coda, A. A. Rangelov, D. N. Neshev, and G. Montemezzani, "Broadband adiabatic light transfer in optically induced waveguide arrays," Phys. Rev. A **87**, 013806 (2013).

[288] A. Barak, Y. Lamhot, L. Friedland, and M. Segev, "Autoresonant dynamics of optical guided waves," Phys. Rev. Lett. **103**, 123901 (2009).

[289] E.-M. Graefe, A. A. Mailybaev, and N. Moiseyev, "Breakdown of adiabatic transfer of light in waveguides in the presence of absorption," Phys. Rev. A **88**, 033842 (2013).

[290] S. Longhi, "Transfer of light waves in optical waveguides via a continuum," Phys. Rev. A **78**, 013815 (2008).

[291] F. Dreisow, A. Szameit, M. Heinrich, R. Keil, *et al.*, "Adiabatic transfer of light via a continuum in optical waveguides," Opt. Lett. **34**, 2405 (2009).

[292] J. A. Vaitkus, M. J. Steel, and A. D. Greentree, "Digital waveguide adiabatic passage part 1: theory," Opt. Express **25**, 5466 (2017).

[293] V. Ng, J. A. Vaitkus, Z. J. Chaboyer, T. Nguyen, *et al.*, "Digital waveguide adiabatic passage part 2: experiment," Opt. Express **25**, 2552 (2017).

[294] S. Longhi, "Photonic transport via chirped adiabatic passage in optical waveguides," J. Phys. B **40**, F189 (2007).

[295] R. Menchon-Enrich, A. Llobera, J. Vila-Planas, and V. J. Cadarso M., "Light spectral filtering based on spatial adiabatic passage," Light Sci. Appl. **2**, e90 (2013).

[296] L.-T. Feng, M. Zhang, Z.-Y. Zhou, M. Li, *et al.*, "On-chip coherent conversion of photonic quantum entanglement between different degrees of freedom," Nat. Commun. **7**, 11985 (2016).

[297] A. Mohanty, M. Zhang, A. Dutt, S. Ramelow, *et al.*, "Quantum interference between transverse spatial waveguide modes," Nat. Commun. **8**, 14010 (2017).

[298] A. Ymeti, J. S. Kanger, R. Wijn, P. V. Lambeck, and J. Greve, "Development of a multichannel integrated interferometer immunosensor," Sens. Actuator B-Chem. **83**, 1 (2002).

[299] Z. Weissman and A. Hardy, "2-D mode tapering via tapered channel waveguide segmentation," Electronics Lett. **28**, 1514 (1992).

[300] M. H. Chou, M. A. Arbore, and M. M. Fejer, "Adiabatically tapered periodic segmentation of channel waveguides for mode-size transformation and fundamental mode excitation," Opt. Lett. **21**, 794 (1996).

[301] R. Heilmann, C. Greganti, M. Gräfe, S. Nolte, *et al.*, "Tapering of femtosecond laser-written waveguides," Appl. Opt. **57**, 377 (2018).

[302] T. Liu, A. S. Solntsev, A. Boes, T. Nguyen, *et al.*, "Experimental demonstration of bidirectional light transfer in adiabatic waveguide structures," Opt. Lett. **41**, 5278 (2016).

[303] J. Leuthold, R. Hess, J. Eckner, P. A. Besse, and H. Melchior, "Spatial mode filters realized with multimode interference couplers," Opt. Lett. **21**, 836 (1996).

[304] Y. Huang, G. Xu, and S.-T. Ho, "An ultracompact optical mode order converter," IEEE Photonic Tech. Lett. **18**, 2281 (2006).

[305] V. A. Vysloukh, Y. V. Kartashov, and K. Staliunas, "Efficient mode conversion in guiding structures with longitudinal modulation of nonlinearity," Opt. Lett. **40**, 4631 (2015).

[306] Y. B. Ovchinnikov, "A planar waveguide beam splitter," Opt. Commun. **220**, 229 (2003).

[307] J. Liu, Z. Zhang, S. Chang, C. Flueraru, and C. P. Grover, "Directly writing of 1-to-N optical waveguide power splitters in fused silica glass using a femtosecond laser," Opt. Commun. **253**, 315 (2005).

[308] W. Burns and A. Milton, "An analytic solution for mode coupling in optical waveguide branches," IEEE J. Quantum Electron. **16**, 446 (1980).

[309] J. Love and N. Riesen, "Single-, few-, and multimode Y-junctions," J. Light. Technol. **30**, 304 (2012).

[310] N. Riesen and J. D. Love, "Design of mode-sorting asymmetric Y-junctions," Appl. Opt. **51**, 2778 (2012).

[311] G. Li, K. A. Winick, A. A. Said, M. Dugan, and P. Bado, "Waveguide electro-optic modulator in fused silica fabricated by femtosecond laser direct writing and thermal poling," Opt. Lett. **31**, 739 (2006).

[312] Y. Liao, J. Xu, Y. Cheng, Z. Zhou, *et al.*, "Electro-optic integration of embedded electrodes and waveguides in $LiNbO_3$ using a femtosecond laser," Opt. Lett. **33**, 2281 (2008).

[313] D. Comparat, "General conditions for quantum adiabatic evolution," Phys. Rev. A **80**, 012106 (2009).

[314] X. Sun, H.-C. Liu, and A. Yariv, "Adiabaticity criterion and the shortest adiabatic mode transformer in a coupled-waveguide system," Opt. Lett. **34**, 280 (2009).

[315] K. S. Kaur, A. Z. Subramanian, Y. J. Ying, D. P. Banks, *et al.*, "Waveguide mode filters fabricated using laser-induced forward transfer," Opt. Express **19**, 9814 (2011).

[316] M. Zhang, K. Chen, W. Jin, and K. S. Chiang, "Electro-optic mode switch based on lithium-niobate Mach–Zehnder interferometer," Appl. Opt. **55**, 4418 (2016).

[317] E. Schipper, A. Brugman, C. Dominguez, L. Lechuga, *et al.*, "The realization of an integrated Mach-Zehnder waveguide immunosensor in silicon technology," Sens. Actuator B-Chem. **40**, 147 (1997).

[318] L. N. Binh, "Lithium niobate optical modulators: Devices and applications," J. Cryst. Growth **288**, 180 (2006).

[319] R. S. Weisand and T. K. Gaylord, "Lithium niobate: Summary of physical properties and crystal structure," Appl. Phys. A **37**, 191 (1985).

[320] M. Hammer and O. V. Ivanova, "Effective index approximations of photonic crystal slabs: a 2-to-1-D assessment," Opt. Quant. Electron. **41**, 267 (2009).

[321] D. Castaldini, P. Bassi, P. Aschieri, S. Tascu, *et al.*, "High performance mode adapters based on segmented SPE:$LiNbO_3$ waveguides," Opt. Express **17**, 17868 (2009).

[322] T. Lunghi, F. Doutre, A. P. Rambu, M. Bellec, *et al.*, "Broadband integrated beam splitter using spatial adiabatic passage," Opt. Express **26**, 27058 (2018).

[323] C. Brading, *Symmetries in Physics: Philosophical Reflections* (Cambridge University Press, 2003).

[324] S. Coleman and J. Mandula, "All possible symmetries of the S-matrix," Phys. Rev. **159**, 1251 (1967).

[325] R. Haag, J. T. Łopuszański, and M. Sohnius, "All possible generators of supersymmetries of the S-matrix," Nucl. Phys. B **88**, 257 (1975).

[326] T. Grover, D. N. Sheng, and A. Vishwanath, "Emergent space-time supersymmetry at the boundary of a topological phase," Science **344**, 280 (2014).

[327] B. I. Halperin, "Quantized Hall conductance, current-carrying edge states, and the existence of extended states in a two-dimensional disordered potential," Phys. Rev. B **25**, 2185 (1982).

[328] A. H. MacDonald and P. Středa, "Quantized Hall effect and edge currents," Phys. Rev. B **29**, 1616 (1984).

[329] X.-L. Qi, Y.-S. Wu, and S.-C. Zhang, "General theorem relating the bulk topological number to edge states in two-dimensional insulators," Phys. Rev. B **74**, 45125 (2006).

[330] X.-L. Qi and S.-C. Zhang, "Topological insulators and superconductors," Rev. Mod. Phys. **83**, 1057 (2011).

[331] N. Goldman, J. C. Budich, and P. Zoller, "Topological quantum matter with ultracold gases in optical lattices," Nat. Phys. **12**, 639 (2016).

[332] M. Xiao, G. Ma, Z. Yang, P. Sheng, *et al.*, "Geometric phase and band inversion in periodic acoustic systems," Nat. Phys. **11**, 240 (2015).

[333] J. Ningyuan, C. Owens, A. Sommer, D. Schuster, and J. Simon, "Time- and site-resolved dynamics in a topological circuit," Phys. Rev. X **5**, 021031 (2015).

[334] C. L. Kane and T. C. Lubensky, "Topological boundary modes in isostatic lattices," Nat. Phys. **10**, 39 (2014).

[335] Y. Tokura, K. Yasuda, and A. Tsukazaki, "Magnetic topological insulators," Nat. Rev. Phys. **1**, 126 (2019).

[336] G. Jotzu, M. Messer, R. Desbuquois, M. Lebrat, *et al.*, "Experimental realization of the topological haldane model with ultracold fermions," Nature **515**, 237 (2014).

[337] L. Lu, J. D. Joannopoulos, and M. Soljačić, "Topological photonics," Nat. Photonics **8**, 821 (2014).

[338] A. B. Khanikaev and G. Shvets, "Two-dimensional topological photonics," Nat. Photonics **11**, 763 (2017).

[339] Y. Wu, C. Li, X. Hu, Y. Ao, *et al.*, "Applications of topological photonics in integrated photonic devices," Adv. Opt. Mater. **5**, 1700357 (2017).

[340] B.-Y. Xie, H.-F. Wang, X.-Y. Zhu, M.-H. Lu, *et al.*, "Photonics meets topology," Opt. Express **26**, 24531 (2018).

[341] Y. E. Kraus, Y. Lahini, Z. Ringel, M. Verbin, and O. Zilberberg, "Topological states and adiabatic pumping in quasicrystals," Phys. Rev. Lett. **109**, 106402 (2012).

[342] M. Hafezi, S. Mittal, J. Fan, A. Migdall, and J. M. Taylor, "Imaging topological edge states in silicon photonics," Nat. Photonics **7**, 1001 (2013).

[343] J. K. Asbóth, L. Oroszlány, and A. Pályi, *A short course on topological insulators* (Springer International Publishing, 2016).

[344] M. Atala, M. Aidelsburger, J. T. Barreiro, D. Abanin, *et al.*, "Direct measurement of the Zak phase in topological Bloch bands," Nat. Phys. **9**, 795 (2013).

[345] S. Nakajima, T. Tomita, S. Taie, T. Ichinose, *et al.*, "Topological Thouless pumping of ultracold fermions," Nat. Phys. **12**, 296 (2016).

[346] L. Wang, M. Troyer, and X. Dai, "Topological charge pumping in a one-dimensional optical lattice," Phys. Rev. Lett. **111**, 026802 (2013).

[347] A. Blanco-Redondo, I. Andonegui, M. J. Collins, G. Harari, *et al.*, "Topological optical waveguiding in silicon and the transition between topological and trivial defect states," Phys. Rev. Lett. **116**, 163901 (2016).

[348] S. Weimann, M. Kremer, Y. Plotnik, Y. Lumer, *et al.*, "Topologically protected bound states in photonic parity–time-symmetric crystals," Nat. Mat. **16**, 433 (2016).

[349] A. Blanco-Redondo, B. Bell, D. Oren, B. J. Eggleton, and M. Segev, "Topological protection of biphoton states," Science **362**, 568 (2018).

[350] M. Wang, C. Doyle, B. Bell, M. J. Collins, *et al.*, "Topologically protected entangled photonic states," Nanophotonics **8**, 1327 (2019).

[351] J. Zak, "Berry's phase for energy bands in solids," Phys. Rev. Lett. **62**, 2747 (1989).

[352] S. Ryu and Y. Hatsugai, "Topological origin of zero-energy edge states in particle-hole symmetric systems," Phys. Rev. Lett. **89**, 077002 (2002).

[353] J.-W. Rhim, J. H. Bardarson, and R.-J. Slager, "Unified bulk-boundary correspondence for band insulators," Phys. Rev. B **97**, 115143 (2018).

[354] A. Kitaev, V. Lebedev, and M. Feigelman, "Periodic table for topological insulators and superconductors," AIP Conf. Proc. **1134**, 22 (2009).

[355] S. Ryu, A. P. Schnyder, A. Furusaki, and A. W. W. Ludwig, "Topological insulators and superconductors: tenfold way and dimensional hierarchy," New J. Phys. **12**, 065010 (2010).

[356] A. M. Streltsov and N. F. Borrelli, "Study of femtosecond-laser-written waveguides in glasses," J. Opt. **19**, 2496 (2002).

[357] J. Dalibard, F. Gerbier, G. Juzeliūnas, and P. Öhberg, "Colloquium: Artificial gauge potentials for neutral atoms," Rev. Mod. Phys. **83**, 1523 (2011).

[358] M. Aidelsburger, S. Nascimbene, and N. Goldman, "Artificial gauge fields in materials and engineered systems," C. R. Phys. **19**, 394 (2018).

[359] R. O. Umucalilar and I. Carusotto, "Artificial gauge field for photons in coupled cavity arrays," Phys. Rev. A **84**, 043804 (2011).

[360] M. C. Rechtsman, J. M. Zeuner, A. Tünnermann, S. Nolte, *et al.*, "Strain-induced pseudomagnetic field and photonic landau levels in dielectric structures," Nat. Photonics **7**, 153 (2012).

[361] N. Goldman, G. Juzeliūnas, P. Öhberg, and I. B. Spielman, "Light-induced gauge fields for ultracold atoms," Rep. Progress Phys. **77**, 126401 (2014).

[362] Y. Lumer, M. A. Bandres, M. Heinrich, L. J. Maczewsky, *et al.*, "Light guiding by artificial gauge fields," Nat. Photonics **13**, 339 (2019).

[363] K. Fang, Z. Yu, and S. Fan, "Realizing effective magnetic field for photons by controlling the phase of dynamic modulation," Nat. Photonics **6**, 782 (2012).

[364] N. Goldman and J. Dalibard, "Periodically driven quantum systems: Effective Hamiltonians and engineered gauge fields," Phys. Rev. X **4**, 031027 (2014).

[365] C. Jörg, F. Letscher, M. Fleischhauer, and G. v. Freymann, "Dynamic defects in photonic Floquet topological insulators," New J. Phys. **19**, 083003 (2017).

[366] L.-H. Wu and X. Hu, "Scheme for achieving a topological photonic crystal by using dielectric material," Phys. Rev. Lett. **114**, 223901 (2015).

[367] L. Allen, M. Beijersbergen, R. Spreeuw, and J. Woerdman, "Orbital angular momentum of light and the transformation of Laguerre-Gaussian laser modes," Phys. Rev. A **45**, 8185 (1992).

[368] C. N. Alexeyev, N. A. Boklag, and M. A. Yavorsky, "Higher order modes of coupled optical fibres," J. Opt. **12**, 115704 (2010).

[369] J. Wang, J.-Y. Yang, I. M. Fazal, N. Ahmed, *et al.*, "Terabit free-space data transmission employing orbital angular momentum multiplexing," Nat. Photonics **6**, 488 (2012).

[370] Y. Chen, J. Gao, Z.-Q. Jiao, K. Sun, *et al.*, "Mapping twisted light into and out of a photonic chip," Phys. Rev. Lett. **121**, 233602 (2018).

[371] Z. Xie, S. Gao, T. Lei, S. Feng, *et al.*, "Integrated (de)multiplexer for orbital angular momentum fiber communication," Photon. Res. **6**, 743 (2018).

[372] L. Zhu, A. Wang, S. Chen, J. Liu, *et al.*, "Orbital angular momentum mode groups multiplexing transmission over 26-km conventional multi-mode fiber," Opt. Express **25**, 25637 (2017).

[373] G. Xavier and G. Lima, "Quantum information processing with space-division multiplexing optical fibres," Commun. Phys. **3**, 9 (2020).

[374] K. Dholakia and T. Čižmár, "Shaping the future of manipulation," Nat. Photonics **5**, 335 (2011).

[375] M. Padgett and R. Bowman, "Tweezers with a twist," Nat. Photonics **5**, 343 (2011).

[376] X.-W. Luo, X. Zhou, J.-S. Xu, C.-F. Li, *et al.*, "Synthetic-lattice enabled all-optical devices based on orbital angular momentum of light," Nat. Commun. **8**, 16097 (2017).

[377] S. W. Hell and J. Wichmann, "Breaking the diffraction resolution limit by stimulated emission: stimulated-emission-depletion fluorescence microscopy," Opt. Lett. **19**, 780 (1994).

[378] J. Fischer and M. Wegener, "Three-dimensional optical laser lithography beyond the diffraction limit," Laser Photonics Rev. **7**, 22 (2013).

[379] L. Marrucci, C. Manzo, and D. Paparo, "Pancharatnam-berry phase optical elements for wave front shaping in the visible domain: Switchable helical mode generation," Appl. Phys. Lett. **88**, 221102 (2006).

[380] M. Beijersbergen, R. Coerwinkel, M. Kristensen, and J. Woerdman, "Helical-wavefront laser beams produced with a spiral phaseplate," Opt. Commun. **112**, 321 (1994).

[381] L. Zhu and J. Wang, "Arbitrary manipulation of spatial amplitude and phase using phase-only spatial light modulators," Sci. Rep. **4**, 7441 (2014).

[382] X. Cai, J. Wang, M. J. Strain, B. Johnson-Morris, *et al.*, "Integrated compact optical vortex beam emitters," Science **338**, 363 (2012).

[383] J. Sun, M. Moresco, G. Leake, D. Coolbaugh, and M. R. Watts, "Generating and identifying optical orbital angular momentum with silicon photonic circuits," Opt. Lett. **39**, 5977 (2014).

[384] A. Crespi and F. Bragheri, "Projecting light beams with 3D waveguide arrays," J. Phys. B **50**, 014002 (2017).

[385] D. Naidoo, F. S. Roux, A. Dudley, I. Litvin, *et al.*, "Controlled generation of higher-order Poincaré sphere beams from a laser," Nat. Photonics **10**, 327 (2016).

[386] C. Jörg, G. Queraltó, M. Kremer, G. Pelegrí, *et al.*, "Experimental observation of Aharonov-Bohm caging using orbital angular momentum modes in optical waveguides," arXiv e-prints (2020), arXiv:2004.07038.

[387] J. Vidal, R. Mosseri, and B. Douçot, "Aharonov-Bohm cages in two-dimensional structures," Phys. Rev. Lett. **81**, 5888 (1998).

[388] J. Vidal, B. Douçot, R. Mosseri, and P. Butaud, "Interaction induced delocalization for two particles in a periodic potential," Phys. Rev. Lett. **85**, 3906 (2000).

[389] K. Fang, Z. Yu, and S. Fan, "Photonic Aharonov-Bohm effect based on dynamic modulation," Phys. Rev. Lett. **108**, 153901 (2012).

[390] S. Longhi, "Aharonov–Bohm photonic cages in waveguide and coupled resonator lattices by synthetic magnetic fields," Opt. Lett. **39**, 5892 (2014).

[391] S. Mukherjee and R. R. Thomson, "Observation of localized flat-band modes in a quasi-one-dimensional photonic rhombic lattice," Opt. Lett. **40**, 5443 (2015).

[392] M. Di Liberto, S. Mukherjee, and N. Goldman, "Nonlinear dynamics of aharonov-bohm cages," Phys. Rev. A **100**, 043829 (2019).

[393] G. Gligorić, P. P. Beličev, D. Leykam, and A. Maluckov, "Nonlinear symmetry breaking of aharonov-bohm cages," Phys. Rev. A **99**, 013826 (2019).

[394] S. Mukherjee, M. Di Liberto, P. Öhberg, R. R. Thomson, and N. Goldman, "Experimental observation of Aharonov-Bohm cages in photonic lattices," Phys. Rev. Lett. **121**, 075502 (2018).

[395] M. Kremer, I. Petrides, E. Meyer, M. Heinrich, *et al.*, "A square-root topological insulator with non-quantized indices realized with photonic Aharonov-Bohm cages," Nat. Commun. **11**, 907 (2020).

[396] F. Liu, T. Xu, S. Wang, Z. H. Hang, and J. Li, "Polarization beam splitting with gauge field metamaterials," Adv. Opt. Mat. , 1801582 (2019).

[397] Y. Hadad, A. B. Khanikaev, and A. Alù, "Self-induced topological transitions and edge states supported by nonlinear staggered potentials," Phys. Rev. B **93**, 155112 (2016).

[398] R. Keil, B. Pressl, R. Heilmann, M. Gräfe, *et al.*, "Direct measurement of second-order coupling in a waveguide lattice," Appl. Phys. Lett. **107**, 241104 (2015).

[399] J. Polo, J. Mompart, and V. Ahufinger, "Geometrically induced complex tunnelings for ultracold atoms carrying orbital angular momentum," Phys. Rev. A **93**, 033613 (2016).

[400] A. Turpin, G. Pelegrí, J. Polo, J. Mompart, and V. Ahufinger, "Engineering of orbital angular momentum supermodes in coupled optical waveguides," Sci. Rep. **7**, 44057 (2017).

[401] C. N. Alexeyev, A. N. Alexeyev, N. A. Boklag, and M. A. Yavorsky, "Effect of the spin–orbit interaction on polarization conversion in coupled waveguides," J.Opt. A **11**, 125404 (2009).

[402] S. Dottermusch, D. Busko, M. Langenhorst, U. W. Paetzold, and B. S. Richards, "Exposure-dependent refractive index of nanoscribe ip-dip photoresist layers," Opt. Lett. **44**, 29 (2019).

[403] E. Waller and G. von Freymann, "Spatio-temporal proximity characteristics in 3D μ-printing via multi-photon absorption," Polymers **8**, 297 (2016).

[404] C. Jörg, *Interfaces and defects in topological model systems of 3D micro-printed waveguides*, Ph.D. thesis, Technische Universität Kaiserslautern (2019).

[405] S. Mukherjee, H. K. Chandrasekharan, P. Öhberg, N. Goldman, and R. R. Thomson, "State-recycling and time-resolved imaging in topological photonic lattices," Nat. Commun. **9**, 4209 (2018).

[406] V. Sala, D. Solnyshkov, I. Carusotto, T. Jacqmin, *et al.*, "Spin-orbit coupling for photons and polaritons in microstructures," Phys. Rev. X **5**, 011034 (2015).

[407] Z.-Y. Zhou, Y. Li, D.-S. Ding, W. Zhang, *et al.*, "Orbital angular momentum photonic quantum interface," Light Sci. Appl. **5**, e16019 (2016).

[408] A. Perez-Leija, R. Keil, A. Kay, H. Moya-Cessa, *et al.*, "Coherent quantum transport in photonic lattices," Phys. Rev. A **87**, 012309 (2013).

[409] N. Lang and H. P. Büchler, "Topological networks for quantum communication between distant qubits," npj Quantum Inf. **3**, 47 (2017).

[410] S. Longhi, G. L. Giorgi, and R. Zambrini, "Landau–zener topological quantum state transfer," Adv. Quantum Tech. **2**, 1800090 (2019).